ESCOLA DE DOUTORAMENTO
INTERNACIONAL DA USC

Carlos Damián
Rodríguez Fernández

Tese de doutoramento

An experimental and
computational research on the
optical properties of ionic
liquids

Santiago de Compostela, 2021

Programa de Doutoramento en Láser, Fotónica e Visión

AN EXPERIMENTAL AND COMPUTATIONAL RESEARCH ON THE OPTICAL PROPERTIES OF IONIC LIQUIDS

Carlos Damián Rodríguez Fernández

SANTIAGO DE COMPOSTELA

2021

DECLARACIÓN DO AUTOR/A DA TESE

D./
Dna.   **Carlos Damián Rodríguez Fernández**

Título da   Estudo experimental e computacional das propiedades ópticas
tese: dos líquidos iónicos

Presento a miña tese, seguindo o procedemento axeitado ao Regulamento, e declaro que:

1) A tese abarca os resultados da elaboración do meu traballo.
2) De ser o caso, na tese faise referencia ás colaboracións que tivo este traballo.
3) Confirmo que a tese non incorre en ningún tipo de plaxio doutros autores nin de traballos presentados por min para a obtención doutros títulos.
4) A tese é a versión definitiva presentada para a súa defensa e coincide a versión impresa coa presentada en formato electrónico

E comprométome a presentar o Compromiso Documental de Supervisión no caso de que o orixinal non estea na Escola.

En **Santiago de Compostela**, **20 de Decembro de 2021**.

Sinatura electrónica

AUTORIZACIÓN DO DIRECTOR DA TESE

Estudo experimental e computacional das propiedades ópticas dos líquidos iónicos

D. Luis Miguel Varela Cabo

INFORMA:

Que a presente tese, correspóndese co traballo realizado por D. Carlos Damián Rodríguez Fernández , baixo a miña dirección, e autorizo a súa presentación, considerando que reúne os requisitos esixidos no Regulamento de Estudos de Doutoramento da USC, e que como director desta non incorre nas causas de abstención establecidas na Lei 40/2015.

De acordo co indicado no Regulamento de Estudos de Doutoramento, declara tamén que a presente tese de doutoramento é idónea para ser defendida en base á modalidade de Monográfica con reproducción de publicaciones, nos que a participación do/a doutorando/a foi decisiva para a súa elaboración e as publicacións se axustan ao Plan de Investigación.

En Santiago de Compostela, 20 de Decembro de 2021

AUTORIZACIÓN DO DIRECTOR DA TESE

Estudo experimental e computacional das propiedades ópticas dos líquidos iónicos

D./Dna. María Elena López Lago

INFORMA:

Que a presente tese, correspóndese co traballo realizado por D. Carlos Damián Rodríguez Fernández, baixo a miña dirección e autorizo a súa presentación, considerando que reúne os requisitos esixidos no Regulamento de Estudos de Doutoramento da USC, e que como director desta non incorre nas causas de abstención establecidas na Lei 40/2015.

De acordo co indicado no Regulamento de Estudos de Doutoramento, declara tamén que a presente tese de doutoramento é idónea para ser defendida en base á modalidade de Monográfica con reprodución de publicacións, nos que a participación do/a doutorando/a foi decisiva para a súa elaboración e as publicacións se axustan ao Plan de Investigación.

En Santiago de Compostela, 27 de Decembro de 2021

AUTORIZACIÓN TITOR DA TESE

Estudo experimental e computacional das propiedades ópticas dos líquidos iónicos

D. Raúl de la Fuente Carballo

INFORMA:

Que a presente tese, correspóndese co traballo realizado por D. Carlos Damián Rodríguez Fernández, baixo a miña titorización, e autorizo a súa presentación, considerando que reúne os requisitos esixidos no Regulamento de Estudos de Doutoramento da USC, e que como titor desta non incorre nas causas de abstención establecidas na Lei 40/2015.

De acordo co indicado no Regulamento de Estudos de Doutoramento, declara tamén que a presente tese de doutoramento é idónea para ser defendida en base á modalidade de Monográfica con reproducción de publicaciones, nos que a participación do/a doutorando/a foi decisiva para a súa elaboración e as publicacións se axustan ao Plan de Investigación.

En Santiago de Compostela, 29 de Decembro de 2021

Resumo

Os líquidos iónicos son materiais exclusivamente compostos por ións e que se atopan en estado líquido a temperaturas por debaixo dos 100 °C. Este tipo de sales fundidos a baixa temperatura foron descritos por primeira vez por Paul Walden en 1914, pero non recibiron o interese que merecían ata finais do século XX, cando se sintetizaron as primeiras familias de líquidos iónicos estables en contacto con aire e auga. Dende ese momento, os líquidos iónicos convertéronse en obxecto dunha intensa actividade científica polo seu único *set* de propiedades, que inclúe, entre outras: estabilidade química e térmica, baixa inflamabilidade, extremadamente baixa presión de vapor ou ampla xanela electroquímica. Porén, a característica máis interesante dos líquidos iónicos é a súa grande flexibilidade en canto a estrutura e composición, o que permite deseñar as súas propiedades á medida, motivo polo cal son tamén coñecidos como líquidos intelixentes ou de deseño.

A posibilidade de deseñar as propiedades dos líquidos iónicos á carta, fixo deles materiais con potenciais aplicacións nos máis diversos eidos científicos e industriais. Neste sentido, existen numerosos estudos sobre o rendemento de líquidos iónicos para capturar dióxido de carbono, para mellorar a eficiencia de lubricantes mecánicos, para incrementar as capacidades de almacenaxe de baterías, ou como medio máis ecolóxico e eficiente para levar ao cabo procesos de catálise ou separación química. Non obstante, existen aínda ámbitos nos que o papel que poden xogar os líquidos iónicos está por determinar, como é o caso da fotónica, que é a disciplina científica que toma como obxecto de estudo a luz e a súa interacción coa materia. A fotónica é un eido con numerosas aplicacións industriais, incluíndo láseres, pantallas dixitais, febras ópticas ou sensores fotónicos. Nestas aplicacións, a escolla das propiedades ópticas dos materiais é primordial: buscamos materiais que emitan ou reemitan luz cunhas certas características espectrais, que absorban unhas certas lonxitudes de onda ou que presenten unha

dispersión material, resposta non linear ou forma de polarizar axeitadas aos nosos intereses. E por suposto, todo isto, sen nunca esquecer a obrigada procura de maior eficiencia e menor pegada ecolóxica. Neste sentido, os líquidos iónicos, materiais verdes con propiedades altamente sintonizables, son candidatos idóneos para xogar un papel relevante na fotónica do futuro.

Os estudos dispoñibles sobre propiedades ópticas en líquidos iónicos, amosan uns materiais con grande potencialidade: o seu índice de refracción pode sintonizarse coa escolla de ións, poden presentar unha ampla gama de cromismos, incluídos termocromismo, fotocromismo e electrocromismo, exhibir respostas non lineais relevantes ou estabilizar fases de cristal líquido. Desafortunadamente, aínda é preciso coñecer mellor as relacións destas prometedoras propiedades ópticas coa estrutura dos líquidos iónicos para que estes poidan implementarse en aplicacións fotónicas reais, como poden ser sensores ópticos de diversa índole, febras ópticas de núcleo líquido, lentes líquidas de focal variable, ou como cristais líquidos en dispositivos de visualización.

O propósito desta tese é estudar as propiedades ópticas dos líquidos iónicos, nomeadamente dispersión material, resposta non linear, espectro de absorción e carácter de cristal líquido, así como as principais relacións destas propiedades coa súa estrutura a diferentes escalas características. A fin última deste esforzo investigador é identificar os mecanismos máis prometedores para o deseño intelixente das propiedades ópticas dos líquidos iónicos e facilitar, deste modo, a súa inclusión como materiais de primeira orde no eido da fotónica. Para acadar este obxectivo, estudáronse unha grande cantidade de líquidos iónicos nas páxinas desta tese, tanto dende un punto de vista experimental como computacional. É xustamente esta metodoloxía híbrida a que permite achegarse ao mundo dos líquidos iónicos dende moi diversas escalas características. O traballo experimental aporta unha visión efectiva das propiedades macroscópicas e mesoscópicas destes líquidos, mentres que a metodoloxía computacional, que inclúe simulacións de dinámica molecular (MD) e teoría do funcional

densidade (DFT), ofrece a posibilidade de achegarse a estes sistemas a través de escalas microscópicas, que abranguen dende as poucas ducias de nanómetros ata aos poucos angstroms.

Esta tese está estruturada en catro partes ben diferencias: introdución, material e métodos, resultados e conclusións. A introdución, formada polo capítulo 1, conta cunha motivación na que se expón o porqué da investigación realizada, unha explicación completa sobre que son os líquidos iónicos e a importancia dos materiais no eido da fotónica, e un resumo das propiedades ópticas máis interesantes que poden presentar os líquidos iónicos. Ademais, contén unha breve descrición dos principais obxectivos desta tese.

A segunda parte, composta polo capítulo 2, contén unha sección adicada aos materiais e unha serie de seccións adicadas á metodoloxía. Na sección de materiais, indícanse nome, abreviación e estrutura de todos os líquidos iónicos considerados nalgún punto da tese. Pola outra banda, nas seccións de metodoloxía, ofrécese unha detallada explicación dos diferentes métodos experimentais e computacionais empregados. Na sección de metodoloxía experimental, recóllense os modelos dos equipos e protocolos de medida para as principais técnicas experimentais, como, por exemplo, difracción de raios X (DRX), resonancia magnética nuclear (NMR) ou calorimetría diferencial de varrido (DSC). Non obstante, é nas técnicas de caracterización ópticas onde se fai especial fincapé. Neste sentido, esta sección ofrece unha descrición en profundidade da novidosa técnica empregada para medir a dispersión material dos distintos líquidos iónicos, a técnica coñecida como Refractometría Espectral por Interferencia de Banda Ancha (REIBA) ou, en inglés, Refractive Index Spectroscopy by Broadband Interference (RISBI). O dispositivo REIBA empregado nesta tese implementouse manualmente no noso laboratorio e o seu método de funcionamento, especificacións técnicas, así como unha completa análise da súa incerteza instrumental, poden consultarse neste apartado. En canto ás seccións de metodoloxía computacional, nelas explícanse os fundamentos teóricos da dinámica molecular (MD) e da teoría do funcional densidade (DFT), xunto cos principais pasos

seguidos para executar as simulacións de cada tipo. A maiores, ofrécese unha explicación detallada do cálculo das principais magnitudes de interese por medio das simulacións, como pode ser a polarizabilidade electrónica en DFT ou a función de distribución radial en MD.

A terceira parte desta tese, que comprende os capítulos do 3 ao 9, recolle os principais resultados da investigación realizada. Os capítulos son autoconclusivos e cada un deles presenta o traballo correspondente a unha publicación científica distinta.

O capítulo 3, ofrece unha primeira aproximación ás propiedades ópticas dos líquidos iónicos. Especificamente, neste capítulo, abórdase, dende unha perspectiva puramente experimental, a dispersión material de 14 líquidos iónicos nun amplo rango espectral, que abrangue dende os 400 nm ata os 1000 nm. As medidas realizadas indican que, para todos os líquidos iónicos estudados, a dispersión é normal, é dicir, o índice de refracción medra ao decrecer a lonxitude de onda. Ademais, obsérvase unha dominancia dos anións na resposta refractiva dos líquidos iónicos baseados nas derivacións máis comúns do catión imidazolium. Esta forte dependencia do índice de refracción co anión permite obter sinxelamente materiais con índices por riba ou baixo dun determinado valor limiar, ferramenta que é de utilidade no eido do guiado de ondas. Pola contra, variacións nas cadeas alquílicas dos catións imidazolium producen discretos cambios de índice que permiten un deseño moi preciso do mesmo. Non obstante, o efecto de variar a cadea alquílica do catión parece ter diferentes tendencias dependendo do contraión específico ao que este estea emparellado, así, para certas combinacións de ións, alongar a cadea alquílica aumenta o índice pero, para outras, o efecto é o contrario. Para explicar isto, é necesario baixar ao celme microscópico do índice de refracción, que é, de acordo co modelo de Lorentz-Lorenz, o cociente entre a polarizabilidade electrónica e o volume do par iónico que forma o material. Variacións na lonxitude da cadea alquílica producen cambios lineais tanto na polarizabilidade como no volume molar, que poden incrementar ou diminuír o cociente global entre polarizabilidade e volume do par iónico, determinando así o crecemento ou decrecemento

do índice de refracción. Ademais, dado que este depende do cociente de dúas magnitudes lineais, a variación do mesmo é sempre sublinear baixo cambios na lonxitude de cadeas alquílicas. Finalmente, para posibilitar á comunidade científica acceso as curvas de dispersión dos 14 líquidos iónicos medidos, axustouse unha fórmula de Cauchy aos valores experimentais. Tanto os parámetros de axuste como os valores dos índices de refracción a lonxitudes de onda discretas, preséntanse neste capítulo.

O capítulo 4 ten como finalidade expandir o coñecemento sobre a dispersión material dos líquidos iónicos acadado no capítulo anterior ao contemplar, de xeito explícito, a súa dependencia coa temperatura. Neste caso, a dispersión material de 14 líquidos iónicos baseados no catión imidazolium mediuse no rango espectral que abrangue dende os 400 nm ata os 1000 nm e a 6 temperaturas diferentes entre os 20 °C e os 40 °C. O índice de refracción a todas as lonxitudes de onda decrece a medida que aumenta a temperatura, é dicir, os líquidos iónicos presentan un coeficiente termo-óptico negativo. Pola outra banda, nesta ocasión, axustamos unha fórmula de Sellmeier ás curvas de dispersión material dos diferentes líquidos iónicos, o que ofrece relevante información sobre a relación da mesma coa súa estrutura. A fórmula de Sellmeier escollida contén unha única resonancia que está situada no ultravioleta. A posición desta resonancia é invariable ante o cambio de anión ou lonxitude da cadea alquílica do catión, o que indica unha clara orixe no heterociclo do catión imidazolium. A forza do resoador neste modelo é unha función linear da temperatura, é dicir, o efecto da temperatura na dispersión é aproximadamente unha translación da curva de dispersión en índice. Unha reflexión máis en profundidade sobre o coeficiente termo-óptico revela que, case na súa totalidade, a dependencia da dispersión material coa temperatura aparece a través do coeficiente de expansión térmica do líquido, é dicir, da dependencia do volume molar coa temperatura. Non obstante, a refractividade molar (polarizabilidade electrónica) presenta unha dependencia térmica residual que da lugar ás curvas da dispersión do coeficiente termo-óptico que se ofrecen neste capítulo para os distintos líquidos. Finalmente, mencionar que a

forza dos resoadores deste modelo presentan unha certa dependencia coa lonxitude das cadeas alquílicas do catión imidazolium, que se trata máis en profundidade no seguinte capítulo.

O capítulo 5 ten como obxectivo profundizar máis polo miúdo na relación da dispersión material coa estrutura dos líquidos iónicos. Para levar ao cabo esta investigación, precisouse medir a dispersión material nun rango espectral marcadamente máis amplo que nos capítulos anteriores, dende os 300 nm ata os 1550 nm, e a varias temperaturas, entre os 20 °C e os 40 °C. Neste caso, estudouse unha única familia de líquidos iónicos, a 1-alquil-3-metilimidazolium tetrafluoroborato, da cal consideramos 7 membros. A diferenza do capítulo anterior, esta vez unha formula de Sellmeier cunha única resonancia non é abondo para reproducir correctamente a curva de dispersión material, senón que, como mínimo, hai que considerar tres resonancias para reproducir correctamente a fenomenoloxía observada. Ademais, no canto de realizar o axuste unicamente sobre a dispersión material, este tamén se leva ao cabo sobre a refractividade molar, o que permite aproveitarse da aditividade desta magnitude para separar a contribución á dispersión das cadeas alquílicas das do resto do líquido iónico. Das tres resonancias consideradas, dúas están situadas no rango ultravioleta e unha terceira no infravermello. Estas tres resonancias son fixas para todos os membros da familia baixo estudo, puidéndose distinguir as resonancias asociadas á cadea alquílica do catión imidazolium das asociadas ao resto do líquido iónico. En canto ás forzas dos resoadores, estas presentan dependencias tanto na temperatura como na lonxitude de cadea alquílica do catión imidazolium. A maiores, neste capítulo, impleméntase un modelo semi-empírico para predicir mediante cálculos DFT a dispersión material dos líquidos iónicos desta familia con incertezas por debaixo de $4{\cdot}10^{-3}$. O modelo empregado toma a dispersión material como función de dúas variables mutuamente independentes: o volume molar, que contén a dependencia en temperatura, e a refractividade molar, que contén a dependencia espectral.

O capítulo 6 está orientado a cristais líquidos iónicos, e, máis en concreto, céntrase no estudo do 1-etil-3-metilimidazolium decilsulfato,

un líquido iónico moi higroscópico que, ao absorber auga da atmosfera, convértese nun cristal líquido liotrópico. Esta fase de cristal líquido caracterizouse mediante unha ampla batería de técnicas experimentais, incluíndo, calorimetría diferencial de varrido (DSC), resonancia magnética nuclear (NMR), difracción de raios X (XRD) ou microscopía de polarización (POM). O emprego combinado destas técnicas, permitiu determinar o rango de estabilidade da fase de cristal líquido, de -40 °C a 37 °C, así como a súa estrutura, unha mesofase esméctica de tipo A coas cadeas alquílicas dos ións decilsulfato non interdixitadas. O cristal líquido iónico aliñouse macroscopicamente e a dispersión da súa birrefrinxencia medíuse mediante REIBA e refractometría tipo Abbe como función da temperatura. Os resultados das dúas técnicas apuntan a unha birrefrinxencia acromática dentro do noso rango de incerteza, e, ademais, independente da temperatura.

O capítulo 7, en contraposición cos capítulos anteriores de vocación claramente experimental, ten como obxectivo desenvolver un método para predicir por medios exclusivamente computacionais o índice de refracción dos líquidos iónicos e avaliar a posible influencia que a deslocalización de carga exerce nesta magnitude. O método aquí presentado procura predicir as propiedades dos líquidos iónicos a partires, unicamente, de cálculos *ab initio* sobre os seus ións constituíntes. Trátase dun procedemento computacionalmente eficiente e que ofrece a grande vantaxe de permitir a estimación do índice de refracción dunha grande cantidade de líquidos iónicos partindo dun número limitado de simulacións. Para reconstruír a polarizabilidade e volume molecular do par iónico mediante os valores dos ións constituíntes, asumimos polarizabilidades aditivas en termos de ións, se ben é certo, que, dentro de cada ión, a presenza de deslocalización de carga en orbitais π conxugados fai que a polarizabilidade non sexa aditiva en termos atómicos. En canto ao volume molecular, para obter un volume do par iónico representativo do que ten na fase condensada, empregamos unha corrección cuadrática en termos da suma do volume simulado dos ións constituíntes. Os coeficientes desta corrección cuadrática obtivéronse semi-empiricamente para un

set de líquidos iónicos e extrapoláronse ao resto de combinacións. A densidade de polarizabilidade, cociente entre polarizabilidade e volume molecular, analizouse para un grande número de ións, incluíndo os anións máis comúns e tres grupos de catións que difiren na presenza de deslocalización de carga nas súas estruturas. Esta análise posibilita entender como afecta cada especie iónica ao índice de refracción cando forma parte dun líquido iónico. Ademais, seguindo a metodoloxía desenvolta neste capítulo, preséntase un completo atlas do índice de refracción estimado para máis de 1216 líquidos iónicos. Este mapa amosa claramente que a deslocalización de carga, tanto en anións como en catións, xoga un papel fundamental no índice de refracción dos líquidos iónicos. A razón disto é que, en orbitais π conxugados, a polarizabilidade electrónica medra de xeito non linear co número de átomos, o que se traduce en maiores densidades de polarizabilidade que nos orbitais con carga altamente localizada. Neste sentido, un resultado relevante deste capítulo é que a introdución intelixente de zonas de deslocalización de carga en catións, ofrece a posibilidade de crear líquidos iónicos con índices de refracción superiores a 2.0.

O capítulo 8 ten como finalidade ofrecer unha perspectiva ampla das hiperpolarizabilidades e susceptibilidades non lineais dos líquidos iónicos, e máis da influencia da deslocalización de carga nestas magnitudes. Para elo, emprégase unha aproximación computacional inspirada na realizada no capítulo anterior para a polarizabilidade electrónica. Neste capítulo, procúrase determinar a resposta non linear dos líquidos iónicos por medio das respostas individuais dos ións constituíntes, empregando como variables fundamentais as hiperpolarizabilidades de primeira e segunda orde xunto co volume molecular. Os ións considerados son unha serie de anións comunmente empregados no eido dos líquidos iónicos e tres grupos de catións que difiren na presenza de deslocalización de carga nas súas estruturas. Mentres que o tratamento de volumes é similar ao do capítulo anterior, nesta ocasión, a aditividade de hiperpolarizabilidades para a estimación da hiperpolarizabilidade do par iónico non está asegurada. Por ese motivo, neste capítulo

realizase unha valoración do principio de aditividade da primeira e segunda hiperpolarizabilidade mediante a comparación dos valores obtidos de simulacións de pares iónicos e ións illados. Os resultados amosan que mentres que a primeira hiperpolarizabilidade non é en absoluto aditiva, a segunda hiperpolarizabilidade si o é. A rotura da aditividade para a primeira hiperpolarizabilidade é, posiblemente, debida á forte dependencia xeométrica desta magnitude, que é nula en moléculas centrosimétricas. Coa fin de determinar o rol de cada ión na resposta non linear dos líquidos iónicos dos que forman parte, a densidade de hiperpolarizabilidade de cada un deles (cociente desta magnitude co volume molecular) estudouse ao detalle. Ademais, aproveitando a aditividade da segunda hiperpolarizabilidade, neste capítulo preséntase un mapa da susceptibilidade de terceira orde do efecto Kerr electro-óptico (EOKE) para máis de 1496 combinacións de ións. Os resultados amosan claramente que as respostas ópticas non lineais máis relevantes están vencelladas á aparición de extensas rexións de carga deslocalizada.

O capítulo 9 presenta os metais de transición como unha atractiva alternativa para o deseño de líquidos iónicos con propiedades ópticas distintas das estudadas nos capítulos anteriores. En concreto, estúdanse unha serie de dopaxes do líquido iónico 1-butil-3-metilimidazolium tiocianato con aluminio e diversos metais de transición: níquel, manganeso, ferro e cromo. Trátase dun estudo primordialmente computacional con certas achegas experimentais, como poden ser espectros de absorción ou difractogramas de raios X, que serven de contraste cos cálculos. O efecto da introdución dos metais nos líquidos iónicos estudouse mediante simulacións de dinámica molecular (MD), que revelaron que os anións tiocianato complexan octahedricamente aos metais nas rexións polares dos mesmos. Esta complexación, que ten lugar dentro dun ambiente altamente cargado, acontece baixo un sutil equilibrio da coordinación ambidentada dos ións tiocianato e a participación dos mesmos en esferas de coordinación de varios metais mediante *bridging*. Porén, a influenza máis grande dos diferentes metais atópase nas propiedades ópticas dos líquidos iónicos, nomeadamente

no espectro de absorción. Simulacións TD-DFT dos complexos metal-tiocianato apuntan a que son estes mesmos os que, en exclusiva, gobernan a resposta óptica destes sistemas, xogando os catións imidazolium unicamente un papel secundario de compensación de carga. Ademais, estudáronse en profundidade os espectros de absorción producidos por cada un dos líquidos dopados con metais de transición e identificáronse as principais transicións electrónicas observadas.

Finalmente, a derradeira parte desta tese, composta polo capítulo 10, presenta as conclusións xerais do traballo doutoral, nas que se recollen as principais achegas realizadas á comunidade científica. Estas conclusións apuntan a diversas aplicacións dos líquidos iónicos no eido da fotónica e deixan claro a grande posibilidade de deseño intelixente das propiedades ópticas destes líquidos. Para rematar, inclúense uns breves comentarios sobre as liñas de investigación futura que abre este traballo.

Resumen

Los líquidos iónicos son materiales exclusivamente compuestos por iones y que se encuentran en estado líquido a temperaturas por debajo de los 100 °C. Este tipo de sales fundidas a baja temperatura fueron descritas por primera vez por Paul Walden en 1914, pero no recibieron el interés que merecían hasta finales del siglo XX, cuando las primeras familias de líquidos iónicos estables en contacto con aire y agua fueron sintetizadas. Desde ese momento, los líquidos iónicos se convirtieron en objeto de una intensa actividad científica por su único *set* de propiedades, que incluye, entre otras: estabilidad química y térmica, baja inflamabilidad, diminuta presión de vapor o amplia ventana electroquímica. Sin embargo, la característica más interesante de los líquidos iónicos es su gran flexibilidad en cuanto a estructura y composición, que permite diseñar líquidos iónicos con propiedades a medida, motivo por el cuál son también conocidos como líquidos inteligentes o de diseño.

La posibilidad de diseñar las propiedades de los líquidos iónicos a la carta, hizo de ellos materiales con potenciales aplicaciones en los más diversos campos científicos e industriales. En este sentido, existen numerosos estudios sobre el rendimiento de líquidos iónicos para capturar dióxido de carbono, para mejorar la eficiencia de lubricantes mecánicos, para incrementar la capacidad de almacenaje de baterías, o como medio más ecológico y eficiente para realizar procesos de catálisis o separación química. Sin embargo, existen aún ámbitos en los que el papel que pueden jugar los líquidos iónicos está por determinar, como es el caso de la fotónica, que es la disciplina científica que toma como objeto de estudio la luz y su interacción con la materia. La fotónica es un campo con numerosas aplicaciones industriales, incluyendo láseres, pantallas digitales, fibras ópticas o sensores fotónicos. En estas aplicaciones, la elección de las propiedades ópticas de los materiales empleados es primordial: buscamos materiales que emitan o re-emitan luz con unas ciertas características espectrales, que absorban unas

ciertas longitudes de onda o que presenten una dispersión material, respuesta no lineal o forma de polarizar adecuadas a nuestros intereses. Y, por supuesto, todo esto sin nunca olvidar la obligada búsqueda de mayor eficiencia y menor huella ecológica. En este sentido, los líquidos iónicos, materiales verdes con propiedades altamente sintonizables, son candidatos idóneos para jugar un papel relevante en la fotónica del futuro.

Los estudios disponibles sobre propiedades ópticas en líquidos iónicos, muestran unos materiales con gran potencialidad: su índice de refracción puede ser sintonizado con la elección de los iones constituyentes, tienen la capacidad de presentar una amplia gama de cromismos, incluidos termocromismo, fotocromismo y electrocromismo, exhibir respuestas no lineales relevantes o estabilizar fases de cristal líquido. Desafortunadamente, aun es necesario conocer más en profunidad las relaciones de estas prometedoras propiedades ópticas con la estructura de los líquidos iónicos para que éstos puedan ser implementados en aplicaciones fotónicas reales, como pueden ser sensores ópticos de diversa índole, fibras ópticas de núcleo líquido, lentes líquidas de focal variable, o como cristales líquidos en dispositivos de visualización.

El propósito de esta tesis es estudiar las propiedades ópticas de los líquidos iónicos, y, más concretamente, la dispersión material, respuesta no lineal, espectro de absorción y carácter de cristal líquido en relación con la estructura de estos materiales. El fin último de este esfuerzo investigador es identificar los mecanismos más prometedores para el diseño inteligente de las propiedades ópticas de los líquidos iónicos y facilitar, de este modo, su inclusión como materiales de primera orden en el campo de la fotónica. Para conseguir este objetivo, una gran cantidad de líquidos iónicos son estudiados en las páginas de esta tesis, tanto desde un punto de vista experimental como computacional. Es justamente esta metodología híbrida, la que permite acercarse al mundo de los líquidos iónicos desde muy diversas escalas características. El trabajo experimental aporta una visión efectiva de las propiedades macroscópicas y mesoscópicas de estos líquidos,

mientras que la metodología computacional, que incluye simulaciones de dinámica molecular (MD) y teoría del funcional densidad (DFT), ofrece la posibilidad de acercarse a estos sistemas a través de escalas microscópicas, que abarcan desde las pocas decenas de nanómetros hasta unos cuantos angstroms.

Esta tesis está estructurada en cuatro partes bien diferencias: introducción, material y métodos, resultados y conclusiones. La introducción, formada por el capítulo 1, cuenta con una motivación en la que se expone el porqué de la investigación realizada, una explicación completa sobre qué son los líquidos iónicos y la importancia de los materiales en el campo de la fotónica y, un resumen de las propiedades ópticas más interesantes que los líquidos iónicos pueden presentar. Además, contiene una breve descripción de los principales objetivos de esta tesis.

La segunda parte, compuesta por el capítulo 2, contiene una sección dedicada a los materiales y una serie de secciones dedicadas a la metodología. En la sección de materiales, se indican nombre, abreviación y estructura de todos los líquidos iónicos considerados en algún punto de la tesis. Por otro lado, en las secciones de metodología, se ofrece una detallada explicación de los diferentes métodos experimentales y computacionales empleados. En la sección de metodología experimental, se recogen los modelos de los equipos y protocolos de medida para las principales técnicas experimentales como, por ejemplo, difracción de rayos X (DRX), resonancia magnética nuclear (NMR) o calorimetría diferencial de barrido (DSC). Sin embargo, es en las técnicas de caracterización óptica donde se hace especial hincapié. En este sentido, esta sección ofrece una descripción en profundidad de la novedosa técnica empleada para medir la dispersión material de los distintos líquidos iónicos, la técnica conocida como Refractometría Espectral por Interferencia de Banda Ancha (REIBA) o, en inglés, Refractive Index Spectroscopy by Broadband Interference (RISBI). El dispositivo REIBA empleado en esta tesis fue manualmente implementado en nuestro laboratorio y su método de funcionamiento y especificaciones técnicas pueden ser consultadas

en este apartado, junto con un completo análisis de su incertidumbre instrumental. En cuanto a las secciones de metodología computacional, en ellas se explican los fundamentos teóricos de la dinámica molecular (MD) y de la teoría del funcional densidad (DFT), incluyendo los principales pasos seguidos para ejecutar las simulaciones de cada tipo. A mayores, se ofrece una explicación detallada del cálculo de las principales magnitudes de interés por medio de las simulaciones, como puede ser la polarizabilidad electrónica en DFT o la función de distribución radial en MD.

La tercera parte de esta tesis, que comprende los capítulos del 3 al 9, recoge los principales resultados de la investigación realizada. Los capítulos son autoconclusivos y cada uno de ellos presenta el trabajo correspondiente a una publicación científica distinta.

El capítulo 3, ofrece una primera aproximación a las propiedades ópticas de los líquidos iónicos. Específicamente, en este capítulo se aborda, desde una perspectiva puramente experimental, la dispersión material de 14 líquidos iónicos en un amplio rango espectral, que abarca desde los 400 nm hasta los 1000 nm. Las medidas realizadas indican que, para todos los líquidos iónicos estudiados, la dispersión es normal, es decir, el índice de refracción aumenta al decrecer la longitud de onda. Además, se observa una clara dominancia de los aniones en la respuesta refractiva de los líquidos iónicos basados en las derivaciones más comunes del catión imidazolium. Esta fuerte dependencia del índice de refracción con el anión, permite obtener sencillamente materiales con índices por arriba o debajo de un determinado valor umbral, herramienta que es de utilidad en el campo del guiado de ondas. Por el contrario, variaciones en las cadenas alquílicas de los cationes imidazolium producen discretos cambios de índice que permiten un diseño muy preciso del mismo. Sin embargo, el efecto de variar la cadena alquílica del catión parece seguir diferentes tendencias dependiendo del contraión específico al que está emparejado, así, para ciertas combinaciones de iones, elongar la cadena alquílica aumenta el valor del índice pero, para otras, el efecto es el contrario. Para explicar esto, es necesario bajar al origen microscópico del índice de

refracción, que es, de acuerdo que con el modelo de Lorentz-Lorenz, el ratio entre la polarizabilidad electrónica y el volumen del par iónico que forma el material. Variaciones en la longitud de la cadena alquílica producen cambios lineales tanto de polarizabilidad como en volumen molar, que pueden incrementar o disminuir el ratio global entre la polarizabilidad y el volumen del par iónico, determinando así el crecimiento o decrecimiento del índice de refracción. Además, dado que este depende del ratio de dos magnitudes lineales, la variación del mismo es siempre sublineal bajo cambios en la longitud de las cadenas alquílicas. Finalmente, para posibilitar a la comunidad científica el acceso a las curvas de dispersión de los 14 líquidos iónicos medidos, se ajustó una fórmula de Cauchy a los valores experimentales. Estos parámetros de ajuste, así como los valores de los índices de refracción a longitudes de onda discretas se proporcionan en este capítulo.

El capítulo 4 tiene como finalidad ampliar el conocimiento sobre la dispersión material de los líquidos iónicos conseguido en el capítulo anterior al contemplar, de manera explícita, su dependencia con la temperatura. En este caso, la dispersión material de 14 líquidos iónicos basados en el catión imidazolium fue medida en el rango espectral que abarca desde los 400 nm hasta los 1000 nm a 6 temperaturas diferentes entre los 20 °C y los 40 °C. El índice de refracción a todas las longitudes de onda medidas decrece conforme aumenta la temperatura, es decir, los líquidos iónicos presentan un coeficiente termo-óptico negativo. Por otro lado, en esta ocasión, ajustamos una fórmula de Sellmeier a la dispersión material de los diferentes líquidos iónicos, lo que ofrece relevante información sobre la relación de la misma con su estructura. La fórmula de Sellmeier escogida contiene una única resonancia que está situada en el ultravioleta. La posición de esta resonancia es invariable ante el cambio de anión o longitud de la cadena alquílica del catión, lo que indica un claro origen en el heterociclo del catión imidazolium. La fuerza del resonador en este modelo es una función lineal de la temperatura, es decir, el efecto de la temperatura en la dispersión es aproximadamente una traslación de la curva de dispersión en índice. Una reflexión más en profundidad sobre el coeficiente

termo-óptico revela que, casi en su totalidad, la dependencia de la dispersión material con la temperatura aparece a través del coeficiente de expansión térmica del líquido, es decir, de la dependencia del volumen molar con la temperatura. No obstante, la refractividad molar (polarizabilidad electrónica) presenta una dependencia térmica residual que da lugar a las curvas de la dispersión del coeficiente termo-óptico que se ofrecen en este capítulo para los distintos líquidos. Finalmente, mencionar que la fuerza de los resonadores de este modelo presentan una cierta dependencia con la longitud de las cadenas alquílicas en el catión imidazolium, que es tratada en mayor profundidad en el siguiente capítulo.

El capítulo 5 tiene como objetivo profundizar más en detalle en la relación de la dispersión material con la estructura de los líquidos iónicos. Para llevar a cabo esta investigación, fue necesario medir la dispersión material en un rango espectral marcadamente más amplio que en los capítulos anteriores, desde los 300 nm hasta los 1550 nm y a varias temperaturas, entre los 20 °C y los 40 °C. Una única familia de líquidos iónicos es estudiada, la 1-alquil-3-metilimidazolium tetrafluoroborato, de la cual consideramos 7 miembros. A diferencia del capítulo anterior, en este caso una formula de Sellmeier con una única resonancia no es suficiente para reproducir correctamente la curva de dispersión material. Por ello, en esta ocasión, empleamos una fórmula de Sellmeier con tres resonancias que permite describir la dispersión de los 7 líquidos estudiados simultáneamente. Además, en este caso, la magnitud de ajuste no es sólo la dispersión material, sino también la refractividad molar, lo que permite aprovecharse de la aditividad de esta magnitud para separar las contribuciones a la dispersión de las cadenas alquílicas de las del resto del líquido iónico. De las tres resonancias consideradas, dos están situadas en el rango ultravioleta y una tercera en el infrarrojo. Estas tres resonancias son fijas para todos los miembros de la familia bajo estudio, pudiéndose distinguir las resonancias asociadas a las cadenas alquílicas del catión imidazolium de las asociadas al resto del líquido iónico. En cuanto a las fuerzas de los resonadores, éstas presentan dependencias tanto en la temperatura

como en la longitud de cadena alquílica del catión imidazolium. A mayores, en este capítulo se implementa un modelo semi-empírico para predecir mediante cálculos DFT la dispersión material de los líquidos iónicos de este familia con incertidumbres por debajo de $4 \cdot 10^{-3}$. El modelo empleado toma la dispersión material como función de dos variables mutuamente independientes: el volumen molar que contiene la dependencia en temperatura, y la refractividad molar, que contiene la dependencia espectral.

El capítulo 6 está orientado a cristales líquidos iónicos, y, más en concreto, se centra en el estudio del 1-etil-3-metilimidazolium decilsulfato, un líquido iónico muy higroscópico que, al absorber agua de la atmósfera, se convierte en un cristal líquido liotrópico. Esta fase de cristal líquido es caracterizada mediante una amplia batería de técnicas experimentales, incluyendo, calorimetría diferencial de barrido (DSC), resonancia magnética nuclear (NMR), difracción de rayos X (XRD) o microscopía de polarización (POM). El empleo combinado de estas técnicas, permitió determinar el rango de estabilidad de la fase de cristal líquido, de -40 °C a 37 °C, así como su estructura, una mesofase esméctica de tipo A con las cadenas alquílicas de los iones decilsulfato no interdigitadas. El cristal líquido iónico fue alineado macroscópicamente y la dispersión de su birrefringencia medida mediante REIBA y refractometría tipo Abbe como función de la temperatura. Los resultados de las dos técnicas apuntan a una birrefringencia acromática dentro de nuestro rango de incertidumbre, y, además, independiente de la temperatura.

El capítulo 7, en contraposición con los capítulos anteriores de vocación claramente experimental, tiene como objetivo desarrollar un método para predecir por medios exclusivamente computacionales el índice de refracción de los líquidos iónicos y evaluar la posible influencia que la deslocalización de carga ejerce en esta magnitud. El método aquí presentado busca predecir las propiedades de los líquidos iónicos a partir, únicamente, de cálculos *ab initio* sobre sus iones constituyentes. Se trata de un procedimiento computacionalmente eficiente y que ofrece la gran ventaja de permitir la estimación del índice

Carlos Damián Rodríguez Fernández

de refracción de una gran cantidad de líquidos iónicos partiendo de un
número limitado de simulaciones. Para reconstruir la polarizabilidad
y volumen molecular del par iónico mediante los valores de los
iones constituyentes, asumimos polarizabilidades aditivas en términos
de iones, si bien es cierto, que, dentro de cada ión, la presencia
de deslocalización de carga en orbitales π conjugados hace que la
polarizabilidad no sea aditiva a nivel atómico. En cuanto al volumen
molecular, para obtener un volumen del par iónico representativo del
que tiene en la fase condensada, empleamos una corrección cuadrática
en base a la suma del volumen simulado de los iones constituyentes.
Los coeficientes de esta corrección cuadrática fueron obtenidos
semi-empíricamente para un *set* de líquidos iónicos y extrapolados
para el resto de combinaciones. La densidad de polarizabilidad, ratio
entre polarizabilidad y volumen molecular, es analizada para un gran
número de iones, incluyendo los aniones más comunes y tres grupos
de cationes que difieren en la presencia de deslocalización de carga
en sus estructuras. Este análisis posibilita entender como afecta cada
especie iónica al índice de refracción cuando forma parte de un líquido
iónico. Además, siguiendo la metodología desarrollada en este capítulo,
se presenta un completo atlas del índice de refracción estimado para
más de 1216 líquidos iónicos. Este mapa muestra claramente que la
deslocalización de carga, tanto en aniones como en cationes, juega un
papel fundamental en el índice de refracción de los líquidos iónicos.
La razón de esto es que, en orbitales π conjugados, la polarizabilidad
electrónica crece de manera no lineal con el número de átomos, lo
que se traduce en mayores densidades de polarizabilidad que en los
orbitales con carga altamente localizada. En este sentido, un resultado
relevante de este capítulo es que la introducción inteligente de zonas de
deslocalización de carga en cationes, ofrece la posibilidad de diseñar
líquidos iónicos con índices de refracción superiores a 2.0.

El capítulo 8 tiene como finalidad ofrecer una perspectiva
amplia de las hiperpolarizabilidades y susceptibilidades no lineales
de los líquidos iónicos, y de la influencia de la deslocalización de
carga en estas magnitudes. Para ello, se emplea una aproximación

computacional inspirada en la empleada en el capítulo anterior para la polarizabilidad electrónica. En este capítulo, se pretende determinar la respuesta no lineal de los líquidos iónicos por medio de las respuestas individuales de los iones constituyentes, empleando como variables fundamentales las hiperpolarizabilidades de primer y segundo orden y el volumen molecular. Los iones considerados son una serie de aniones comúnmente empleados en el campo de los líquidos iónicos y tres grupos de cationes que difieren en la presencia de deslocalización de carga en sus estructuras. Mientras que el tratamiento de volúmenes es similar al del capítulo anterior, en esta ocasión, la aditividad de hiperpolarizabilidades para la estimación de la hiperpolarizabilidad del par iónico no está asegurada. Por ese motivo, en este capítulo se realiza una valoración del principio de aditividad de la primera y segunda hiperpolarizabilidad mediante la comparación de los valores obtenidos de simulaciones de pares iónicos e iones aislados. Los resultados muestran que mientras que la primera hiperpolarizabilidad no es en absoluto aditiva, la segunda sí lo es. La ruptura de la aditividad para la primera hiperpolarizabilidad es, posiblemente, causada por la fuerte dependencia geométrica de esta magnitud, que es nula en moléculas centrosimétricas. Con el fin de determinar el rol de cada ión en la respuesta no lineal de los líquidos iónicos de los que forman parte, la densidad de hiperpolarizabilidad de cada uno de ellos, ratio de esta magnitud con el volumen molecular, es estudiada en detalle. Además, aprovechando la aditividad de la segunda hiperpolarizabilidad, en este capítulo se presenta un mapa de la susceptibilidad de tercer orden para el efecto Kerr electro-óptico (EOKE) para más de 1496 combinaciones de iones. Los resultados demuestran claramente que las respuestas ópticas no lineales más relevantes están ligadas a la aparición de extensas regiones de carga deslocalizada.

El capítulo 9 presenta los metales de transición como una atractiva alternativa para el diseño de líquidos iónicos con propiedades ópticas distintas de las estudiadas en los capítulos anteriores. En concreto, se estudian una serie de dopajes del líquido iónico 1-butil-3-metilimidazolium tiocianato con aluminio y diversos

metales de transición: níquel, manganeso, hierro y cromo. Se trata de un estudio primordialmente computacional con ciertas aportaciones experimentales, como pueden ser espectros de absorción o difractogramas de rayos X, que sirven de contraste con los cálculos. El efecto de la introducción de los metales en los líquidos iónicos es estudiado mediante dinámica molecular (MD), donde se revela que los metales forman complejos octahédricos con los aniones tiocianato en las regiones polares de los mismos. La formación de estos complejos, dentro de un ambiente altamente cargado, sucede bajo un sutil equilibrio de la coordinación ambidentada de los iones tiocianato y la participación de los mismos en esferas de coordinación de varios metales mediante *bridging*. Sin embargo, la influencia más grande de los diferentes metales se encuentra en las propiedades ópticas de los líquidos, especialmente en el espectro de absorción. Simulaciones TD-DFT de los complejos metal-tiocianato apuntan a que son estos mismos los que, en exclusiva, gobiernan la respuesta óptica de estos sistemas, jugando los cationes imidazolium únicamente el papel secundario de compensación de carga. Además, el espectro de absorción producido por cada uno de los líquidos iónicos dopados con metales de transición se estudió en detalle y se identificaron las principales transiciones electrónicas observadas.

Finalmente, la última parte de esta tesis, compuesta por el capítulo 10, presenta las conclusiones generales del trabajo doctoral, en las que se recogen las principales aportaciones realizadas a la comunidad científica. Estas conclusiones apuntan a diversas aplicaciones de los líquidos iónicos en el campo de la fotónica y dejan claro la gran posibilidad de diseño inteligente de las propiedades ópticas de estos líquidos. Para concluir, se incluyen unos breves comentarios sobre las líneas de investigación futura que abre el trabajo realizado en esta tesis.

Summary

Ionic liquids are materials that are exclusively composed of ions and which are in the liquid state at temperatures below 100 °C. These low-temperature molten salts were pioneering described by Paul Walden in 1914, but did not receive the interest they deserved until the end of the XX century, when the first families of air and water stable ionic liquids were synthesized. Since that time, ionic liquids became the subject of intense scientific activity because of their unique set of properties, which include, among others: chemical and thermal stability, low flammability, negligible vapor pressure or wide electrochemical window. However, the most interesting feature of ionic liquids is their extraordinary flexibility regarding structure and composition, which allows an accurate tailoring of their properties, reason why they are known as smart or designer liquids.

The possibility of designing ionic liquids with task-specific properties has made them materials with potential applications in the most diverse scientific and industrial fields. In this regard, there are numerous studies on the performance of ionic liquids to capture carbon dioxide, to improve the efficiency of mechanical lubricants, to increase the storage capacity of batteries, or as greener and more efficient solvents to perform catalysis or chemical separation processes. However, there are still areas, as photonics, where the role that ionic liquids could play has yet to be determined. Photonics is the scientific discipline that studies light and its interaction with matter, and it has numerous industrial applications including lasers, digital displays, optical fibers or photonic sensors. In these applications, the choice of the materials according to their optical properties is fundamental: we are looking for materials that emit or re-emit light with certain spectral characteristics, that absorb certain spectral ranges, or that present material dispersion or nonlinear response suitable to our interests. And, of course, all this without forgetting the compulsory search for better efficiency and smaller ecological footprint. In this regard, ionic liquids,

green materials with highly tunable properties, are ideal candidates to play a relevant role in the photonics of the future.

The available studies on the optical properties of ionic liquids show that they are materials with promising potential in photonics: their refractive index can be tuned with the choice of the constituent ions, they have the ability to exhibit a wide range of chromisms, including thermochromism, photochromism, and electrochromism, relevant nonlinear responses or stabilizing liquid crystal phases. Hence, they could be suitable materials for applications such as optical sensors of various kinds, liquid-filled variable focus lenses, liquid-core optical fibers, as well as active materials for nonlinear optics or as liquid crystals in displays and other related applications. Unfortunately, the relationships of these properties with the structure of ionic liquids still need to be further understood before implement them in real photonic applications.

The purpose of this thesis is to study the optical properties of ionic liquids, and, more specifically, the material dispersion, nonlinear response, absorption spectrum and liquid crystal character in relation to the structure of these materials. We also aim to identify the most promising mechanisms for the smart design of the optical properties of ionic liquids and facilitate their inclusion as relevant materials in the field of photonics. To achieve this goal, a large number of ionic liquids are studied in the pages of this thesis, both from an experimental and computational point of view. This hybrid methodology is just what allows us to approach the world of ionic liquids from very different characteristic scales. The experimental work provides an effective view of the macroscopic and mesoscopic properties of these liquids, while the computational methodology, which includes molecular dynamics (MD) and density functional theory (DFT) simulations, offers the possibility of addressing them at microscopic scales.

This thesis is structured in four parts: introduction, material and methods, results and conclusions. The introduction, comprised by chapter 1, includes a motivation of the realized research work, a

complete explanation of what ionic liquids are and the importance of the materials in the field of photonics, and a summary of the most interesting optical properties that ionic liquids can exhibit. Furthermore, it also contains a brief description of the main objectives of this thesis.

The second part, composed by chapter 2, contains a section dedicated to materials and a series of sections dedicated to methodology. In the materials section, the name, abbreviation and structure of all the ionic liquids that are considered at some point in the thesis are detailed. On the other hand, in the methodology sections, a detailed explanation of the different employed experimental and computational methods is given. In the experimental methodology section, the equipment models and measurement protocols for the main experimental techniques used, such as X-ray diffraction (XRD), nuclear magnetic resonance (NMR) or differential scanning calorimetry (DSC), are included. However, it is in the optical characterization techniques where special emphasis is placed. In this sense, this section offers an in-depth description of the novel technique used to measure the material dispersion of the different ionic liquids, Refractive Index Spectroscopy by Broadband Interference (RISBI). The RISBI device used in this thesis was manually implemented in our laboratory and its method of operation and technical specifications can be consulted in this section, together with a complete analysis of its instrumental uncertainty. On the other hand, in the computational methodology sections, the theoretical foundations of molecular dynamics and density functional theory are explained, including the main steps followed to run the simulations of each type. In addition, a detailed explanation of the calculation of the main quantities of interest by means of the simulations, such as the electronic polarizability in DFT or the radial distribution function in MD, is given.

The third part of this thesis, comprising chapters 3 to 9, presents the main results of the doctoral research. The chapters are self-conclusive and each one of them presents the work corresponding to a different scientific publication.

USC
UNIVERSIDADE
DE SANTIAGO
DE COMPOSTELA

Chapter 3 offers a first approach to the optical properties of ionic liquids. Specifically, this chapter deals, from a purely experimental perspective, with the material dispersion of 14 ionic liquids in a wide spectral range, from 400 nm to 1000 nm. The measurements performed indicate that, for all the ionic liquids studied, the material dispersion is normal, i.e., the refractive index increases with decreasing wavelength. Furthermore, a clear dominance of anions is observed in the refractive response of the ionic liquids based on the most common derivatives of the imidazolium cation. This strong dependence of the refractive index on the anion makes it possible to easily obtain materials with indices above or below a certain threshold value, a useful tool in the field of waveguiding. Conversely, variations in the alkyl chains of the imidazolium cations produce modest changes in the refractive index that allow a very precise tailoring of it. However, the effect of varying the alkyl chain of the cation appears to have different trends depending on the specific counterion it is paired with, since, for certain ion combinations, elongating the alkyl chain increases the index but, for others, the effect is the opposite. To explain this, it is necessary to go down to the microscopic origin of the refractive index, which is, according to the Lorentz-Lorenz model, the ratio between the electronic polarizability and the volume of the ionic pair forming the material. Variations in the length of the alkyl chain produce linear changes in both polarizability and molar volume, which can increase or decrease the global ratio between polarizability and volume of the ionic pair, and, accordingly, its refractive index. Moreover, since the refractive index depends on the ratio of two linear quantities, its variation is always sublinear upon changes in the alkyl chain length. Finally, in order to make the dispersion curves of the 14 measured ionic liquids available to the scientific community, a Cauchy formula was fit to the experimental data. Both the fitting parameters and the values of the refractive indices at certain discrete wavelengths, such as that of the sodium D line, 589 nm, are given in this chapter.

Chapter 4 aims to extend the knowledge on the material dispersion of ionic liquids gained in the previous chapter by explicitly considering

its dependence on temperature. In this case, the material dispersion of 14 ionic liquids based on the imidazolium cation was measured in the spectral range spanning from 400 nm to 1000 nm at 6 different temperatures between 20 °C and 40 °C. The refractive index at all the wavelengths decreases with increasing temperature, i.e. the ionic liquids exhibit a negative thermo-optical coefficient (TOC). On the other hand, a Sellmeier formula was fit to the material dispersion of the different ionic liquids, which gives relevant information about the relation of the dispersion with their structure. The chosen Sellmeier formula contains a single resonance which is located in the ultraviolet. The position of this resonance is invariant to the change of anion or alkyl chain length of the cation, indicating a clear origin in the heterocycle of the imidazolium cation. The strength of the resonator in this model is a linear function of temperature, i.e., the effect of temperature on dispersion is approximately a translation of that in terms of refractive index. A more in-detail analysis of the origins of the thermo-optical coefficient reveals that, almost entirely, the dependence of material dispersion on temperature appears through the thermal expansion coefficient of the liquid, i.e., the dependence of molar volume on temperature. However, the molar refractivity (electronic polarizability) presents a residual thermal dependence that gives rise to the thermo-optical coefficient dispersion curves given in this chapter for the studied liquids. Finally, it is worth mentioning that the strength of the resonators of this model shows a certain dependence on the length of the alkyl chains of the imidazolium cation, which is discussed in more detail in the next chapter.

Chapter 5 aims to go into more detail on the relationship of material dispersion with the structure of ionic liquids. To address this objective, it was necessary to measure the material dispersion in a much wider spectral range than previously, from 300 nm to 1550 nm and at various temperatures between 20 °C and 40 °C. A single family of ionic liquids is studied, the 1-alkyl-3-methylimidazolium tetrafluoroborate, of which we consider 7 members. Unlike the previous chapter, in this case a Sellmeier formula with a single resonance is not enough to correctly

reproduce the material dispersion curve. Therefore, on this occasion, we employ a Sellmeier formula with three resonances that allows us to describe, simultaneously, the dispersion of the 7 liquids studied. Moreover, in this case, we also used as fitting magnitude the molar refractivity, which allows us to take advantage of its additivity to separate the contributions to dispersion of the alkyl chains from those of the rest of the ionic liquid. Of the three resonances considered, two are located in the ultraviolet range and a third in the infrared. These three resonances are the same for all the members belonging to the family under study, being possible to distinguish between those associated to the alkyl chain of the cation and those belonging to the rest of the ionic liquid. Regarding the resonator strengths, they are dependent on both temperature and alkyl chain length of the imidazolium cation. Furthermore, a semi-empirical model is implemented to predict by DFT calculations the material dispersion of the ionic liquids of this family with uncertainties below $4 \cdot 10^{-3}$. The model employed takes the material dispersion as a function of two mutually independent variables: the molar volume, which contains the temperature dependence, and the molar refractivity, which contains the spectral one.

Chapter 6 focuses on ionic liquid crystals, and, more specifically, on the study of 1-ethyl-3-methylimidazolium decylsulfate, a very hygroscopic ionic liquid that, upon absorption of water from the atmosphere, is converted into a lyotropic liquid crystal. This liquid crystal phase is characterized by a wide range of experimental techniques, including differential scanning calorimetry (DSC), nuclear magnetic resonance (NMR), X -ray diffraction (XRD) or polarization microscopy (POM). The combined use of these techniques allows us to determine the stability range of the liquid crystal phase, from -40 °C to 37 °C, as well as to determine its structure, which is a smectic A mesophase with the alkyl chains of the decylsulfate ions not interdigitated. The ionic liquid crystal was macroscopically aligned and its birefringence dispersion measured as a function of temperature by Abbe refractometry and RISBI. The results of the two techniques point to an achromatic birefringence within our uncertainty range, and,

moreover, independent of temperature.

Chapter 7, in contrast to the previous chapters, which are clearly experimental in nature, aims to develop a purely computational strategy to predict the refractive index of ionic liquids, as well as to evaluate the possible influence that charge delocalization exerts on this magnitude. The method presented here is devoted to estimate the refractive index of ionic liquids by means of, exclusively, ab initio calculations on their constituent ions. This way of proceeding ensures computational efficiency while offering the advantage of allowing the estimation of the refractive index of a large number of ionic liquids from a limited number of simulations. To reconstruct the polarizability and molecular volume of the ionic pair by means of the values of the constituent ions, we assume additive polarizabilities in terms of ions. Nevertheless, it is worth clarifying that, within each ion, the presence of charge delocalization in conjugated π orbitals makes the polarizability non additive at the atomic level. Regarding the molecular volume, to obtain a volume of the ionic pair representative of that in the condensed phase, we employ a quadratic correction based on the sum of the simulated volume of the constituent ions. The coefficients of this quadratic correction were semi-empirically obtained for one set of ionic liquids and extrapolated to the rest of combinations. The polarizability density, the ratio between polarizability and molecular volume, is analyzed for a large number of ions, including the most common anions and three groups of cations that differ in the presence of charge delocalization in their structures. This analysis provides insightful information about how each ionic species affect the refractive index when they are part of an ionic liquid. In addition, following the methodology developed in this chapter, a complete atlas of the estimated refractive index for 1216 ionic liquids is presented. This map clearly shows that charge delocalization in both anions and cations plays a fundamental role in the refractive index of ionic liquids. The reason for this is that, in π conjugated orbitals, the electronic polarizability grows nonlinearly with the number of atoms, which results in higher polarizability densities than those found in orbitals with highly localized charge. In this regard,

a relevant result of this chapter is that the smart tailoring of charge delocalization regions in cations offers the possibility of designing ionic liquids with refractive indices higher than 2.0.

Chapter 8 aims to provide a broad perspective on the hyperpolarizabilities and nonlinear susceptibilities of ionic liquids as well as to determine the influence of charge delocalization on these quantities. For this purpose, a computational approach inspired by the one used in the previous chapter for electronic polarizability is employed. In this chapter, the goal is to determine the nonlinear response of ionic liquids by means of the individual responses of their constituent ions, using as fundamental variables the first and second order hyperpolarizabilities and the molecular volume. The ions considered are a series of anions commonly employed in the field of ionic liquids and three groups of cations that differ in the extent of charge delocalization in their structures. While the treatment of volumes is similar to that of the previous chapter, on this occasion, the additivity of ionic hyperpolarizabilities for the estimation of the hyperpolarizability of the ionic pair is not assured. For that reason, an assessment of the additivity principle of the first and second hyperpolarizabilities is performed by comparing the values obtained from simulations of ion pairs and isolated ions. The results show that while the first hyperpolarizability is not additive at all, the second one is. The breakdown of additivity for the first hyperpolarizability is possibly caused by the strong geometrical dependence of this magnitude, which is zero in centrosymmetric molecules. In order to determine the role of each ion in the nonlinear response of the ionic liquids of which they are part, the hyperpolarizability density of each ion, the ratio of this quantity to the molecular volume, is studied in detail. Furthermore, taking advantage of the additivity of the second hyperpolarizability, a map of the third-order susceptibility for the electro-optical Kerr effect (EOKE) for 1496 ion combinations is presented in this chapter. The results clearly demonstrate that the most relevant nonlinear optical responses are associated to the occurrence of extensive regions of delocalized charge.

USC
UNIVERSIDADE
DE SANTIAGO
DE COMPOSTELA

xl

Chapter 9 presents transition metals as an attractive alternative for the design of ionic liquids with interesting optical properties. Specifically, the materials upon study are a series of ionic liquids based on the 1-butyl-3-methylimidazolium thiocyanate doped with aluminum and various transition metals: nickel, manganese, iron and chromium. This chapter is mainly a computational study with certain experimental contributions, such as absorption spectra or X-ray diffractograms, which serve as a contrast to the calculations. The effect of the introduction of metals into ionic liquids is studied by molecular dynamics simulations (MD), which reveal that the metals form octahedral complexes with thiocyanate anions in the polar regions of the bulk. The formation of these complexes in those highly charged environments, happens under a delicate equilibrium of the ambidentate coordination of thiocyanate anions and the participation of them in coordination spheres of various metals by bridging. However, the largest influence of the different metals is found in the optical properties of the liquids, especially in the absorption spectra. TD-DFT simulations of metal-thiocyanate complexes suggest that these are who govern the optical response of these ionic liquids, with the cations playing only the secondary role of charge compensation. The absorption spectrum produced by each one of the ionic liquids is studied in detail and the main electronic transitions are described.

Finally, the last part of this thesis, chapter 10, presents the general conclusions of the doctoral work, in which the main contributions made to the scientific community are collected. These conclusions include various applications of ionic liquids in the field of photonics and highlight key mechanisms to tailor their optical properties. To conclude, some brief comments on the lines of future research opened by the work carried out in this thesis are included.

USC
UNIVERSIDADE
DE SANTIAGO
DE COMPOSTELA

Entrai mociños entrai
pola porta para dentro,
quen che me dera saber
que traen no pensamento.

Agradecementos

Esta tese recolle o traballo de investigación que realicei durante os últimos cinco anos. Tamén, pero doutro xeito, recolle as achegas de moita xente: agarimos, consellos e momentos inesquecibles. Dalgunha forma, esta tese é tan vosa coma miña. Ao escribir estas liñas doume conta dunha cousa, de que deberiamos agradecer máis a miúdo, e non só no momento de rematar as teses:

- Aos meus directores de tese, Luis e Elena, e máis ao meu titor Raúl. Por sempre axudarme a percorrer este camiño, ensinarme o que é a investigación e polas instructivas discusións científicas.

- Aos compañeiros de NaFoMat, a todos, sen excepción. A Hadrián, Txema, Trini, Álex e Víctor por axudarme sempre que lles foi posible coa tese, polos cafés computacionais en directo ou en remoto, os Mallos, as porras electorais e os cinefórums. A Sema, Chus, Pablo e Jujo por ser os meus experimentais favoritos, estar sempre aí, agardando para axudar e, tamén, para tomar un café (ou unha caña).

- A Hans-Peter Steinrück e Florian Maier, por darme a oportunidade de unirme ao seu grupo durante todo un verán. Tamén aos meus compañeiros de laboratorio, Bettina Heller, Francesco Greco e Sunghwan Shin, por acollerme como a un máis no grupo e ensinarme todo o que sei de cervexa alemá e XPS.

- Aos xa doutores Bilal Algnamat, e, moi especialmente, Yago Arosa, polos moitos bos momentos que pasamos xuntos, as innumerables horas de traballo en conxunto, os grandes consellos, e os apaixoados debates científicos.

- Ás miñas compañeiras e compañeiros de despacho, Ana, Bruno, Héctor e demais, pola nosa afición común aos cursos do PFID, as

xeniais conversas de despacho e por sempre sacarme un sorriso. Tamén a Ester e Ana, que cadrar con elas sempre aleda o día.

• Á miña xente do grupo de divulgación USC-OPTICA (formerly USC-OSA) e USC-EPS. Polas reunións virtuais, as reunións con xantar incluído, as contribucións a congresos e as moitas cousas que fixemos xuntos. E, en especial, a Alicia Muñoz polas súas ideas, a Alejandro Doval por ser a voz sensata e a Bastián Carnero polo seu grande espírito twitchero.

• Aos meus pais, aos meus avós e á miña familia. Aos meus irmáns pequenos, que xa non o son tanto, fonte de ilusión e enerxía. A todos vós, por estar sempre ao meu carón, por apoiarme sempre.

• A Óscar Lantes, por compartir a súa vida comigo.

• A Damián, Fontán, Mariamo, Eric, Tino e Oliva polos xantares e conversas de todos os días, e por Valle-Inclán.

• Aos meus amigos de "Compostela": Macamen, María, Xan, Ángeles, Rubén, Fernando, Begoña e Javi. Polas Próximas, as Cicerone, os Palas, os San Xoáns, Vs de Verão, ceas e demais saídas que me axudaron a desconectar da tese cando máis o precisaba.

• As miñas amigas da Coruña, especialmente, a Ana, Andrés, Helena, Joel e Lara, por estar aí dende hai tanto tempo que case non podo lembrar a vida sen vós.

• Aos meus amigos físicos de polo mundo adiante: Iagos, Darío, Samuel, Isidro e Pablo, que sempre que podemos nos xuntamos para falar das teses, da ciencia e rir un pouco.

• Á Escola e ao Instrumental de Cantigas e Agarimos, e á Escola da Gentalha do Pichel por ensinarme a importancia da tradición e axudarme a levar a tese coa música por diante. A Brais, Antía e María por tantas bailas que botamos xuntos.

Contents

III Results   57

Carlos Damián Rodríguez Fernández

List of Figures

liv

lviii

USC
UNIVERSIDADE
DE SANTIAGO
DE COMPOSTELA

USC
UNIVERSIDADE
DE SANTIAGO
DE COMPOSTELA

List of Tables

Part I

Introduction

1. Introduction

1.1 Motivation

Photonics is the name of the scientific discipline that digs into the nature of light. The number of questions that photonics tries to answer is wide: What is light? How does it arises? How does it travels through the space? How does it interact with matter and with itself? All these questions, among others have been asked since the very same birth of scientific thought, and a great effort to answer them has been done through ages. All in all, light is intimately related to life. It provides the energy to keep the natural equilibrium on Earth as well as it sets the footstep of the pass of time in nature through the different astronomical cycles: days, nights and seasons. In this regard, light is a cornerstone of all the human cultures and the discovery of fire is a double milestone in our history. It not only provided heat but it was the first accessible mechanism to humans to create light, the first way to remove the impairing darkness of the ancient societies. The importance of light in the ancient, and not so ancient, cultures is also reflected in the role that light played in their beliefs and its relation to religions. Our societies have changed over time, and in parallel with the development of the scientific thought, we were able to answer the questions formulated above in their original conception. Nevertheless, if we think about the questions that are addressed by photonics in our days, we will realize that, at the end, most of the questions are still the same and what has changed is the context. Nowadays we wonder how a specific kind of beam would propagate, how is light produced by a new light source or how would it interact with a new material.

Meanwhile, light has become the basis of a large number of scientific applications and technologies with industrial implementations much beyond lightning. It is not strange to find lasers that systematically

3

cut steel with extreme precision and others that smoothly touch CDs and DVDs to transform their surfaces in music and images. It is possible to observe the structure of molecules or cells through the way they absorb or emit light. Furthermore, the interaction of light with matter can be engineered to design optical systems that are able to correct deficiencies in vision, magnifying tiny objects, bringing closer distant objects (and with them part of the infinity of cosmos) or producing materials with enhanced optical responses or unusual behaviors in the propagation of light. In this regard, the advent of the photonics era has initiated a race to find new materials whose optical responses improve that of the current materials. Greener and more efficient solutions are needed, materials whose optical response can be finely tuned to achieve the best feasible performance.

Ionic liquids are a family of materials that present very interesting physico-chemical properties including negligible vapor pressure, low flammability as well as high thermal, electrical and chemical stability. However, their most fascinating property is their highly tailorable character, which offers the unique opportunity to the field of photonics of designing materials with task-specific photonic responses. The amount of properties of optical interest that ionic liquids exhibit and which are susceptible to be tuned is large, including material dispersion, nonlinear optical response, different types of chromism and even liquid crystalline character.

All the work presented throughout these pages contributes to the fundamental effort of finding tomorrow's photonic materials. Specifically, this thesis is devoted to expand the current knowledge about the optical properties of ionic liquids by directly addressing the relation with their microscopic structure at different characteristic scales. We aim to describe the key elements to tune the optical response of ionic liquids, pointing out the elements which, in the future, will allow their use as photonic materials.

1.2 Photonics and materials

Science and industry have always been looking for novel and improved materials with potential applications going further the best available technology at each time. In the field of photonics, the situation is not different, but, maybe, it is even more true than in any other field. The evolution of this discipline over time can not be understood without considering the huge impact that the discovering and implementation of different materials have had on it. The number of examples is large and it is not my purpose to cite them all here, but it is interesting to mention some of them.

In optics, light propagation is engineered through the sequential introduction of different transmissive, reflective and refractive elements. Each one of these elements relies on a physical material whose optical properties were tuned to provide the optimal performance. In this regard, apart from the importance of the shape and surface properties of those elements, their composing material plays a fundamental role. For refractive elements, refractive index, material dispersion and thermo-optical coefficient (TOC) can be tuned by changing the composition of the glasses, while for reflective or transmissive elements, their composition determines their performance in a desired wavelength range.

Other example of the importance of materials in photonics are liquid crystals, a family of materials which are a research area on their own because of their particular way of interacting with light. Liquid crystals are liquids that present a certain extent of orientational -and even translational- order and, in consequence, they show birefringence due to the existence of, at least, two different refractive indices. The tailoring of the interaction of light with these materials yielded an extensive research area as well as the development of the currently widespread liquid crystal display (LCD) technology.

A further type of materials that play a relevant role in photonics are

USC
UNIVERSIDADE
DE SANTIAGO
DE COMPOSTELA

those that present relevant nonlinear optical (NLO) responses. They can either suffer deep reversible changes in their optical response due to their strong interaction with light or induce them in the light they are irradiated with. NLO materials together with high intensity lasers are the basic components of the nonlinear optics research area, which includes the study of a large set of nonlinear phenomena, from second harmonic generation (SHG) or Third Harmonic Generation (THG), where the doubling and tripling of the input light frequency is produced, to Electro-Optical Kerr Effect (EOKE), where the application of an stationary electric field transforms the material in birefringent.

As it can be observed from the previous examples, photonics and material science are two disciplines that present strong synergies and the importance of the development of new photonic materials is currently well established. It is in this framework, where ionic liquids (ILs) arise. They are a wide set of materials with excellent physicochemical properties that are extraordinary candidates to play a leading role in the field of photonics due to their high degree of tunability and the deep impact that this tunability has in their optical properties.

1.3 Ionic liquids

Ionic Liquids (ILs) are a family of purely ionic materials that are liquid at temperatures below 100 ºC, i.e., low and even room temperature molten salts. From the chemistry point of view, they are poorly coordinated salts that melt at low temperatures due to the large volume and shape differences of their ions. The existence of ILs is known since 1914, when Paul Walden described ethylammonium nitrate for first time.[1] However, despite their relatively early discovery, ILs did not attract too much attention up to the decade of 1980, when they started to be used as solvents for the study of transition metal complexes.[2–6] Notwithstanding, it was not up to the beginning of the nineties that ILs became a hot topic on chemistry, due, in part, to the successful synthesis of the first water and air stable family of ILs.[7] Since then,

USC
UNIVERSIDADE
DE SANTIAGO
DE COMPOSTELA

ILs have attracted more and more attention due to their unique set of properties which, among others, are:

- **Negligible vapor pressure and high thermal stability:** The strong coulombic interactions between ions prevent ILs from evaporation up to relatively high temperatures.[8–10] For this reason, their ionic character also provides them with a large thermal stability,[11–16] much higher than that of common solvents which often suffer from early evaporation or degradation.

- **Solvation power:** The presence of strong polar regions associated to the charged parts of the ions, in combination with the nonpolar regions associated to their organic parts, yields a nanostructurated bulk. This confers ILs the ability to dissolve both polar and nonpolar molecules, for which ILs are also known as universal solvents.[17–23]

- **High electrochemical stability:** The purely ionic nature of ILs makes them show high electrical conductivity[24–28] due to the large number of charge carriers present in their bulk and a good electrochemical window due to the electrochemical stability of the ions.

- **Tunability:** ILs are the combination of two different ions. Both of them are suitable to be carefully designed to tune the properties of the resulting IL, reason why ILs are also known as "designer solvents".[29–32] In fact, in addition to the design possibilities offered by the ion combination, new horizons can be explored upon consideration of metal doping or introduction of a third ion.

As a consequence of this set of exclusive properties, ILs have been progressively introduced in more and more applications in very different fields such as mechanical lubrication,[33–39] separation technology,[40–48] synthesis and catalysis,[17,20,49–53] nanoparticle and nanoplatelet deposition,[54–58] CO_2 capture,[22,30,59–62] energy storage[63–68] or green energy production.[69–72] This wide sort of applications are

evidences of the versatility of these materials to be applied in different fields. Hence, consequently, one could legitimately wonder which is the possible extent of applications of ILs in the field of photonics, question we address in the following section.

1.4 Ionic liquids as photonic materials

ILs are versatile materials that can be finely tuned to exhibit task-specific properties, a feature that is of great interest from the photonics' perspective. In the last years, there was an increasing number of contributions dealing with optical properties of ILs, but this figure is still far from that of other physical magnitudes. The need of further research is specially evident when considering ILs based on cations going beyond the imidazolium one, where there is a generalized and evident lack of available experimental data. Despite these limitations, it is being more and more frequent finding contributions that use ILs as the basic material of different photonic devices and applications. For instance, taking advantage of the tunable and potentially high refractive index of ILs, Deetfles et al.[73] proposed their usage as immersion liquids for gems' and minerals' characterization and, recently, they were proposed as immersion liquids for other applications.[74] Other research groups[75–78] were able to design and implement different strategies to build functional variable focus lenses using ILs.

ILs were also explored as functionalized waveguiding materials with promising results. Guo et al.[79] designed an IL-based optical fiber with all-optically switchable light transmission by exploiting the TOC of the IL while He et al.[80] used the strong response of ILs to electric fields to create a waveguide with electrically modulated transmission. Indeed, the particular response of ILs to electric fields is also the basis of their potential usage in electro-optical devices.[81]

Furthermore, some IL-based systems were also proposed as photonic sensors for different magnitudes. As an example, in Ref. [82] a sensor for detecting ammonia in human breath was developed on

the basis of a slab optical waveguide containing an IL, or in Ref. [83] an IL was proposed as a humidity sensor due to the influence of environmental water in its optical response.

ILs have also been tested as active light emitting materials for display technology[84] or as performance enhancers in light-emitting electrochemical cells (LEECS).[85] Other examples of the possibilities that ILs have in the field of photonics include their usage as tunable photonic crystals,[86] or as active nonlinear optical materials.[87,88] Finally, it is noteworthy mentioning that ILs were also proposed as key materials for building high-quality mirrors for space telescopes.[89,90]

As it is shown by the plethora of previous applications, ILs are versatile materials with a promising future in photonics. In this regard, the amount of applications of ILs in photonics is considerably larger than those presented in this brief summary, since ILs have the possibility to be tuned to exhibit designed optical responses. The number of tailorable optical properties of ILs is wide, comprising, among others, the following ones:

- **Refractive index and material dispersion:** Refractive index is the ratio of the speed of light in vacuum to the speed of light in the medium. It is a decisive magnitude from the photonics point of view since the design of whichever refractive element, such as lenses or immersion liquids, relies on it. Material dispersion is the dependence of refractive index with wavelength. It is possible to distinguish between normal dispersion, where refractive index increases when decreasing the wavelength, and anomalous dispersion, when the behavior is just the opposite. Material dispersion and other dispersive properties such as Abbe number, group index, group velocity and group velocity dispersion are fundamental magnitudes for choosing specific materials for photonic applications. In the case of Abbe number, V_{Abbe}, it is a qualitative parameter that summarizes the material dispersion of any material, since it is defined by means of the refractive index measured at different wavelengths: $V_{Abbe} = (n_D - 1)/(n_F - n_C)$,

where n_D, n_F and n_C are, respectively, the refractive index at the wavelengths of the corresponding Fraunhofer spectral lines, D = 589.0 nm, F = 486.13 nm and C = 656.28 nm. Unlike refractive index at a single wavelength, contributions dealing with material dispersion are extremely scarce. In fact, apart from our own work, we could barely find a bunch of contributions measuring the refractive index of ionic liquids at more than one wavelength. [74,77,91–94]

- **Thermo-Optical Coefficient (TOC):** It is the coefficient that measures the variation of the refractive index with temperature. This parameter is not negligible for liquid matter, and it will determine the specific refractive properties of an IL in a certain temperature range. Because of the non optical scope of the majority of works dealing with refractive index, thermo-optical coefficients are not usually analyzed. However, the thermophysical scope of some of these works lead the authors to measure the refractive indices at several temperatures, [95–100] which provides an indirect way to estimate the TOC for different ILs.

- **Luminescence:** It is the ability of a material to emit light as a response to a certain stimulus. It is possible to distinguish between different types of luminescence according to the nature of the stimulus that produces the light emission: photoluminescence when the origin is light, electroluminescence when it is an electric field, thermoluminescence when it is temperature, etc. Among the different kinds of luminescence, photoluminescence is the most common one in ILs. As a consequence of the presence of organic regions in standard pure ILs, they are photoluminescent materials by their own upon excitation with the proper wavelengths. [101] Nevertheless, their luminescence can be enhanced and tuned following different strategies. For instance, it can be done by doping with transition metal complexes [102–109] or by introducing organic chromophores in the structure of at

USC
UNIVERSIDADE
DE SANTIAGO
DE COMPOSTELA

10

least one of the ions.[84,110–112]

- **Chromism:** It is the capability of a material to change its color (absorption spectrum) as a response to a certain stimulus. As in the case of luminescence, there are different kinds of chromism as a function of the origin of the stimulus that produces the color change: thermochromism when it is temperature, electrochromism when it is an electric field or photochromism when it is light. ILs are able to exhibit different kinds of chromism upon a proper design of their structure. There are evidences of strong thermochromic,[113,114] electrochromic[115–118] or photochromic[119] effects on ILs.

- **Nonlinear optical response:** It is the nonlinear coupling of light with matter, which is dependent on the material structure and it is only accessible at very high irradiances. There is a large portfolio of nonlinear optical processes that appear in the interaction of a material with light. There are evidences that ILs can be designed to show important nonlinear absorption,[88,120] nonlinear thermal response,[121,122] nonlinear second order phenomena at surfaces and solid state[123–126] as well as third order phenomena.[87,127,128] Furthermore, this plethora of interactions can be exploited not only with photonic purposes but also to gain insight inside the bulk[129–134] and interfaces of ILs in contact with air,[135] quartz[136,137] or even electrified electrodes.[138–140]

- **Mesophase formation:** Popularly known as Liquid Crystal (LC) phases, are the intermediate phases between the solid and liquid states of matter. They are fluid states that present a certain extent of orientational, and even translational order, which can provide them with birefringence. Upon alignment, they often present at least two privileged directions, each one with its own refractive index. The refractive index of smaller value is known as fast refractive index since light travels faster in that axis, and, for the opposite reason, the refractive index of higher value is known as slow refractive index. When LCs are not aligned,

USC
UNIVERSIDADE
DE SANTIAGO
DE COMPOSTELA

11

they spontaneously organize in microscopic domains that, upon observation in polarizing microscopy, present characteristic patterns known as textures, which are distinctive of different LC mesophases.

ILs can be tuned to present liquid crystal phases, forming the family of materials called ionic liquid crystals (ILCs).[141–144] Formation of ILCs can be induced by the introduction of long alkyl chains in the ions[145–147] or by the direct introduction of mesogenic cores in their structure.[108,111,148] ILCs commonly show smectic A mesophases (SmA),[141–144] which are characterized by the formation of bilayers that markedly segregate the polar and nonpolar parts of the ions at the same time that the coulombic energy is minimized. However, other mesophases can be induced by a proper selection of the ions.[149]

1.5 Microscopic electronic response and macroscopic optical properties in liquids

When an external microscopic (local) electric field, $\vec{F}^{loc}$, acts over a molecule, it induces a dipole on this molecule, $\vec{\mu}$. The form of this dipole in the direction i, μ_i, is:

$$
\begin{aligned}
\mu_i = \mu_i^{(0)} &+ \sum_j \alpha_{ij} \cdot F_j^{loc} + \frac{1}{2} \sum_j \sum_k \beta_{ijk} \cdot F_j^{loc} F_k^{loc} \\
&+ \frac{1}{6} \sum_j \sum_k \sum_l \gamma_{ijkl} \cdot F_j^{loc} F_k^{loc} F_l^{loc} + ...,
\end{aligned}
\tag{1.1}
$$

where $\mu_i^{(0)}$ is a possible permanent dipole, and α_{ij}, β_{ijk} and γ_{ijkl} are, respectively, the components of the linear polarizability, first order hyperpolarizability and second order hyperpolarizability tensors of the molecule. In addition, i, j, k, and l stand for the Cartesian components of the field on each dimension of the dipole, polarizability

and hyperpolarizability tensors. On the other hand, from a macroscopic perspective, when a macroscopic electric field $\vec{F}$ is applied over a material, it induces an electric polarization $\vec{P}$. The component of this polarization in the direction i, P_i, is:

$$
\begin{aligned}
P_i = P_i^{(0)} + \varepsilon_0 \sum_j \chi_{ij}^{(1)} \cdot F_j + \frac{1}{2}\varepsilon_0 \sum_j \sum_k \chi_{ijk}^{(2)} \cdot F_j F_k \\
+ \frac{1}{6} \sum_j \sum_k \sum_l \varepsilon_0 \chi_{ijkl}^{(3)} \cdot F_j F_k F_l + ...,
\end{aligned} \tag{1.2}
$$

where $\chi_{ij}^{(1)}$, $\chi_{ijk}^{(2)}$ and $\chi_{ijkl}^{(3)}$ are the components of the nth order susceptibilities of the material and ε_0 the vacuum electric permittivity. From an optical perspective, the linear susceptibility, $\chi_{ij}^{(1)}$, is the responsible of the refractive response of the material since, at optical frequencies, the electric permittivity, ε, is related to its refractive index:

$$
\chi_{ij}^{(1)} = \varepsilon_{ij} - 1 = n_{ij}^2 - 1, \tag{1.3}
$$

On the other hand, higher order susceptibilities (also known as nonlinear susceptibilities) are responsible for its nonlinear optical response. Specifically, $\chi_{ijk}^{(2)}$ is responsible for the second order nonlinear phenomena, such as second-harmonic generation (SHG) or the Pockels Effect, while $\chi_{ijkl}^{(3)}$ is responsible for third order nonlinear phenomena, such as Electric Field Induced Second Harmonic Generation (EFISH), Third Harmonic Generation (THG) or the Electro-Optical Kerr Effect (EOKE).

In any material the macroscopic polarization $\vec{P}$ can be related to the microscopic dipoles induced by that field, $\vec{\mu}$:

$$
P_i = \rho \mu_i, \tag{1.4}
$$

where ρ is the number density of microscopic dipoles (density of molecules) in the material, $V_N / N = 1/\rho$, being N the total number of particles and V_N the volume these particles occupy. Eq. (1.4) opens a way to predict the macroscopic optical properties of any material

USC
UNIVERSIDADE
DE SANTIAGO
DE COMPOSTELA

from those of its composing molecules. Specifically, refractive index from electronic polarizability and nth order nonlinear susceptibilities by means of the corresponding hyperpolarizabilities. However, it is important to take into account that the electric field at the microscopic level, $\vec{F}^{loc}$, differs, in general, from the macroscopically applied external field, $\vec{F}$, because of the influence of the dipoles of the neighboring molecules. For this reason, it is necessary to introduce a field factor that estimates the effective electric field at the microscopic level when a macroscopic field is applied. The most famous correction is the Lorentz field factor, which models the molecules in the bulk of a material as spheres:

$$\vec{F}^{loc} = \frac{n^2 + 2}{3}\vec{F},$$ (1.5)

where n is the refractive index of the material at the field frequency. Writing together Eqs. (1.1), (1.2), (1.4) and (1.5), the relation between the nth order susceptibility and electronic polarizability or nth order hyperpolarizability can be found:

$$\chi_{ij}^{(1)}(-\omega_a; \omega_a) = f(\omega_a) \cdot \frac{\alpha_{ij}}{\varepsilon_0 V},$$ (1.6)

$$\chi_{ijk}^{(2)}(-\omega_a; \omega_b, \omega_c) = f(\omega_a)f(\omega_b)f(\omega_c) \cdot \frac{\beta_{ijk}}{\varepsilon_0 V},$$ (1.7)

$$\chi_{ijkl}^{(3)}(-\omega_a; \omega_b, \omega_c, \omega_d) = f(\omega_a)f(\omega_b)f(\omega_c)f(\omega_d) \cdot \frac{\gamma_{ijkl}}{\varepsilon_0 V},$$ (1.8)

where V is the molecular volume of the molecules in the material and $f(\omega_i)$ is the Lorentz field factor, $f = \frac{n^2(\omega_i)+2}{3}$ at the frequency ω_i. Note that the convention of denoting the frequencies of the input fields as positive and the frequencies of the induced polarization as negative is used. It is, for the nonlinear phenomena of susceptibility $\chi_{ijk}^{(2)}(-\omega_a; \omega_b, \omega_c)$, the input frequencies are ω_b and ω_c, and the output frequency ω_a.

Finally, it is compulsory to mention that, combining Eqs. (1.6) and (1.3), the famous Lorentz-Lorenz equation is obtained:

$$\frac{n^2 - 1}{n^2 + 2} = \frac{\alpha}{3\epsilon_0 V},\tag{1.9}$$

This equation relates the refractive index of a liquid with the electronic polarizability of its constituent molecules under the approach of considering them as spheres.

1.6 Objectives

The global objective of this thesis is studying and rationalizing a series of optical properties of ILs, namely material dispersion, nonlinear optical response, absorption spectrum, and liquid crystalline character in relation with their structure. In order to accomplish this task, both experimental and computational techniques are used, which allow us to address these relations in different characteristic scales, ranging from macroscopic perspectives to those of mesoscales of several microns length or down to microscopic systems of sizes from tens of nanometers to that of individual molecules. The objectives of this thesis are:

- Measuring the material dispersion of some of the most common imidazolium-based ionic liquids in the spectral range from 400 nm to 1000 nm. Furthermore, addressing the effect of different anions and alkyl chain of the imidazolium cation in refractive index from the perspective of the Lorentz-Lorenz model (chapter 3).

- Evaluating the influence of temperature in the material dispersion of imidazolium-based ionic liquids and finding a physically meaningful, but simple, way to model their material dispersion within the range from 400 nm to 1000 nm (chapter 4).

- Modeling material dispersion in relation to the molecular structure of ionic liquids using a very broad spectral range, from 300 nm to

USC
UNIVERSIDADE
DE SANTIAGO
DE COMPOSTELA

1550 nm. Finding the key elements to set a procedure for semi-empirically predicting the material dispersion of the ionic liquids by computational methods (chapter 5).

- Determining the structure of an ionic liquid crystal and demonstrating that they can be aligned and optically characterized by measuring their birefringence dispersion (chapter 6).

- Drawing a holistic picture of refractive indices in the world of ionic liquids by means of density functional theory calculations. Evaluating the relevance of charge delocalization as a refractive index tailoring tool (chapter 7).

- Finding the relation of the nonlinear optical responses of ionic liquids with their structure. Performing an evaluation of the role that charge delocalization plays in the strength of those magnitudes (chapter 8).

- Addressing the structural effects of doping ionic liquids with transition metals. Characterizing the impact in their optical properties, namely absorption spectrum (chapter 9).

Part II

Materials and Methods
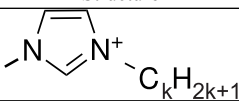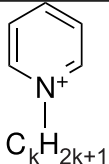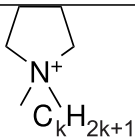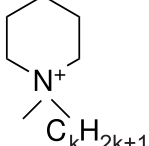
2. Materials and Methods

2.1 Materials

ILs considered in this thesis and nomenclature

Throughout this thesis, more than 1500 different binary ILs were considered to some extent and named as [A][B], being $[A]^+$ the cation, and $[B]^-$, the anion. In Tables 2.1 and 2.2, the names and molecular structures of all the families of ions that formed part of the ILs included in this thesis are shown.

Table 2.1: Names, abbreviatures and structures of the cations considered in this thesis.

Compound	Abbreviation	Structure
1-alkyl-3-methylimidazolium	$[C_k\text{mim}]^+$	
1-alkylpyridinium	$[C_k\text{py}]^+$	
1-alkyl-1-methylpyrrolidinium	$[C_k\text{mpyrr}]^+$	
1-alkyl-1-methylpiperidinium	$[C_k\text{mpip}]^+$	
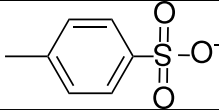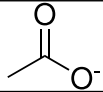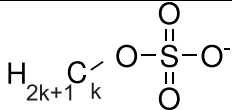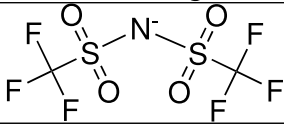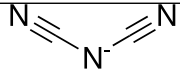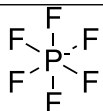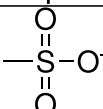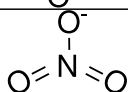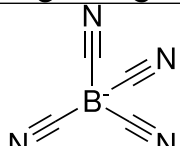
1-alkyl-1-methylmorpholinium	$[C_k mmor]^+$	
1-alkyl-3-methylthiazolium	$[C_k mthia]^+$	
1-alkylquinolinium	$[C_k quin]^+$	
Alkylamonnium	$[N_{0,0,0,k}]^+$	
Alkyl(Trimethyl)Ammonium	$[N_{1,1,1,k}]^+$	
Alkyl(Tributyl)phosphonium	$[P_{4,4,4,k}]^+$	
Tetraoctylphosphonium	$[P_{8,8,8,8}]^+$	
Tetradecyl(trihexyl)phosphonium	$[P_{6,6,6,14}]^+$	
1-allyl-3-methylimidazolium	$[allylmim]^+$	
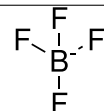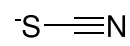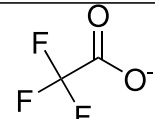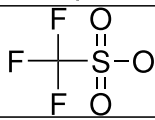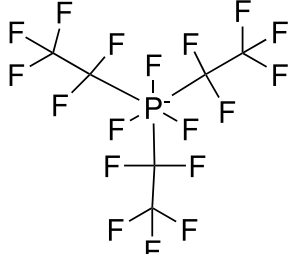
1,3-diallylimidazolium	[1,3-diallylim]$^+$	
1-benzyl-3-methylimidazolium	[benzylmim]$^+$	
1,3-dibenzylimidazolium	[1,3-dibenzylim]$^+$	
1-crotyl-3-methylimidazolium	[crotylmim]$^+$	
1-ethoxy-3-methylimidazolium	[eomim]$^+$	
1,3-diethoxyimidazolium	[1,3-dieoim]$^+$	
1-ethylnitrile-3-methylimidazolium	[enmim]$^+$	
1,3-diethylnitrileimidazolium	[1,3-dienim]$^+$	
1-methyl-3-vinylimidazolium	[vinylmim]$^+$	
1,2-divinylimidazolium	[1,2-divinylim]$^+$	
1,3-divinylimidazolium	[1,3-divinylim]$^+$	
1-meth(oxyethyl)$_k$-3-methylimidazolium	[m(eo)$_k$mim]$^+$	
1-methyl-3-perfluoroalkylimidazolium	[F$_k$mim]$^+$	
1-polyenyl-3-methylimidazolium	[uC$_k$mim]$^+$	

Table 2.2: Names, abbreviatures and structures of the anions considered in this thesis.

Compound	Abbreviation	Structure
4-methylbenzenesulfonate	$[Tos]^-$	
Acetate	$[Oac]^-$	
Alkylsulfate	$[C_kSO_4]^-$	
Bis(trifluoromethylsulfonyl)imide	$[NTf_2]^-$	
Bromide	$[Br]^-$	Br-
Chloride	$[Cl]^-$	Cl-
Dicyanamide	$[DCA]^-$	
Hexafluorophosphate	$[PF_6]^-$	
Methylsulfonate	$[C_1SO_3]^-$	
Nitrate	$[NO_3]^-$	
Tetracyanoborate	$[B(CN)_4]^-$	

Tetrafluoroborate	$[BF_4]^-$	
Thiocyanate	$[SCN]^-$	
Trifluoroacetate	$[Oaf]^-$	
Trifluoromethanesulfonate	$[OTf]^-$	
Trifluorotris(perfluoroethyl)phosphate	$[FAP]^-$	

23

Managing ILs for optical purposes

ILs are materials which are easily contaminated and, in consequence, they have to be very carefully manipulated. The impact of the presence of impurities on the optical properties of ILs is huge, probably much more important than in other physical properties. As an example, Fig. 2.1 shows a histogram of the relative deviation of the refractive indices measured in this thesis for the $[C_k\text{mim}][BF_4]$ family of ILs with respect to those in bibliography measured in the same conditions, $\Delta n = (n_{lit} - n_{ThisWork})/n_{ThisWork}$. It collects more than 130 values of refractive indices at the sodium D line, taken by 30 different authors and at different temperatures.[40,95,97–99,150–175] The histogram evidences the large differences between authors when measuring the refractive index of ILs, even when the considered IL family is one of most widely studied. Data in the histogram have a mean of $1.37 \cdot 10^{-4}$ with a standard deviation of $1.14 \cdot 10^{-3}$. The outliers marked in the figure were discarded for the mean calculation since they correspond to specific authors showing systematic deviations with respect to the literature mean values. However, even proceeding in this way, the large standard deviation of the distribution, much larger than the experimental resolution claimed in most of the publications, provides a striking evidence of the importance of taking care of impurities when measuring optical properties of ILs. There are three main factors that dramatically alter these properties:

- **Water:** Most of ILs are highly hygroscopic, even those which are considered to be not too much hygroscopic do actually absorb considerable amounts of water from the environment. The incorporation of water molecules into ILs reduces their refractive index, since water refractive index is commonly less than that of pure ILs. This reduction of refractive index by water contamination is not negligible, but in fact, it is an important source of error in refractive index measurements. For
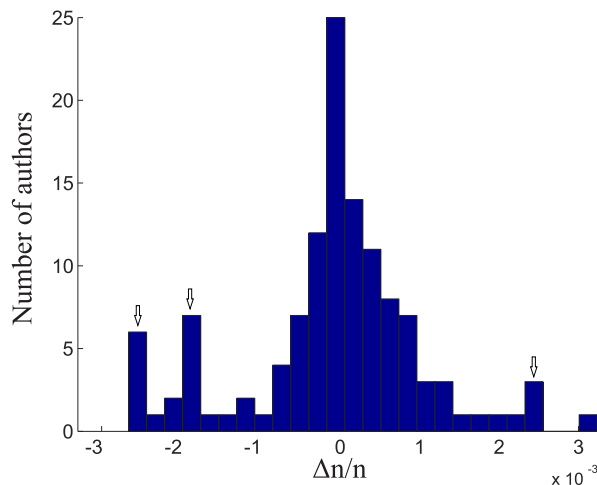
Figure 2.1: Histogram of the relative deviation of the refractive indices measured in this thesis for the [C$_k$mim][BF$_4$] family of ILs with respect bibliography, $\Delta n = (n_{lit} - n_{ThisWork})/n_{ThisWork}$. It comprises more than 130 values of refractive indices taken by 30 different authors at the sodium D line and distinct temperatures.[*]

[*]Reprinted from: C.D. Rodríguez-Fernández, Y. Arosa, B. Algnamat, E. López Lago and R. de la Fuente, An experimental and computational study on the material dispersion of 1-alkyl-3-methylimidazolium tetrafluoroborate ionic liquids, *Phys. Chem. Chem. Phys.*, 2020, **22**, 14061 - 14076.

this reason, when possible, the measurements that form part of this thesis were done on vacuum-dried ILs. The drying process consists in keeping the IL for at least 48 hours in a vacuum chamber under pressure below $1 \cdot 10^{-3}$ atm. After that, in order to check the performance of the drying process, the residual amount of water was always measured using a Mettler-Toledo Karl-Fisher Tritrator. When drying was not possible, tritration of the amount of water in the IL was performed, and then the measured refractive index was corrected by considering the experimental IL as a mixture of the pure IL with water.[176]

• **Impurities from synthesis:** During synthesis, it is common that some impurities remain in the ILs. These impurities are

25

frequently negligible for most purposes, but they are not so for photonic applications, since they affect optical properties such as photon absorption or refractive index.[177] Most pure ILs are expected to be transparent since they are indeed organic molecules without significant absorption in the visible range. Nevertheless, the presence of some kinds of impurities produces coloration in ILs which modify their absorption spectrum. In addition, the changes in the absorption spectrum produce a direct impact in the refractive index of the IL, which can be visualized through the Kramers-Kronig relations.[178] In general trends, the presence of absorption in the impure IL yields an increase of refractive index with respect to that of the pure IL.

- **Degradation:** When an IL is kept during a long time after its synthesis under improper conditions, e.g., in the presence of water after accidental hydration, or under exposition to other degrading agents, it is susceptible of suffering a partial degradation. The most common evidence of degradation in an IL is the progressive change of its coloration, which usually darkens as the degradation increases. Again, the presence of coloration means that the visible absorption spectrum of the IL is modified. Hence, in the view of the Kramers-Kronig relations, material dispersion in the nearby spectral ranges is also expected to be affected.[178]

2.2 Experimental methods

Throughout this thesis, a wide plethora of experimental techniques and methodologies were employed, being possible to make an important distinction between the measurement of optically related magnitudes and the others. Optical properties such as material dispersion, birefringence or optical absorption were measured by means of a highly flexible home-made device. This device is a spectrally resolved white light interferometer which implements a characterization technique

known as Refractive Index Spectroscopy by Broadband Interferometry, RISBI.[179–181] Non optical magnitudes, such as density, NMR or XRD spectra, were measured using commercial devices together with complementary optical measurements required by RISBI to operate, such as reference refractive indices at discrete wavelengths.

RISBI

The Refractive Index Spectroscopy by Broadband Interferometry, RISBI, foundations[179–181] are set in a standard Michelson interferometer illuminated with white light coupled to a spectrometer. The intensity at the output of the interferometer is given by:

$$I(\lambda) = I_0(\lambda) \left[1 + \nu(\lambda) \cos \varphi(\lambda)\right], \tag{2.1}$$

where $I_0(\lambda)$ is the background intensity, $\nu(\lambda)$ is the visibility function and $\varphi(\lambda)$ is the phase difference between the arms of the interferometer. If there is a material (sample) of refractive index $n(\lambda)$ and thickness d in one of the arms, the phase difference takes the form:

$$\varphi(\lambda) = \frac{4\pi}{\lambda} \left\{d\left[n(\lambda) - n_A\right] - n_A L\right\}, \tag{2.2}$$

where n_A is the refractive index of air and L is the path difference in air between both arms. However, as the mathematical operation to obtain $\varphi(\lambda)$ from the irradiance pattern $I(\lambda)$ in Eq. (2.1) involves an arccosine, there is an unavoidable ambiguity on the retrieved phase, $\varphi_{exp}(\lambda)$:

$$\varphi(\lambda) = \varphi_{exp}(\lambda) + 2\pi k, \tag{2.3}$$

with $k \in Z$. Combining Eqs. (2.1), (2.2) and (2.3), the material dispersion $n(\lambda)$ of the sample can be obtained:

$$n(\lambda) = n_A + \frac{1}{d}\left[\frac{\varphi_{exp}(\lambda)\lambda}{4\pi} + \frac{k\lambda}{2} + n_A L\right]. \tag{2.4}$$

According to Eq. (2.4), using the phase of the white light interferogram, $\varphi(\lambda)$, it is possible to extract the material dispersion of any material if

its thickness, d, the air path difference in the arms of the interferometer, L, and the arbitrary k factor are known.

In order to fully determine the k value, a reference refractive index of the sample, n_0, at a single wavelength, λ_0, is required:

$$k = \frac{2}{\lambda_0}[d(n_0 - n_A) - n_A L] - \frac{\varphi_{exp}(\lambda_0)}{2\pi}. \tag{2.5}$$

Typically, due to experimental uncertainties, the value obtained in this way will not be an integer, but it is expected to be close to one. As we know that k must be an integer, we must round it and use the nearest integer (nint) to obtain the refractive index:

$$n(\lambda) = n_A + \frac{1}{d}\left[\frac{\varphi_{exp}(\lambda)\,\lambda}{4\pi} + \frac{\text{nint}(k)\lambda}{2} + n_A L\right]. \tag{2.6}$$

Our RISBI experimental device is schematically represented in Fig 2.2. It consists on three main parts: a white light source, an interferometer and a set of spectrometers:

- **Illumination source**: Depending on the spectral range of interest, the illuminating source is a halogen lamp with a black body like emission spectrum (400 – 1550 nm) or a deuterium lamp (255 – 520 nm), both stabilized to obtain a constant intensity. The beam exiting the light source is collimated and the intensity is homogenized. In the case of using the halogen lamp, a filter is also added to the set up to reduce the intensity of the light in the red and infrared spectrum.

- **The interferometer**: A commercial Michelson interferometer modified to satisfy our needs was employed. The reference arm of the interferometer has a moving mirror that is displaced by a lever connected to a micrometer screw. The micrometer screw has a resolution of 2 μm and the lever reduces the displacement by a 3/25 factor. The samples are located on the measuring arm
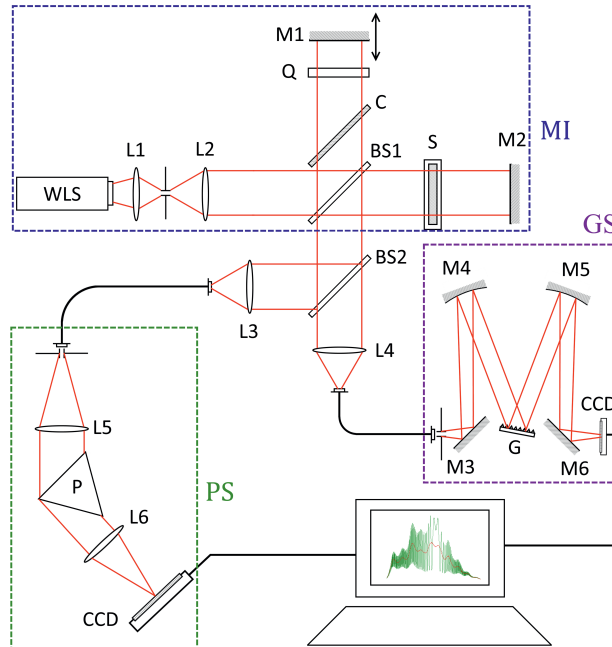
Figure 2.2: Scheme of the experimental set-up. WLS white light source, L1-L6 lenses, M1-M6 mirrors, BS1-BS2 beam splitters, C compensating plate, S sample, Q quartz plate, P prism, G diffraction grating.[*]

---

of the interferometer inside a quartz cell. The cell is coupled to a circulating water bath that controls the temperature of the sample, which is monitored by means of a thermocouple. In order to partially compensate the quartz of the walls of the measuring cell, a quartz plate of similar thickness is also introduced in the reference arm. The output of the Michelson interferometer is focused on an optical fiber that transports the signal to the spectrometer of interest.

• **The set of spectrometers**: Four different spectrometers are used

for different purposes. Three of them are devoted to resolve the interferogram produced by the sample in different spectral regions (infrared, visible and ultraviolet), while, the fourth one, is devoted to measure the length difference between the spectrometer arms, L.

- The infrared spectrometer covers the region of $950 - 1550$ nm. It is a grating spectrometer of 50 mm focal length with a transmission grating of 300 lines/mm. The output is registered by an infrared array camera of dimensions 320 x 256 pixels, each one of 30 μm wide.[180]

- The visible (VIS) spectrometer covers the region of $400 - 1000$ nm. It is a prism spectrometer of 315 mm focal length. The usage of a prism instead of a diffraction grating allows obtaining higher resolution.[179] The output is recorded by a high resolution CCD linear camera with 3648 pixels 8×200 μm^2 wide.[179]

- The ultraviolet spectrometer covers the region from $255 - 520$ nm. It is a prism spectrometer of 500 mm of focal length and using reflective optics (mirrors), instead of refractive optics, in order to reduce chromatic aberrations. The output is taken by a CCD linear camera of 3648 pixels 8×200 μm^2 wide.[181]

- The fourth spectrometer is used to determine the displacement (length difference) between the arms of the interferometer, L. It is a commercial Czerny-Turner spectrometer of 0.5 m focal length and a rotating grating of 1200 lines/ mm. The output is coupled to a CCD camera with 1204×128 pixels of dimensions 24×24 μm^2 each.[179]

Evaluation of uncertainty in RISBI

The uncertainty of refractive index at the wavelength λ in RISBI measurements, $S(n)$ can be obtained by applying the uncertainty propagation formula to Eq. (2.4):

$$
\begin{aligned}
S(n) = \frac{1}{d} \Bigg\{ & \left[\frac{\lambda}{2\pi} S(\varphi) \right]^2 + \Big[\lambda S(k) \Big]^2 + \left[d \frac{n - n_{eq}}{\lambda} S(\lambda) \right]^2 \\
& + \Big[(n_A S(L) \Big]^2 + \Big[(n - n_A) S(d) \Big]^2 + \Big[(d + L) S(n_A) \Big]^2 \Bigg\}^{1/2},
\end{aligned}
\tag{2.7}
$$

where, in the third and fifth addends, the expression was abbreviated by introducing n and n_{eq}, which is the group index ($n_g = n - \lambda dn/d\lambda$) at the so-called equalization wavelength, the point where the derivative of the phase in Eq. (2.2) is zero. According to Eq. (2.7), the uncertainty in the refractive index measurement is determined by the terms associated to the uncertainties in phase, in the arbitrary parameter k, in the wavelength, in the sample thickness, in the path difference in air and in the refractive index of air. These different contributions to uncertainty have different origins and analytic forms, which are in-deep discussed in Ref. [182]. As a summary, we could say that:

- $S(\varphi)$ arises from the noise in the experimental interferograms and the algorithm employed to extract the phase from those data.

31

- $S(k)$ comes from the uncertainty associated to the arbitrary k factor determination. It is mathematically zero with samples of thickness below a certain threshold which is determined by the experimental setup.

- $S(\lambda)$ is related to the uncertainty in the spectrometer calibration, the assignation to each pixel in the detector to its equivalence in terms of wavelength.

- $S(L)$ is estimated from a procedure similar to that of the spectral calibration, but performed with the objective of evaluating the path difference in air.

- $S(d)$ is related to the experimental uncertainty in the determination of the thickness of the measuring cell.

- $S(n_A)$ is the uncertainty in the refractive index of air. This refractive index is well known in terms of pressure, relative humidity and temperature and it is the smallest contribution to the overall uncertainty.

The precise contribution of those uncertainties to refractive index is dependent on the specific configuration of the RISBI system during the measurement process. In order to illustrate the contribution of the different parameters to the overall refractive index uncertainty, we show an estimation made with a sample of thickness $d = 2$ mm for an arbitrary measúrement made with our device, see Table 2.3. Typically, the largest uncertainty in our device is that associated to the path difference in air, but uncertainties in the sample thickness, calibration and phase are also important. Nevertheless, it must be emphasized that uncertainties in the sample thickness, k, and path different in air are dependent on the thickness of the sample upon measurement. In Fig. 2.3, the contribution to the refractive index uncertainty of these parameters is represented as a function of the sample thickness.

Table 2.3: Magnitude of different uncertainty contributions to the refractive index uncertainty for a sample of d = 2 mm thick in an arbitrary measurement with our device.

Contribution	$S(n) \cdot 10^{-5}$
Sample thickness	3.3
Phase (k, φ)	< 2
Calibration (λ)	< 3.5
Path difference	< 6.8
Air index, n_A	0.001
Total	$7.6 - 8.3$

The uncertainty in the refractive index is smaller when using thin
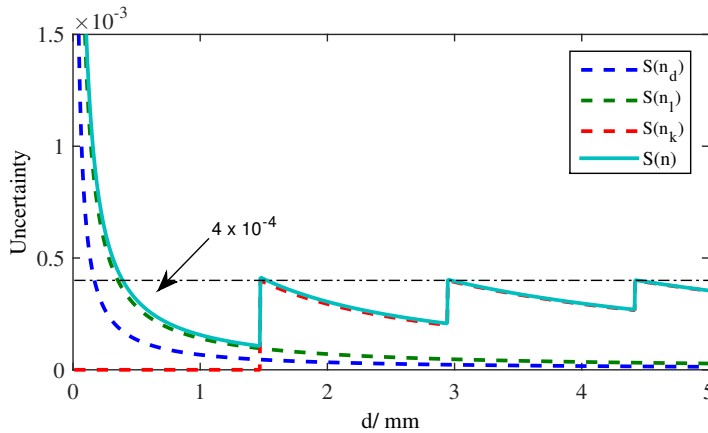
Figure 2.3: Evolution of the uncertainty in the refractive index with the sample thickness, d.

samples, since the k contribution is mathematically zero and the dominant uncertainties are those associated to sample thickness and path difference in air. When the sample thickness is increased, the k uncertainty increases and becomes the dominant contribution to

33

the refractive index uncertainty, largely worsening the accuracy of the RISBI technique. Hence, the most adequate sample thickness for measuring with RISBI are those approximately within the range of $0.5 - 1.5$ mm. Here, unless stated otherwise, we employed samples of 1 mm thickness, which ensure that our measurements present an uncertainty $S(n) < 2 \cdot 10^{-4}$.

Material dispersion

Material dispersion of ILs was measured by means of RISBI in a wide spectral range and at different temperatures. The spectral range varies depending on the work, since the operating spectral range of the RISBI was progressively increased over time by introducing spectrometers that widen the original visible range of performance.

The procedure to measure the material dispersion of an IL using our RISBI apparatus is the following:

- **a)** The quartz cell that is going to content the sample is characterized. The inner thickness d is determined by using a RISBI procedure where liquids of known refractive index are measured (acetone, ethanol, distilled water, etc.) and the cell inner thickness retrieved, Eq. (2.2). The phase contribution of the cell walls not compensated by the quartz plate is measured by introducing the empty cell in the measuring arm. Later, this residual contribution to phase will be subtracted from that of the IL.

- **b)** The background intensity in each spectrometer is measured, I_0. This measurement is done without sample in the RISBI device and its is required to extract the phase from Eq. (2.1) easily.

- **c)** The quartz cell filled with an IL, or any other liquid sample, is introduced in the measuring arm of the interferometer. The cell and plate faces are checked to be normal to the light beam and the

measuring temperature is set by means of the coupled circulating water bath. After that, the path difference between arms is adjusted using the moving mirror to introduce the stationary point in the middle of the interferogram. The presence of the stationary point (condition $\partial n / \partial \lambda = 0$) increases the visibility function and facilitates the measurement, Fig 2.4. Several images of the interferogram are taken in order to obtain significant statistics of the measurement.

- **d)** The visibility function is calculated using the technique described in Refs. [179] and [183]. For doing that, first, the background intensity I_0 is subtracted in Eq. (2.1) and, after that, the lower and upper envelopes of the resulting interferogram are determined by interpolation of minima and maxima. In this step the extreme corresponding to the stationary phase point must be ignored. Once both envelopes have been determined, their subtraction yields the visibility function, $\nu(\lambda)$.

- **e)** Sample cell and compensating quartz plate are removed from the experimental device in order to measure the length difference between arms, L, with the Czerny-Turner spectrometer.[184]

- **f)** The experimental phase, $\varphi_{exp}(\lambda)$, in blue in Fig. 2.4, is retrieved from Eq. (2.1), except for an arbitrary $2\pi k$ factor. This ambiguity is removed by measuring a reference refractive index of the sample at a discrete wavelength, Eq. (2.5), using an Abbe refractometer (ATAGO DR2-M2) with temperature control. Even though only one refractive index is needed, we measured up to 5 other values to check the final value of k.

- **g)** The material dispersion is calculated from the corrected phase by using Eq. (2.4). The resulting noisy material dispersion could be smoothed and analyzed by fitting to it any well-known dispersion formula, which often yield differences between measured and fitted values below $1 \cdot 10^{-6}$, much smaller than the accuracy of the technique.

USC
UNIVERSIDADE
DE SANTIAGO
DE COMPOSTELA

35
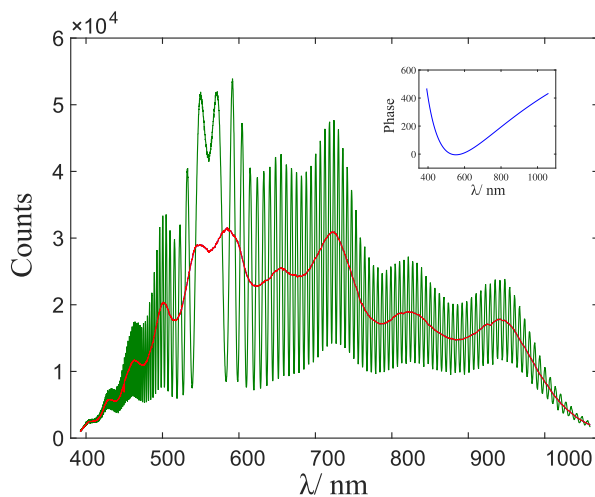
Figure 2.4: Example of $I(\lambda)$, $I_0(\lambda)$ and the phase obtained for a [C$_2$mim][OTf] sample.[*]

- **h)** Finally, the validity of the final material dispersion is tested by comparing the indices obtained by RISBI with those measured in the Abbe refractometer. As a representative example, in Fig. 2.5, the refractive indices of the liquid [C$_2$mim][OTf] obtained by both Abbe refractometry and RISBI are plotted, together with their absolute deviation at discrete wavelengths.

Birefringence

Birefringence of aligned ILCs samples was measured at different temperatures throughout a wide spectral range using a variation of RISBI. This variation consists in introducing a polarizer at the output of the interferometer, but before the spectrometer. When light passes

36
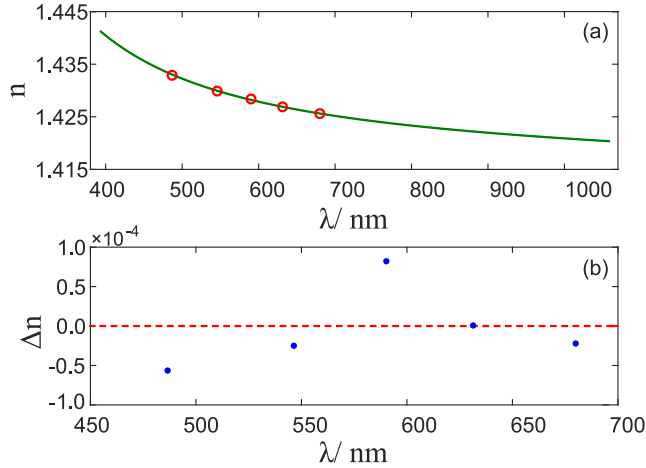
Figure 2.5: (a) Final refractive index for the [C$_2$mim][OTf] sample. (b) Deviations from calculated indices and Abbe refractometer ones.[*]

---

through the aligned sampled, the beams are decomposed in two orthogonal polarization states. During the propagation of these states through the liquid crystal, they accumulate different phase differences, φ_f or φ_s, depending on whether they propagate in the direction of the fast, n_f, or slow, n_s, refractive index. The rotating polarizer allows to select the interferogram, $I_f(\lambda)$ or $I_s(\lambda)$, produced by each one of the phases:

$$I_{f/s}(\lambda) = I_0(\lambda)\left[1 + \nu_{f/s}(\lambda)\cos\varphi_{f/s}(\lambda)\right], \qquad (2.8)$$

where $\nu_{f/s}$ is the visibility function of the corresponding interferogram. As in Eq. (2.2), both phases are a function of the sample thickness, d, and length difference between the arms of the interferometer, L:

$$\varphi_{f/s}(\lambda) = \frac{4\pi}{\lambda}\Big\{d\left[n_{f/s}(\lambda) - n_A\right] - n_A L\Big\} + 2\pi k_{f/s}, \qquad (2.9)$$

where $k_{f/s}$ is the arbitrary factor for each phase. The phase difference between the phases extracted for the fast and slow axes, $\Delta\varphi = \varphi_f - \varphi_s$,

37

can be related to the birefringence of the sample, $\Delta n = n_f - n_s$, and the difference between the arbitrary factors, $\Delta k = k_f - k_s$:

$$\Delta\varphi = \frac{4\pi}{\lambda}d\Delta n(\lambda) + 2\pi\Delta k. \qquad (2.10)$$

According to Eq. (2.10), our modified RISBI technique allows measuring birefringence dispersion of samples on a similar way that material dispersion is retrieved in isotropic samples.

Additionally, fast and low refractive indices were also measured using an ATAGO DR2-M2 Abbe refractometer. For doing that, prior to the measurements, it is required to align the ILC in the prism of the refractometer. Then, the introduction of a polarizer after the ocular of the refractometer allows separately measuring each one of the both indices. Temperature control is performed by means of a circulating water bath.

Absorption spectrum

Absorption spectrum of the samples was measured using our RISBI apparatus as a standard spectrophotometer: One of the interferometer arms is deactivated while the other arm, coupled to the spectrometers, allows measuring irradiance variations as a function of the wavelength. In order to measure the absorption spectrum in this configuration, first, the lamp irradiance is measured without any sample, $I_0(\lambda)$, and, after that, the sample is introduced and the new irradiance is measured, $I(\lambda)$. Afterwards, if the width of the sample inside the cell is known, d, it is possible to exploit the Lambert-Beer law $I(\lambda) = I_0(\lambda)e^{-A(\lambda)d}$, to extract the absorption coefficient, $A(\lambda)$.

Mass density

Mass density of selected ILs was measured using an Anton Paar DSA-5000 M vibrating tube density and sound velocity meter. The

device is calibrated with bi-distilled water and dry air at atmospheric pressure and its resolution is $2 \cdot 10^{-6}$ g/cm^3. The apparatus incorporates a temperature control with an uncertainty of 0.01 K. ILs were introduced in the vibrating tube by means of a syringe. Special attention was paid to avoid introducing bubbles inside the tube, since these bubbles produce wrong density measurements.

X-ray diffraction

X-Ray Diffraction (XRD) patterns of [C$_2$mim][DSO$_4$] were taken by means of a PANAlytical Empyrean diffractometer working at the wavelength Cu(λ(Kα)) = 1.5406 Å. The beam was collimated by an optical system including a W/Se doubled layered mirror and the radiation sensor was a PIXcel3D solid-state detector. Samples were prepared by introducing them within an XRD-devoted capillary of dimensions 80 mm length, external diameter 1.00 mm and wall thickness 0.01 mm. XRD spectra were measured over both wide and small angle regions. The small angle region covered from 0.15° to 4° and it was recorded with an angular step of 0.01° and an integration time of 30 s. The wide angle region covered from 2° to 40°, with a resolution of 0.03° step and an integration time of 13 s. The mathematical fittings of the diffractograms was made by means of the software Highscore Plus 3.0d.

XRD patterns of the Ni^{2+} and Fe^{3+} doped ILs of chapter 9, were measured in a Bruker Kappa-APEX-II diffractometer. The X-ray source was a Mo X-ray tube operating at 50 kV and 30 mA filtered by a graphite monochromer λ(K(α_1)) = 0.71073 Å. The detection was made by a bidimensional detector of the type APEX II and the sample was measured inside a glass capillary of 0.7 mm of diameter.

Differential scanning calorimetry

Differential Scanning Calorimetry (DSC) measurements were performed on a DSC Q100 device of TA Instruments. Calibration of the apparatus was done using the melting points of indium and zinc, and heat flow calibration using the fusion enthalpy of indium, standards provided by TA Instruments. The reference in the measurement is a 40 μl aluminum pan. Temperature ramps were done in an inert nitrogen atmosphere with samples of mass ranging between 3 and 5 mg inside an aluminum pan similar to that of the reference. A pinhole in the pan allows water evaporation.

Nuclear magnetic resonance

^{1}H and ^{13}C Nuclear Magnetic Resonance (NMR) spectra were measured by means of a Bruker NEO 750, 17.61 T, 750 MHz with temperature control over neat samples. The ILs were introduced in a glass capillary that was placed in a 5 mm NMR tube filled with deuterated water (D_2O) which serves as chemical shift reference.

Aligment of ionic liquid crystals

ILCs tend to spontaneously align over polished glass surfaces forming pseudo-isotropic textures. This ordering has been historically exploited to study the anisotropic conductivity of some ILCs.[185,186] Notwithstanding, upon this alignment, the optical axis of the ILC is perpendicular to the glass walls, which complicates its optical characterization. Planar aligned samples, those with optical interest, have their optical axis in parallel with the glass walls. Classical approaches for aligning LCs such as rubbing the glass surfaces or applying electric and magnetic fields did not work for the ILCs we

studied, possibly due to their high viscosity.

Nevertheless, it was possible to obtain the desired alignment by applying friction to the ILC samples during the clearing point transition from isotropic liquid to the LC phase. Following this procedure, planar aligned samples mounted between two microscopy slides and a separator were produced in lateral areas of centimeters and thickness reaching 150 μm. Thicker samples were aligned by totally drying the ILC, heating it above the clearing point and introducing it within a glass cell of the desired thickness. After that, the hygroscopy of the ILCs is used as an aligning mechanism: the incorporation of water from the room creates a privileged direction within the cell that aligns the ILC in direction of the water gradient.

Additionally, it was also possible to align the liquid crystal samples on the prism of an Abbe refractometer, following a procedure based on pouring the ILC on the prism and applying slow cycles of heating and cooling.

Polarizing optical microscopy

Textures of ILC samples were observed using a Nikon Eclipse Ni−U optical microscope in a cross polarizers configuration coupled with a TU PLAN FLUOR 10×/0.30 OFN 25 WD 17.5 objective. Pictures of the textures were taken with a Nikon 750 camera.

Computational methodology

Computational methods are powerful tools to obtain insight into the microscopic origins of the macroscopic optical properties of ILs. In addition, simulations are a fast way to explore the effect of different ion combinations on different properties without synthesizing, purifying and measuring them. Two different computational strategies were exploited in this work: Molecular Dynamics and Density Functional

41

Theory to characterize $1 - 10$ nm and $0.1 - 1$ nm scales, respectively.

2.3 Molecular Dynamics

Molecular Dynamics (MD) is a simulation technique which is able to predict the dynamics of a system of N atoms in time by numerically resolving the (classical) Newton's equations of motion:

$$m_i \frac{\partial^2 \vec{r}_i}{\partial t^2} = \vec{F}_i, i = 1...N, \tag{2.11}$$

where m_i is the mass of the particle i, $\vec{r}_i$ its position, t the time and $\vec{F}_i$ the associated force, which can be expressed as the gradient of the potential energy of the system V_F with respect the i particle:

$$\vec{F}_i = -\frac{\partial V_F}{\partial \vec{r}_i}. \tag{2.12}$$

By integrating Eq. (2.12), the time series of positions, velocities and accelerations (forces) of all the particles of the system are obtained. This integration can be performed following different algorithms requiring the discretization of time in steps of size Δt, such as the Velocity Verlet or the leap-frog. In this thesis, the leap-frog algorithm was the one chosen for integration, and its scheme for the evolution of the dynamic magnitudes of the system is:

$$\vec{a}_i = -\frac{1}{m_i} \frac{\partial V_F}{\partial \vec{r}_i},$$

$$\vec{v}_i(t + \frac{1}{2}\Delta t) = \vec{v}_i(t - \frac{1}{2}\Delta t) + \vec{a}_i(t)\Delta t,$$

$$\vec{r}_i(t + \Delta t) = \vec{r}_i + \vec{v}_i(t + \frac{1}{2}\Delta t)\Delta t. \tag{2.13}$$

In addition to the resolution of the equations of motion, usually MD packages also incorporate barostats, thermostats or molecular constraints that yield simulations with a close resemblance to real

systems. MD simulations are able to handle thousands of molecules, providing direct insight into the microscopic structure of the studied systems within simulation boxes of few nanometers of lateral size. This feature made MD simulations one of the most popular approaches to shed light into the nanoscopic structure of ILs.[132,187–192]

Here, simulations were performed with the GROMACS package,[193–195] which implements highly parallelized algorithms that allow fast calculations of large systems as well as compatibility with the most widespread force fields such as OPLS,[196,197] CHARMM,[198] GROMOS,[199] or AMBER.[200] These force fields differ in the computational expressions used to describe the potential energy and, in consequence, also in their parametrization of molecules. We employed an IL-optimized version of the OPLS-AA (Optimized Potentials for Liquid Simulations, All Atom) force field,[201,202] which considers two general kinds of interactions:

$$V_F = V_{nonbonded} + V_{bonded}. \tag{2.14}$$

The term $V_{nonbonded}$ contains interactions between atoms of different molecules and atoms that, within a molecule, are separated by at least three bonds. On the other hand, the V_{bonded} term includes interactions between bonded atoms which can be separated as much as three bonds. The $V_{nonbonded}$ interactions are made up of the standard Lennard Jones (LJ) and Coulomb potentials. The LJ potential describes both the van der Waals dispersion (attractive) and Pauli repulsive forces that suffer uncharged particles separated by large distances, while the Coulomb potential takes into account the permanent interactions between charged moieties:

$$V_{nonbonded} = V_{LJ} + V_{Coulomb} =$$
$$\sum_i \sum_{j \neq i} 4\varepsilon_{ij}[(\frac{\sigma_{ij}}{r_{ij}})^{12} - (\frac{\sigma_{ij}}{r_{ij}})^6]f_{ij} + \sum_i \sum_{j \neq i} \frac{q_i q_j}{r_{ij}^2}f_{ij}, \tag{2.15}$$

where ε_{ij} is the depth of the LJ potential and f_{ij} is an empirical factor that allows using the same parameters both for intra and inter molecular

interactions. It takes the value 0.5 when the atoms are separated by just three bonds and 1 when they are separated a larger number of bonds or belong to different molecules.

Regarding bonded interactions, they include the bond potential, V_{bonds}, associated to two atoms separated by a bond length, r, the angular potential, V_θ, associated to three atoms forming an angle, θ, and the dihedral torsion potential, $V_{dihedral}$, associated to fours atoms in a dihedral of angle, ϕ:

$$V_{bonded} = V_{bonds} + V_{angles} + V_{dihedrals} =$$
$$\sum_{bond} k_r(r - r_{eq})^2 + \sum_{angle} k_\theta(\theta - \theta_{eq})^2 +$$
$$\sum_{dihedrals} \frac{k_{v1}}{2}[1 + cos(\phi)] + \frac{k_{v2}}{2}[1 - cos(2\phi)] + \frac{k_{v3}}{2}[1 + cos(3\phi)].$$

(2.16)

According to Eq. (2.16), bonds and angles are modeled by a standard harmonic potential with regard to their respective equilibrium positions, r_{eq}, for bond lengths and, θ_{eq}, for angles. On the other hand, the dihedral torsion potential is expressed as the expansion on a series of cosines. Furthermore, the different k constants that appear in the different kinds of bonded interactions (k_r, k_θ, $k_{v1,v2,v3}$) are the coupling constants of the potential with the perturbation on each parameter.

Running MD simulations

The steps for performing the MD simulations included in this thesis are the following:

- **a)** Creating the simulation box containing the initial configuration of the system. This step is crucial since an ill-defined starting point could lead to a failed simulation or unrealistic results. We created the simulation box using the PACKMOL software[203], which implements a smart packing of the molecules of the system

within a box of the desired dimensions. After the initial packing, the rest of simulation steps are carried out with the GROMACS software.

- **b)** Minimizing the energy of the system. In our case we used a steepest descendent algorithm, which ensures a fast relaxation of the geometry of the molecules and provides a good starting point to initiate the proper MD simulation. The number of steps allowed during the energy minimization process was $1 \cdot 10^6$.

- **c)** Equilibration: it consisted on a long MD simulation of 20 ns whose purpose is to equilibrate the system. The time step was set to 2 fs and the number of steps $1 \cdot 10^7$.

- **d)** Production: A 10 ns simulation is initiated after the equilibration. This production run provides the static and dynamic magnitudes to analyze. Unless explicitly mention otherwise, the time step was set to 2 fs and the number of steps was $1 \cdot 10^7$.

Furthermore, during the minimization, equilibration and run steps long range electrostatic interactions were treated by means of a fourth order Particle-Mesh Ewald (PME) algorithm[204] with a grid of 12 nm spacing and cubic interpolation. The Lennard-Jones interaction cutoff was established at 1.1 nm and the LINCS algorithm[205] was used to keep bonds rigid. Additionally, the stabilization and production runs were performed using a leap-frog algorithm in a NPT ensemble, which means that the number of molecules (N), pressure (P) and temperature (T) are kept constant during the simulation. Temperature and pressure were kept constant by the respective usage of a V-rescale thermostat (coupling constant of 0.1 ps) and a Parrinello-Rahman barostat (relaxation time constant 0.1 ps and compressibility constant $4.5 \cdot 10^{-5}$ bar). Moreover, periodic boundary conditions were imposed. Finally, post-processing of the production run was performed using the post-processing tools of the GROMACS package in combination with other computational tools developed in our research group. We will

USC
UNIVERSIDADE
DE SANTIAGO
DE COMPOSTELA

now briefly review some of the main magnitudes that we calculated in our studies.

Radial distribution function

The Radial Distribution Function (RDF) provides the probability of finding a species j at a certain distance of a species i. It is defined as:

$$g_{ij}(\vec{r}) = \frac{N}{\rho_N N_i N_j} \left\langle \sum_{\alpha=1}^{N_i} \sum_{\beta \neq \alpha}^{N_j} \delta(\vec{r} + \vec{r_\beta} - \vec{r_\alpha}) \right\rangle \quad i \neq j, \qquad (2.17)$$

being N the total number of particles of the system, ρ_N is its number density and N_i and N_j the number of particles of the species i and j. The α and β subscripts run over all the particles of species i and j in the system, which are located at $\vec{r}_\alpha$ and $\vec{r}_\beta$, respectively. The $\delta(r)$ is the Dirac's Delta function and the brackets indicate that the ensemble average is taken. The RDF provides very relevant information about the spatial distribution of the molecules within the simulation box. Furthermore, its Fourier transform is connected to the static structure factor, $S(q)$, which describes how light is diffracted by the system and is closely related to experimental X-ray diffraction patterns.

Velocity auto correlation function

The Velocity Auto Correlation Function (VACF) describes the evolution in time of the correlation of the velocity of a particle with respect to its initial value. In a discrete time formalism, it is defined as:

$$C(j\Delta t) = \frac{1}{N-j} \sum_{i=0}^{N-1-j} v(i\Delta t)v\left[(i+j)\Delta t\right], \qquad (2.18)$$

where Δt is the temporal frame, N is the total number of available frames, and $v(t)$ is the velocity of the particle i. The VACF provides

important information about the dynamics of a molecule and about how it interacts with the rest of molecules within the simulation box. Additionally, its Fourier transform is closely related to the vibrational Density of States (vDOS), which provides access to the low energy vibrational frequencies of the system.

2.4 Density Functional Theory

Density Functional Theory (DFT) is a quantum mechanical procedure commonly employed to approximately solve the Schrödinger equation of many-electron systems. All DFT simulations in this thesis were performed using the Gaussian 16 software,[206] which is frequently used to model and analyze different quantum mechanical magnitudes of molecules, complexes, crystals or even chemical reactions. From the perspective of photonics, DFT can be employed to obtain insights in the microscopic origins of optical responses, since it allows calculating orbital distribution, ground state energy, electronic transitions, volume, polarizability, hyperpolarizabilities and other optics-related magnitudes.

The Schrödinger equation can be written as follows:[207]

$$i\hbar\frac{\partial}{\partial t}\Psi(\vec{r},t) = \hat{H}\Psi(\vec{r},t), \tag{2.19}$$

where $\Psi(\vec{r},t)$ is the wavefunction of the system, that depends both on position $\vec{r}$ and time t, $\hat{H}$ is the Hamiltonian, i is the imaginary unit and $\hbar = h/2\pi$ the reduced Planck's constant. The stationary version of this equation is:

$$E_n\phi_n(\vec{r}) = \hat{H}\phi_n(\vec{r}), \tag{2.20}$$

where E_n is the energy of the nth stationary state of the system and ϕ_n the corresponding stationary wavefunction. The Hamiltonian of a many-

USC

electron body can be written as:

$$\hat{H} = -\frac{\hbar^2}{2m} \sum_i \nabla_i^2 + \frac{1}{8\pi\varepsilon_0} \sum_{i,j} \frac{e^2}{|\vec{r}_i - \vec{r}_j|} - \frac{1}{4\pi\varepsilon_0} \sum_{i,I} \frac{Z_I e^2}{|\vec{r}_i - \vec{R}_I|}$$
$$-\frac{\hbar^2}{2M} \sum_I \nabla_I^2 + \frac{1}{8\pi\varepsilon_0} \sum_{I,J} \frac{Z_I Z_J e^2}{|\vec{R}_I - \vec{R}_J|},$$

(2.21)

where the first term is the kinetic energy of the electrons, the second their Coulomb repulsion, the third one is the Coulomb attraction between electrons and nuclei, the forth is the kinetic energy of the nuclei and, finally, the fifth term is the Coulomb repulsion between nuclei. Solving the Schrödinger equation associated to this Hamiltonian is complex. Nevertheless, this problem can be significantly simplified by invoking the Born-Oppenheimer approximation, which assumes that the masses of the nuclei are much larger than that of the electrons and, in consequence, their velocity is much lower. In this approximation, the electrons are considered to instantaneously follow the nuclei motion and to interact between them under an external constant potential, $v_{ext}(\vec{r})$, induced by the nuclei. Using the Born-Oppenheimer approximation in Eq. (2.21) leads to a total decoupling between the electronic and nuclear degrees of freedom, so only electronic terms are retained in the Hamiltonian. Despite it, solving the resulting electronic Hamiltonian is still challenging even with the currently available computational power.

An alternative and more computationally affordable approach to solve the Schrödinger equation of the previous electronic Hamiltonian can be stated with the aid of the Hohenberg-Kohn theorems,[208] which establish the following:

- **a)** The external potential, $v_{ext}(\vec{r})$, applied over the electrons of a system is an unique functional of the electronic density, $\rho(\vec{r})$.

- **b)** The electronic density that minimizes the total energy of the system is the electronic density of the ground state.

Both theorems together transform solving the Schrödinger equation into a variational problem where electronic density minimizes the ground state energy of the system. Unfortunately, neither of the theorems hints how the electronic density can be calculated. In consequence, an extra approximation has to be made to completely address the problem: substituting the explicit interaction between electrons by an effective functional acting on the electronic cloud. Under these hypothesis, the Schrödinger equation can be transformed in the Kohn-Sham equation, reducing the many-body problem to a single-body problem:[207]

$$\left(-\frac{\hbar^2}{2m}\nabla^2 + V_{eff}(\vec{r})\right)\psi_i(\vec{r}) = \varepsilon_i\psi_i(\vec{r}), \tag{2.22}$$

where $\psi_i(\vec{r})$ is the Kohn-Sham orbital of the virtual independent electron i whose energy is ε_i. The total electronic density of the system can be calculated through the Kohn-Sham orbitals $\rho(\vec{r}) = \sum_i^N |\psi_i(\vec{r})|^2$ and the effective functional $V_{eff}(\vec{r})$ is:

$$V_{eff}(\vec{r}) = V_{ext}(\vec{r}) + V_H(\vec{r}) + V_{xc}(\vec{r}), \tag{2.23}$$

where $V_{ext}(\vec{r})$ is an external contribution that includes the interaction with the nuclei and

$$V_H(\vec{r}) = \int \frac{e^2}{|\vec{r} - \vec{r'}|}\rho(\vec{r'})d^3\vec{r'}, \tag{2.24}$$

which is Hartree's effective repulsion between electrons. Lastly, the $V_{xc}(\vec{r})$ term is the exchange correlation functional. It stands for all the many-body interactions that are not included in the rest of the terms. The total energy $E[\rho]$ of a system given by the Kohn-Sham equation is:

$$E[\rho] = T_{ks} + \int V_{ext}(\vec{r})\rho(\vec{r})d\vec{r} + \int V_H(\vec{r})\rho(\vec{r})d\vec{r} + E_{xc}[\rho], \tag{2.25}$$

being $T_{ks} = \int d\vec{r}\sum_i \nabla\varphi_i^\dagger\vec{r}\nabla\varphi_i(\vec{r})$ the Kohn-Sham kinetic energy and E_{xc} the energy associated to the exchange correlation functional.

Functionals

The biggest challenge of DFT methods is that no exact form for the V_{xc} functional is known. For this reason, different approximations were historically explored giving rise to diverse DFT functionals:

- **Local Density Approximation (LDA)**: In this approximation it is assumed that the electronic density is a smoothly varying spatial function.[207] The exchange and correlation energies are considered to be independent $E_{xc} = E_x + E_c$ and both function of the electronic density value at each point of the space. On the basis of the slowly varying electronic density, the functional form of the exchange-correlation terms is extrapolated from that of a free-electron gas substituting ρ_f by $\rho(\vec{r})$. While there is no general analytical expression for the correlation energy, which has to be numerically evaluated, the exchange energy is given by Thomas-Fermi theory: $E_x = \int \rho(\vec{r}) \varepsilon_x^{LDA}[\rho(\vec{r})] d(\vec{r}) = -\frac{3}{4}(3\pi)^{1/3} \int \rho(\vec{r})^{4/3} d\vec{r}$.

- **Generalized Gradient Approximation (GGA)**: In this approximation, the exchange-correlation energy functional goes a step further than in LDA, as it is considered not only dependent on the electronic density at each point of the space, but also on its spatial derivative (gradient).[207] $E_x = \int \rho(\vec{r}) \varepsilon_x^{GGA}[\rho(\vec{r}), \nabla \rho(\vec{r})] d\vec{r}$. It is worth to mention that following the same reasoning as in GGA, there are meta-GGA functionals that incorporate also the dependence on the second derivative of the electronic density: $E_x = \int \rho(\vec{r}) \varepsilon_x^{meta-GGA}[\rho(\vec{r}), \nabla \rho(\vec{r}), \nabla^2 \rho(\vec{r})] d\vec{r}$.

- **Hybrid Functionals**: This is the most popular family of approximations due to their accuracy in relation with their computational cost. These functionals are produced by an empirical mixture of the exact Hartree-Fock exchange energy

USC
UNIVERSIDADE
DE SANTIAGO
DE COMPOSTELA

50

2. Materials and Methods

and the exchange-correlation energy produced by one or more of the previous approximations.[209] The most famous hybrid functional, the B3LYP one (Becke, 3 parameter, Lee-Yang-Parr),[210] which includes a combination of LDA and GGA correlation-exchange energies with the exact Hartree-Fock exchange of the form: $E_{xc}^{B3LYP} = E_x^{LDA} + a_0(E_x^{HF} - E_x^{LDA}) + a_x(E_x^{GGA} - E_x^{LDA}) + E_c^{LDA} + a_c(E_c^{GGA} - E_c^{LDA})$, being $a_0 = 0.20$, $a_x = 0.72$ and $a_c = 0.81$. The GGA exchange terms are given by the Becke 88 exchange functional,[211] while the correlation energy in the GGA part is provided by the Lee, Yang and Parr functional[212] and the LDA part by the Vosko, Wilk and Nusair functional (VWN).[213]

Basis sets

Additionally to the DFT functional, the other key ingredient in DFT calculations is the basis set, which is the group of functions that are used to describe the atomic orbitals of the atoms in the simulations. Basis sets are introduced in computational chemistry since Slater orbitals, those obtained from the linear combination of atomic orbitals theory (LCAO), are very computationally expensive to work with. Hence, in molecular chemistry, atomic orbitals are usually described by linear combinations of Gaussian functions of different exponents, $\phi_{slater} = \sum_i^N c_i\phi_i$, where $\phi_i = \frac{2\alpha_i}{\pi}e^{-\alpha_i r^2}$ are the Gaussian functions and, α_i and c_i, coefficients obtained by fitting to the Slater orbitals. For instance, in the Slater-Type Orbitals n-Gaussian hierarchy of basis sets, STO-nG,[214] the n indicates the number of Gaussian functions linearly combined to describe each one of the involved Slater orbitals. Thus, in the STO-3G basis set, the s orbital of an hydrogen atom would be described by the combination of three Gaussian functions, $\phi_s = c_1\phi_1 + c_2\phi_2 + c_3\phi_3$. Furthermore, this basis set follows a minimum basis set approach, which consists in only considering the strictly necessary orbitals to provide a basic description of each atom. For instance, for describing the nitrogen atom, only one

USC
UNIVERSIDADE
DE SANTIAGO
DE COMPOSTELA

51

1s, one 2s and three 2p orbitals are considered.

Currently, there is a large number of available families of basis sets, which offer much more realistic approaches to the real orbital structures of atoms, for instance, including extra components to properly describe the valence orbitals. Some of these more sophisticated basis sets are those of the Pople group,[215] which include the famous 6-31G basis set, or those of the correlation consistent hierarchy of the Dunning group.[216] Furthermore, the basis sets can be enhanced by adding them both polarization and diffuse functions, which make molecular orbitals even more realistic.

Finally, it is important to mention the existence of pseudopotentials, which are basis sets that replace the description of the inner shells of electrons and the nuclei by an effective potential.[217–219] This strategy is followed in the description of large atoms with a large number of electrons, and it is implemented, for instance, in the LanL2MB and LanL2DZ basis sets.

Level of theory

The level of theory is the combination of functional and basis set employed in the DFT calculations. In our case, except indicated otherwise, our simulations were performed at the B3LYP/6-311++G(d,p) level. It means that we use the B3LYP functional together with the 6-311++G(d,p) basis set, which incorporates both diffuse and polarization functions.

Geometry optimization in DFT calculations

In order to calculate any optical property by means of DFT, the geometry of the molecules must be properly optimized at the level of theory which is being used. The process followed to optimize the geometry of any molecule in this thesis is the following:

USC
UNIVERSIDADE
DE SANTIAGO
DE COMPOSTELA

- **a)** Initial geometry of the molecules is created and a rough optimization of the geometry is performed, both steps are performed using the Avogadro program.[220]

- **b)** Geometry of the molecule is DFT-optimized using the Berny algorithm at the same level of theory which will be used to calculate the rest of properties of interest.[221]

- **c)** The stability of the optimized geometry is analyzed by means of a vibrational analysis. If there are imaginary frequencies in the result, the geometry is not stable and the molecule must be reoptimized.

Vibrational spectra

The energy of a geometrically-optimized molecule can be expanded in a Taylor series around the equilibrium positions of its nuclei,[222] $\vec{x} = \vec{r} - \vec{r}_0$:

$$E = E_0 + \sum_{i=1}^{3N} \left(\frac{\partial E}{\partial x_i} \right)_{\vec{x}=0} x_i + \frac{1}{2} \sum_{i=1}^{3N} \sum_{j=1}^{3N} \left(\frac{\partial^2 E}{\partial x_i \partial x_j} \right)_{\vec{x}=0} x_i x_j + ...,$$

(2.26)

where i and j are indices to label the coordinates of the different atoms in the molecule and N is the total number of atoms. Note that the first term of the expansion series is zero since the expression is evaluated at the equilibrium position. Hence, at the lowest order we obtain:

$$E = E_0 + \frac{1}{2} \sum_{i=1}^{3N} \sum_{j=1}^{3N} H_{i,j}(\vec{x}=0) x_i x_j,$$

(2.27)

where $H_{i,j}(\vec{x}=0)$ is the Hessian matrix at $\vec{r}_0$:

$$H_{i,j} = \left(\frac{\partial^2 E}{\partial x_i \partial x_j} \right)_{x=0}.$$

(2.28)

USC
UNIVERSIDADE
DE SANTIAGO
DE COMPOSTELA

53

Now, taking into account that the force at each i coordinate, F_i, can be expressed in terms of the acceleration in that direction, $F_i = m_i \, d^2x_i/dt^2$, and also as a function of the energy, $F_i = -\partial E/\partial x_i$, the equations of the motion of the molecule can be written as

$$\frac{d^2 x_i}{dt^2} = A_{i,j}x_j, \qquad (2.29)$$

where $A_{i,j} = H_{i,j}/m_i$, is the mass-weighted Hessian matrix. A specific set of solutions of the previous equation are those of the eigenvalue problem:

$$\vec{A}\vec{e} = \eta\vec{e}, \qquad (2.30)$$

where $\vec{e}$ is the eigenvector and η the corresponding eigenvalue. Supposing the initial condition $x(t = 0) = 0$ and $dx(t = 0)/dt = 0$, the position of the atoms is described by a harmonic oscillator $\vec{x} = a\cos(\omega t)\vec{e}$ where $\omega = \sqrt{\eta}$ and a is an arbitrary constant. The solutions to Eq. (2.29) verifying these conditions are known as normal modes and they can be identified with the vibrational modes of the molecule upon study, which have an amplitude determined by a and an oscillation frequency ω. In general, any solution of Eq. (2.29) is a linear combination of those given by Eq. (2.30), so any vibrational motion of the molecules can be described by the normal modes of vibration. In DFT, the mass-weighted Hessian of the molecules is calculated, and then Eq. (2.30) solved to obtain the normal modes of vibration of the molecules. It provides the vibrational spectra of the molecule, (both Raman and infrared) as well as a method for checking the stability of the geometry upon study. If the frequencies involved in the solutions are negative, it means that the geometry is not at a minimum of energy and that the geometry optimization procedure was not satisfactory.

Polarizability and hyperpolarizability calculations

Electronic polarizability and hyperpolarizability were computed dynamically, i.e., as a function of the electric field wavelength, by using

the Couple-Perturbed Hartree Fock method (CPHF).[223] The CPHF theory is a perturbative theory than can be used to estimate the change in energy of an optimized system when it is perturbed by an external agent, such as an electric field. Hence, in the framework of this theory, the frequency-dependent contribution to energy arising from an external wavelength-dependent electric, $\vec{F}$, can be calculated. Additionally, we know that the variation of energy of any system produced by an electric field is related to the induced dipole since $E = E_0 - \vec{\mu} \cdot \vec{F}$, being E_0 the energy of the system before applying the electric field and $\vec{\mu}$ the induced dipole. According to the definition of $\vec{\mu}$ given in Eq. (1.1), the total energy of the system is:

$$E(\omega) = E_0 - \vec{\mu}^{(0)} \cdot \vec{F}(\omega) - \vec{\alpha} \cdot \vec{F}(\omega)\vec{F}(\omega) - \frac{1}{2}\vec{\beta}\vec{F}(\omega)\vec{F}(\omega)\vec{F}(\omega)$$
$$-\frac{1}{6}\vec{\gamma} \cdot \vec{F}(\omega)\vec{F}(\omega)\vec{F}(\omega)\vec{F}(\omega) + ..., \tag{2.31}$$

Hence, applying the so-called finite field method, which consists in deriving n times the energy with respect to the applied electric field, the wavelength-dependent polarizability and the wavelength-dependent hyperpolarizabilities can be obtained as

$$\vec{\alpha} = \frac{\partial^2 E}{\partial F^2} \tag{2.32}$$

$$\vec{\beta} = \frac{\partial^3 E}{\partial F^3} \tag{2.33}$$

$$\vec{\gamma} = \frac{\partial^4 E}{\partial F^4} \tag{2.34}$$

Calculation of the molecular volume of ions

The molecular volume of any chemical species can be estimated by means of its electronic density distribution. Usually, this electronic

density is larger in the regions where the orbitals of two adjacent atoms overlap forming a chemical bond, and it monotonically decreases as we move apart from the molecule. According to Bader, Ref. [224], the volume inside an isosurface where the electronic density decays to 0.001 electrons/Bohr^3 is in markedly agreement with experimental van der Waals volumes of molecules in gas phase. Hence, this isosurface is often used to determine the volume of molecules in ab initio simulations, as we did in this thesis. In our case, the molecular volume was estimated utilizing the Monte-Carlo procedure available in Gaussian. Since the algorithm can provide significantly different results after each execution,[225] maybe also by influence of the internal rotations, the volume calculation was repeated 100 times for each ion to obtain good statistics.

Absorption spectra

Absorption spectra are calculated by means of the time-dependent density functional theory (TD-DFT), method which provides a strategy to calculate the electronic transitions from the ground state of a molecule to excited states.[226,227] TD-DFT is a generalization of the standard DFT to explicitly consider the time dependence of the Schrödinger equation. The fundamental theorem of the TD-DFT is the Runge-Gross theorem,[228] which is a time-dependent extension of that of Hohenberg and Kohn.

Part III

Results

3. Material dispersion and electronic polarizability of imidazolium-based ionic liquids

[a] Grupo de Nanomateriais, Fotónica e Materia Branda, Departamentos de Física Aplicada e de Física de Partículas, Universidade de Santiago de Compostela.

[b] Departamento de Física Aplicada, Universidade de Santiago de Compostela.

[c] Departamento de Física e Ciencias da Terra, Facultade de Ciencias, Universidade da Coruña.

The high tunability of ILs can be exploited to provide liquids (and even solids) with tailor-made refractive index and material dispersion. Evidence of the practical importance of tuning these properties in photonics is the plethora of recent applications exploiting the refractive index of ILs, including their usage for high refractive index glass and crystal analysis,[229] liquid-filled variable focus lenses[75,76] or liquid-core optical fibers.[230] Nevertheless, these pioneering applications arise in a context where the knowledge about the material dispersion of ILs and the relation with their structure is limited. Up to date, the most widely used tools to measure the refractive index of ILs were commercial refractometers, which usually measure the refractive index at a single wavelength, the sodium D line. Using this kind of devices, Tariq et al.[150] and Seki et al.[97] measured the refractive index at the D line of several ILs at different temperatures. Other examples are the works of Rilo et al.[231] and Pereiro et al.,[232,233] who measured the refractive index of binary mixtures of imidazolium-based ILs with different solvents. Furthermore, some authors started to relate those measurements

with the electronic polarizability of ILs, i.e., with their chemical structure.[97,150,234,235] Nevertheless, the number of studies dealing with the determination of refractive index at several wavelengths and with the analysis of material dispersion is much more scarce. In Refs. [77], [94], and [236], the refractive indices of ILs at a discrete number of wavelengths were measured and the results extrapolated to describe material dispersion over a certain spectral range by numerical fitting.

In this chapter, we address our very first approach to the experimental determination of the material dispersion of ILs.[237] Oppositely to other works oriented to measure dispersion, our RISBI technique retrieves a quasi-continuous value of refractive index in a wide spectrum. At the time this work was done, our device was able to measure material dispersion in the spectral range from 400 nm to 1000 nm.[179] The refractive index of 14 ILs, commonly found in literature were measured at a fixed temperature of $T = 300$ K. These ILs were combinations of members of the 1-alkyl-3-methylimidazolium family of cations with different frequently used anions. From our measurements, the corresponding electronic polarizability dispersion was calculated, the first step to understand how the molecular structure of ILs affects their material dispersion. These calculations were done assuming the Lorentz-Lorenz formalism, Eq. (1.9), and using experimental densities from literature. Additionally, in this first contact with ILs, the relevance of the presence of water in the accurate measurement of their refractive index is highlighted. In order to account for it, the effect of water in our measurements was corrected by means of the Newton formula for binary mixtures.

3.1 Materials

The 14 imidazolium-based ILs studied in this chapter are those marked with a symbol in Table 3.1. In order to facilitate the analysis of the effect of anions and that of the cation alkyl chain length, the ILs were divided in four groups according to their composition, see color

code in the table: $[C_k\text{mim}][BF_4]$, $[C_k\text{mim}][NTf_2]$, $[C_2\text{mim}][X]$ and $[C_4\text{mim}][X]$. The densities of this set of ILs are required both to

Table 3.1: Ion combinations that have been analyzed in this work. Group: I (blue), II (red), III (green) and IV (yellow).

	$[BF_4]^-$	$[NTf_2]^-$	$[C_1SO_4]^-$	$[C_2SO_4]^-$	$[C_6SO_4]^-$	$[OTf]^-$
$[C_2\text{mim}]^+$	● (blue/green)	● (red/green)		● (green)	● (green)	● (green)
$[C_3\text{mim}]^+$	● (blue)	● (red)				
$[C_4\text{mim}]^+$	● (blue/yellow)	● (red/yellow)	● (yellow)			● (yellow)
$[C_6\text{mim}]^+$	● (blue)	● (red)				
$[C_8\text{mim}]^+$	● (blue)					

perform the water correction as well as the electronic polarizability calculation referred later in this chapter. These density values were directly extracted from literature when measurements at our working temperature were available.[164,238–240] Otherwise, we performed a linear interpolation with literature data to obtain the density value at our working temperature.[171,241–243] The finally employed density values for each IL are shown in Table 3.2. Since most ILs are highly hygroscopic

Table 3.2: Bibliographic densities employed in the correction of the refractive indices and electronic polarizability calculations.

Ionic Liquid	ρ^a (300 K) kg/m^3	Ionic Liquid	ρ^a (300 K) kg/m^3
$[C_2\text{mim}][BF_4]$	1282.0(1.1)[171]	$[C_4\text{mim}][NTf_2]$	1434.6(11)[239]
$[C_3\text{mim}][BF_4]$	1234.2(1.1)[243]	$[C_6\text{mim}][NTf_2]$	1371.8(5.2)[242]
$[C_4\text{mim}][BF_4]$	1200.8(2.9)[238]	$[C_4\text{mim}][C_1SO_4]$	1204.4(1.4)[164]
$[C_6\text{mim}][BF_4]$	1143.0(2.5)[238]	$[C_2\text{mim}][C_2SO_4]$	1236.5 (9.9)[239]
$[C_8\text{mim}][BF_4]$	1102.1(2.1)[238]	$[C_2\text{mim}][C_6SO_4]$	1129.1 (1.1)[240]
$[C_2\text{mim}][NTf_2]$	1518.7(5.8)[242]	$[C_2\text{mim}][OTf]$	1384.3 (2.4)[241]
$[C_3\text{mim}][NTf_2]$	1474.1(5.6)[242]	$[C_4\text{mim}][OTf]$	1297.2 (1.5)[241]

^{a}The uncertainty of the measurements was extracted from the information provided by the NIST ILThermo Database of Ionic Liquids (http://ilthermo.boulder. nist.gov/) consulted last time on March 29th, 2017.

materials, they easily absorb water from the environment. The presence of these water impurities produce a significant decrease of the refractive index of ILs. In order to take this effect into account, we corrected the measured refractive indices by considering them an ideal binary Newton mixture:[176]

$$\left(n^2 - 1\right) = \left(n_1^2 - 1\right)\phi_1 + \left(n_2^2 - 1\right)\phi_2, \tag{3.1}$$

where n is the refractive index of the mixture (measured sample), n_1 and n_2 are the refractive indices of the mixture compounds (pure IL and water) and, ϕ_1 and ϕ_2, their volume fractions. The volume fractions of ILs and water were calculated by means of the densities in Table 3.2 and measuring the amount of water on each IL by tritration by means of a Mettler Toledo Karl-Fisher coulometer. The relative mass of water determined for the different ILs studied was in the range between 0.1–1%, enough to induce deviations in the refractive index as large as $1 \cdot 10^{-3}$.

3.2 General considerations

A very first optical analysis is placing the ILs in an Abbe diagram, a representation of the Abbe number versus the refractive index of a material at a certain wavelength. In our case, we use the refractive index at the sodium D line. Abbe diagrams are a very simple way to study the optical effect that different anions have over imidazolium-based cations. Fig. 3.1 shows the 14 measured ILs represented on an Abbe diagram. It is straightforward to realize that the graph reveals three different clusters according to the anion influence:

- $[BF_4]^-$, $[OTf]^-$: ILs containing these two anions present low dispersion (Abbe number 51–52) and refractive indices between 1.40 and 1.44, the lowest indices among those ILs considered in this chapter.

- $[NTf_2]^-$: ILs belonging to this family present similar refractive indices than those containing $[BF_4]^-$ or $[OTf]^-$ anions, but higher Abbe numbers. There is an exception to this trend, which is possibly caused by contamination of the sample.

- $[C_1SO_4]^-$, $[C_2SO_4]^-$, $[C_6SO_4]^-$: ILs containing sulfates are those with higher indices, $n \approx 1.475$, and present Abbe numbers close to 50.
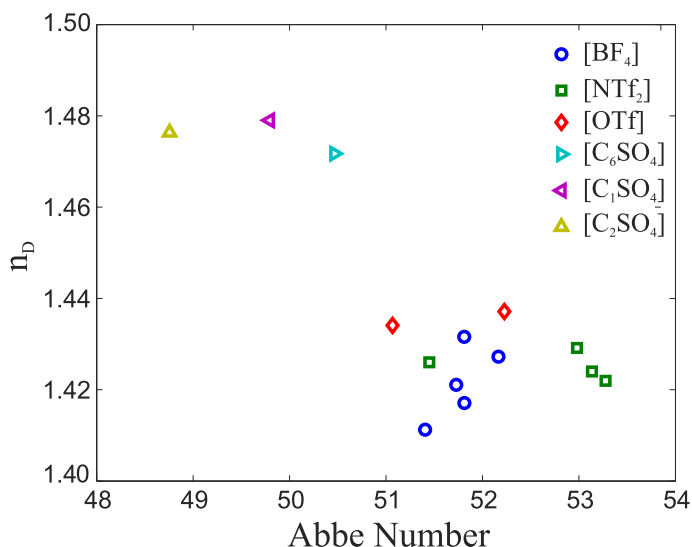
Figure 3.1: Abbe number and refractive index at the sodium D line of the studied ILs.

The material dispersion of each IL was fitted to a Cauchy formula to make it simpler to analyze and to compare with that of the other ILs:

$$n(\lambda) = a_0 + a_1/\lambda^2 + a_2/\lambda^4 + a_3/\lambda^6 + a_4\lambda^2. \tag{3.2}$$

The obtained coefficients are shown in Table 3.3 and the refractive index at some Fraunhofer lines are shown in Table 3.4. All the ILs in this chapter shown normal material dispersion which means that i) refractive index, and ii) its dispersion (slope) increases at short wavelengths. This

behavior is expected since at the shortest wavelength measured, 400 nm, the proximity of the strong absorption peaks of ILs in the UV range rises the value of refractive index, see Kramers-Kronig relationships.[178] The normal material dispersion is transferred to the electronic polarizability that also increases as the wavelength decreases. In order to gain insight into the cation and anion effects on ILs, the different groups are going to be separately discussed.

Table 3.3: Cauchy coefficients from Eq. (3.2) fitting to the material dispersion of each IL.

Ionic Liquid	a_0	$a_1 \cdot 10^3 / \text{nm}^2$	$a_2 \cdot 10^7 / \text{nm}^4$	$a_3 \cdot 10^{12} / \text{nm}^6$	$a_4 \cdot 10^{-9} / \text{nm}^{-2}$
[C$_2$mim][BF$_4$]	1.4026	2.512	32.94	-21.59	-2.290
[C$_3$mim][BF$_4$]	1.4075	3.113	17.88	-7.933	-1.879
[C$_4$mim][BF$_4$]	1.4105	3.721	4.430	2.500	-1.614
[C$_6$mim][BF$_4$]	1.4161	3.953	0.952	4.542	-1.215
[C$_8$mim][BF$_4$]	1.4206	3.930	1.994	3.885	-1.664
[C$_2$mim][NTf$_2$]	1.4117	3.590	5.158	1.808	-1.570
[C$_3$mim][NTf$_2$]	1.4137	3.615	5.371	1.418	-1.628
[C$_4$mim][NTf$_2$]	1.4169	3.323	10.24	-1.123	-3.725
[C$_6$mim][NTf$_2$]	1.4184	3.843	1.550	4.186	-1.550
[C$_4$mim][C$_1$SO$_4$]	1.4684	3.134	36.32	-22.111	-2.503
[C$_2$mim][C$_2$SO$_4$]	1.4641	4.260	10.12	-1.357	-2.334
[C$_2$mim][C$_6$SO$_4$]	1.4627	2.278	54.14	-37.82	-3.158
[C$_2$mim][OTf]	1.4232	3.747	7.942	0.399	-1.653
[C$_4$mim][OTf]	1.4259	3.928	3.090	4.050	-1.172

Table 3.4: Abbe number and refractive indices at some Fraunhofer lines A
(759.37 nm), B (686.72 nm), C (656.28 nm), D (589.0 nm), E (527.04 nm), F
(486.13 nm) and G (430.80 nm).

Ionic Liquid	A	B	C	D	E	F	G	V_{Abbe}
[C_2mim][BF_4]	1.4065	1.4081	1.4089	1.4112	1.4142	1.4169	1.4219	51.4
[C_3mim][BF_4]	1.4123	1.4139	1.4148	1.4171	1.4191	1.4228	1.4279	51.8
[C_4mim][BF_4]	1.4161	1.4178	1.4187	1.4211	1.4241	1.4268	1.4319	51.8
[C_6mim][BF_4]	1.4223	1.4240	1.4248	1.4272	1.4303	1.4330	1.4381	52.2
[C_8mim][BF_4]	1.4265	1.4283	1.4292	1.4316	1.4347	1.4375	1.4427	51.8
[C_2mim][NTf_2]	1.4172	1.4189	1.4197	1.4220	1.4250	1.4276	1.4326	53.3
[C_3mim][NTf_2]	1.4192	1.4208	1.4217	1.4240	1.4270	1.4297	1.4347	53.1
[C_4mim][NTf_2]	1.4208	1.4226	1.4235	1.4260	1.4291	1.4318	1.4369	51.4
[C_6mim][NTf_2]	1.4242	1.4259	1.4268	1.4291	1.4322	1.4349	1.4399	53.0
[C_4mim][C_1SO_4]	1.4733	1.4752	1.4762	1.4790	1.4826	1.4858	1.4919	49.8
[C_2mim][C_2SO_4]	1.4704	1.4725	1.4735	1.4764	1.4800	1.4833	1.4894	48.8
[C_2mim][C_6SO_4]	1.4662	1.4681	1.4690	1.4717	1.4752	1.4784	1.4841	50.5
[C_2mim][OTf]	1.4290	1.4307	1.4316	1.4341	1.4373	1.4401	1.4454	51.1
[C_4mim][OTf]	1.4321	1.4338	1.4347	1.4371	1.4403	1.4431	1.4483	52.2

3.3 Group I: [$C_k$mim][BF_4]

In this group the alkyl chain length of the 1-alkyl-3-methylimidazolium
cation is varied in presence of the [BF_4]$^-$ anion. Fig. 3.2 shows the
variation of the refractive index and the electronic polarizability of this
group for five different lengths of the alkyl chain, $k = 2, 3, 4, 6$ and 8
in the spectral range from 400 nm to 1000 nm. As carbon atoms
are added to the alkyl chain of the imidazolium cation, the refractive
index increases, but sublinearly. For a particular alkyl chain length,
the refractive index decreases as the wavelength increases and the
chromatic dispersion strongly increases below 550 nm. Electronic
polarizability also increases as carbon atoms are added to the alkyl chain
of the cation. The increase of electronic polarizability with the carbon
number is relatively large compared with that of the refractive index
and, oppositely to it, linear. The variation of electronic polarizability
for each new added carbon is of order 10^{-2}, whereas for refractive
index only the 10^{-3} order is affected. Moreover, for a certain carbon

65
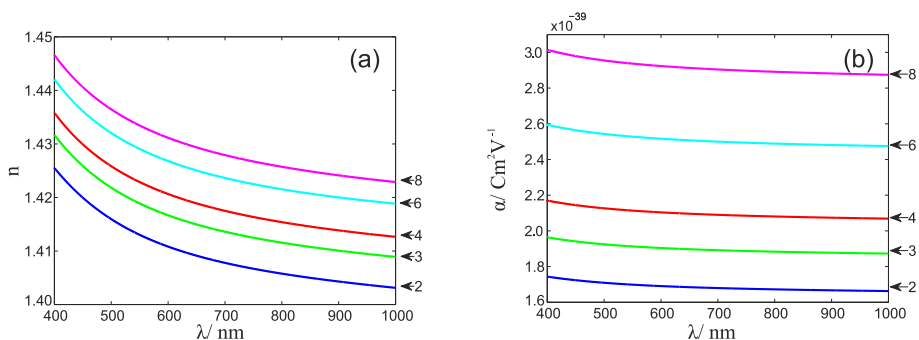
Figure 3.2: Refractive index (a) and electronic polarizability (b) of the group I of ILs [C$_k$mim][BF$_4$] with k = 2, 3, 4, 6, 8 from 400 nm to 1000 nm.

chain length, polarizability dispersion is of order 10^{-2} while material dispersion is of order 10^{-3}. In order to analyze the linearity of electronic polarizability, Fig. 3.3 shows the polarizability at different Fraunhofer lines (A, D, F and G) for different lengths of the alkyl chain of the imidazolium cation as well as a linear fit to the data, including the fitting values. In the figure, the linear dependence of the polarizability on the length of the carbon chain is evident. It is well-known that the electronic polarizability of a molecular compound can be usually interpreted as the sum of the individual electronic polarizabilities of atoms or groups of atoms that constitute the molecule.[234,244–246] These results are in perfect agreement with that statement. From this point of view, the slope of the linear fits represents the contribution to the net electronic polarizability of each CH$_2$ group in the alkyl chain. Since the slopes are approximately independent of the wavelength in the considered spectral range, it could be say that the contribution of carbon atoms in the alkyl chain is achromatic, on average $0.2075(32) \cdot 10^{-39}$ Cm^2/V per carbon atom. The independent terms cause the separation between the different curves. They were plotted against the wavelength but no linear relationship was found. However, a low degree polynomial could be enough to parameterize it.
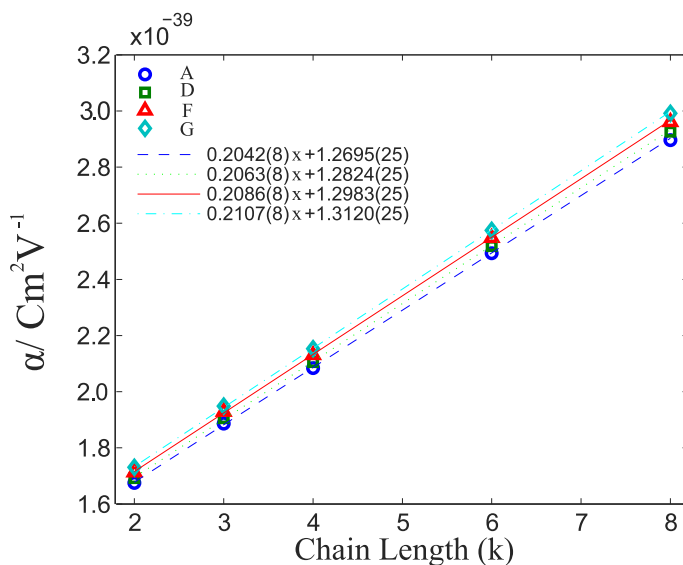
Figure 3.3: Evolution of electronic polarizability of Group I of ILs [$C_k$mim][BF_4] as a function of the number of CH_2 units, k, at different Fraunhofer lines: A (circles), D (squares), F (triangles), G (diamonds).

3.4 Group II: [$C_k$mim][NTf_2]

In this group, the alkyl chain length of the 1-alkyl-3-methylimidazolium cation is varied in presence of the bis(trifluoromethylsulfonyl)imide anion, [NTf_2]$^-$. Fig. 3.4 shows the refractive index and electronic polarizability for $k = 2$, 3, 4 and 6 in the spectral range from 400 nm to 1000 nm. Qualitatively, the refractive index behavior is similar to that of the previous group, showing a sublinear increase with the chain length. For one specific carbon chain length, the refractive index diminishes as the wavelength increases just as expected for normal dispersion. Similarly to the previous case, the most intense dispersion region goes from about 550 nm down. These trends are also observed for electronic polarizability, it grows with carbon number and decreases when the wavelength increases.
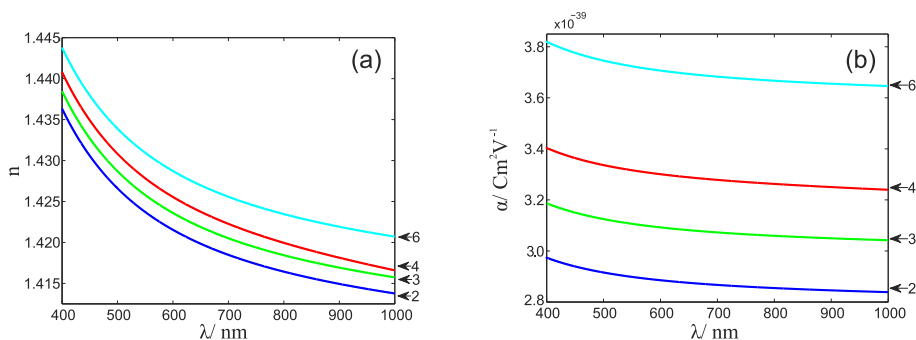
Figure 3.4: Refractive index (a) and electronic polarizability (b) of the group II of ILs [C$_k$mim][NTf$_2$] with k = 2, 3, 4, 6 from 400 nm to 1000 nm.

The electronic polarizability in ILs belonging to group II is definitively larger than that of ILs in group I. For the IL family bearing the [NTf$_2$]$^-$ anion it varies in the range $3 - 3.8 \cdot 10^{-39}$ Cm^2/V, whereas, for that with the [BF$_4$]$^-$ anion, it is within $1.8 - 3 \cdot 10^{-39}$ Cm^2/V. This difference in polarizabilities is interesting since both families of ILs present similar refractive indices. Further insights about this issue will be given later in this chapter. As with the samples of group I, the electronic polarizability curves are almost parallel and the distance between them seems to be proportional to the number of carbons in the alkyl chain. Fig. 3.5 shows the evolution of the electronic polarizability for the wavelengths at four Fraunhofer lines (A, D, F and G) as a function of the number of carbons in the alkyl chain of the imidazolium cation. Again, electronic polarizability follows a linear trend with a slope independent of the wavelength. The average value of the slopes in this family is $0.2069(93) \cdot 10^{-39}$ Cm^2/V, practically the same obtained for those ILs in group I, which indicates that this value is independent of the anion. This result is in total agreement with the hypothesis of additivity of electronic polarizability in alkyl chains previously reported by other authors.[234,244–246]
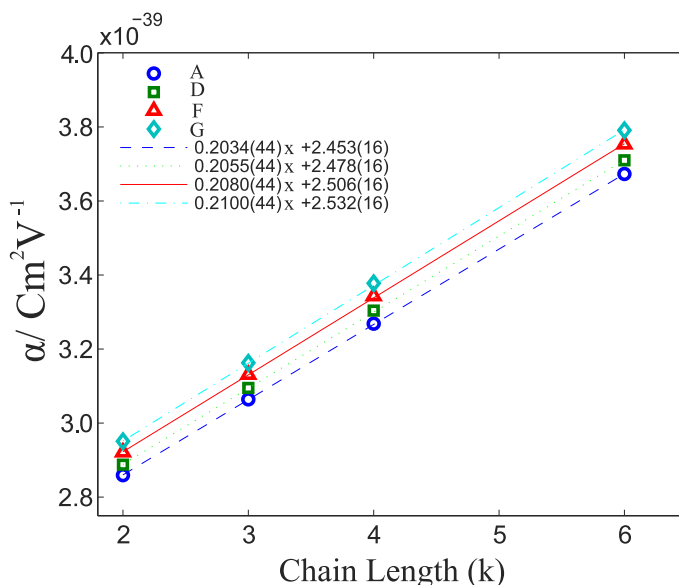
Figure 3.5: Evolution of electronic polarizability of Group II of ILs [$C_k$mim][NTf$_2$] as a function of the number of CH$_2$ units, k, at different Fraunhofer lines: A (circles), D (squares), F (triangles), G (diamonds).

3.5 Group III: [C$_2$mim][X]

In this group, the 1-ethyl-3-methylimidazolium cation is paired with five different anions: [BF$_4$]$^-$, [NTf$_2$]$^-$, [OTf]$^-$, [C$_2$SO$_4$]$^-$ and [C$_6$SO$_4$]$^-$. Fig. 3.6 shows the refractive index and electronic polarizability for the different anions in the spectral range from 400 nm to 1000 nm. The material dispersion curves are nearly parallel and present similar qualitative behavior for all the ILs. The refractive index values vary between 1.4 and 1.5 in the studied spectral range. Nevertheless, the values are highly anion-dependent with the refractive index decreasing in this order: [C$_2$SO$_4$]$^-$ > [C$_6$SO$_4$] > [OTf]$^-$ > [NTf$_2$]$^-$ > [BF$_4$]$^-$. ILs containing sulfate-based anions present the highest refractive indices, which range between 1.47 and 1.50, while the rest of ILs have lower

69

refractive indices, between 1.40 and 1.45.
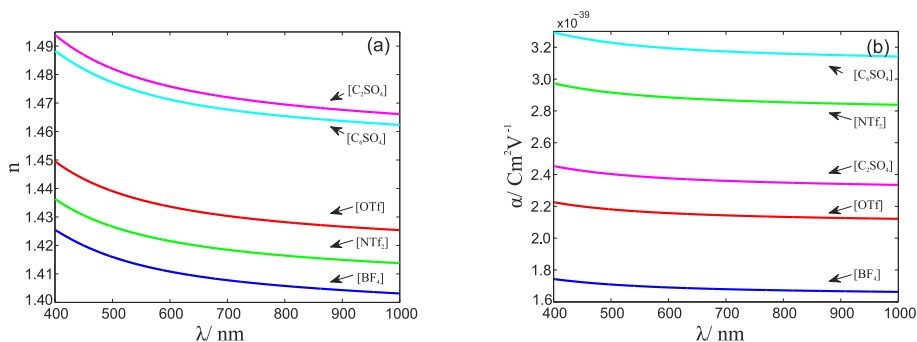
Figure 3.6: Refractive index (a) and electronic polarizability (b) of the group III of ILs [C$_2$mim][X] from 400 nm to 1000 nm.

On the other hand, the electronic polarizability varies from $1.6 \cdot 10^{-39}$ to $3.2 \cdot 10^{-39}$ Cm^2/V. The curves are almost parallel and the order of anions producing from higher polarizability to lower one is: $[C_6SO_4]^- > [NTf_2]^- > [C_2SO_4]^- > [OTf]^- > [BF_4]^-$. From this ordering, it can be seen that the trends of ILs with different anions and the same cation are different for refractive index and electronic polarizability, something already observed when comparing electronic polarizability and refractive index of ILs belonging to Groups I and II. This fact can be explained according to the Lorenz-Lorentz equation, Eq. (1.9), where the refractive index depends on the ratio between the electronic polarizability of a molecule, α, and its molecular volume, V. This ratio provides a direct way to physically understand what is happening at the molecular level in the studied groups. Table 3.5 presents the molecular volumes calculated in Refs. [240], [244] and [245] for several anions as well as our experimental electronic polarizability at the D line of ILs made of those anions combined with the $[C_2mim]^+$ cation.

Table 3.5 shows that $[C_2mim][NTf_2]$ electronic polarizability is high, but also the molecular volume of the $[NTf_2]^-$ anion is also huge.

Table 3.5: Bibliographic molar volume of the anions and experimental electronic polarizability at the D line for the Group III of ILs.

Anions	V / Å^3			α/ Cm^2/V
	Ekaterina et al.[244]	Bica et al.[245]	Anabela et al.[240]	This work
$[BF_4]^-$	66.1	77.6	-	1.6921(15)
$[NTf_2]^-$	216.2	246.8	-	2.888(11)
$[C_1SO_4]^-$	-	107.4	122.27	2.1708(71)
$[C_2SO_4]^-$	138.8	134.4	152.24	2.379(19)
$[C_6SO_4]^-$	-	-	264.80	3.1970(09)
$[OTf]^-$	119.9	128.1	-	2.1597(38)

As a consequence, the refractive index of $[C_2mim][NTf_2]$ is low. In fact, its refractive index is close to that of the $[C_2mim][BF_4]$, which presents much smaller polarizability, but also smaller volume. ILs with intermediate molecular volumes and average polarizabilities, such as $[C_2mim][OTf]$, present slightly higher refractive indices. On the other hand, the ILs with sulfate-based anions present high polarizabilities, which together with the small volume of most of these anions, leads to ILs with high refractive indices. In the case of increasing the alkyl chain in alkylsulfate anion, the increase of polarizability does not compensate the increase of molecular volume, which explains why $[C_2mim][C_6SO_4]$ has lower refractive index than $[C_2mim][C_6SO_4]$, with longer alkyl chain.

3.6 Group IV: $[C_4mim][X]$

In this group, the imidazolium cation 1-butyl-3-methylimidazolium is mixed with different anions: $[C_1SO_4]^-$, $[OTf]^-$, $[NTf_2]^-$ and $[BF_4]^-$. Fig. 3.7 shows the refractive index and electronic polarizability for the different anions in the spectral range from 400 nm to 1000 nm. The situation is the same as in group III. The maximum dispersion happens in the range below 550 nm. The specific order of anions producing from higher refractive index to the lower ones is: $[C_1SO_4]^- > [OTf]^- > [NTf_2]^- > [BF_4]^-$, the same as in Group

III. With regard to the polarizability, the trends are also the same as those of the ILs belonging to Group III. Again, the ILs containing sulfate-based anions have the highest refractive indices despite not producing the highest polarizability among the considered ILs.
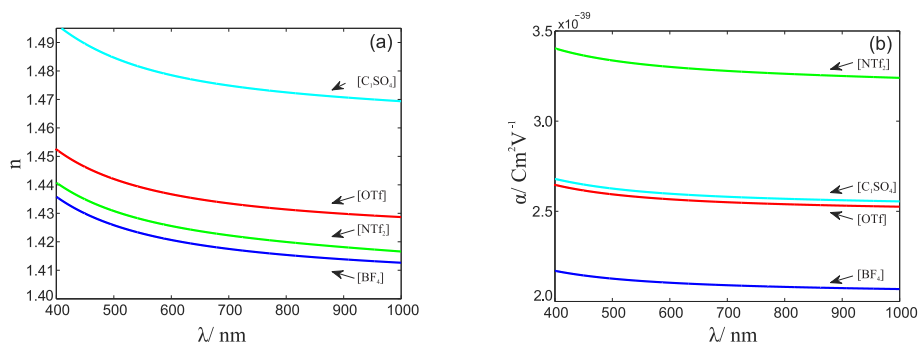
Figure 3.7: Refractive index (a) and electronic polarizability (b) of the group IV of ILs [C_4mim][X] from 400 nm to 1000 nm.

3.7 Conclusions

The RISBI technique has been shown to provide a successful method to measure the material dispersion of ILs over a wide spectral range with high precision, $S(n) < 2 \cdot 10^{-4}$. According to the Lorentz-Lorenz equation, the refractive index of ILs is related to the ratio of polarizability and molecular volume of their ions. It means that the highest refractive indices will be obtained by mixing those ionic species that offer the highest polarizability in the smallest volume possible. Tailoring the imidazolium cation alkyl chain length produces a linear increase in both electronic polarizability and molar volume, which, however, induces a sublinear variation of the refractive index. The effect of increasing the alkyl chain length could lead to an increase of the IL refractive index, as it happens in the presence of tetrafluoroborate anions, or to a decrease of it, as it happens for alkylsulfate anions.

These different trends are caused by the balance of the ratio of the electronic polarizability and molar volume of the CH_2 units with that of the rest of the IL. Hence, the evolution of the refractive index with chain length is highly dependent on the specific ion combination upon consideration.

3.8 Acknowledgments

4. Modeling the temperature-dependent material dispersion of imidazolium-based ionic liquids

Grupo de Nanomateriais, Fotónica e Materia Branda, Departamentos de Física Aplicada e de Física de Partículas, Universidade de Santiago de Compostela.

Material dispersion, i.e., the refractive index dependence on wavelength is a relevant magnitude to optically characterize materials. However, when dealing with liquids, including ILs, the refractive index dependence on temperature is also of major importance. The variation of refractive index with temperature is measured by a magnitude known as thermo-optical coefficient, TOC, which could also present a slight wavelength dependence. A large number of works focused on thermodynamic properties such as those of Tariq et al.[150] or Seki et al.[97], measure the refractive indices of ILs at different temperatures. However, usually the TOC is not analyzed in detail. An exception to this generalization could be the pioneering work of Chiappe et al.,[94] where the temperature dependence of the refractive index at several wavelengths is measured.

In this chapter, the focus is on the temperature and structural dependence of the material dispersion of ILs. Hence, material dispersion at different temperatures within the interval from 298 K to 323 K and in the spectral region from 400 nm to 1000 nm is measured using our RISBI device. The ILs considered are combinations of

1-alkyl-3-methylimidazolium cations with three different anions, tetrafluoroborate, $[BF_4]^-$, bis(trifluoromethylsulfonyl)imide, $[NTf_2]^-$, and trifluoromethanesulfonate, $[OTf]^-$.

The first part of the chapter is focused on the dependence of refractive index with wavelength, temperature, cation alkyl chain length, and anion. Afterwards, a model for the material dispersion is introduced on the basis of a one-resonance Sellmeier dispersion formula. The dependence of the fitting coefficients with temperature and IL structure is analyzed in deep. The model proposed in this chapter is able to successfully reproduce the experimental data, both as a function of temperature and of wavelength within the experimental uncertainty.

4.1 Materials

The ILs are combinations of the 1-alkyl-3-methylimidazolium family of cations, $[C_k mim]^+$, with three different anions, tetrafluoroborate, $[BF_4]^-$, bis-(trifluoromethylsulfonyl)imide, $[NTf_2]^-$, and trifluoro-methanesulfonate, $[OTf]^-$, all of them supplied by IoLiTec. The material dispersion of the ILs in Table 4.1 was measured in the range from 400 nm to 1000 nm at several temperatures after drying them by stirring in vacuum for at least 48 h. For clarity, the ILs were arranged

Table 4.1: Ion combinations that have been analyzed in this work. Group: I (blue), II (red), III (green) and IV (yellow).

Cation	$[BF_4]^-$	$[NTf_2]^-$	$[OTf]^-$
$[C_2 mim]^+$	blue/green	red/green	green
$[C_3 mim]^+$	blue	red	
$[C_4 mim]^+$	blue/yellow	red/yellow	yellow
$[C_6 mim]^+$	blue	red	
$[C_8 mim]^+$	blue		

into the four groups. Group I contains combinations of the $[C_k mim]^+$

cation with $k = 2, 3, 4, 6, 8$ and the $[BF_4]^-$ anion. Group II is composed by combinations of $[C_k mim]^+$ with $k = 2, 3, 4, 6$ and the $[NTf_2]^-$ anion. Group III comprises the $[C_2 mim]^+$ cation with $[BF_4]^-$, $[NTf_2]^-$ and $[OTf]^-$ anions and, Group IV, contains the $[C_4 mim]^+$ cation with the same set of anions.

4.2 General considerations

Material dispersion at a temperature of 298 K of the ILs considered in this chapter is shown in Fig. 4.1. Values of the refractive indices of these ILs at selected wavelengths and temperatures can be found in the Supplementary Material of this chapter, in Table 4.S1. In all cases the dispersion is normal, i.e., refractive index decreases as wavelength increases, and the dispersion is higher for smaller wavelengths. Furthermore, the dispersion curves of the different ILs show similar trends, which indicates that the chromatic dispersion of the considered liquids shares a common origin.

In Groups I and II, where imidazolium cations with different alkyl chain lengths share a common anion, refractive index increases with the chain length. On the other hand, Groups III and IV include ILs with a common cation paired with different anions. In both cases, anions increase the refractive index as: $[BF_4]^- < [NTf_2]^- < [OTf]^-$. Regarding the temperature dependence, refractive index of all the ILs decreases as temperature increases. The effect on the material dispersion is, qualitatively, a translation of the material dispersion curve, which, as explained later in the text, is originated in the linear dependence of mass density with temperature.

4.3 Material dispersion and alkyl chain

Refractive index of ILs based on imidazolium cations with the studied anions increases with the alkyl chain length of the cation, but this
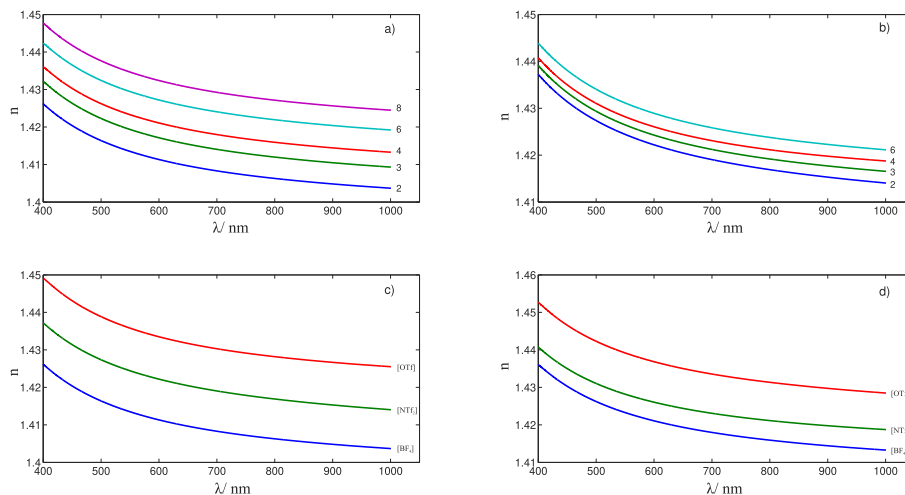
Figure 4.1: Material dispersion of the refractive index at T = 298 K for a) Group I, [C$_k$mim][BF$_4$]. b) Group II, [C$_k$mim][NTf$_2$]. c) Group III, [C$_2$mim][X]. d) Group IV, [C$_4$mim][X].

increase is sublinear. Nevertheless, as shown in the previous chapter, electronic polarizability, presents a clearly linear dependence on the alkyl chain length of the imidazolium cation. According to the Lorenz-Lorenz equation, Eq. (1.9), the ratio of the electronic polarizability and the molecular volume of the molecules in a liquid determines its refractive index. The polarizability of a mole of molecules is usually expressed in terms of a magnitude known as molar refractivity, R, which in the SI system has units of volume:

$$R = \frac{\alpha}{3\varepsilon_0} N_A, \tag{4.1}$$

where ε_0 is the vacuum permittivity and N_A the Avogadro number. Note that in the cgs system, it is the electronic polarizability the magnitude which has units of volume. Combining Eq. (4.1) and Eq. (1.9), the Lorentz-Lorenz equation can be expressed in terms of the

78

molar refractivity as

$$\frac{n^2 - 1}{n^2 + 2} = \frac{R}{V_m},$$

(4.2)

where $V_m = M/\rho$ is the molar volume of the liquid, being M its molecular mass and ρ its mass density. This expression can be rearranged to be expressed in terms of a magnitude known as free molar volume, $f_m = V_m - R$, which is the difference between the molar volume and the molar refractivity:

$$n^2 - 1 = \frac{3R}{V_m - R} = \frac{3R}{f_m}.$$

(4.3)

Hence, in the light of this expression, the molar refractivity could be interpreted as the fraction of volume polarizable. When the molar volume is much larger than the molar refractivity, $V_m >> R$, we obtain $n^2 - 1 \rightarrow 3R/V_m = \alpha/\varepsilon_0 N_A V_m$, which is the usual expression for the refractive index of gases. Conversely, when $R >> V_m$, it yields $n \rightarrow \sqrt{2}i$, i.e., when the polarizable volume exceeds the dimensions of the molecular volume itself, it yields an imaginary refractive index, in resemblance to that of metals below the plasma frequency. Note that the $1/3$ factor relating polarizability and molar refractivity comes from the Lorenz-Lorentz assumption of spherical molecules and the corresponding Lorentz field factor, see chapter 1. Eq. 4.3 is highly interesting since it establishes that the macroscopic relation between refractive index and molar volume comes from the degree of molecular packing in a liquid. Dense liquids present high molecular packing with low free volumes that yield high refractive indices. Oppositely, low density liquids have large molar free volumes that produce lower refractive indices.

Molar refractivity can be experimentally calculated if both refractive index and molar volume (mass density) of a liquid are known. In our case, we calculated the molar refractivity by means of the refractive index at the D line and molar volumes obtained by our experimental densities, see Table 4.S2. Fig. 4.2 shows both the molar volumes and refractivity of the 11 ILs studied in this chapter

79

as a function of the alkyl chain length of the imidazolium cation at T = 298 K.
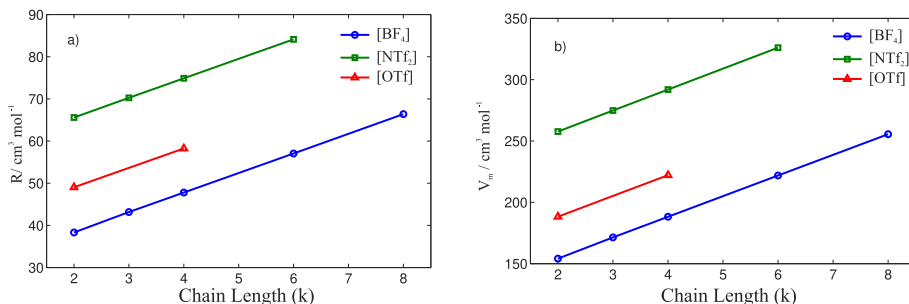
Figure 4.2: (a) Molar refractivity, R, at the D line and (b) molar volume, V_m of the studied ILs as a function of the alkyl chain length at T = 298 K.

At a fixed wavelength and temperature, molar refractivity increases with the alkyl chain length, k, following a clear linear trend, which we fitted to $R = R_0 + R_k \cdot k$. Fitting parameters at different wavelengths and temperatures are given in Table 4.2. The order of anions producing from

Table 4.2: Coefficients of the linear fit of molar refractivity, R, to the cation chain length at different wavelengths and temperatures, $R = R_0 + R_k \cdot k$.

		[$C_k$mim][BF$_4$]		[$C_k$mim][NTf$_2$]	
λ/ nm	T/ K	R_0/ cm^3/mol	R_k/ cm^3/mol	R_0/ cm^3/mol	R_k/ cm^3/mol
430.1		29.743	4.7637	57.572	4.7275
486.1		29.429	4.7178	56.989	4.6836
589.0	298.15	29.074	4.6649	56.320	4.6345
656.3		28.928	4.6430	56.042	4.6152
822.7		28.702	4.6092	55.600	4.5875
	298.15	29.074	4.6649	56.320	4.6345
	303.15	29.056	4.6702	56.338	4.6372
589.0	308.15	29.061	4.6710	56.384	4.6296
	313.15	29.068	4.6703	56.367	4.6374
	318.15	29.071	4.6722	56.361	4.6408
	323.15	29.077	4.6711	56.390	4.6359

lower to higher refractivities is: [BF$_4$]$^-$ < [OTf]$^-$ < [NTf$_2$]$^-$, the same found for electronic polarizability in the previous chapter. The slope of

80

molar refractivity is similar for the three studied groups since in all cases
it reflects the contribution to electronic polarizability of the CH_2 unit.
On the other hand, intercepts are fairly different. They are related to the
overall polarizability of the imidazolium ring and that of the different
anions. Hence, since cations are common to all the ILs, the differences
in intercepts must be exclusively produced by the anions. Heavy anions
such as $[NTf_2]^-$ produce larger intercept values than lighter anions such
as $[BF_4]^-$, essentially, due to the larger number of atoms contributing
to the overall electronic polarizability in $[NTf_2]^-$ than in $[BF_4]^-$.

As already noted by other authors,[150] and, as it is also observed
in Fig. 4.2, molar volume is a linear function of the cation alkyl chain
length too. The coefficients of a linear fit to these data, $V_m = V_0 + V_k \cdot k$,
are given in Table 4.3. The linear increase of molar volume with the

Table 4.3: Coefficients of the linear fit of molar volume, V_m, to the cation chain
length at different temperatures, $V_m = V_0 + V_k \cdot k$.

	[C$_k$mim][BF$_4$]		[C$_k$mim][NTf$_2$]	
T(K)	V_0/ cm^3/mol	V_k/ cm^3/mol	V_0/ cm^3/mol	V/ cm^3/mol
298.15	120.55	16.879	223.57	17.084
303.15	120.89	16.935	224.31	17.141
308.15	121.23	16.991	225.06	17.200
313.15	121.58	17.045	225.81	17.258
318.15	121.93	17.099	226.56	17.318
323.15	122.28	17.154	227.30	17.378

alkyl chain length is originated by elongation of the molecule in a given
direction. In this process, the molecule takes the form of a spheroid or
an ellipsoid rather than a sphere. Since in all cases the deformation is
the same, and it only takes place in the cation, V_k is independent of the
anion. It takes a value of $V_k \approx 17$ cm^3/mol in all families, in accordance
with previous works,[150] and roughly corresponding to the molar volume
of a CH_2 group.

In the case of increasing the alkyl chain length of the cation,
both free molar volume and molar refractivity vary linearly with the
chain length. However, intercepts and slopes of both magnitudes are

81
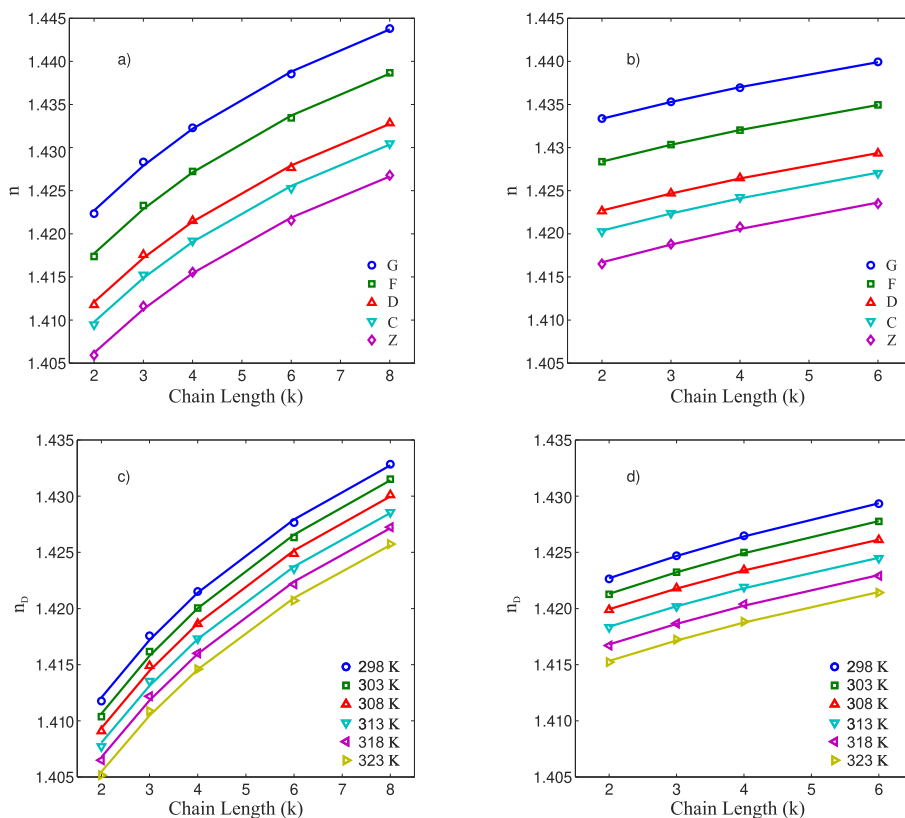
Figure 4.3: Refractive indices at different Fraunhofer lines: G (λ = 430.1 nm), F (λ = 486.1 nm), D (λ = 589.0 nm), C (λ = 656.3 nm), and Z (λ = 822.7 nm) as a function of the alkyl chain length. (a) Group I, [C$_k$mim]BF$_4$] and (b) Group II, [C$_k$mim][NTf$_2$]. Refractive index at the sodium D line as a function of alkyl chain length at different temperatures. (c) Group I and (d) Group II.

different. Thus, the refractive index is determined by the ratio of two linear functions of different coefficients, reason why it increases below linearity when increasing the alkyl chain length of imidazolium cations. This rational function[245] in terms of molar refractive and molar free volume is able to reproduce the trends of refractive index at whatever wavelength and temperature, as shown in Fig. 4.3. The difference

between experimental and fitted data is always less than $4.4 \cdot 10^{-4}$ for
ILs with the $[\mathrm{BF_4}]^-$ anion and less than $2.7 \cdot 10^{-4}$ for those with the
$[\mathrm{NTf_2}]^-$ anion.

4.4 Material dispersion and temperature

In order to obtain a closer insight into the dependence of material
dispersion on temperature, we took logarithms and differentiated
Eq. (4.2) with respect to temperature as

$$\frac{1}{\rho}\frac{\partial \rho}{\partial \mathrm{T}} + \frac{1}{R}\frac{\partial R}{\partial \mathrm{T}} = \frac{6n}{(n^2-1)(n^2+2)}\frac{\partial n}{\partial \mathrm{T}}. \qquad (4.4)$$

The first term corresponds to minus the coefficient of thermal expansion,
$\alpha_T = -\frac{1}{\rho}\frac{\partial \rho}{\partial \mathrm{T}}$. Analogically, the second term is the thermal coefficient
of molar refractivity or electronic polarizability, $\frac{1}{R}\frac{\partial R}{\partial \mathrm{T}} = \frac{1}{\alpha}\frac{\partial \alpha}{\partial \mathrm{T}}$. Finally,
the last term contains the thermo-optical coefficient, $\mathrm{TOC} = \frac{\partial n}{\partial \mathrm{T}}$, which
contains the dependence of refractive index on temperature. According
to Eq. (4.4), the thermo-optical coefficient of a liquid depends on the
balance between its thermal expansion and the thermal dependence of
its electronic polarizability.

It is possible to perform a fast estimation of the influence of the
thermal dependence of the electronic polarizability in the thermo-optical
coefficient of ILs by using the temperature-dependent data of refractive
index and density shown in Tables 4.S1, 4.S2 and 4.S3. It turns out that
the electronic polarizability coefficient lies within $0.2 - 2.5 \cdot 10^{-5}$ K^{-1}
for all compounds, wavelengths, and temperatures, while, the thermal
expansion coefficient is within the range of $5.8 - 6.8 \cdot 10^{-4}$ K^{-1}. In
other words, the contribution of electronic polarizability to the thermo-
optical coefficient is just $0.3 - 7.6\%$ that of the thermal expansion. This
result contradicts those of Ref. [94], where the electronic polarizability
dependence on temperature of imidazolium-based ionic liquids with a
phosphorus-containing anion was found to be comparable to thermal
expansion. In accordance with our results, when an IL has a positive

thermal expansion coefficient its refractive index decreases with temperature (i.e., negative TOC), and, oppositely, in the unusual case of negative thermal expansion coefficients, refractive index would increase with temperature.

Refractive index dependence on temperature for different spectral lines for both ILs in Groups I and II are shown in Fig. 4.4. Refractive index presents a clearly linear trend with temperature, the same as mass density, see Table 4.S3. The thermo-optical coefficient corresponds to the slope of these straight lines and it is always negative since refractive index decreases with temperature. The absolute value of the TOC for all the considered ILs is always less than $1 \cdot 10^{-3}$ K^{-1}.
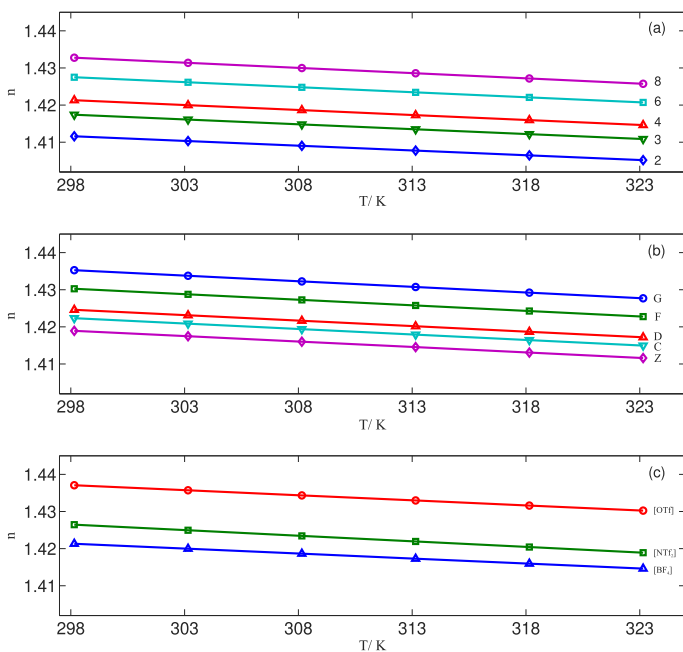
Figure 4.4: Refractive indices as a function of temperature. (a) ILs from Group I, [C$_k$mim][BF$_4$], at the sodium D line. (b) Refractive index of [C$_3$mim][NTf$_2$] at different Fraunhofer lines. (c) ILs sharing the [C$_4$mim]$^+$ cation at the sodium D line.

4.5 Modeling temperature-dependent material dispersion

In order to model the dependence of material dispersion on wavelength
and temperature, we fitted the experimental data to a temperature-
dependent dispersion equation. The equations generally used to model
material dispersion are those of Cauchy and Sellmeier.[247] While the
Cauchy equation is simpler, it merely corresponds to an expansion in
powers of λ^{2x}, with x being an integer, the Sellmeier equation provides
more information about the IL. Indeed, Cauchy equation is nothing but
an approximation of the Sellmeier equation far from resonances. The
general expression of the Sellmeier equation is:

$$n^2 - 1 = \sum_{i=1}^{N} \frac{c_i \lambda^2}{\lambda^2 - \lambda_i^2}, \tag{4.5}$$

where the constants c_i and λ_i are related with the absorption spectra
of the material to model. The coefficient λ_i is the position of the i
absorption peak and c_i is its strength. When using Sellmeier formulas to
describe the refractive index over a wide spectral range, it is common to
employ three resonances with two of them located in the UV region and
the other one in the IR. Typically, the ultraviolet resonances are below
200 nm, and the infrared resonances are above 3 μm. The proximity
of the ultraviolet resonances to the visible range is responsible for the
normal material dispersion observed in ILs. Furthermore, the curvature
of the material dispersion curves in our liquids also indicates that the
ultraviolet resonances dominate over the infrared ones.

One of the simplest Sellmeier formulas is that which considers
just one single resonance placed in the UV. The value of the resonant
wavelength seems to be independent of temperature, while the strength
of the resonance varies almost linearly with it. Furthermore, it was
observed that for ILs sharing the same anion, the position of the i-th
resonance λ_i is independent of the length of the alkyl chain of the
imidazolium cation. Therefore, we consider the temperature-dependent

USC
UNIVERSIDADE
DE SANTIAGO
DE COMPOSTELA

Sellmeier formula:

$$n^2(\lambda, \mathrm{T}) - 1 = [c_1 + c_2 \Delta \mathrm{T}] \frac{\lambda^2}{\lambda^2 - \lambda_{UV}^2}, \qquad (4.6)$$

where $\Delta \mathrm{T} = \mathrm{T} - \mathrm{T}_0$, with T_0 the reference temperature, $\mathrm{T}_0 = 310.5$ K, the center of the measured temperature interval and λ_{UV} is independent of the alkyl chain length. Keeping λ_{UV} fixed slightly worsens the numerical accuracy of our model, but it provides a more insightful picture of the relation between the refractive index and the molecular structure of ILs. The fitting coefficients are listed in Table 4.4 and the procedure followed to fit the material dispersion of each family of ILs to Eq. (4.6) was the following:

1. The UV resonance, λ_{UV}, is determined.

2. The coefficients c_1 and c_2 are obtained by linearly fitting the spectra at different temperatures using the least-squares method.

Table 4.4: Coefficients of the Sellmeier fit of Eq. (4.6) to the material dispersion, wavelength in microns.

Ionic Liquid	$\lambda_{UV}^2/$ $10^{-2}\mu m^2$	c_1	$c_2/$ 10^{-4} K^{-1}
[C$_2$mim][BF$_4$]		0.951573 (98)	-7.010 (11)
[C$_3$mim][BF$_4$]		0.967156 (12)	-7.179 (14)
[C$_4$mim][BF$_4$]	1.1326 (12)	0.977712 (11)	-7.355 (13)
[C$_6$mim][BF$_4$]		0.994587 (14)	-7.483 (16)
[C$_8$mim][BF$_4$]		1.008824 (11)	-7.763 (13)
[C$_2$mim][NTf$_2$]		0.981063 (23)	-8.049 (27)
[C$_3$mim][NTf$_2$]	1.1010 (10)	0.986695 (11)	-8.156 (13)
[C$_4$mim][NTf$_2$]		0.991627 (15)	-8.309 (18)
[C$_6$mim][NTf$_2$]		0.998810 (11)	-8.701 (13)
[C$_2$mim][OTf]	1.1450 (10)	1.011676 (12)	-7.701 (14)
[C$_4$mim][OTf]		1.020564 (15)	-7.588 (18)

From the data in the table, it is clear that the resonant wavelength λ_{UV} does not strongly depend on the anion. Both c_1 and c_2 coefficients increase in absolute value with the alkyl chain length, which suggests that not only refractive indices but, also the thermo-optical coefficient, present a dependence on the number of carbons in the alkyl chain. For cations with the same alkyl chain, the value of the coefficients increases as $[\mathrm{BF_4}]^- < [\mathrm{NTf_2}]^- < [\mathrm{OTf}]^-$ for c_1 and $[\mathrm{BF_4}]^- < [\mathrm{OTf}]^- < [\mathrm{NTf_2}]^-$ for c_2. Furthermore, the temperature-independent term c_1 dominates over the temperature-dependent term c_2, which, for any wavelength and temperature, is more than 1000 times smaller. Examples of the goodness of this fit are shown in Fig. 4.5, where the deviations of our model and the experimental data for the three ILs is less than $3.5 \cdot 10^{-5}$, one order of magnitude below experimental uncertainty.
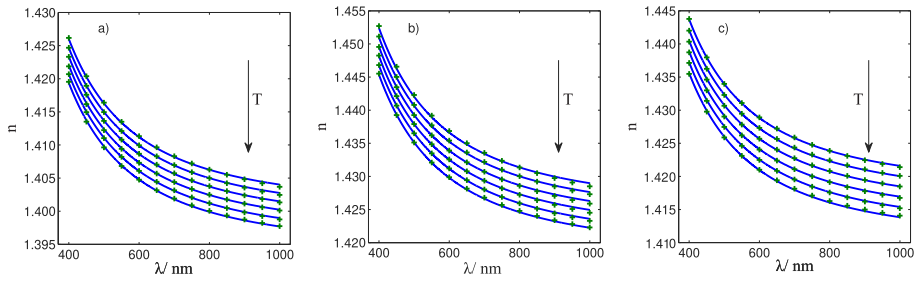
Figure 4.5: Material dispersion at different temperatures: experimental data at selected wavelengths (crosses) and fit (lines). (a) [C$_2$mim][BF$_4$]. (b) [C$_4$mim][OTf]. (c) [C$_6$mim][NTf$_2$]. Temperature decreases up down and goes from 298 K to 323 K in steps of 5 K.

The thermo-optical coefficient can be obtained differentiating Eq. (4.6) with respect the temperature and taking into account that both c_1 and λ_{UV} are temperature independent:

$$\frac{\partial n}{\partial \mathrm{T}} = \frac{c_2}{2n} \frac{\lambda^2}{\lambda^2 - \lambda_{UV}^2}. \tag{4.7}$$

However, this expression can be further simplified. Denoting n_0 the refractive index at the reference temperature, $n_0^2 = 1 + c_1 \frac{\lambda^2}{\lambda^2 - \lambda_{UV}^2}$ and

Δn^2 as $\Delta n^2 = n^2 - n_0^2 = c_2 \Delta T \frac{\lambda^2}{\lambda^2 - \lambda_{UV}^2}$, we have $\left|\frac{\Delta n^2}{n_0}\right| \leq 1 \cdot 10^{-3}$ for every λ and T. Henceforth, making the approximation $n \approx n_0$ in the denominator of Eq. (4.7), the following expression is obtained:

$$\frac{\partial n}{\partial T} \approx \frac{1}{2n_0 \Delta T} \Delta n^2(\lambda, T), \qquad (4.8)$$

and with the same level of approximation, the refractive index verifies:

$$n(\lambda, T) \approx n_0(\lambda) + \frac{\Delta n^2(\lambda, T)}{2n_0(\lambda)}. \qquad (4.9)$$

According to Eq. (4.8), the thermo-optical coefficient is not a temperature dependent magnitude, but it is a dispersive magnitude, since it depends on the wavelength. In fact, it is seen that within the framework of our model, the thermo-optical coefficient dispersion follows a single resonance Sellmeier dispersion formula with the peculiarity that the strength of the resonator is negative. Using Eq. (4.8), the thermo-optical dispersion can be estimated for the different ILs, see Fig. 4.6. Several features are remarkable there: i) thermo-optical coefficient increases in absolute value with the chain length for the families of ILs that share a common anion. As noted in Ref. [248], this could result from higher dilatation coefficients associated to lower degrees of hydrogen bonding. With respect to ILs sharing the same cation, the order of anions increasing the thermo-optical coefficient is $[BF_4]^- < [OTf]^- < [NTf_2]^-$, which could also be attributed to a change in the thermal dilatation that follows the same trend. ii) Dispersion is normal, as it is that of refractive index: it increases in absolute value decreasing the wavelength, so the dispersion is higher at shorter wavelengths that at larger ones. At the limit of very large wavelengths, $\lambda >> \lambda_{UV}$, the thermo-optical coefficient tends to a constant value of $\frac{c_2}{2\sqrt{1+c_1}}$. It is worth to mention that the thermo-optical dispersion shown here disagrees with the analysis of other authors, who considered that the thermo-optical coefficient is independent of the wavelength.[91,94] In this regard, the dispersion measured here for the thermo-optical coefficient in the whole spectral range is about a 4%, larger than that of refractive index, which is less than 2%.
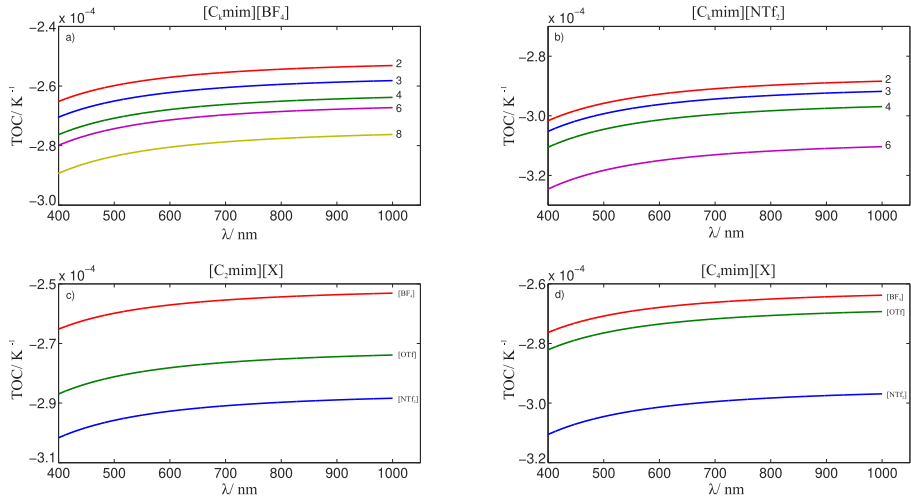
Figure 4.6: Dispersion of the thermo-optical coefficient calculated by means of a single-resonance Sellmeier dispersion formula.
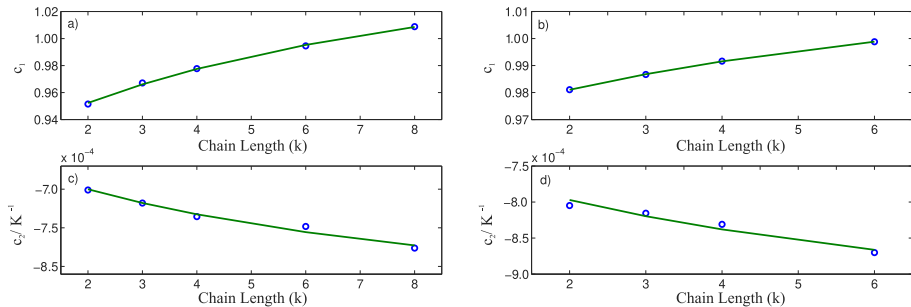
Figure 4.7: Coefficients c_1 and c_2 fitted to the ratio of two linear functions of the alkyl chain length. (a,c) Group I of ILs. (b,d) Group II of ILs.

Finally, it is interesting to mention that the c_1 and c_2 coefficients are dependent of the alkyl chain length, see Fig. 4.7. In fact, combining Eq. (4.6) and Eq. (4.3), it turns out that the coefficients c_1 and c_2 must be a rational function of the alkyl chain length. It is possible to perform

89

this type of fitting for both coefficients using the Groups I and II of ILs, see Fig. 4.7. In order to do that:

1. We fitted the temperature-independent coefficient c_1.
2. The c_2 coefficient was calculated constraining the denominator to be the same denominator as in c_1.

The good behavior of the rational fitting confirms our predictions and evidences that the resonator strengths are dependent on the alkyl chain length. Further insights in this relationship will be provided in the following chapter, where we used a more sophisticated Sellmeier equation over a wider spectral range to analyze this dependence.

4.6 Conclusions

Material dispersion of the studied imidazolium-based ionic liquids is normal at all the temperatures and within the considered spectral range for all the ILs. On the other hand, thermo-optical coefficient is always negative, which means that the refractive index decreases as temperature rises at any wavelength. The thermodynamic origin of this trend is originated in the dependence of the thermo-optical coefficient on the thermal-expansion coefficient, while the temperature-dependence of electronic polarizability is less important. Both material dispersion and thermo-optical coefficient can be tailored by tuning the alkyl chain length of the cation, an interesting mechanism to design ILs with task-specific material dispersion and thermo-optical coefficient. Furthermore, a single-resonance temperature-dependent Sellmeier dispersion equation is enough to describe the material dispersion within the studied spectral and thermal ranges with remarkable accuracy. With regard to the resonance in this model, it is placed in the UV and it does not depend on temperature or on the specific IL considered. Hence, the position of the absorption peak is probably governed by the imidazolium ring, which is the structural element common to all the ILs. Indeed, it explains the shape of the observed dispersion, similar for all the ILs and independent of temperature or anion nature.

Furthermore, the strength of the resonator is a linear function of the temperature, which explains the translation experimentally observed for material dispersion with it. Finally, a certain dependence of the resonator strength in the cation alkyl chain length was also observed.

4.7 Acknowledgments

4.8 Supplementary material

Table 4.S1: Refractive index of studied ILs at different temperatures and wavelengths G = 430.1 nm, F = 486.1 nm, D = 589.0 nm, C = 656.3 nm and Z = 822.7 nm.

Ionic Liquid	T/ K	G	F	D	C	Z
$[C_2mim][BF_4]$	298.15	1.4224	1.4174	1.4117	1.4095	1.4059
	303.15	1.4210	1.4159	1.4104	1.4081	1.4046
	308.15	1.4196	1.4146	1.4091	1.4069	1.4034
	313.15	1.4182	1.4132	1.4077	1.4055	1.4022
	318.15	1.4170	1.4120	1.4065	1.4043	1.4009
	323.15	1.4155	1.4106	1.4051	1.4030	1.3997
$[C_3mim][BF_4]$	298.15	1.4284	1.4233	1.4176	1.4152	1.4116
	303.15	1.4270	1.4219	1.4161	1.4138	1.4102
	308.15	1.4256	1.4206	1.4149	1.4126	1.4090
	313.15	1.4242	1.4191	1.4135	1.4113	1.4078
	318.15	1.4228	1.4178	1.4122	1.4099	1.4065
	323.15	1.4213	1.4163	1.4109	1.4086	1.4053
$[C_4mim][BF_4]$	298.15	1.4324	1.4272	1.4215	1.4192	1.4156
	303.15	1.4309	1.4257	1.4200	1.4177	1.4141
	308.15	1.4293	1.4243	1.4186	1.4164	1.4129
	313.15	1.4279	1.4229	1.4173	1.4151	1.4116
	318.15	1.4266	1.4216	1.4160	1.4138	1.4103
	323.15	1.4251	1.4201	1.4146	1.4124	1.4090
$[C_6mim][BF_4]$	298.15	1.4386	1.4334	1.4276	1.4253	1.4216
	303.15	1.4372	1.4321	1.4263	1.4240	1.4203
	308.15	1.4358	1.4307	1.4249	1.4225	1.4188
	313.15	1.4343	1.4292	1.4235	1.4212	1.4177
	318.15	1.4329	1.4278	1.4221	1.4199	1.4163
	323.15	1.4313	1.4263	1.4207	1.4184	1.4150
$[C_8mim][BF_4]$	298.15	1.4439	1.4387	1.4328	1.4305	1.4268
	303.15	1.4425	1.4373	1.4315	1.4292	1.4255
	308.15	1.4410	1.4359	1.4301	1.4278	1.4241
	313.15	1.4395	1.4343	1.4285	1.4262	1.4226
	318.15	1.4381	1.4329	1.4272	1.4249	1.4214
	323.15	1.4365	1.4314	1.4257	1.4235	1.4200
$[C_2mim][NTf_2]$	298.15	1.4334	1.4284	1.4226	1.4203	1.4165
	303.15	1.4319	1.4269	1.4212	1.4190	1.4154
	308.15	1.4304	1.4254	1.4199	1.4176	1.4141
	313.15	1.4289	1.4239	1.4183	1.4160	1.4125
	318.15	1.4271	1.4222	1.4167	1.4145	1.4111
	323.15	1.4257	1.4207	1.4152	1.4130	1.4095
$[C_3mim][NTf_2]$	298.15	1.4354	1.4303	1.4247	1.4224	1.4188
	303.15	1.4338	1.4288	1.4232	1.4210	1.4175
	308.15	1.4323	1.4273	1.4218	1.4196	1.4161
	313.15	1.4306	1.4257	1.4202	1.4180	1.4145
	318.15	1.4291	1.4241	1.4186	1.4164	1.4130
	323.15	1.4276	1.4227	1.4172	1.4150	1.4117

92

[C$_4$mim][NTf$_2$]	298.15	1.4370	1.4320	1.4265	1.4242	1.4208
	303.15	1.4354	1.4305	1.4250	1.4228	1.4194
	308.15	1.4338	1.4289	1.4234	1.4212	1.4179
	313.15	1.4324	1.4274	1.4219	1.4197	1.4163
	318.15	1.4308	1.4258	1.4204	1.4182	1.4149
	323.15	1.4290	1.4241	1.4188	1.4167	1.4136
[C$_6$mim][NTf$_2$]	298.15	1.4401	1.4351	1.4293	1.4270	1.4234
	303.15	1.4386	1.4336	1.4279	1.4257	1.4221
	308.15	1.4370	1.4320	1.4263	1.4240	1.4204
	313.15	1.4355	1.4305	1.4249	1.4226	1.4192
	318.15	1.4338	1.4289	1.4233	1.4211	1.4176
	323.15	1.4321	1.4272	1.4217	1.4195	1.4161
[C$_2$mim][OTF]	298.15	1.4453	1.4399	1.4339	1.4315	1.4278
	303.15	1.4439	1.4385	1.4326	1.4303	1.4266
	308.15	1.4423	1.4370	1.4311	1.4288	1.4252
	313.15	1.4408	1.4355	1.4297	1.4274	1.4238
	318.15	1.4393	1.4341	1.4283	1.4260	1.4225
	323.15	1.4378	1.4326	1.4269	1.4246	1.4212
[C$_4$mim][OTF]	298.15	1.4487	1.4434	1.4373	1.4348	1.4309
	303.15	1.4472	1.4418	1.4358	1.4334	1.4296
	308.15	1.4456	1.4403	1.4343	1.4319	1.4282
	313.15	1.4443	1.4389	1.4330	1.4306	1.4268
	318.15	1.4428	1.4375	1.4316	1.4292	1.4256
	323.15	1.4414	1.4361	1.4303	1.4280	1.4244

Table 4.S2: Density (g/cm^3) as a function of temperature.

	T/ K					
IL	298.15	303.15	308.15	313.15	318.15	323.15
[C$_2$mim][BF$_4$]	1.2849	1.2812	1.2774	1.2736	1.2699	1.2661
[C$_3$mim][BF$_4$]	1.2371	1.2334	1.2297	1.2261	1.2225	1.2188
[C$_4$mim][BF$_4$]	1.2010	1.1975	1.1939	1.1904	1.1869	1.1834
[C$_6$mim][BF$_4$]	1.1452	1.1418	1.1384	1.1349	1.1315	1.1281
[C$_8$mim][BF$_4$]	1.1043	1.1008	1.0974	1.0941	1.0908	1.0875
[C$_2$mim][NTf$_2$]	1.5185	1.5134	1.5084	1.5034	1.4984	1.4934
[C$_3$mim][NTf$_2$]	1.4747	1.4698	1.4648	1.4600	1.4551	1.4502
[C$_4$mim][NTf$_2$]	1.4366	1.4319	1.4271	1.4223	1.4176	1.4129
[C$_6$mim][NTf$_2$]	1.3722	1.3676	1.3631	1.3585	1.3539	1.3494
[C$_2$mim][OTf]	1.3821	1.3779	1.3737	1.3695	1.3654	1.3613
[C$_4$mim][OTf]	1.2977	1.2937	1.2898	1.2859	1.2820	1.2781

Table 4.S3: Molar mass of the ILs and coefficients of a linear fit of the densities to temperature, $\rho = \rho_0 + \rho_T \cdot T$.

IL	M/ g/mol	ρ_0/ g/cm^3	ρ_T / g/ (cm^3 K)
[C$_2$mim][BF$_4$]	197.97	1.303727	-7.52 $\cdot 10^{-4}$
[C$_3$mim][BF$_4$]	212.00	1.255326	-7.30 $\cdot 10^{-4}$
[C$_4$mim][BF$_4$]	226.02	1.218664	-7.06 $\cdot 10^{-4}$
[C$_6$mim][BF$_4$]	254.08	1.162222	-6.82 $\cdot 10^{-4}$
[C$_8$mim][BF$_4$]	282.13	1.120984	-6.71 $\cdot 10^{-4}$
[C$_2$mim][NTf$_2$]	391.31	1.543503	-10.0 $\cdot 10^{-4}$
[C$_3$mim][NTf$_2$]	405.34	1.499123	-9.79 $\cdot 10^{-4}$
[C$_4$mim][NTf$_2$]	419.36	1.460342	-9.49 $\cdot 10^{-4}$
[C$_6$mim][NTf$_2$]	447.41	1.394977	-9.12 $\cdot 10^{-4}$
[C$_2$mim][OTf]	260.23	1.402843	-8.32 $\cdot 10^{-4}$
[C$_4$mim][OTf]	288.29	1.317291	-7.85 $\cdot 10^{-4}$

5. Material dispersion and molecular structure in 1-alkyl-3-methylimidazolium tetrafluoroborate ionic liquids

In the previous chapter, a single-resonance Sellmeier equation was used to model the material dispersion dependence on temperature of several families of ILs. Despite the simplicity of that model, material dispersion was properly described in both spectral and thermal ranges, and some relations of the parameters in the model with the structure of the ILs were established: the UV resonance was independent of the IL and the strength of the resonator was related to the number of carbons in the alkyl chain of the cation.

In this chapter, we would like to expand the spectral range where material dispersion is measured with the objective of gaining further insights into the relation of this magnitude with molecular structure and temperature. As the spectral range is enlarged, our theoretical model has also to be extended. Now, a three-resonance Sellmeier model is used to properly fit the material dispersion over the spectral range considered[249–251]. From the parameters of the fitting, the influence on material dispersion of temperature and structural features, such as the alkyl chain length of the imidazolium cation, is analyzed in detail.

Material dispersion was measured for only one family of ILs, $[C_k\text{mim}][BF_4]$, using RISBI. The spectral range of measurement goes from 300 nm to 1550 nm, and the temperature varies between 293 K and 313 K. Despite only one IL family is considered, the methodology followed here is fairly general and could be applied to characterize other IL families, including those differing in the alkyl chain length of imidazolium[252,253], pyridinium[254,255], pyrrolidinium[256,257] or piperidinium[258] cations or alkylsulfate anions[259,260].

The experimental measurements of material dispersion were complemented with ab initio calculations of electronic polarizability dispersion and absorption spectrum. These wavelength-dependent calculations were used together with a semi-empirical model to faithfully reproduce the experimental material dispersion in both spectral and thermal ranges. To our knowledge, this simple semi-empirical model constitutes the first computational approach for modeling the material dispersion of ILs, fundamental to producing ionic liquids with tailored optical properties.

5.1 Materials

Seven high-purity ILs based on the combination of the 1-alkyl-3-methylimidazolium cation with the tetrafluoroborate anion were studied, $[C_k\text{mim}][BF_4]$ with k = 2, 3, 4, 6, 7, 8 and 10. The ILs were purchased from IoLiTec. Special attention was paid to their transparency, and their water content was checked by titration. Because of the high purity required to perform material dispersion analysis in such a broad spectral range, an upper limit of 700 ppm of water content was established for the measured liquids. ILs presenting water amounts higher than this limit were subjected to a drying process to fit this requirement. The purity and the amount of water in each IL can be consulted in Table 5.1. The densities of the ILs were measured at different temperatures and can be consulted in Table 5.S1 of the Supplementary Material of this chapter.

Table 5.1: List of ILs employed in this chapter, CAS number, purity provided by the supplier and water content.

IL	CAS	Purity/ %	Water/ ppm
$[C_2mim][BF_4]$	143314-16-3	99.1	258
$[C_3mim][BF_4]$	244193-48-4	99.1	343
$[C_4mim][BF_4]$	174501-65-6	99.8	464
$[C_6mim][BF_4]$	244193-50-8	99.9	240
$[C_7mim][BF_4]$	244193-51-9	99.9	296
$[C_8mim][BF_4]$	244193-52-0	99.8	238
$[C_{10}mim][BF_4]$	244193-56-4	99.8	600

5.2 General considerations

Material dispersion of the different ILs at a temperature T = 303 K and within the spectral range from 300 nm to 1550 nm is shown in Fig. 5.1. Refractive index at a certain wavelength increases with the chain length and, for all the liquids, dispersion is normal, with a maximum variation of the refractive index because of wavelength of $5.2 \cdot 10^{-2}$. The refractive indices of the different ILs at selected wavelengths and temperatures are shown in Tables 5.S2, 5.S3 and 5.S4 of the Supplementary Material of this chapter. Because of the broad spectral range addressed, a single resonance Sellmeier equation is not enough to properly describe material dispersion. Fig. 5.2 compares the experimental data of $[C_4mim][BF_4]$ at 303 K with the predictions of the one-resonance model used in the previous chapter and those of the model proposed by Wu et al.[74] Both approaches correctly describe material dispersion in the range from 0.4 μm to 1 μm. Nevertheless, at shorter and longer wavelengths, they clearly diverge from experimental data. Hence, models beyond one resonance have to be considered to describe material dispersion in such a broad spectral range. After performing extensive numerical simulations, we concluded that a

97
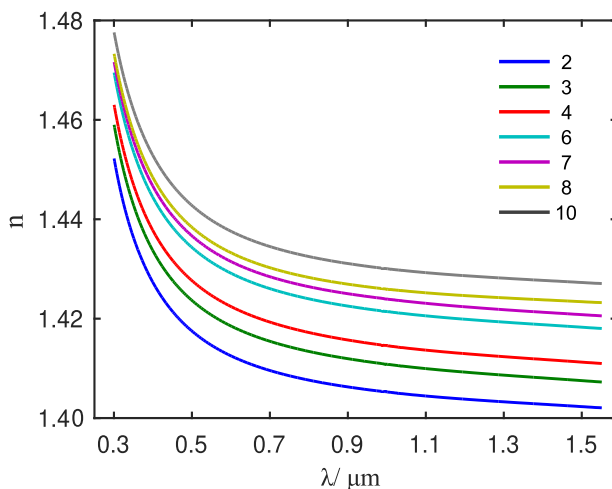
Figure 5.1: Experimental material dispersion of [C$_k$mim][BF$_4$] ILs with k = 2, 3, 4, 6, 7, 8, and 10 in the range from 300 nm to 1550 nm at T = 303 K.

modified three-resonance Sellmeier model provides both accuracy in the dispersion description and a good interpretation of its relation with the molecular structure of the ILs.

5.3 Three-resonance Sellmeier model

A standard three-resonance Sellmeier model has the following analytical expression:

$$n^2(\lambda, k, \mathrm{T}) - 1 = \sum_{i=1}^{3} \frac{c_i(k, \mathrm{T})\lambda^2}{\lambda^2 - \lambda_i^2(k, \mathrm{T})}. \tag{5.1}$$

In this equation, $\lambda_i(k, \mathrm{T})$ represents the wavelength of the resonance i and $c_i(k, \mathrm{T})$ its strength, both depending on the alkyl chain length of the cation, k, and temperature, T. In order to validate this expression, an initial fit was carried out for each liquid at each temperature. From this fit, seed values of $\lambda_i(k, \mathrm{T})$ and $c_i(k, \mathrm{T})$ were obtained and used
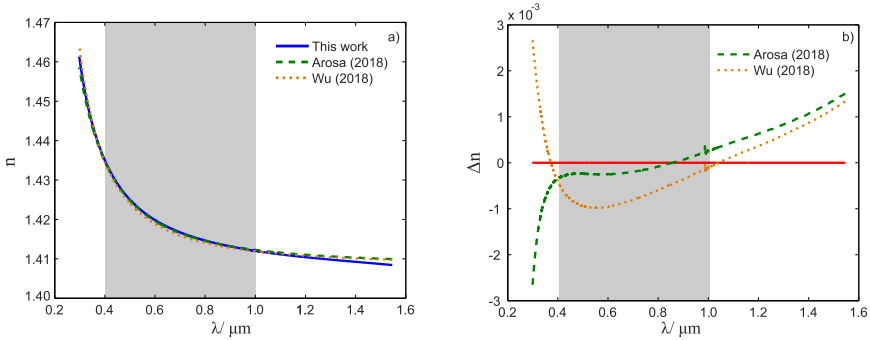
Figure 5.2: (a) Experimental material dispersion of [C$_4$mim][BF$_4$] at 303 K and comparison with one-resonance Sellmeier models proposed by Wu[74] and that of the previous chapter, Arosa.[261] The grey area marks the validity of the spectral range of these models. (b) Absolute deviations of each model with respect to experimental data.

to perform a more sophisticated fit to Eq. (5.1). In this process, we discovered that the position of the resonances λ_i is almost independent of temperature and alkyl chain length. Two of them were placed in the UV region, while, the third one, is located in the IR region, very far from our measurement region, $\lambda_{IR} \approx 50 \ \mu$m » λ. In the event of a resonance placed very far and at larger wavelengths than the measuring range, the following approximation can be made:

$$\frac{c_i\lambda^2}{\lambda^2 - \lambda_i^2} \approx -\frac{c_i}{\lambda_i^2}\lambda^2 = d_i\lambda_i^2. \tag{5.2}$$

Introducing Eq. (5.2) into Eq. (5.1) and taking into account that the position of the resonances is independent of temperature and alkyl chain length, we obtain the three-resonance Sellmeier model of this chapter:

$$n^2(\lambda, k, \text{T}) - 1 = \frac{c_1(k, \text{T})\lambda^2}{\lambda^2 - \lambda_1^2} + \frac{c_2(k, \text{T})\lambda^2}{\lambda^2 - \lambda_2^2} + d_3(k, \text{T})\lambda^2. \tag{5.3}$$

99

5.4 Temperature dependence of material dispersion

In order to study the temperature influence on the material dispersion within the framework of our model, the experimental data of each IL was separately fitted to Eq. (5.3) by means of a two-step procedure:

1. Experimental curves are fitted to Eq. (5.3) without imposing any constraint. Hence, a pair of values λ_1 and λ_2 is obtained for each liquid and temperature.

2. A second fit is implemented constraining the values of λ_1 and λ_2 to be constant, and using the mean values from the previous fit as a seed.

For the seven ILs, the trends of the strength of the resonances with temperature were found to be similar. In Fig. 5.3, that for the $[C_{10}mim][BF_4]$ is shown. As in the previous chapter, temperature is expressed with respect to the center of the measured interval, $T_0 = 303$ K. The c_1 coefficient clearly presents a linear dependence on temperature, its slope is negative and, in accordance with the previous chapter, closely related to the thermo-optical coefficient. The rest of the coefficients do not show any evident trend with temperature. Hence, we chose to make a new fit for each IL in which we forced c_2 and d_3 to be temperature-independent and c_1 to vary linear with temperature, $c_1 = c_1' + c_1''\Delta T$:

$$n^2(\lambda, T) - 1 = \frac{(c_1' + c_1''\Delta T)\lambda^2}{\lambda^2 - \lambda_1^2} + \frac{c_2\lambda^2}{\lambda^2 - \lambda_2^2} + d_3\lambda^2 \qquad (5.4)$$

The fitting parameters of Eq. (5.4) for all the studied liquids are presented in Table 5.2 together with the deviation of the model with respect to experimental values, σ. According to the value of the different strengths, the resonance with the major contribution to refractive index is that placed at the shortest wavelength of the UV
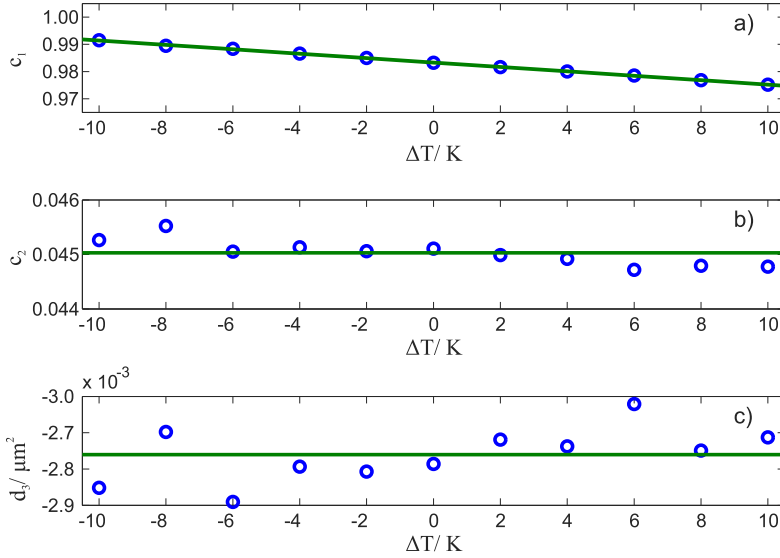
Figure 5.3: Temperature dependence of the resonance strengths of $[C_{10}mim][BF_4]$ with respect to the center of our measuring interval, $T_0 = 303$ K. (a) c_1 and a linear regression on ΔT, (b) c_2 and its average value. (c) d_3 and its average value.

Table 5.2: Parameters and standard deviation of the temperature-dependent Sellmeier fit of Eq. (5.4) to the material dispersion of each IL.

Ionic Liquid	$\lambda_1/$ μm	c_1'	$c_1''/$ $10^{-4}\,\mathrm{K}^{-1}$	$\lambda_2/$ μm	$c_2/$ 10^{-2}	$d_3/$ $10^{-3}\,\mu\mathrm{m}^{-2}$	$\sigma/$ 10^{-5}
$[C_2mim][BF_4]$		0.9079	-71.0		5.09	-1.7	4.7
$[C_3mim][BF_4]$		0.9234	-76.2		5.17	-2.3	6.4
$[C_4mim][BF_4]$		0.9356	-73.5		5.10	-3.2	4.8
$[C_6mim][BF_4]$	0.0944	0.9556	-79.5	0.2033	4.89	-2.3	4.7
$[C_7mim][BF_4]$		0.9641	-78.6		4.71	-1.9	5.8
$[C_8mim][BF_4]$		0.9684	-81.4		4.73	-1.5	4.2
$[C_{10}mim][BF_4]$		0.9821	-84.6		4.57	-1.9	4.7

spectrum, λ_1. The relative contribution of the second UV resonance, λ_2, is less than 10%, while the contribution of the IR resonance is residual, less than 1%. The most relevant feature in Table 5.2 is that the coefficient c_1 increases with the cation alkyl chain length with the same functional form that refractive index at a fixed wavelength does. This behavior can be observed in Fig. 5.4, where c_1 and refractive index at the sodium D line, n_D, are shown as a function of the alkyl chain length. The asymptotic trend that both magnitudes show has already been pointed out by previous authors[94,245] and also analyzed in the previous chapter.
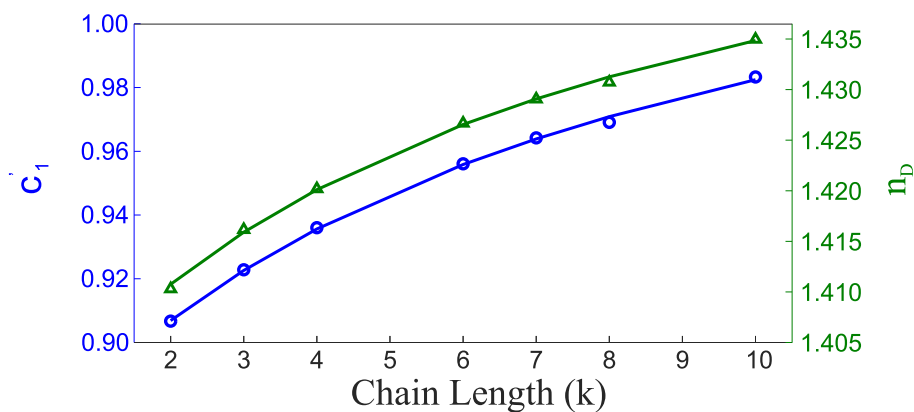
Figure 5.4: Refractive index at the D line, n_D, and the fitting coefficient c_1' as a function of the alkyl chain length.

5.5 Alkyl chain length dependence of material dispersion

The material dispersion dependence on the alkyl chain length, k, is addressed in terms of molar refractivity, $R(k, \lambda)$. Since it is a practically temperature-independent magnitude, as demonstrated in the previous chapter, this approach provides a way to carry out a

temperature independent analysis of the influence of the alkyl chain length in dispersion. Assuming that molar refractivity dispersion obeys a functional form similar to that of material dispersion in Eq. (5.3), it is possible to describe it in terms of a three-resonance Sellmeier dispersion rewritten in terms of molar refractivity:

$$R(k, \lambda) = \frac{c_1 \lambda^2}{\lambda^2 - \lambda_1^2} + \frac{c_2 \lambda^2}{\lambda^2 - \lambda_2^2} + d_3 \lambda^2. \qquad (5.5)$$

Experimental molar refractivity dispersion, $R(k, \lambda)$, can be obtained from the experimental material dispersion by using the molar volumes obtained throughout the experimental densities in Table 5.S1 and the Lorentz-Lorenz equation expressed in terms of molar refractivity:

$$\frac{R(k, \lambda)}{V_m(k, \mathrm{T})} = \frac{n^2(k, \lambda, \mathrm{T}) - 1}{n^2(k, \lambda, \mathrm{T}) + 2}. \qquad (5.6)$$

In the following, the analysis is carried out at the center of our temperature interval, the reference temperature T_0 = 303 K. The first step to understand the molar refractivity dispersion dependence on the alkyl chain length is analyzing it at specific wavelengths, Fig. 5.5. Molar refractivity is a linear function of the alkyl chain length independently of the considered wavelength, as well as molar volume. The linear dependence of $R(k, \lambda)$ and $V_m(k, \mathrm{T})$ on the alkyl chain length permits express them as a function of the number of carbons in the alkyl chain, k:

$$V_m(k, \mathrm{T}) = V_0(\mathrm{T}) + k \cdot V_{alkyl}(\mathrm{T}), \qquad (5.7)$$

$$R(k, \lambda) = R_0(\lambda) + k \cdot R_{alkyl}(\lambda). \qquad (5.8)$$

Eq. (5.7) shows that there is a minimum volume for our family of ILs, $V_0(\mathrm{T})$, which corresponds to that of the 1-methylimidazolium tetrafluoroborate, $[C_0\text{mim}][BF_4]$. This minimum volume increases by an amount $V_k(\mathrm{T})$ for each CH_2 unit added to the $[C_0\text{mim}]^+$ cation as a cylinder that increases its length. Regarding Eq. (5.8), there is

USC
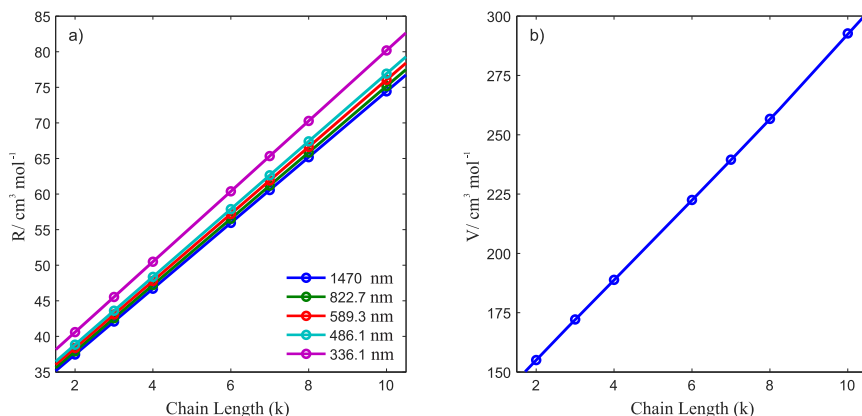
Figure 5.5: (a) Molar refractivity at different spectral lines and (b) molar volume, both as a function of the alkyl chain length.

a minimum molar refractivity, $R_0(\lambda)$, which corresponds to that of [C_0mim][BF_4], and it increases in steps of $R_{alkyl}(\lambda)$ for each CH_2 unit added. This linear trend is closely related to that of electronic polarizability, which approximately increases linearly with the number of atoms in a molecule. [235,245]

The linear growth of both $V_m(k, T)$ and $R(k, \lambda)$ with the alkyl chain length together with Eq. (5.6) indicates that there are both an upper ($k \to \infty$) and a lower ($k \to 0$) limit for the refractive index of families of ILs differing in the length of an alkyl chain. [245] Assuming that both $R_0(\lambda)$ and $R_{alkyl}(\lambda)$ verify a dispersion equation similar to that given by Eq. (5.5), it is possible to model molar refractivity dispersion in terms of two independent contributions, one arising from [C_0mim][BF_4] and the other from the alkyl chain length. For doing that:

1. $R(k, \lambda)$ is fit at each wavelength to a linear function with respect to the alkyl chain length, k. Dispersion curves of $R_0(\lambda)$ and $R_{alkyl}(\lambda)$ are obtained.

USC
UNIVERSIDADE
DE SANTIAGO
DE COMPOSTELA

104

2. Both $R_0(\lambda)$ and $R_{alkyl}(\lambda)$ are separately fit to Eq. (5.5).

Fig. 5.6 shows $R_0(\lambda)$ and $R_{alkyl}(\lambda)$ dispersion and the deviation of the model with respect to experimental data. The fitting parameters are shown in Table 5.3. The strengths of the resonances are very different
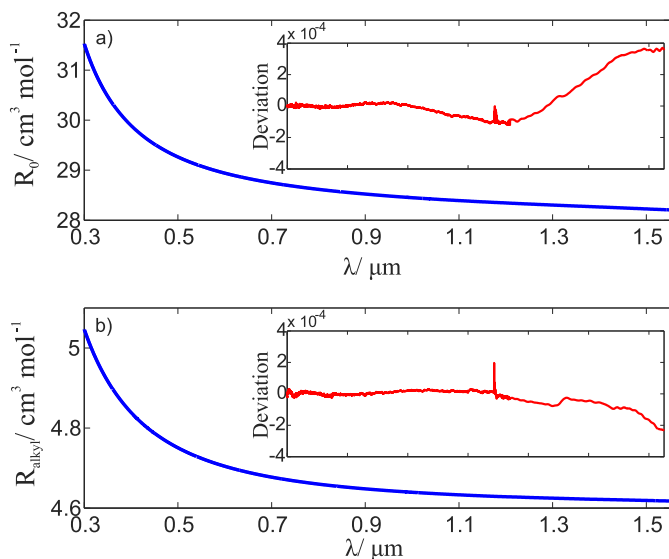
Figure 5.6: Molar refractivity dispersion of (a) $R_0(\lambda)$ and (b) $R_{alkyl}(\lambda)$. The insets show in each case the absolute deviation of the experimental curves from the dispersion described by Eq. (5.5).

Table 5.3: Parameters and standard deviation of the coefficients of the fit of the temperature dependent Sellmeier model given by Eq. (5.5) to the material dispersion of each IL.

	$\lambda_1/\,\mu m$	$\lambda_2/\,\mu m$	$c_1/\,cm^3\,mol^{-1}$	$c_2/\,cm^3\,mol^{-1}$	$d_3/\,cm^3\,mol^{-1}\mu m^{-2})$
$R_0(\lambda)$	80.6	206.7	27.0630	1.2408	-0.0858
$R_{Alkyl}(\lambda)$	84.6	183.5	4.5162	0.0883	0

for R_0 and R_{alkyl}, being those associated to R_0 much more intense

105

than those of R_{alkyl}. This difference is not strange since R_0 contains the contribution of the [C_0mim][BF$_4$] while R_{alkyl} only contains the contribution of a CH$_2$ unit. Nevertheless, as the influence of R_{alkyl} grows linearly with the number of carbons in the alkyl chain, the exact balance between both strengths depends on the alkyl chain length considered. Interestingly, the influence of the IR resonance d_3 on R_{alkyl} was found to be negligible, less than $8 \cdot 10^{-5}$ in the whole spectrum. In consequence, we forced it to be 0 in the fitting to Eq. (5.5). The negligible value of the IR resonance means that the dispersion in the IR range is not influenced by the alkyl chain of the imidazolium cation.

Other very interesting feature to analyze is the reason why the resonance positions for R_0 and R_{alkyl} do not coincide. In the case of the resonance λ_1, the separation of the resonances is only 4.0 nm while in the case of λ_2, it is much larger, 23.2 nm. In order to explain the differences in the positions of the resonances, the absorption spectrum of different parts of the [C_4mim][BF$_4$] IL was simulated by DFT and shown in Fig. 5.7. For the resonance λ_1, two values are found from
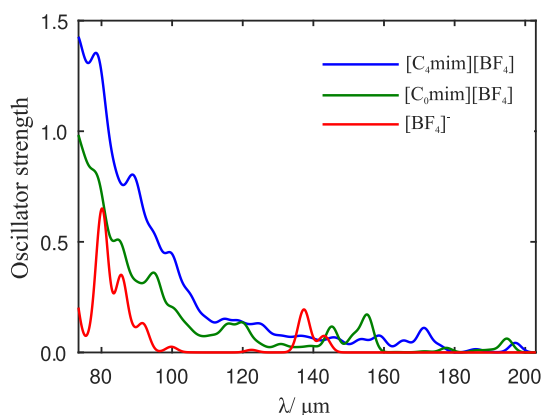
Figure 5.7: Simulated absorption spectrum from different parts of the IL: [C$_4$mim][BF$_4$], [C$_0$mim][BF$_4$] and [BF$_4$]$^-$.

the fittings, 80.6 nm for R_0 and 84.6 nm for R_{alkyl}. It is clear upon analyzing the simulated absorption spectra that [C$_4$mim][BF$_4$] presents

two strong absorption peaks around these wavelengths, one at 78.5 nm
and the other at 88.9 nm. These peaks present a certain contribution
from the $[BF_4]^-$ anion and they appear in both the $[C_4mim][BF_4]$ and
$[C_0mim][BF_4]$ absorption spectra. The fact that the fitting in terms
of R_0 and R_{alkyl} detects one peak or the other suggests that there are
different influences of the alkyl chain length in both peaks.

Regarding λ_2 resonance of R_0, it could be attributed to the
clear absorption peak shown by Fig. 5.7 at around 197 nm, which
is unequivocally associated with the imidazolium ring of the
$[C_0mim][BF_4]$ part of the IL. On the other hand, the λ_2 resonance found
at 183.5 nm for R_{alkyl} could correspond to the complex structure found
in the region from 159 nm to 177 nm, probably associated with the alkyl
chain. With the purpose of obtaining a deeper insight into the behavior
of the resonances with the alkyl chain length, the absorption spectra of
some members of the family of ILs studied were calculated and plotted
in Fig.5.8. In the first place, the absorption peak placed at 200 nm
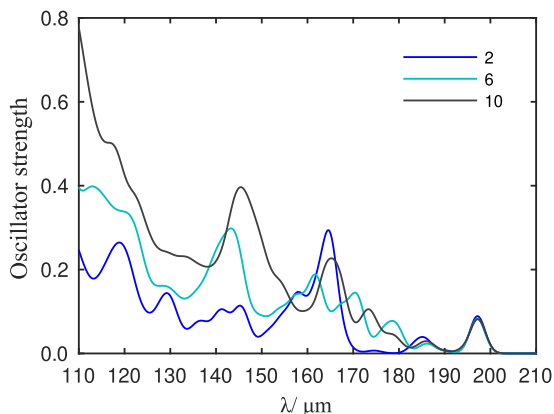
Figure 5.8:   Simulated absorption spectra for the family of ILs $[C_kmim][BF_4]$ with
k = 2, 6 and 10.

does not change in shape or position upon carbon increase, behavior
expected for a resonance independent of the alkyl chain length. Hence,
it reinforces our association of this peak with the imidazolium ring

107

of [C$_0$mim][BF$_4$] and with the λ_2 resonance of R_0. Moreover, in the range from 140 nm to 175 nm, there are a number of peaks that are strongly dependent both in strength and position on the alkyl chain. This complex structure is probably related to the λ_2 resonance of R_{alkyl} at 183.5 nm whose exact position we were not able to exactly reproduce because of the simplicity of our model. Finally, in the short wavelength region, there is a very evident increase of the strength of the absorption peaks with the number of carbons in the alkyl chain, which suggests a probable increase of the strength of the λ_1 resonance of R_{alkyl} with them.

5.6 Prediction of the material dispersion of ILs

It has been stated before that the refractive index of a material can be related to its molar refractivity and molar volume through the Lorentz–Lorenz equation, Eq. (5.6). Refractive index depends on temperature and wavelength. However, molar refractivity could be considered as a temperature independent magnitude. Hence, under this approach, temperature dependence of refractive index must exclusively arise from the implicit temperature dependence of the molar volume $V_m(T) = M/\rho(T)$. Moreover, since the molar volume is a wavelength independent magnitude, refractive index dependence on wavelength must exclusively come from the dependence of $R(\lambda)$ on wavelength. Hence, the Lorentz–Lorenz equation describes the refractive index dependence on temperature and wavelength as arising from the product of two totally independent magnitudes: molar volume, only depending on temperature, and molar refractivity, only depending on wavelength:

$$\frac{n^2(\lambda, T) - 1}{n^2(\lambda, T) + 2} = \frac{R(\lambda)}{V_m(T)} = K_\lambda(\lambda) K_T(T). \qquad (5.9)$$

Eq. (5.9) can be exploited to predict the material dispersion of ILs at any temperature if the molar refractivity dependence on wavelength and molar volume dependence on temperature are known.

Molar refractivity can be estimated by calculating the electronic polarizability by standard ab initio calculations, as routinely performed by other authors.[97,244,262,263] Often, these calculations are carried out in the limit of a static field and the information about the wavelength dependence (dispersion) of the electronic polarizability is lost. Nevertheless, there are ab initio strategies to predict this wavelength dependence, such as that of the CPHF theory.[264]

Regarding molecular volume, it can be calculated through DFT or molecular dynamics (MD) simulations. However, despite both computational approaches provide qualitatively good results, the small relative deviations with respect to experimental values[244,265,266] have a deep impact in the refractive index prediction. Notwithstanding, the wide available database of experimental densities of ILs could be used to study the refractive index of ILs that were not optically characterized.

In order to analyze the ability of Eq. (5.9) to predict refractive index dispersion, we simulated the electronic polarizability of the $[C_k mim][BF_4]$ family at thirteen different wavelengths, from 300 nm to 1500 nm, in steps of 100 nm by means of CPHF and the B3LYP/6-311++G(d,p) level of theory.

From electronic polarizability, molar refractivity can be readily calculated and compared with experimental molar refractivity at a fixed temperature, Fig. 5.9. The CPHF calculation is able to approximately reproduce the experimental molar refractivity dispersion with a root mean square (RMS) relative deviation that ranges from $3.9 \cdot 10^{-3}$ ($k = 4$) to $1.15 \cdot 10^{-2}$ ($k = 8$). For all the ILs, the deviation is similar for most of the wavelengths except for the region of shortest wavelengths. In these regions, there is a strong change in the curvature of the deviation, which could be produced by the worst performance of the CPHF method as the simulation gets closer to the position of the UV resonances. On the other hand, the sign of the deviations in almost the whole spectra depends on the alkyl chain length. For compounds with $k < 4$, the trend is to underestimate the molar refractivity, which means that our calculations predict a lower electronic polarizability than the

experimental one. In contrast, for $k > 4$, the trend is the opposite and there is a clear trend to overestimate the electronic polarizability. In
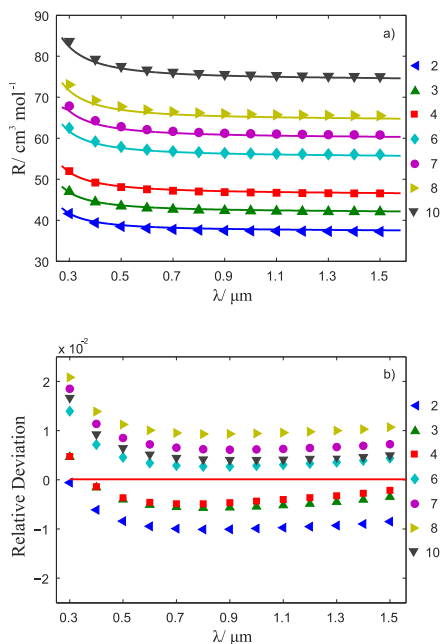
Figure 5.9: (a) Experimental molar refractivity dispersion (solid line) and simulated molar refractivity dispersion (markers) at 303 K for the 7 analyzed ILs. (b) Relative deviation of the simulated data points from the experimental values.

order to obtain a closer insight into this phenomenon, we compared the performance of the level of theory in our simulations with the experimental results as a function of both alkyl chain length and wavelength. The simulated molar refractivity is, as the experimental one, linear upon addition of CH_2 units. Hence, the difference between both magnitudes, $\Delta R = R_{exp} - R_{sim}$, is also a linear function of the number of carbons in the alkyl chain:

$$\Delta R = \Delta R_0(\lambda) + k \cdot \Delta R_{alkyl}. \qquad (5.10)$$

In this equation, ΔR_0 is the error in predicting the molar refractivity in the limit of having a zero carbon alkyl chain, [C_0mim][BF_4]. On the other hand, ΔR_{alkyl} describes the error in estimating the contribution to molar refractivity of the CH_2 units. Fig. 5.9 shows both ΔR_0 and ΔR_{alkyl} as a function of the wavelength.

The error in the prediction of molar refractivity comes from an interesting balance between ΔR_0 and ΔR_{alkyl}. The molar refractivity of ΔR_0 is always underestimated, while the molar refractivity of ΔR_{alkyl} is always overestimated and its influence grows with the length of the alkyl chain. The mean value of ΔR_{alkyl} in the whole spectral range is 0.13 $cm^3 \cdot mol^{-1}$ while the mean value of ΔR_0 is -0.53 $cm^3 \, mol^{-1}$. Thus, at $k = |\frac{\Delta R_0}{\Delta R_{alkyl}}| \approx 4.08$, the errors in both components are compensated and the overall error is minimum. In consequence, for $k > 4$ the molar refractivity is overestimated because of the overestimation associated with ΔR_{alkyl} dominates over the underestimation provided by ΔR_0. Regarding the error as a function
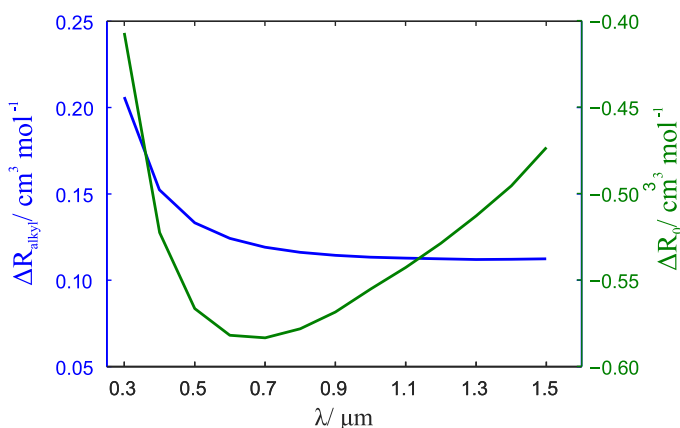
Figure 5.10: Fitting parameters of a linear fit at different wavelengths of $\Delta R = R_{exp} - R_{sim}$ to the number of carbons, k, in the alkyl chain of each compound.

of the wavelength, ΔR_0 presents a very dispersive behavior with a

variation in the whole spectral range of 0.17 cm^3 mol^{-1}. On the other hand, ΔR_{alkyl} presents a much less dispersive behavior and its variation in the spectral range is 0.10 cm^3 mol^{-1}, the most important contribution (0.054 cm^3 mol^{-1}) being made in the step from 400 nm to 300 nm. Thus, from the spectral point of view, the deviation contribution of the alkyl chain is very achromatic (except for 300 nm) and the main contribution to the chromatic error is provided by the limitations in the calculation of the dispersive response of the [C$_0$mim][BF$_4$] unit.

According to our model, Eq. (5.9), merging the computationally obtained electronic polarizability dispersion with the experimental density we measured, it is possible to predict the refractive index over the whole thermal and spectral ranges, Fig. 5.11. The RMS of the
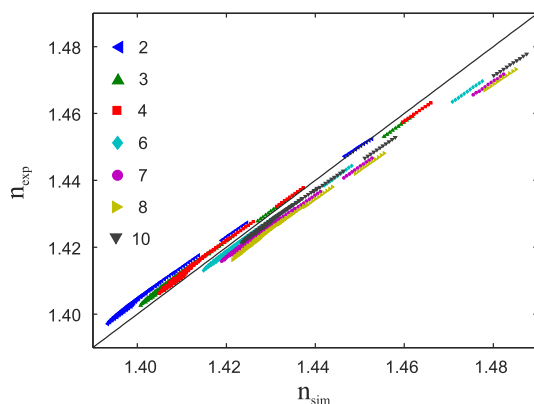
Figure 5.11: Simulated refractive index, n_{sim}, versus experimental refractive index, n_{exp} for the ILs. The shown refractive indices belong to all the simulated wavelengths, from 300 nm to 1500 nm in steps of 100 nm, and temperatures, from 293 K to 313 K in steps of 2 K.

simulated data with regard to the experimental one, considering all the wavelengths and temperatures, is less than $4 \cdot 10^{-3}$. For each IL, the difference between both predicted and experimental refractive indices is uniform in the thermal and spectral ranges with the exception of the shortest wavelengths, 300 nm. Hence, the model reflects

the temperature effect on refractive index in a proper way and the main deviations arise from the limitations in the prediction of the dispersive component of the refractive index (especially at the shortest wavelengths).

Comparing the performance of our refractive index prediction method with other published approaches,[245,267,268] we obtain similar or better relative deviations despite using a much simpler strategy. However, there are some differences that are worth to note. The previous models are only able to predict the refractive index at the sodium D line while our approach provides refractive indices in a wide spectral and thermal range. On the other hand, the previous works studied a much wider range of ILs while we restricted our analysis only to the $[C_k\text{mim}][\text{BF}_4]$ family.

5.7 Conclusions

Material dispersion of ILs can be modeled by means of Sellmeier formulas with different number of resonances. An intelligent selection of the Sellmeier formula allows relating the fitting parameters with structural factors of the studied ILs as well as with their thermal response. On the other hand, expressing the Lorentz-Lorenz equation in terms of molar refractivity, allows separating the thermal and dispersive contributions to material dispersion in two independent components. This separation opens a way to predict the material dispersion of ILs by means of ab initio calculations of the electronic polarizability together with the use of experimental or computational volumes. This approach for predicting material dispersion was tested with the family of ILs addressed in this work and RMS below than $4 \cdot 10^{-3}$ were obtained. The main contribution to the error in this semi-empirical model is not the temperature description, but the limitations in the prediction of the electronic polarizability dispersion. In consequence, the best performance could be obtained by employing a higher level of theory in the electronic polarizability dispersion calculation.

5.8 Acknowledgments

5.9 Supplementary material

In this section the supplementary material corresponding to this chapter can be consulted, including experimental densities, and refractive indices at selected wavelengths and temperatures.

Table 5.S1: Experimental densities in g/cm^3 of the selected ILs at 11 different temperatures.

ρ (g/cm^3)							
T/ K	[C$_2$mim][BF$_4$]	[C$_3$mim][BF$_4$]	[C$_4$mim][BF$_4$]	[C$_6$mim][BF$_4$]	[C$_7$mim][BF$_4$]	[C$_8$mim][BF$_4$]	[C$_{10}$mim][BF$_4$]
293	1.284358	1.238723	1.204041	1.148754	1.126412	1.105994	1.066633
295	1.282830	1.237252	1.202615	1.147344	1.125030	1.104628	1.065257
297	1.281303	1.235780	1.201193	1.145930	1.123640	1.103250	1.063879
299	1.279776	1.234306	1.199769	1.144513	1.122252	1.101871	1.062504
301	1.278257	1.232833	1.198353	1.143160	1.120861	1.100490	1.061129
303	1.276741	1.231365	1.196937	1.141802	1.119475	1.099112	1.059756
305	1.275226	1.229899	1.195519	1.140441	1.118134	1.097730	1.058382
307	1.273712	1.228434	1.194140	1.139080	1.116799	1.096369	1.057007
309	1.272196	1.226969	1.192694	1.137711	1.115456	1.095046	1.055636
311	1.270689	1.225511	1.191276	1.136346	1.114119	1.093716	1.054265
313	1.269186	1.224050	1.189870	1.134985	1.112780	1.092389	1.052892

Table 5.S2: Experimental refractive index at selected wavelengths at T=293 K.

IL	336.1 nm	486.1 nm	589.0 nm	633 nm	822.7 nm	1470 nm
[C$_2$mim][BF$_4$]	1.4398	1.4185	1.4129	1.4114	1.4073	1.4025
[C$_3$mim][BF$_4$]	1.4465	1.4247	1.4190	1.4173	1.4130	1.4077
[C$_4$mim][BF$_4$]	1.4505	1.4284	1.4229	1.4123	1.4168	1.4114
[C$_6$mim][BF$_4$]	1.4571	1.4353	1.4296	1.4280	1.4236	1.4184
[C$_7$mim][BF$_4$]	1.4594	1.4377	1.4319	1.4303	1.4261	1.4210
[C$_8$mim][BF$_4$]	1.4611	1.4394	1.4337	1.4321	1.4279	1.4235
[C$_{10}$mim][BF$_4$]	1.4655	1.4438	1.4380	1.4364	1.4321	1.4274

Table 5.S3: Experimental refractive index at selected wavelengths at T=303 K.

IL	336.1 nm	486.1 nm	589.0 nm	633 nm	822.7 nm	1470 nm
$[C_2mim][BF_4]$	1.4372	1.4159	1.4103	1.4088	1.4047	1.3999
$[C_3mim][BF_4]$	1.4435	1.4219	1.4162	1.4146	1.4104	1.4052
$[C_4mim][BF_4]$	1.4477	1.4260	1.4202	1.4186	1.4143	1.4089
$[C_6mim][BF_4]$	1.4541	1.4324	1.4267	1.4251	1.4209	1.4158
$[C_7mim][BF_4]$	1.4563	1.4348	1.4291	1.4275	1.4233	1.4185
$[C_8mim][BF_4]$	1.4581	1.4635	1.4308	1.4292	1.4250	1.4204
$[C_{10}mim][BF_4]$	1.4263	1.4407	1.4350	1.4334	1.4292	1.4244

Table 5.S4: Experimental refractive index at selected wavelengths at T=313 K.

IL	336.1 nm	486.1 nm	589.0 nm	633 nm	822.7 nm	1470 nm
$[C_2mim][BF_4]$	1.4346	1.4133	1.4078	1.4062	1.4201	1.3972
$[C_3mim][BF_4]$	1.4405	1.4190	1.4135	1.4119	1.4078	1.4028
$[C_4mim][BF_4]$	1.4449	1.4233	1.4176	1.4160	1.4117	1.4064
$[C_6mim][BF_4]$	1.4511	1.4295	1.4239	1.4223	1.4181	1.4132
$[C_7mim][BF_4]$	1.4533	1.4319	1.4263	1.4247	1.4206	1.4159
$[C_8mim][BF_4]$	1.4551	1.4335	1.4279	1.4263	1.4221	1.4174
$[C_{10}mim][BF_4]$	1.4592	1.4377	1.4320	1.4304	1.4262	1.4214

6. An optical approach to ionic liquid crystals

[a] Grupo de Nanomateriais, Fotónica e Materia Branda, Departamentos de Física Aplicada e de Física de Partículas, Universidade de Santiago de Compostela.

[b] Departamento de Química Orgánica, Universidade de Vigo.

[c] Departamento de Física e Ciencias da Terra, Universidade da Coruña

In the previous chapters, we have experimentally studied the material dispersion of several families of imidazolium-based ionic liquids. Those ILs considered up to the moment are macroscopically isotropic liquids, i.e., the spatial dimensions of the microheterogeneities of their nanostructurated bulk are much smaller than those of the wavelengths considered. Nevertheless, there are ILs whose nanostructurated bulk reaches dimensions comparable to those of the wavelengths of the visible light, which provides them with macroscopic anisotropic character. In other words, some ILs are also liquid crystals.[141–144,269,270] This chapter is devoted to provide an optical perspective to this subset of ILs known as Ionic Liquid Crystals (ILCs).

ILCs can show mesomorphic behavior on their own[146,147] or in the presence of water, both in solution[271,272] or just under limited hydration.[273] The behavior of ILCs can be tuned by properly choosing the combination of cation and anion. However, usually, the mesogenic character is tailored by means of the cation.[106,274–276] An easy way to obtain mesogenic cations is increasing the length of the alkyl chains

attached to the widespread imidazolium cation in combination with the appropriate anion.[146,147] However, new and more sophisticated approaches have been developed recently such as attaching mesogenic radicals to imidazolium or similar cations[111,112,275,276] or introducing these cations as a part of larger structures.[84] Furthermore, there is also an intense activity in the design of new families of intrinsically mesogenic cations.[106,274] The anion influence on the mesogenic character of ILCs is also the focus of some studies,[277] and it is well-known that some anion families promote the liquid crystal behavior, while others could prevent it.[147] In particular, the alkylsulfate family of anions, showing an important surfactant character,[278] has demonstrated a high aggregation ability when forming part of ILs dissolved in water. It drives the formation of micelles[259,279,280] and it is often combined with mesogenic cations to facilitate the achievement of ILCs.[106,274,275,281] Furthermore, it has shown to act as an anionic mesogen when paired to weakly mesogenic cations in cases where small amounts of water are present.[83,272]

The election of the proper cation and anion pair not only produces liquid crystalline behavior in the tailored IL, but also allows choosing the desired liquid crystal phase. For instance, despite the smectic lamellar (SmA) phases are the most common ones,[106,274–277] hexagonal smectic (SmB) phases,[282] columnar rectangular (Col_r) phases,[84] columnar hexagonal (Col_h) phases[84,111,112] or, even, bicontinuous cubic (Cub_{bi}) phases[283] have been obtained by carefully choosing the ILC components.

Further tailoring of the mesogenic cation as well as a smart choosing of its counterion can provide even more interesting tailored properties. For instance, several groups have used luminescent mesogenic cations to create ILCs with tunable luminescence.[84,106,284] The same effect has been obtained by pairing a mesogenic non luminescent cation with a luminescent anion taking advantage of the extra degree of freedom provided by the anion.[111,112] In addition, tailored luminescence can be obtained by replacing the molecular anions by negatively charged luminescent complexes[108,285] or by directly doping the ILCs with

them.[107] The extra degree of freedom provided by the anion can be exploited for obtaining ILCs not only owing tunable luminescence but also owing other designed properties such as photochromism.[286]

Regardless of the evident growth of interest in the photonic properties of ILCs, not all the optical properties of these materials have attracted the same attention. Refractive properties of ILCs such as birefringence dispersion or material dispersion have received little attention despite their importance in common liquid crystal applications including spatial light modulators, displays, tunable spectral filters, phase modulators, polarization controllers or optical shutters.[287]

Some of the scarce examples of refractive studies in ILCs are found in the work of Schlick et al.,[128] who studied the birefringence induced in the isotropic phase of two ILCs because of the electro-optic Kerr effect, or that of Venkatesh et al.,[288] who measured the material dispersion of the average refractive index of several ILCs by Abbe refractometry.

In this chapter, as it has been previously set forth, the aim is to perform an optical study of ILCs. We have chosen the ILC 1-ethyl-3-methylimidazolium decylsulfate $[C_2mim][C_{10}SO_4]$ as a case study. In the following lines we analyze in detail the structure of this liquid, the impact of the structure in its optical properties and we provide, for the first time, to the best of our knowledge, measurements of the neat birefringence dispersion of an ILC.
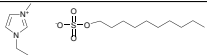
6.1 Materials

1-Ethyl-3-methylimidazolium decylsulfate $[C_2mim][C_{10}SO_4]$ is an IL composed by an imidazolium cation owning two short alkyl chains and an alkylsulfate anion containing a ten carbons alkyl chain, Table 6.1. It is an isotropic liquid in its neat condition, but it becomes an ionic liquid crystal in contact with water due to self-assembly. In the lyotropic liquid crystal phase, it takes the form of a stable birefringent hydrogel with water mass fractions ranging from 0.04 to 0.4 at ambient temperature.

USC
UNIVERSIDADE
DE SANTIAGO
DE COMPOSTELA

The sample used in this chapter was synthesized and purified following the procedure described in Ref. [83]. The chemical precursors were used without further purification and bought from different commercial distributors: 1-methylimidazolium and 1-decanol (Sigma-Aldrich, 0.99 mass purity), methanesulfonic acid (Aldrich, anhydrous), tert-butyl methyl ether (Panreac, 0.995 mass purity), toluene (Merck 0.99 mass purity), and diethyl sulfate (Fluka, 0.99 mass purity). The mass purity of the intermediate compound 1-ethyl-3-methylimidazolium ethylsulfate was checked to be > 0.99 by ^{1}H NMR and ^{13}C NMR analysis and the spectra compared with previously published data. The final product 1-ethyl-3- methyimidazolium decylsulfate mass purity was checked to be > 0.99 by ^{1}H NMR and high resolution mass spectroscopy (MS).

The liquid crystal properties studied in this chapter were measured in samples saturated with water by atmospheric absorption under laboratory conditions (295 K, 1012 hPa and relative humidity 58%), i.e., they contain water mass fractions of 0.042 or, equivalently, a molar fraction of water of $x_{water} = 0.46$. Further information about the specific techniques and methodologies followed in this chapter, can be found in the chapter of Experimental methods of this thesis.

Table 6.1: Specifications of the $[C_2mim][C_{10}SO_4]$ sample.

IL	Abbreviation	Chemical Structure
1-ethyl-3-methylimidazolium decylsulfate	$[C_2mim][C_{10}SO_4]$	
Molecular Mass /g mol^{-1}	Mass fraction purity	Water mass fraction in saturation
348.45	> 0.99 H^{1}NMR and MS	0.042

6.2 Phase transitions and DSC

In order to characterize the phase transitions of our $[C_2mim][C_{10}SO_4]$ hydrated sample, a set of Differential Scanning Calorimetry (DSC) experiments were carried out and compared with those of a dried one, Fig. 6.1. The applied thermal cycles were the following ones:

1. From 303 K to 323 K with a 1 K/min ramp to detect the clearing point or the fusion from liquid crystal mesophase to isotropic liquid phase.

2. From 323 K to 193 K at 5 K/min ramp to detect the hydrated sample solidification point.

3. From 193 K to 353 K at 5 K/min ramp to establish the hydrated sample melting point.

4. From 353 K to 398 K at 20 K/min and, after that, an isotherm for 45 min at 398 K to evaporate the water contained in the sample.

5. From 398 K to 193 K at 10 K/min to determine the solidification point of the dried sample.

6. From 193 K to 373 K at 10 K/min to find the dried sample melting point.

The transition from the liquid crystal phase to the isotropic liquid phase, known as clearing point, is found at 309 K, coinciding with the value reported in Ref. [83] at the same water concentration. Hence, the thermal range of existence of the mesophase is from this temperature, 309 K, to that found in the cooling cycle for the solidification point, 233 K.

Interestingly, in the cooling cycle of the hydrated sample, not just a single solidification point is observed, but a two-step solidification

121
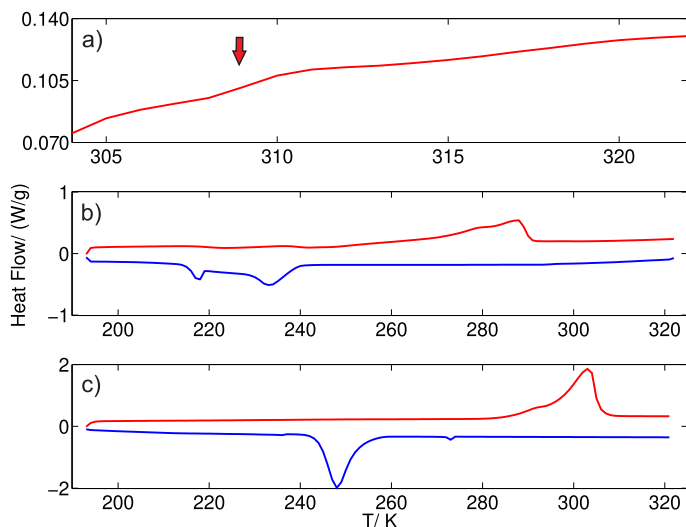
Figure 6.1: Thermograms of the sample at several heating ramps and hydration conditions. Heating ramps are in positive heating flow values while cooling ramps are in negative heating flow values. (a) Heating of the hydrated sample (0.042 water mass fraction) at 1 K/ min. The arrow highlights the transition between the ILC state and the isotropic liquid state (clearing point). (b) Cooling and heating cycle of the sample at 5 K/min. (c) Cooling and heating cycle of the sample at 10 K/min after applying an isotherm of 398 K during 45 min for dehydrating the sample.

process at temperatures 233 K and 217 K is visible. This kind of two-step solidification procedure is often associated to the difficulties of ILs, as glass-former materials, to crystallize during DSC cooling ramps because of their large number of conformational degrees of freedom.[16] On the other hand, only one melting point appears at 288 K in the heating cycle. This large difference between the solidification points and the melting point, $\Delta T = 55$ K, is usual in the thermal behavior of ILs.[16,289]

With respect to the dried sample, solidification happens upon cooling at 248 K while melting starts during the heating cycle at 303 K. A small peak at 273 K can be found in the cooling cycle corresponding to the crystallization of water residuals in the sample. Hence, the presence of water reduces the melting point in relation to the dried sample, and increases the solidification point. Moreover, the

122

solidification dynamics seems to be facilitated when water is eliminated from the sample as only one sharp peak is observed in the thermogram.

6.3 NMR spectrum

^{13}C NMR and ^{1}H NMR spectra of a hydrated [C_2mim][$C_{10}SO_4$] neat sample were measured at several temperatures, Fig. 6.2. At temperatures from 333 K to 309 K, the proton-coupled ^{13}C NMR spectrum contains a large number of sharp and intense peaks. The doublet at lowest field (137 ppm) is produced by the carbon located in position 2 of the imidazolium ring, while the pair of doublets centered at 124 ppm and 123 ppm corresponds to carbons in positions 4 and 5. The next triplet at higher field (centered at 67 ppm) is produced by the carbon 9 bonded to the sulfate group and the other multiplets at lower ppm correspond to the imidazolium alkyl groups and the rest of anion tail carbons. The width of these peaks is related to long transversal relaxation times, T_2, of carbon nuclei,[290] that reveal a weak spin−spin coupling between molecules. We associate this weak coupling to a high molecular mobility in the bulk of the material, since the sample is in the isotropic liquid state at these thermal conditions.

When temperature decreases below 309 K, there is a redistribution of the position, or shift, of some of the peaks as well as a general broadening of the signals in the spectra. This effect is more important as temperature decreases: the broad peaks gain intensity while the sharp peaks fade. Looking at the DSC data, this temperature corresponds to the clearing point of the ILC, transition which is markedly reflected in the NMR spectra. The larger widths of the new peaks reflect much shorter transversal relaxation times than those observed in the isotropic liquid. These shorten relaxation times are a piece of evidence of an enhanced spin−spin coupling between molecules that makes relaxation easier. Since larger spin−spin interactions points to a much lower mobility of molecules, these observations are compatible with the formation of the molecular aggregates involved in the stabilization of

USC
UNIVERSIDADE
DE SANTIAGO
DE COMPOSTELA
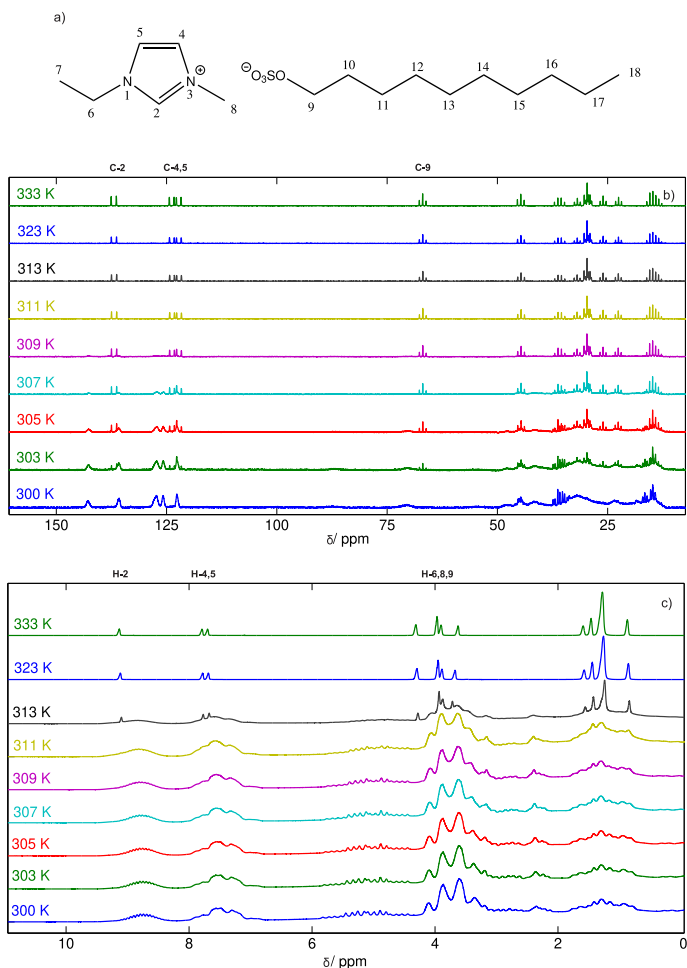
Figure 6.2: (a) Labeled molecular scheme of [C$_2$mim][C$_{10}$SO$_4$]. (b) ^{13}C NMR and (c) ^{1}H NMR spectra of hydrated [C$_2$mim][C$_{10}$SO$_4$] at temperatures of 300 K, 303 K, 305 K, 307 K, 309 K, 311 K, 313 K, 323 K, and 333 K.

liquid crystal domains.

Notice that broadening affects peaks in the whole spectra, but shifts are especially important in the peaks associated with carbons in the charged regions of the molecules, those in the imidazolium cycle and

the carbon bonded to the oxygen in the alkylsulfate anion. According to the XRD results presented later in this chapter, the ILC presents a lyotropic lamellar phase, a bilayer structure that segregates the material in nonpolar regions (alkyl chains) and strongly polar regions (ion charged heads). The confinement of the charged parts of the molecules in the polar areas enhances the interaction between ions and produces strong heterogeneities that explain the broadening and shifting of these signals in the ILC mesophase. Enhanced chemical shifts and/or broadening of existing peaks in the ^{13}C NMR spectra, were previously described as indicators of the formation of aggregates in other ILCs[291] and other NMR studies on ILCs can be found in Ref. [292].

Regarding the ^{1}H NMR spectra, at 333 K only broad singlets can be detected due to the sample viscosity. However, similar chemical shifts can be appreciated when comparing with the ^{1}H NMR spectrum of the sample dissolved in CDCl$_3$ of Ref. [83]. The H atom located in position 2 in the imidazolium ring appears at 9.14 ppm, followed by two singlets at 7.79 ppm and 7.71 ppm caused by H atoms 4 and 5. Then, three singlets corresponding to protons located in positions 6 (4.32 ppm, 2H), 8 (3.97 ppm, 3H), and 9 (3.90 ppm, 2H) can be observed. Finally, the rest of protons in the alkyl chain of the anion emerge as four broad singlets between 1.68 ppm and 0.82 ppm.

At 313 K some new broad peaks begin to appear, while the ones at higher temperatures start to broaden. Below 311 K, the broad peaks dominate the spectrum and high frequency modulations appear in some regions. The evolution of the peaks in the ^{1}H spectra as a function of temperature can be analyzed in an analogous way to that employed for the ^{13}C spectra. The features observed at temperatures below 311 K are consistent with the appearance of molecular aggregates in the liquid crystal phase where molecules are tightly packed and interactions between them are stronger. A similar aggregation behavior for other neat 1-ethyl-3-methyl-imidazolium alkyl sulfates has been probed by NMR studies.[293]

6.4 Texture analysis

Hydrated $[C_2mim][C_{10}SO_4]$ samples show a noticeable optical birefringence which is absent in dried liquid samples. This birefringence is caused by the existence of microscopic liquid crystal domains, regions where molecules present a certain degree of orientational order, which can be observed by means of Polarizing Optical Microscopy (POM). When observed between cross polarizers, the birefringence patterns shown by the material provide valuable information about the liquid crystal mesophase. Fig. 6.3a shows a 10 μm sample of
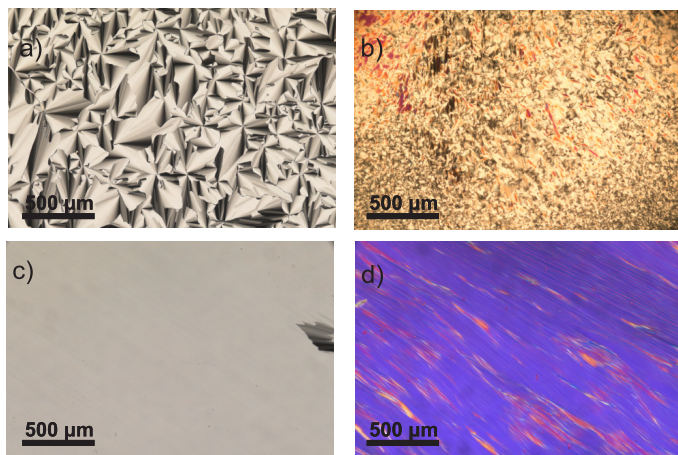
Figure 6.3: (a) Polarizing optical microscopy (POM) textures of $[C_2mim][C_{10}SO_4]$ in home-made cells of different thicknesses: (a) 10 μm natural (without treatment) sample, (b) 150 μm natural sample, (c) 10 μm planar aligned sample, (d) 150 μm planar aligned sample.

$[C_2mim][C_{10}SO_4]$ on a random or spontaneous (without treatment) configuration. Here, an easily recognizable fan-like texture is observed. Also in Fig. 6.3b, a natural texture is shown, but this time of a sample of 150 μm thick. The increase of the thickness of the sample and the random orientation of the domains in different layers moves the birefringence colors from pale gray to yellow, whereas the size

of the crosses in the texture is importantly reduced. The fan-like texture observed in both samples is associated with several kinds of mesophases, such as smectic phases in thermotropic liquid crystals,[294] or hexagonal and lamellar phases in the case of lyotropic liquid crystals.[272] Since the IL requires water for stabilizing the mesophase, as usual in self-assembly processes, one of these two lyotropic mesophases are the most probable structures, as already suggested in Ref. [83].

In Fig. 6.3c, the texture of a 10 μm planar aligned sample is observed with the typical homogeneous appearance of aligned liquid crystals. A small defect is present in the right side of the picture, which helps us to pay attention to the high degree of homogeneity achieved, specially considering the dimensions of the picture. Looking at the Michel-Levy birefringence color chart,[295] this pale gray color is possibly due to a first order interference phenomenon. Fig. 6.3d shows also a planar aligned sample, but of 150 μm thick. The increase of thickness changes the birefringence color from gray to purple and the texture now resembles soft brush strokes, revealing imperfections despite the clear privileged direction in the alignment. This worse alignment in the 150 μm cell is due to the increase of thickness in the sample. As the sample gets thicker, the friction method (see Experimental methods in chapter 2) becomes less effective in the regions far away from the glass surfaces. Nevertheless, both planar aligned samples show, upon rotation, two extinction positions which are placed at 90° one respect to the other. This behavior, as well as the possibility of obtaining homeotropic textures by other alignment methods, points to a mesophase of uniaxial birefringence. Uniaxial lyotropic mesophases include hexagonal and lamellar phases, both compatible with the fan-like texture observed in natural samples.

6.5 Structure and XRD

In order to determine the structure of the observed mesophase, we performed XRD experiments of our sample. We measure it both inside

a capillary and between Kapton films. Both experiments provided similar results. The XRD spectrum from the capillary measurement is shown in Fig. 6.4.
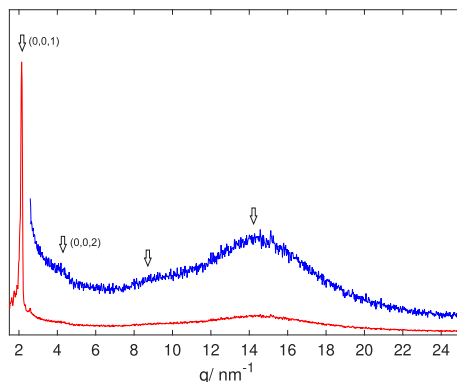
Figure 6.4: XRD spectrum of the sample (red) and zoom of the low intensity region (blue). The arrows highlight from left to right: an intense diffraction peak corresponding to the (0, 0, 1) reflection of a lamellar phase and a recurrent distance of 29.4 Å, a broad peak probably originated by the (0, 0, 2) reflection of the lamellar phase, and two broad bands associated with flexible and much shorter distances.

In the diffractogram, a remarkably intense peak appears at q = 2.1 nm^{-1}, which is associated with a recurrent distance of d = 29.4 Å, and compatible with the (0, 0, 1) reflection of a lamellar lyotropic mesophase. At the position q = 4.2 nm^{-1} we found a broad peak that could be assigned to the (0, 0, 2) reflection of the same lamellar structure. No evidence of an additional hexagonal order within the layers was found and, furthermore, hexagonal phases in imidazolium-based ILCs are rather unusual in concentrated regimes.[144] Thus, according to the XRD results, we propose a lamellar phase where most layers are separated by a distance d = 29.34 Å. In order to understand the origin of this value, DFT simulations were carried out to obtain an optimized geometry for the [C$_2$mim][C$_{10}$SO$_4$] ionic pair. Fig. 6.5a shows the optimized geometry of the ionic pair as well as the associated dimensions in angstroms. The most important alkyl chain of the structure is the one belonging to the decylsulfate anion, of length

a)

b)
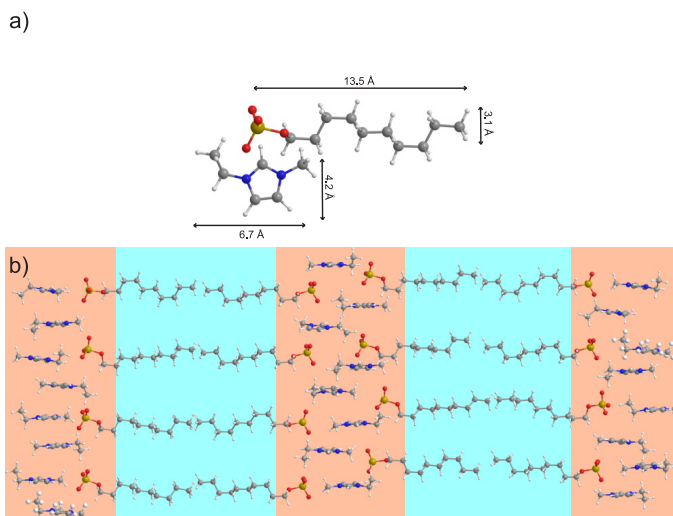
Figure 6.5: (a) Molecular dimensions of the ionic pair $[C_2mim][C_{10}SO_4]$. (b) Recreation of the lamellar phase proposed for the $[C_2mim][C_{10}SO_4]$ ILC. For clarity, water molecules in polar regions are not shown.

$l = 13.5$ Å. As alkyl chains tend to be together due to van der Waals interactions, we expect that the anions stack in pairs with their alkyl chains placed one opposite the other. In this picture, the anion pair presents a characteristic length of $2l \approx 27$ Å. Since this distance is only slightly shorter that found by the X-ray scattering experiments, we suggest that the present ILC organizes in a non interdigitated double layer of dimensions similar to those of a pair of anions.

In the polar regions of the nanosegregated bulk, together with the charged heads of the anions, cations and water molecules are expected to accommodate. In fact, cations are expected to interdigitate the anions as reported for other similar systems.[296,297] However, it is worth to note that recent studies suggest that this interdigitation between ions happens out of the axis determined by the imidazolium rings,[298] since charge screening is still effective, while π-π interactions between imidazolium rings are enhanced in comparison with a purely in-axis alternation.

The strong segregation of the material in nonpolar regions

129

represented by the alkylic bilayer and confined polar regions represented by the charged parts of the ions and the water molecules are artistically recreated in Fig. 6.5b. The nanosegregation of ILs due to alternation of polar and nonpolar regions inside their bulk has been widely studied,[299] it produces diffraction bands at q values about 2.5 nm^{-1}, supporting our interpretation of the distance originated by a bilayer of alkylic chains. This amphiphilically driven bilayer structuration is not unusual in imidazolium based ILCs but, on the contrary, it is rather common.[147]

Coming back to the diffractogram, in the region around the (0, 0, 1) peak, other sharp but low intensity peaks are found which could be interpreted as caused by other possible accommodations of the double bilayer in the bulk of the material. Most of these low probability accommodations correspond to non interdigitated bilayers with characteristic distances ranging from 30 Å to 40 Å. However, the presence of a small sharp peak at larger values q = 2.6 nm^{-1}, originated by distances of 24.2 Å, suggests the existence of some degree of interdigitation in some regions.

In the diffractogram of Fig. 6.4, there are two other peaks, one at q = 8.9 nm^{-1}, which corresponds to a distance of 7.1 Å, and the other at q = 14.5 nm^{-1}, which corresponds to a distance of 4.3 Å. These peaks have characteristic distances much smaller than the previous ones and have a different interpretation. The band at q = 8.9 nm^{-1} is usually associated with charge alternation,[299] the distance relative to the positioning of the cations respect the anions. In terms of our DFT simulation, the lateral dimension of the imidazolium cation is $l_c = 4.2$ Å and that of the anion is $l_a = 3.1$ Å. Hence, for an anion-cation pair, we obtain a distance $d_{a-c} = 7.3$ Å, similar to that of the diffractogram and coherent with the charge alternation hypothesis. As the relative position of cations and anions is flexible, a broad band covering a set of continuum possible distances is produced instead of a peak. On the other hand, the band at q = 14.5 nm^{-1} is often associated with adjacency of nearby atoms[299] and, more specifically, to the labile distance separating the decylsulfate anion alkyl chains inside the lamellar structure.[274,276]

6.6 Material dispersion in the isotropic phase

Isotropic material dispersion (above clearing point) at several temperatures was determined using RISBI, Fig 6.6a. In addition, Table 6.2 shows refractive indices extracted from the experimental curves at some selected wavelengths. The Abbe number of
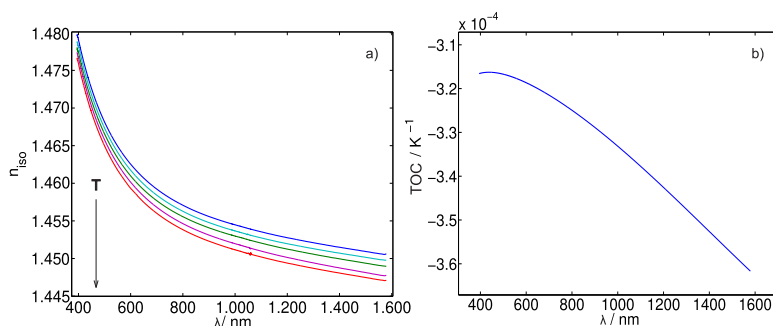
Figure 6.6: (a) Experimental isotropic material dispersion (n_{iso}) of [C$_2$mim][C$_{10}$SO$_4$] as a function of wavelength. From top to bottom, temperatures are 313 K, 315.5 K, 318 K, 320.5 K, and 323 K. (b) Thermo-optical coefficient (TOC) dispersion.

Table 6.2: Isotropic refractive index at selected wavelengths and several temperatures measured by RISBI.

	T/ K				
λ/ nm	313.0	315.5	318.0	320.5	323.0
486	1.4692	1.4684	1.4676	1.4668	1.466
546	1.4651	1.4643	1.4636	1.4628	1.462
589	1.463	1.4622	1.4614	1.4606	1.4598
633	1.4612	1.4604	1.4597	1.4588	1.458
680	1.4598	1.459	1.4582	1.4574	1.4566
823	1.4567	1.4559	1.4552	1.4542	1.4534
1000	1.4545	1.4536	1.453	1.452	1.4512
1200	1.4528	1.452	1.4512	1.4501	1.4494
1400	1.4515	1.4507	1.4499	1.4487	1.4481
1500	1.4509	1.4501	1.4494	1.4481	1.4475

[C$_2$mim][C$_{10}$SO$_4$] is in the range between 52.4 and 53.0 depending on

the specific temperature, corresponding the lowest Abbe number values for the highest temperatures. The material dispersion in the measured spectral range and at all measured temperatures can be expressed in a compact way by means of a Cauchy formula where we introduced an extra temperature-dependent term to take into account thermal effects:

$$n_{iso} = A + B(T - T_0) + \frac{C}{\lambda^2} + \frac{D}{\lambda^4} + \frac{E}{\lambda^6} + F\lambda^2 \qquad (6.1)$$

with n_{iso} as the isotropic refractive index, A, B, C, D, E, and F as the fitting parameters, T as the temperature, and λ as the wavelength. T_0 is a reference temperature, which, in our case, we have set at 318 K, the mean value of the temperature interval. The introduction of the temperature-dependent term allows a straightforward modeling of the effect of temperature in the material dispersion, which is, in a large extent, a translation of the dispersion curves. The fitting parameters are shown in Table 6.3. The maximum deviation of the fitting from

Table 6.3: Fitting parameters of the temperature-dependent Cauchy formula, Eq. (6.1), applied to the isotropic refractive index.

A	B/ K^{-1}	C/ μm^2)	D/ μm^4	E/ μm^6	F/ μm^{-2}
1.5530	-3.2·10^{-4}	3.2·10^{-3}	2.4·10^{-4}	-1.2·10^{-5}	-1.4·10^{-3}

the experimental data is $4.8 \cdot 10^{-4}$, registered at a single isolated point, while the mean deviation is below $1.0 \cdot 10^{-4}$. Even though increasing the number of fitting parameters decreases the deviation from the experimental data, we decided to keep this fitting since it contains the minimum number of parameters required to recover the material dispersion as a function of wavelength and temperature with acceptable accuracy.

The thermo-optical coefficient (TOC) dispersion of the liquid can be calculated taking advantage of the linear dependence of the material dispersion with T, by just fitting the refractive index at each wavelength versus the temperature, Fig. 6.6b. As refractive index decreases with temperature, TOC is negative and its magnitude increases in absolute

terms as we move to larger wavelengths. However, the effect of the dispersion is very small, with variations of order 10^{-5}. In consequence, the TOC can be considered as a constant in Eq. (6.1) for the fitting of the material dispersion.

6.7 Material dispersion in the liquid crystal phase

Multiwavelength Abbe refractometry was employed to measure the refractive index at the fast and slow axes at several discrete wavelengths and at several temperatures. By definition, the fast axis is the one presenting the lower refractive index and the slow axis is that presenting the higher one. Both axes are tightly related to the mesophase exhibited by the ILC and the molecular axis of its molecules. In this case, as the mesophase is uniaxial, the long molecular axis determined by the alkyl chain of the $[C_{10}SO_4]^-$ anion is parallel to the normal vector of the planes of the lamellar phase. Thus, the fast and slow axis can be identified to those in the long dimension of the decylsulfate anion forming the lamellar planes, and its perpendicular direction, respectively. However, as we have not studied the microscopic orientational response of the system when aligned, univocal assignation of the molecular axes to fast and slow indices is not straightforward.

As explained in chapter 2, the liquid crystal samples preparation for Abbe measurements requires spreading the material on a thin film over the prism, which influences the amount of water absorbed by the material when the measurements are not performed in a dried chamber, as in our case. For this reason, we measured the sample both by Abbe refractometry and RISBI and the results are discussed separately, since interesting features can be extracted from each method. Table 6.4 shows the fast refractive indices, n_f, and slow refractive index, n_s, measured by Abbe refractometry, and the data are plotted as a function of T in Fig. 6.7. Both fast and slow indices linearly decrease as temperature raises for a fixed wavelength. TOC was calculated for each set of refractive indices from the slope of the linear fits. No clear TOC dependence on
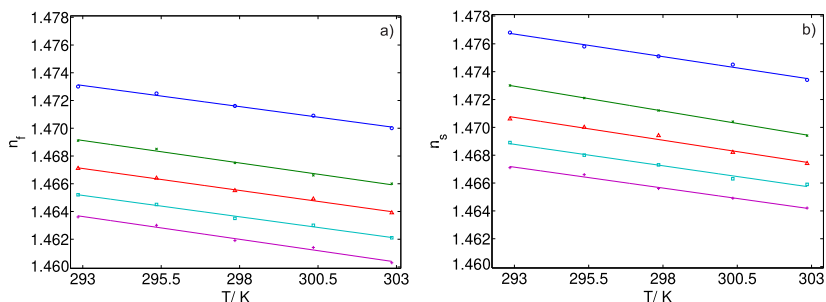
Figure 6.7: Refractive indices measured by Abbe refractometry at 486 nm, 546 nm, 589 nm, 633 nm, and 680 nm (up to down) and at several temperatures. A linear fit to the refractive indices at the same spectral lines as a function of temperature was performed to calculate the TOC. (a) Refractive indices in the direction of the fast axis. (b) Refractive indices in the direction of the slow axis.

Table 6.4: Fast and slow refractive indices measured by Abbe refractometry.

	T/ K	486 nm	546 nm	589 nm	633 nm	680 nm
	293.0	1.473	1.4691	1.4671	1.4652	1.4636
	295.5	1.4725	1.4685	1.4664	1.4645	1.463
n_f	298.0	1.4716	1.4675	1.4655	1.4635	1.4619
	300.5	1.4709	1.4666	1.4649	1.463	1.4614
	303.0	1.47000	1.4660	1.4639	1.4621	1.4603
	293.0	1.4769	1.473	1.4706	1.4689	1.4671
	295.5	1.4758	1.4721	1.4700	1.468	1.4666
n_s	298.0	1.4751	1.4712	1.4694	1.4673	1.4656
	300.5	1.4745	1.4704	1.4682	1.4663	1.4649
	303.0	1.4734	1.4694	1.4674	1.4659	1.4642

wavelength for n_f or n_s was obtained from the Abbe measurements. Furthermore, no evident TOC dependence was found as a function of the considered axis. In consequence, an average TOC can be given for the compound in the ILC state, TOC = −3.2 · 10⁻⁴ K⁻¹. This result suggests that TOC affects both indices with the same strength. Indeed, the TOC in the ILC state is not different from the TOC in the isotropic liquid state, which means that the molecular mechanisms causing the TOC, namely the increased molar volume with respect to the molecular polarizability,[261] act with the same intensity on both states.

Regarding the birefringence, the difference between the fast and slow indices does not present a clear trend with wavelength. Moreover, as TOC is almost the same for both slow and fast indices, this birefringence does not present a clear trend with temperature either. An average birefringence can be obtained subtracting both set of indices at the same temperature and wavelength and averaging the result, $\overline{\Delta n_{T,\lambda}} = 3.60(20) \cdot 10^{-3}$. Fig. 6.8 shows the fast and
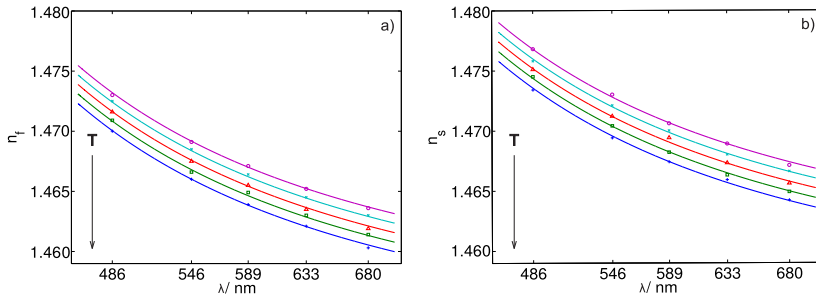
Figure 6.8: Refractive indices measured by Abbe refractometry at temperatures (from up to down) T = 293 K, 295.5 K, 298 K, 300.5 K, and 303 K at several spectral lines. A fit of a Cauchy formula Eq. (6.2) to the data describes both the temperature and wavelength dependence of dispersion. (a) Fast refractive index, n_f. (b) Slow refractive index, n_s.

slow material dispersion corresponding to the Abbe refractometer measurements. In this case, because of the narrower spectral range of the data, a three-term temperature-dependent Cauchy formula is enough to parametrized the material dispersion curves:

$$n_{f/s}(\lambda, T) = n_{0,f/s} + B(T - T_0) + \frac{C}{\lambda^2} \qquad (6.2)$$

In this Cauchy formula, the terms accompanying the temperature and wavelength dependence are the same for both sets of indices as birefringence is almost independent of temperature and wavelength. Thus, the only parameter that differs from the fast index fitting and the slow index fitting is the independent term, $n_{0,f/s}$. In this way, by using four fitting parameters, we described the two sets of measurements at all the available temperatures. The fitting provided by this expression to

135

the experimental data in relation with the number of fitting parameters is very good as the average deviation of the curve with respect to the experimental values is $1.1 \cdot 10^{-4}$, while the maximum deviation registered in any of the curves is $3.7 \cdot 10^{-4}$ for a specific value. The fitting parameters are shown in Table 6.5.

Table 6.5: Coefficients of a temperature-dependent Cauchy formula fit, Eq. (6.2), to the fast and slow refractive indices.

	$n_{0,f/s}$	B/ K^{-1}	C/ $\mu\mathrm{m}^2$
n_s	1.4559	$-3.2\cdot10^{-4}$	$4.6\cdot10^{-3}$
n_f	1.4523	$-3.2\cdot10^{-4}$	$4.6\cdot10^{-3}$

6.8 Birefringence dispersion

Birefringence dispersion was measured with RISBI on a broad spectral range from 400 nm to 1550 nm according to the procedure detailed in the chapter of Experimental methods. Fig. 6.9a shows the phase difference $\Delta\varphi$ between fast and slow refractive indices as a function of the inverse of the wavelength $\sigma = 1/\lambda$, which is clearly linear. Hence, according to Eq. (2.10), a simple linear fit can retrieve the Δk ambiguity and, in consequence, the birefringence dispersion Δn is easily obtained, see Fig. 6.9b. The birefringence dispersion is fairly constant in the studied spectral range, being on average $\overline{\Delta n_\lambda} = 4.21(28) \cdot 10^{-3}$ with a standard deviation of $S(\Delta n) = 2.8 \cdot 10^{-4}$. Birefringence dispersion was also measured at five different temperatures by RISBI in order to extract conclusions about its temperature dependence. Spectral averages of the birefringence as a function of temperature are shown in Fig. 6.10. The birefringence value at each temperature is randomly distributed within our experimental uncertainty and no clear trends were observed. It is worth to note that this uncertainty is the one provided by our experimental method for measuring a specific sample, thus the possible variation of the birefringence by water absorption is not considered. However, it plays an important role in the magnitude of the
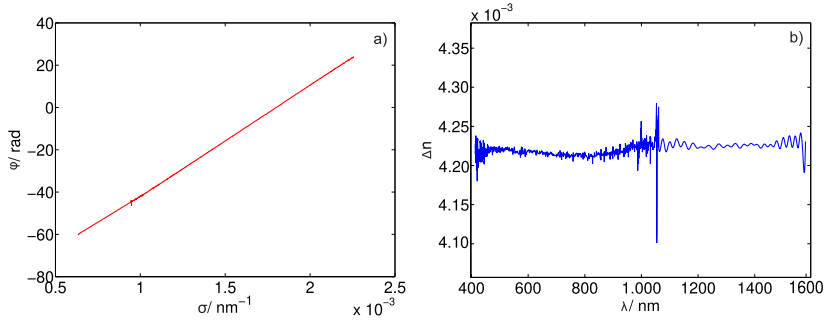
Figure 6.9: (a) Phase retardation, $\varphi(\sigma)$, versus wavenumber, σ, measured by RISBI. (b) Corresponding birefringence dispersion.
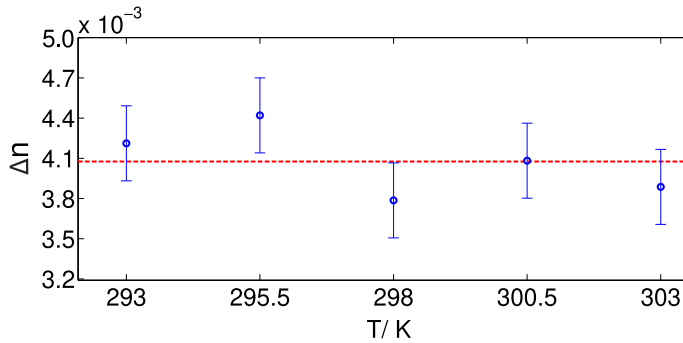
Figure 6.10: Mean birefringence of the sample at temperatures 293 K, 295.5 K, 298 K, 300.5 K, and 303 K. The red line indicates the averaged value of birefringence over temperature.

birefringence since measurements by RISBI and Abbe refractometry differ in $6 \cdot 10^{-4}$. Despite this slight quantitative discrepancy, the qualitative behavior of the birefringence of the material is in total agreement for both techniques: birefringence is largely achromatic and temperature-independent. From the RISBI measurements at different temperatures a reliable average value of birefringence can be obtained, $\overline{\Delta n_{T,\lambda}} = 4.08(12) \cdot 10^{-3}$.

6.9 Conclusions

Ionic liquid crystals are ILs that present liquid crystal mesophases, and they can be analyzed by means of a large number of different experimental techniques, including, among others, DSC, XRD, NMR, POM, Abbe refractometry or RISBI. Each one of these techniques offers a unique point of view of the ionic liquid crystal and their combination allows the univocal determination of the mesophase, its thermal stability and birefringence. In some ionic liquids, the stabilization of mesophases is driven by the incorporation of certain amounts of water in their structure, as it is the case of 1-ethyl-3-methylimidazolium decylsulfate, $[C_2mim][C_{10}SO_4]$. Under our laboratory conditions, this ILC absorbs water from the local atmosphere up to saturation when reaching a water mass fraction of 0.04. Using the above mentioned techniques, a complete determination of the main features of this ILC was performed. The mesophase is stable from 309 K down to the crystallization point at 233 K, and the ^{1}H and ^{13}C NMR spectra evidence a strong confinement of the charged parts of the ions in the polar regions of the mesophase. POM pointed to an optically uniaxial mesophase and XRD clearly suggests a lamellar lyotropic phase where alkyl chains of the anion self-assemble into non interdigitated double layers. In this structure, cations place near the polar heads of the anions creating strong polar regions where absorbed water may be trapped. RISBI measurements on the isotropic phase indicate a normal dispersion and negative thermo-optical coefficient as usual in ionic liquids. Furthermore, Abbe refractometry as well as RISBI measurements in the liquid crystal phase indicate a very low dispersive behavior of the $[C_2mim][C_{10}SO_4]$ birefringence and provided experimental evidence of a uniform TOC over the fast and slow refractive indices. In consequence, the $[C_2mim][C_{10}SO_4]$ birefringence was determined to be $\overline{\Delta n_{T,\lambda}} = 4.08(12) \cdot 10^{-3}$ in the entire thermal and spectral interval. To the best of our knowledge, this is the first time that the birefringence at a single wavelength, not to mention its dispersion, is measured for an

138

ILC.

6.10 Acknowledgments

7. Charge delocalization and non additive polarizability in ionic liquids

[a] Grupo de Nanomateriais, Fotónica e Materia Branda, Departamentos de Física Aplicada e de Física de Partículas, Universidade de Santiago de Compostela.

[b] Department of Computational Biological Chemistry, University of Vienna.

Throughout the previous chapters, the main matter was the experimental determination of the material dispersion of different families of ILs and its rationalization in terms of their molecular structure and temperature. The work collected in those chapters undoubtedly expands the knowledge about refractive index and material dispersion of ILs, traditionally focused on the refractive index at the sodium D line.[93,95,97,99,150,151,153,161,163,164,167,168,172]

Nevertheless, experimental approaches in the field of ILs are only able to cover a limited part of the vast number of possible combinations of cations and anions. For this reason, different authors started using computational and statistical strategies to readily predict the refractive index of new ion combinations.[245,263,267,300–302] These computational efforts are very diverse, and are based in methods ranging from ab initio density functional theory (DFT) calculations[244,263] to neural networks[302] or quantitative structure-property relationship models with predictive capability.[245,267,301]

Most of these works, consider electronic polarizability as an additive magnitude, which means that it is assumed that the electronic

polarizability of each molecular species can be calculated by the addition of those of their atomic components. Throughout the previous chapters, we also have assumed this additive model for polarizability, however, it must be emphasized that these approaches are only reasonable when dealing with systems where most electronic contributions come from σ orbitals with a highly localized charge. In fact, it is well known that the existence of conjugated systems in a molecule, induced by the coupling of π orbitals between adjacent atoms, produces a strong charge delocalization that leads to a non additive behavior of the electronic polarizability.

These substantial deviations of electronic polarizability from additivity have been studied both computationally[303–306] and experimentally[307–310] for different families of molecules presenting conjugated systems in their structures. The possible relevance of charge delocalization effects on the electronic polarizability of ILs was recently suggested.[254] However, it has been scarcely studied up to the moment.

The objective of the current chapter is to provide new insights into the effect that charge delocalization plays in the electronic polarizability of ILs and how it impacts their refractive index. For this reason, the extent of charge delocalization induced by π orbitals in a vast number of ions is studied, and significant trends are depicted both for ions and ILs.

We present here estimations of the refractive index of 1216 ionic pairs, some of them never synthesized. The model developed to move from ions to ILs provides extra insights into how the ion combination affects the resulting refractive index, pointing to new strategies to reach ILs with high refractive indices. This model includes a quadratic volume correction that highly improves the theoretical IL volume calculated by the raw addition of the quantum mechanical volumes of the ions. This correction can improve the prediction of other volume-based magnitudes, such as mass density, using data from ab initio calculations.

7.1 Materials

The polarizability and molecular volume of 92 different ions were simulated by DFT methods. These ions can be divided into a set of common anions, Supplementary Table 7.S1, and three different groups of cations according to their structure.

The first group of cations, Supplementary Table 7.S2, includes seven different cationic heterocyclic families with variable alkyl chain lengths. This group contains highly aromatic cations such as 1-alkylquinolinium, $[C_k quin]^+$, or 1-alkylpyridinium, $[C_k py]^+$, as well as not aromatic cations such as 1-alkyl-1-methylpyrrolidinium, $[C_k mpyrr]^+$, or 1-alkyl-1-methylpiperidinium, $[C_k mpip]^+$. The presence or absence of aromaticity in these different heterocycles is expected to provide valuable information on the influence of charge delocalization on their electronic polarizability and refractive index.

The second cationic group, Supplementary Table 7.S3, includes diverse singly and doubly substituted imidazolium species containing different number and positions of π bonds, such as 1-allyl-3-methylimidazolium, $[allylmim]^+$, 1,3-diallylimidazolium, $[1,3$-diallylim$]^+$, 1-benzyl-3-methylimidazolium, $[benzylmim]^+$, 1,3-dibenzylimidazolium, $[1,3$-dibenzylim$]^+$, 1-crotyl-3-methylimidazolium, $[crotylmim]^+$, 1-ethoxy-3-methylimidazolium, $[eomim]^+$, 1,3-diethoxyimidazolium, $[1,3$-dieoim$]^+$, 1-ethylnitrile-3-methylimidazolium, $[enmim]^+$, 1,3-diethylnitrileimidazolium, $[1,3$-dienim$]^+$, 1-methyl-3-vinylimidazolium, $[vinylmim]^+$, 1,2-divinylimidazolium, $[1,2$-divinylim$]^+$ and 1,3-divinylimidazolium, $[1,3$-divinylim$]^+$.

The last group, Supplementary Table 7.S4, comprises imidazolium-based cations with different kinds of functionalized side chains, e.g., 1-meth(oxyethyl)$_k$-3-methylimidazolium, $[m(eo)_k mim]^+$, 1-methyl-3-perfluoroalkyl-imidazolium, $[F_k mim]^+$, and 1-polyenyl-3-methylimidazolium, $[uC_k mim]^+$. Perfluorinated and oxygenated chains are interesting since their basic units contain elements that go

143

beyond carbon and hydrogen. Lastly, the polyenyl side chain presents a totally delocalized structure produced by the conjugation of the π bonds throughout the chain. It will provide the clearest picture of how charge delocalization influences polarizability.

7.2 Calculation of polarizability and molecular volume to evaluate the refractive index

The Lorentz-Lorenz equation relates electronic polarizability and molecular volume of ILs with their refractive index:

$$\frac{n^2 - 1}{n^2 + 2} = \frac{4\pi}{3}\frac{\alpha_{IL}}{V_{IL}}, \tag{7.1}$$

where V_{IL} is the molecular volume of the IL and α_{IL} its electronic polarizability volume. Please, note that, for convenience, the electronic polarizability volume is used instead of the actual electronic polarizability, being both magnitudes related by a $4\pi\epsilon_0$ factor with $\epsilon_0 = 8.85 \cdot 10^{-12} \mathrm{CV^{-1}m^{-1}}$, the vacuum electric permittivity.

The simulated electronic polarizability of the respective ILs can be calculated by adding the electronic polarizability contributions of their composing ions, i, $\alpha_{IL} = \sum_i \alpha_i$. This form of calculating the total electronic polarizability is quite convenient since it provides flexibility and speed to our calculations. Nevertheless, it has to be managed carefully since additivity on electronic polarizability is not always ensured. In this case, we assume additivity in terms of ions but not in terms of atoms. The assumption of additivity at the ionic level is reasonable because of no significant charge transfer in the optical regime within ionic species is expected, as supported by both available bibliography[244,245,301] and the computational results we present in the following pages.

With regard to the calculation of the molecular volume of the IL, V_{IL}, it is larger than that of the mere addition of the volumes of its constituent ions, $V_{IL} > \sum_i V_i$, behavior that was already reported in

USC
UNIVERSIDADE
DE SANTIAGO
DE COMPOSTELA

144

recent works.[311] For this reason, we decided to use a semi-empirical expression to estimate from the ion volumes, V_i, the ionic liquid volume, V_{IL}. Different combination rules were evaluated to find the expression for V_{IL} which better reproduces the experimental refractive index of the test ILs. We concluded that a quadratic correction in terms of the sum of ionic volumes ($\sum_i V_i$) with two fitting parameters, f_{scale} and f_{int}, is enough to obtain representative IL volumes:

$$V_{IL} = f_{scale} \cdot \sum_i V_i + f_{int} \cdot \left(\sum_i V_i \right)^2 \qquad (7.2)$$

It is possible to obtain some physical insight into the semi-empirical f-factors in the above equation. f_{scale} is a factor whose value is always above the unit, suggesting a generalized underestimation on the calculation of the molecular volume of the ions. According to literature,[224,312] this underestimation is produced because the real volume that a molecule occupies in the condensed phase (the cavity volume) is up to 30 % larger than the molecular one. On the other hand, the second parameter f_{int} summarizes various interactions and packing effects. It can be interpreted as an interaction or excess volume coefficient since it contains quadratic terms arising both from self and cross-interactions. Both factors could also be slightly dependent on the temperature mismatch between experimental data (obtained at room temperature) and calculations (at 0 K).

7.3 Selection of the DFT level of theory

In order to choose the best level of theory to realize the calculations that form part of this chapter, the performance of different potentials and basis sets combinations in the prediction of electronic polarizability and refractive index dispersion of ILs was tested. The tested potentials were B3LYP, CAM-B3LYP, M062X and PBE0 in combination with the 6-311++G(d,p) and aug-cc-pVDZ basis sets. The studied ILs were 1-alkyl-3-methylimidazolium

145

tetrafluoroborate $[C_k\text{mim}][BF_4]$ with k = 2, 3, 4, 6 and 8, 1-alkyl-3-methylimidazolium bis(trifluoromethane)sulfonylimide $[C_k\text{mim}][NTf_2]$ with k = 2, 3, 4 and 6, 1-ethyl-3-methylimidazolium trifluoromethanesulfonate $[C_2\text{mim}][OTf]$ and 1-ethyl-3-methyl-imidazolium alkylsulfate $[C_2\text{mim}][C_k SO_4]$ with k = 2 and 6. The

Table 7.1: Relative error of simulated electronic polarizability with respect to experimental data,[237] $\Delta\alpha = (\alpha_{IL}^{sim} - \alpha_{IL}^{exp})/\alpha_{IL}^{exp}$. The tabulated values correspond to the average of the relative error over the spectral range and the members of each family of ILs.

Electronic polarizability relative error $\Delta\alpha$					
Functional	basis set	$[C_k\text{mim}][BF_4]$	$[C_k\text{mim}][NTf_2]$	$[C_2\text{mim}][OTf]$	$[C_2\text{mim}][C_k SO_4]$
B3LYP	6-31++G(d,p)	1.2%	1.7%	0.5%	1.6%
	aug-cc-pVDZ	6.1%	9.0%	2.4%	8.4%
CAM-B3LYP	6-31++G(d,p)	3.1%	2.2%	3.5%	1.8%
	aug-cc-pVDZ	3.4%	4.9%	3.8%	4.8%
M062X	6-31++G(d,p)	4.1%	3.7%	5.1%	3.2%
	aug-cc-pVDZ	2.6%	3.2%	2.1%	3.8%
PBE0	6-31++G(d,p)	2.1%	1.1%	2.8%	7.3%
	aug-cc-pVDZ	4.3%	5.9%	4.4%	5.8%

relative error in this table, averaged over the spectral range and members of each family of ILs, is below 5 % for most of the levels of theory, being the most accurate the B3LYP/6-31++G(d,p) one, with relative errors below 2 %. Nevertheless, since for calculating refractive index by means of Eq. (7.1) also the IL volume is required, we also analyzed the performance of the previous levels of theory in estimating the refractive index via our volume treatment. The fitting parameters in Eq. (7.2), f_{scale} and f_{int}, are dependent on the level of theory used and, for this reason, they were evaluated for all the DFT functionals and basis sets considered, Table 7.2. The best predictions of refractive indices are those of the B3LYP/6-311++G(d,p) level of theory, as in the polarizability case, which provide uncertainties in the refractive index in the wavelength range of $S(n) \approx 1 \cdot 10^{-2}$ with f_{scale} = 1.0189 and $f_{int} = 3.635 \cdot 10^{-4}$ Å^{-3}. For this reason, it is the level of theory chosen for the realization of the polarizability calculations in this chapter. Except indicated otherwise, all given polarizabilities and refractive indices were calculated at a wavelength of λ = 589 nm.

Table 7.2: Relative error of simulated refractive index, $\Delta n = (n_{sim} - n_{exp})/n_{exp}$, with respect to experimental data. [237] The tabulated values correspond to the average of the relative error over spectral range and members of each family of ILs.

		Refractive index relative error Δn			
Functional	basis set	[C$_k$mim][BF$_4$]	[C$_k$mim][NTf$_2$]	[C$_2$mim][OTf]	[C$_2$mim][C$_k$SO$_4$]
B3LYP	6-31++G(d,p)	0.2%	0.7%	0.5%	1.1%
	aug-cc-pVDZ	2.7%	3.3%	0.1%	0.4%
CAM-B3LYP	6-31++G(d,p)	1.0%	0.9%	1.1%	3.1%
	aug-cc-pVDZ	1.1%	0.8%	4.6%	0.5%
M062X	6-31++G(d,p)	0.5%	0.6%	0.4%	1.4 %
	aug-cc-pVDZ	1.3%	1.7%	2.6%	1.1%
PBE0	6-31++G(d,p)	0.9%	0.8%	1.2%	2.3%
	aug-cc-pVDZ	1.2%	2.4 %	2.3%	1.2%

7.4 A model for polarizability and charge delocalization

A simple model of the electrons in a molecule under the effect of an electric field is a free electron gas composed of 2N electrons confined in a one-dimensional box of length L.[303,313] Its global polarizability can be calculated as the sum of the contributions from each excited state ξ, which can be analytically calculated as the second partial derivative of the energy of that state E_ξ with respect to the perturbing electric field F:[303]

$$\alpha_i = -2 \sum_{\xi=1}^{N} \frac{\partial^2 E_\xi}{\partial F^2} = \frac{4L^4}{a_0} \sum_{\xi=1}^{N} \left(\frac{-2}{3\pi^2 \xi^2} + \frac{10}{\pi^4 \xi^4} \right) \qquad (7.3)$$

where $a_0 = \hbar^2/me^2$ is the atomic Bohr radius. From Eq. (7.3), it is observed that the electronic polarizability presents a fourth-power dependence on the length of the box, that is, the physical extension where the electrons are allowed to move following the electric field. The employment of more realistic approaches to this problem yields different analytical forms for the electronic polarizabilities. However, a power dependence on L is always retained.[313,314] As the effective L where conjugated electrons are allowed to move is larger than that of localized ones, the increase of the size of the delocalization region in a

molecule is expected to produce a non additive increase of the associated electronic polarizability. We have investigated this effect by studying the polarizability of imidazolium cations $[uC_k mim]^+$ with unsaturated side chains of variable length.

For the computation of the atomic polarizabilities of this unsaturated family, α_β, we employed the methods described in Refs. [311] and [315]. The average atomic polarizability of an atom β is obtained as the numerical derivative of the atomic dipole moment $\vec{\mu}_\beta$ with respect to an applied electric field $\vec{F}$,

$$\alpha_\beta = \frac{1}{3}\left(\left.\frac{\partial\mu_{\beta x}}{\partial F_x}\right|_{F_x=0} + \left.\frac{\partial\mu_{\beta y}}{\partial F_y}\right|_{F_y=0} + \left.\frac{\partial\mu_{\beta z}}{\partial F_z}\right|_{F_z=0}\right). \tag{7.4}$$

The atomic dipoles $\vec{\mu}_\beta$ are the net dipole moments in a basin Ω_β arising from the anisotropy of the electron cloud around the nucleus and a charge transfer term,

$$\vec{\mu}_\beta = \vec{\mu}_\beta^P + \vec{\mu}_\beta^{CT}, \tag{7.5}$$

$$\vec{\mu}_\beta^P = \int\limits_{\Omega_\beta} \rho(\vec{r})\cdot(\vec{r}-\vec{R}_\beta)d\vec{r}, \tag{7.6}$$

$$\vec{\mu}_\beta^{CT} = \sum_\gamma q_{b(\beta\gamma)}\cdot\left(\vec{R}_\beta - \vec{R}_{b(\beta\gamma)}\right). \tag{7.7}$$

The first term $\vec{\mu}_\beta^P$ is called the polarization term and can be evaluated by the GDMA code of Misquitta and Stone.[316,317] It contains the electron density $\rho(\vec{r})$ and is defined with respect to the coordinate $\vec{R}_\beta$ of the nucleus β. This contribution describes the local deformability of the electron cloud. The second contribution arises from the charge transfer (CT) between the bonds $b(\beta\gamma)$ between the nuclei β and γ. The bond charge $q_{b(\beta\gamma)}$ can be defined in such a manner[311] that it does not depend on the origin of the coordinate system (even for charged molecules). It is located at the center between the nuclei $\vec{R}_{b(\beta\gamma)} = 1/2\cdot(\vec{R}_\beta+\vec{R}_\gamma)$. The procedure to obtain these atomic dipole moments and their constituting parts is detailed in Refs. [263], [311] and [315]. For the discussion in

USC
UNIVERSIDADE
DE SANTIAGO
DE COMPOSTELA

148

this chapter, the polarizability in Eq. (7.4) can also be decomposed into a polarization and a charge transfer term:

$$\alpha_\beta = \alpha_\beta^P + \alpha_\beta^{CT} \tag{7.8}$$

Intuitively, the charge transfer contribution should strongly depend on the nature of the bonded system. In other words, we expect high α_β^{CT} as a function of the length of the conjugated system. The sum of the atomic polarizabilities α_β is still the molecular electronic polarizability α_i applying this algorithm:

$$\alpha_i = \sum_\beta \alpha_\beta \tag{7.9}$$

However, this does not cast doubt on the non additivity of polarizability as individual atomic polarizabilities, α_β, are not uniform for particular atom types such as sp^2 carbons. In other words, α_β may still be a function of the size of the electron delocalization.

In order to evaluate the importance of charge delocalization within the studied ions, we employed the Multiple Center Bond Order (MCBO) index,[318] which is a quantitative estimator of the degree of charge delocalization in molecules. The MCBO index was calculated in all the cases using the Multiwfn 3.8 program.[319] As we used it to compare molecular fragments of a different number of atoms, we employed here the normalized version of this parameter,[320] and we used as final MCBO index values the average resulting from considering the two opposite directions of the path including the atoms of interest. The absolute value of MCBO index is a quantitative parameter that measures the extent of charge delocalization in a molecular structure. The higher it is, the more significant is the extent of charge delocalization. The sign of the MCBO index is related to the orbital origin of the electrons participating in the delocalization.[321]

USC

149

7.5 Molecular polarizability density, MPD

As the value of the refractive index n of the ILs considered in this study is limited between 1.35 ([F_5mim][FAP]) and 1.69 ([uC_5mim][SCN]), the Lorentz-Lorenz equation, Eq. (7.1), can be approximated with a simple Taylor series:[322]

$$\frac{4\pi}{3}\frac{\alpha_{IL}}{V_{IL}} = \frac{n^2-1}{n^2+2} \approx c_1 \cdot n + c_2 \qquad (7.10)$$

Thus, the overall polarizability density α_{IL}/V_{IL} is roughly a linear function of the refractive index and vice versa. In an ideal mixture, one could expect that the α_{IL}/V_{IL} ratio, and hence, the refractive index, were directly obtained as the usual linear combination of the individual molecular polarizability density of each i ion:

$$\left(\frac{\alpha_{IL}}{V_{IL}}\right)^{ideal} = \sum_i \mathrm{MPD}_i \cdot \phi_i, \qquad (7.11)$$

where the molecular polarizability density, MPD_i, is defined as:

$$\mathrm{MPD}_i = \frac{\alpha_i}{V_i^{\mathrm{MPD}}}, \qquad (7.12)$$

and $\phi_i = V_i^{\mathrm{MPD}} / \sum V_i^{\mathrm{MPD}}$ is the volume fraction of the species i after correcting it by means of Eq. (7.2), $V_i^{\mathrm{MPD}} = f_{scale} \cdot V_i + f_{int} \cdot V_i^2$. However, since V_{IL} involves cross-terms between the volume of its composing ions, the previous linear combination is just an upper limit for the real α_{IL}/V_{IL} ratio and, thus, IL refractive index:

$$\left(\frac{\alpha_{IL}}{V_{IL}}\right)^{real} \leq \sum_i \mathrm{MPD}_i \cdot \phi_i. \qquad (7.13)$$

7.6 Charge delocalization and polarizability on the anion

Most common ILs involve anions that do not include large π systems in their molecular structures, except tosylate. However, usual anions such as acetate, trifluoroacetate, methylsulfate, methylsulfonate, triflate, or bis(trifluoromethane)sulfonylimide possess double bonds and cyanide-based anions such as thiocyanide, dicyanamide, and tetracyanoborate present triple bonds. Acetates, cyanides and methylsulfonyl-based anions have mesomeric structures indicating a delocalized charge region centered at the carbon in acetate and cyanide anions, and in the nitrogen in methylsulfonyl anions. Table 7.3 shows the MCBO index and the MPD_i of some of the considered anions. The MCBO parameter

Table 7.3: Normalized Multi-Center Bond Order (MCBO) indices and MPD_i of the anions. The atomic polarizabilities α_β are taken from Ref. [322].

Anion	|MCBO|	MPD_i	$\alpha_\beta(N)$ /Å^3	$\alpha_\beta(Csp)$ /Å^3	$\alpha_\beta(Csp^2)$ /Å^3	$\alpha_\beta(Csp^3)$ /Å^3
[OTf]$^-$	0.17	0.0609				0.98
[NTf$_2$]$^-$	0.23	0.0641	1.99			1.03
[B(CN)$_4$]$^-$	0.26	0.0703	1.31	1.23		
[C$_1$SO$_4$]$^-$	0.31	0.0660				0.88
[Tos]$^-$	0.40	0.0856			1.29-1.52,1.75	1.10
[C$_1$SO$_3$]$^-$	0.47	0.0686				1.12
[N(CN)$_2$]$^-$	0.49	0.0816	1.78	1.46		
[OAc]$^-$	0.51	0.0796			1.34	1.13
[SCN]$^-$	0.73	0.0863	1.88	2.16		

is a quantitative measurement of the degree of charge delocalization in a molecule, being the [SCN]$^-$ anion the one with the highest value of this parameter. In fact, its MCBO index is even higher than that of tosylate, whose value is also lower than that of other anions showing resonance. Nevertheless, both anions present the highest MPD_i. Concerning the polarizabilities α_β on the atomic level, the situation is less clear. For example, the sp^2 carbons in tosylate show the same polarizability as that of the sp^2 carbon in acetate despite the extensive delocalized system.

The only exception is the carbon bond to the sulfur in tosylate, which has a significantly higher polarizability of 1.75 Å^{-3}. The immediate neighborhood to a highly polarizable sulfur atom also leads to high polarizability of the sp carbon in thiocyanate of $\alpha_\beta = 2.16$ Å^{-3}, which is significantly higher than the polarizability of the carbons in the other cyanides. The presence of sulfur also drives the polarizability of the nitrogen in [NTf$_2$]$^-$. The overall ranking on the MPD$_i$ is depicted in Fig. 7.1. Anions containing many fluorine atoms have lower ratios
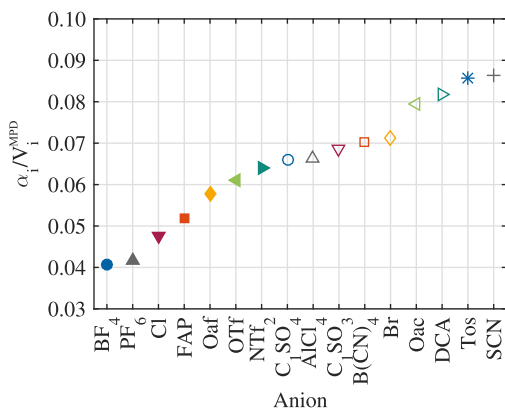
Figure 7.1: Molecular polarizability density MPD$_i$ of the most common anions in ionic liquids.

and are located on the left end of the plot. In the case of [OTf]$^-$ and [NTf$_2$]$^-$, the low polarizability of the fluorine is compensated to some extent by the more polarizable sulfur, carbon and oxygen atoms. The only metal-containing anion considered in this chapter, the [AlCl$_4$]$^-$ has an intermediate MPD$_i$ similar to that of other considered anions. As Al^{3+} is a closed-shell cation, its optical absorption is not expected to be intense. However, the introduction of other kind of metallic complexes with absorption bands closer to the visible range could produce anions with higher MDP$_i$. It is also interesting to note that the introduction of an extra oxygen atom in [C$_1$SO$_3$]$^-$ to form [C$_1$SO$_4$]$^-$, results in a decrease of the MPD$_i$. The anions with some degree of delocalization,

152

e.g., acetate, dicyanamide, tosylate, and thiocyanate have top ratios and are located at the right end of the plot in Fig. 7.1.

7.7 Influence of the cationic core and alkyl chain

We start with the analysis of those cations in Table 7.S2 of the Supporting material section, containing several aromatic and aliphatic cores and aliphatic side chains. Their polarizability volume, α_i, versus their molecular volume, V_i^{MPD}, is depicted in Fig. 7.2a. Increasing
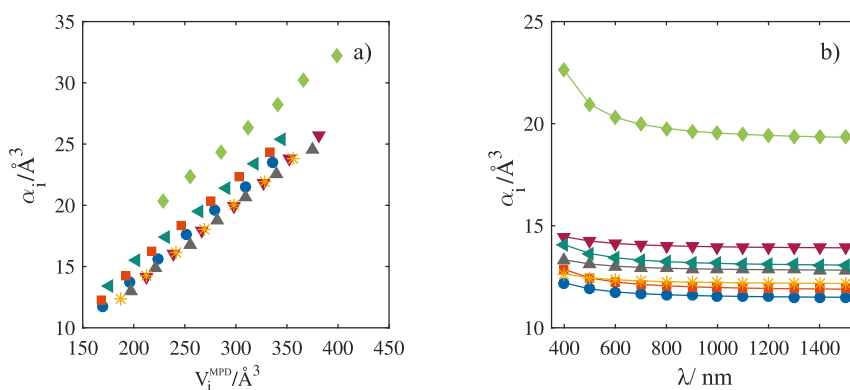
Figure 7.2: a) Electronic polarizability versus molecular volume for different families of alkyl-heterocyclic cations. Members of the same family only differ in the length k of their alkyl chain. Marker legend: $[C_k\text{mim}]^+$ (●), $[C_k\text{mmor}]^+$ (▲), $[C_k\text{mpip}]^+$ (▼), $[C_k\text{py}]^+$ (■), $[C_k\text{mpyrr}]^+$ (∗), $[C_k\text{quin}]^+$ (◆) and $[C_k\text{mthia}]^+$ (◄). b) Electronic polarizability dispersion, $\alpha(\lambda)$, for the cations with alkyl chain $k = 2$.

the side alkyl chain increases both the electronic polarizability and the cation volume, resulting in a linear trend for all cationic species with more or less the same slope, which indicates that electronic polarizability behaves linearly upon addition of the σ electrons of the CH_2 group. However, the corresponding intercepts in Fig. 7.2a differ. On the one hand, this may be due to the different nature of the cationic

153

cores. Although all these cations contain mainly carbons and nitrogens with comparable atomic polarizabilities,[245,301] their hybridization varies between sp^2 and sp^3. Additionally, 1-alkyl-3-methylthiazolium $[C_k\text{mthia}]^+$ contains sulfur and 1-alkyl-1-methylmorpholinium $[C_k\text{mmor}]^+$ has one oxygen. However, the largest intercept is found for 1-alkylquinolinium $[C_k\text{quin}]^+$, which is the largest cation under investigation and also has the most extensive conjugated system, and the lowest intercepts belong to the cations containing only sp^3-hybridized carbons and nitrogens, i.e., 1-alkyl-1-methylpyrrolidinium $[C_k\text{mpyrr}]^+$, 1-alkyl-3-methylpiperidinium $[C_k\text{mpip}]^+$ and 1-alkyl-1-methylmorpholinium $[C_k\text{mmor}]^+$. In order to study the influence of charge delocalization on the intercepts, we have quantified the extent of charge delocalization in each heterocycle by means of the normalized Multi-Center Bond Order (MCBO) index,[320] whose value for each cation is shown in Table 7.4. As expected, aliphatic cations

Table 7.4: Normalized Multi-Center Bond Order (MCBO) indices throughout the heterocycles of the considered cations bearing the same alkyl chain length (k = 2) and corresponding MPD$_i$. For $[C_2\text{quin}]^+$ cation the MCBO index was calculated on the perimeter involving the both cycles. The atomic polarizabilities α_β are taken from Ref. [322].

Cation	|MCBO|	MPD$_i$	α_β(N) /Å^3	α_β(Csp^2) /Å^3	α_β(Csp^3) /Å^3
$[C_2\text{mpyrr}]^+$	0.28	0.0714			
$[C_2\text{mpip}]^+$	0.30	0.0723	1.36		0.84-1.11
$[C_2\text{mmor}]^+$	0.31	0.0718			
$[C_2\text{mim}]^+$	0.58	0.0745	1.15	1.03-1.12	0.89-1.05
$[C_2\text{mthia}]^+$	0.59	0.0822			
$[C_2\text{quin}]^+$	0.59	0.0970			
$[C_2\text{py}]^+$	0.63	0.0783	1.33	1.13-1.22	0.98-1.15

have lower MCBO index than aromatic cations. In fact, the aliphatic pyrrolidinium, piperidinium, or morpholinium cations present similar MCBO indices despite their different structures. The same holds for the

aromatic cations imidazolium, pyridinium, thiazolium and quinolinium. Counter-intuitively, the biggest aromatic cation $[C_k\text{quin}]^+$ does not show the largest MCBO index, despite showing the biggest MPD_i. Despite it, Fig. 7.2a clearly shows that cations with high MCBO index exhibit higher intercepts than the low MCBO index cations.

The electronic polarizabilities of the cations with an ethyl side chain, $k = 2$, are shown as a function of the wavelength $\lambda = 2\pi c/\omega$ in Fig 7.2b. Interestingly, aromatic cations show a stronger correlation between the wavelength and the polarizability than aliphatic cations, as can be seen in the curvature at low wavelengths. From the Kramers-Kronig relationship,[300] this increase of electronic polarizability indicates the existence of an UV resonance, which, according to previous publications,[323] should shift towards the visible range as charge delocalization increases in the cations. Regarding polarizability, its trend differs from that of MCBO index (or MPD_i) since the overall molecular volume plays a decisive role.

Notwithstanding, evidence of the influence of charge delocalization in the electronic polarizability of heterocycles can be subtly found in other reported works. For instance, in Ref. [301] a linear decomposition of the electronic polarizability of ILs in atomic contributions distinguishing between carbon hybridization types yield higher electronic polarizability for the $C(sp^2)$ species, mostly appearing in regions of charge delocalization of IL-forming ions, than for $C(sp^3)$, the representative hybridization of carbon in standard alkyl chains. Another example can be found in Ref. [311], where a decomposition of the electronic polarizability into additive atomic contributions was carried out for different ionic species. In this case, it was found that the N and $C(sp^2)$ atoms in the pyridinium cation have a more considerable contribution to electronic polarizability than those of the imidazolium cation.[311,322] This difference in contributions could be produced by the linearization of the total electronic polarizability of both rings, which, according to our results, is strongly influenced by their different extent of aromaticity. However, the atomic polarizability of the nitrogen in $[C_2\text{mpip}]^+$ was found to be higher than that of nitrogen atoms in the

imidazolium rings (see Table 7.4 and Ref. [322]) although the former cation presents an aliphatic ring system. A difference between sp^2 and sp^3 carbons in the imidazolium and pyridinium is not significant.

7.8 Influence of substituents

In this section, we study the effect that different substituents have on electronic polarizability (see Table 7.S3 in the Supporting Material section). They consist of an imidazolium cation singly and doubly substituted by different groups containing π orbitals, some of them presenting a certain degree of charge delocalization.

The first thing to highlight is that doubling the substituents leads to an increase of the MPD$_i$ compared to the singly substituted imidazolium cation. The various side chains can be grouped into three categories, as shown in Table 7.5: The first category contains aliphatic, ethoxy,

Table 7.5: Normalized Multi-Center Bond Order (MCBO) index and MPD$_i$ of imidazolium cations having different side chains.

Cation	|MCBO|	MPD$_i$
[C$_4$mim]$^+$	0.33	0.0700
[eomim]$^+$	0.33	0.0695
[1,3-dieoim]$^+$	0.34	0.0706
[enmim]$^+$	0.34	0.0693
[1,3-dienim]$^+$	0.32	0.0702
[allylmim]$^+$	0.35	0.0733
[1,3-diallylim]$^+$	0.37	0.0745
[crotylmim]$^+$	0.32	0.0754
[benzylmim]$^+$	0.36	0.0791
[1,3-dibenzylim]$^+$	0.35	0.0820
[vinylmim]$^+$	0.40	0.0757
[1,2-divinylmim]$^+$	0.39	0.0826
[1,3-divinylim]$^+$	0.48	0.0839

and ethylnitrile chains. The first two lack π orbitals in the side chain, and the third contains an sp instead of sp^3 carbon atoms. Cations with these chains have an MCBO index of roughly 0.33, and the MPD_i is around 0.7. The second category gathers cations with side chains containing different number of π orbitals on sp^2 carbons. MCBO index is approximately 0.35, and MPD_i increases with increasing size of the π systems, i.e., the benzylic system has the largest polarizability per volume. A clear example of the impact that a simple isolated double bond has on electronic polarizability is observed in the butyl and crotyl groups. They differ only in the presence of a double bond, but it is enough to increase the crotyl group's electronic polarizability over its saturated equivalent. Hence, the contribution to the electronic polarizability of the extra π orbital clearly overcompensates the loss of the σ orbitals of the two hydrogen atoms that takes place upon unsaturation.

The third category comprises vinylic side chains. Here, the MCBO index is significantly increased to 0.4 and even higher. Also, the MPD_i values are very high. This may indicate that the charge delocalization strengthens the polarizability, since in these cations the π system of the ring is connected to the π system of the side chain forming a single conjugated system. Doubling the vinyl substituent produces the cation with the highest MPD_i, the [1,3-divinylim]$^+$. Position of this doubling induces differences in the MPD_i of the cation, as shown by the different value of [1,2-divinylim]$^+$, suggesting a certain influence of the position of the substitution in the delocalization throughout the imidazolium ring.

7.9 Influence of functionalized chains

In order to evaluate the different impact of σ and π orbitals have on the MPD_i, we turn our attention to the third group of cations. It comprises four different families of cations bearing functionalized side chains of variable length. These side chains are: One perfluorinated chain, where the unit is CF_2, one oxygenated chain, where the unit is an

oxyethyl group, CH_2OCH_2, one polyenylic chain, where the basic unit is a carbon that is respectively linked to its neighbors by a double and a single bond, $-CH=$ or $=CH-$, and one alkyl chain where the basic unit is CH_2. Note that for all the non oxygenated chains, $k = 0$ refers to 1-H-3-methylimidazolium cation, while for the oxygenated chain, it refers to 1-methyl-3-methylimidazolium (see Supplementary Material). In Fig. 7.3a the polarizability dispersion for the different chains with $k = 4$ is shown. The order of units yielding from lowest to highest
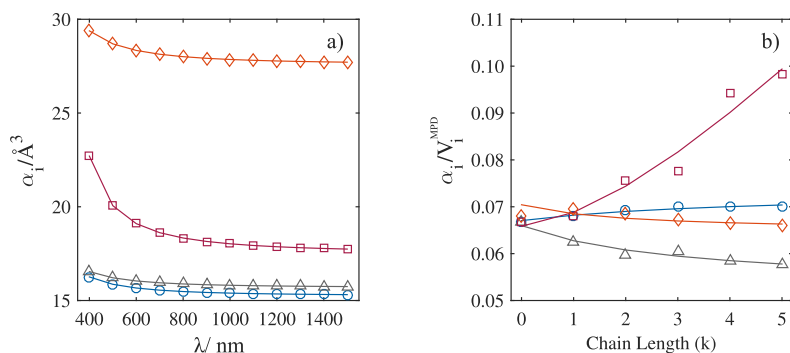
Figure 7.3: a) Electronic polarizability dispersion, $\alpha(\lambda)$, for the imidazolium cation bearing the functionalized chains of length $k = 4$. b) MPD_i at $\lambda = 589$ nm as a function of the chain length, k. Marker legend: $-CH_2-$ (○), $-CF_2-$ (△), $-CH=$ (or $=CH-$) (□) and $-CH_2-O-CH_2-$ (◇).

polarizabilities is: $CH_2 < CF_2 < -CH= < CH_2OCH_2$. The highest value corresponds to the oxygenated chain, which makes sense because its basic unit contains more atoms than the basic units of the other chains. On the other hand, Fig 7.3b shows the MPD_i of the different cations as a function of the chain length. The order from lowest to highest MPD_i is: $CF_2 < CH_2 \approx CH_2OCH_2 < -CH=$. The figure shows that both perfluorinated and oxygenated chains decrease the overall MPD_i of the imidazolium cation as their length increases, although the perfluorinated chain seems to be more efficient for this purpose.

The reason for this decrease is that the ratios between electronic polarizability and volume of the O and F atoms are respectively lower than those of C and H.

It is imperative to highlight the intense influence of charge delocalization in the MPD_i of the polyenylic chain. Except for $k = 1$, it shows much higher values than those of the other chains, which are composed of larger units and exclusively present σ bonds. The significant increase of the MPD_i with k in Fig. 7.3b suggests the breakdown of the hypothesis of additive polarizability.

7.10 Influence of charge delocalization regions of variable length

In order to analyze this behavior in more detail, the electronic polarizabilities and molar volumes of this family of cations, $[uC_kmim]^+$, is compared with its saturated equivalent, $[C_kmim]^+$, in Fig. 7.4. The $[C_kmim]^+$ family contains a standard alkyl chain where bonds between carbons present a clear σ character, which is associated with a robust charge localization. Nevertheless, the polyenyl chain of $[uC_kmim]^+$ presents π conjugation, and thus, electronic delocalization throughout all the chain length. As it is clearly visible in Fig. 7.4a, the molecular volume, V_i^{MPD}, is a linear function of the chain length k in both families of cations. However, different slopes are registered in each case because double bonds are roughly 0.2 Å shorter than single bonds. Furthermore, the saturated side chain contains one more hydrogen per carbon. In the case of electronic polarizability, as shown in Fig. 7.4b, the $[C_kmim]^+$ family presents a linear trend with the chain length while the $[uC_kmim]^+$ family not. In $[C_kmim]^+$, each CH_2 unit seems to have a uniform contribution to the overall polarizability, which is the expected behavior since each CH_2 unit can be rationalized as an electronically independent region. Specifically, each CH_2 unit is made of σ orbitals with very localized charge and, in consequence, according to Eq. (7.3), the overall polarizability of the chain results in the sum of k independent contributions of size L. This fact was exploited in
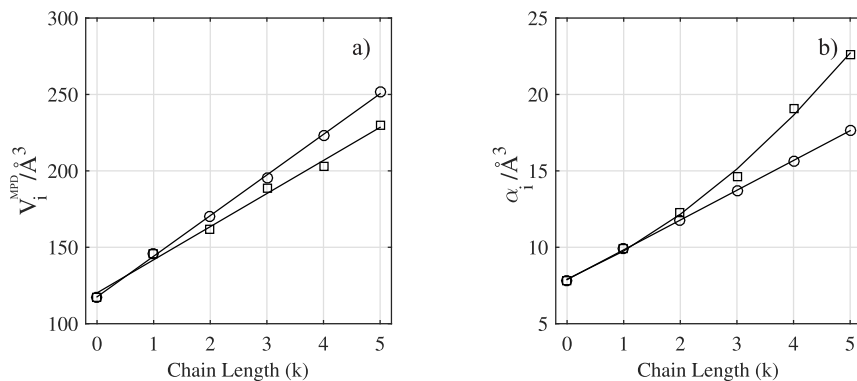
Figure 7.4: a) Molecular volume and b) electronic polarizability as a function of the number of carbons in (○) the alkyl chain of a $[C_k mim]^+$ cation and in (□) the polyenyl chain of $[uC_k mim]^+$ cation. The key difference among both chains is the existence of conjugation along the polyenyl substituent in contrast to the saturated character of the alkyl one.

predicting electronic polarizabilities in our former studies. [245,301]

Nevertheless, the polyenyl chain does not show this linear behavior anymore. In terms of Eq. (7.3), each new unit in the polyenylic chain increases the extension of the delocalization region emerging from the π conjugated system, which produces the nonlinear increase of electronic polarizability with k. As a result, the prediction based on uniform atomic contributions as postulated in Refs. [245] and [301] breaks down. This can also be deduced from the atomic polarizabilities in Fig. 7.5.

Once again, the atomic polarizabilities are decomposed into polarization (α_β^P) and charge transfer (α_β^{CT}) contributions. The local character of the polarizability is determined by the polarization contribution α_β^P. It shows only a slight increase with increasing chain length. Interestingly, there is a zigzag behavior of the carbons C7 to C13 in the aliphatic side chain. The steep increase in the electronic polarizability α_i emerges from the charge transfer contribution α_β^{CT}

160
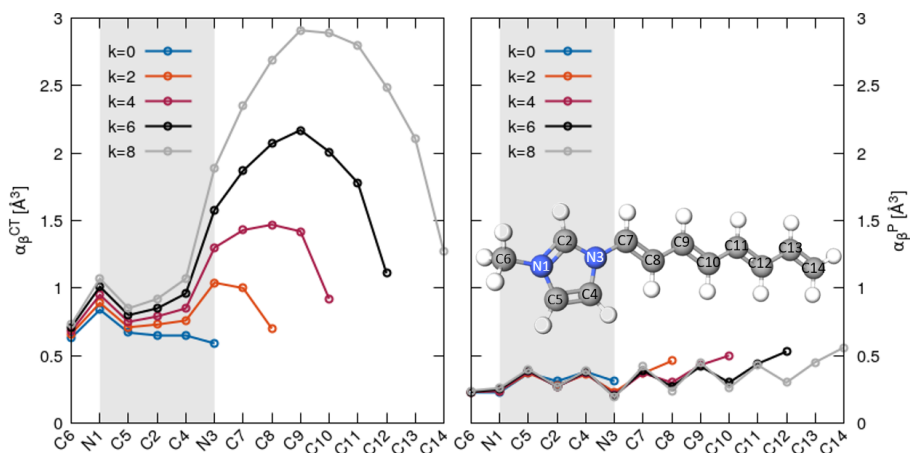
Figure 7.5: Decomposition of the electronic polarizability of $[uC_k mim]^+$ into atomic contributions. The lines have no physical meaning and are just a guide for the eye.

of the side-chain carbons. For example, the atomic polarizability of the carbon C7 increases from 1.00 Å^3 for $k = 2$ to 2.35 Å^3 for $k = 8$ rendering any prediction algorithm based on Designed Regression[245,301] obsolete. Interestingly, the atomic polarizability α_β^{CT} for each sp^2 carbon in the side chain seems to follow a parabolic curve. The atomic polarizability in the middle of the conjugated system is a maximum and decreases towards the end of the conjugated system, as shown in Fig. 7.5a. The conjugated system extends to the heterocyclic core of the imidazolium as the nitrogen N3 and the carbon C4 of the imidazolium ring increase their atomic polarizability with increasing side chain length, k. However, the effect is significantly smaller than the one observed on the side-chain carbons C7-C14.

The overall polarizability of the $[uC_k mim]^+$ family as a function of the chain length k in Fig. 7.4b can be extrapolated by

$$\alpha_i(k) = c_i \cdot \left[V_i^{\text{MPD}}(k) \right]^{\gamma_i}$$

$$\text{MPD}_i(k) = c_i \cdot \left[V_i^{\text{MPD}}(k) \right]^{\gamma_i - 1} \quad (7.14)$$

Here, we also used the fact that the molecular volume $V_i^{\mathrm{MPD}}(k)$, see Fig. 7.4a, is a linear function of the chain length k. The constant c_i depends on the nature of the molecule. Nevertheless, with increasing chain length k, the γ_i-effect of the side chain becomes more important than that of the core unit. The corresponding parameters can be found in Table 7.6. Charge delocalization effects are present if γ_i are above

Table 7.6: Delocalization parameters of several side chains.

Cation	c_i	γ_i
$[\mathrm{F}_k\mathrm{mim}]^+$	0.121	0.870
$[\mathrm{m(eo)}_k\mathrm{mim}]^+$	0.088	0.954
$[\mathrm{C}_k\mathrm{mim}]^+$	0.051	1.057
$[\mathrm{uC}_k\mathrm{mim}]^+$	0.002	1.730

one. This threshold is already visible in Fig. 7.3b. $[\mathrm{F}_k\mathrm{mim}]^+$ and $[\mathrm{m(eo)}_k\mathrm{mim}]^+$ have a $\gamma_i < 1$ and their MPD_i decrease with increasing chain length k. However, $[\mathrm{C}_k\mathrm{mim}]^+$ and $[\mathrm{uC}_k\mathrm{mim}]^+$ possess $\gamma_i > 1$, and, therefore, their MPD_i increase with the chain length. Nevertheless, a significant effect is only visible for $[\mathrm{uC}_k\mathrm{mim}]^+$, whereas the effect for $[\mathrm{C}_k\mathrm{mim}]^+$ seems to level off.

7.11 Designing refractive index based on cation/anion combinations

Combining α_i and V_i^{MPD} of the ions in Eq. (7.1), we produced a map of the estimated refractive index at the sodium D line of 1216 ion pairs, see Fig. 7.6. In this figure, ions are ordered according to their MPD_i values (increasing from bottom to top and left to right) and the numerical values can be consulted in Table S4 of the Supplementary Material section. We studied the accuracy of our estimations by comparing them to available experimental data: 30% of the ILs were predicted with an absolute error below 0.005 in the refractive index and about 50% with an error below 0.01 (see Fig. S1 in the Supplementary Material). The refractive index of more than 75% of the ILs composing

the test group was predicted with an absolute error below 0.02, and 87% was predicted with an error below 0.03. In addition, there is a set of ILs that our model fails to predict their refractive index, which is mainly consistent on ILs based on mono-atomic halogen ions $[Cl]^-$ and $[Br]^-$. Halogen-based ILs comprise about 9.9% of the entire IL test set. The wrong evaluation of their refractive index could be attributed to bulk effects or due to our volume treatment, which could fail when considering mono-atomic ions. Thus, discarding this set of ions, the error we commit in predicting the refractive index is close to the one obtained with the training set employed to calibrate the volume conversion from ions to ILs.

The sequence on the y-axis on the map corresponds to the MPD_i ranking in Fig. 7.1. As expected and visible by the color code in Fig. 7.6, the refractive index n for a given cation follows most often the corresponding MPD_i of the anions.

However, there are exceptions such as those ILs based on the $[FAP]^-$ anion. These ILs present refractive indices markedly lower than the ones which would correspond them according to their position in the MPD_i ranking. This is because the volume V_{IL} is not the sum of the molecular volumes V_i^{MPD}, but a volume-cross term has to be taken into account, see Eq. (7.2). As $[FAP]^-$ is the biggest anion under investigation, its cross-term is the largest, and, consequently, it has a larger impact on the resulting refractive indices.

Many high refractive index compounds with $n > 2.0$ are solid at room temperature, e.g., AsI_3 or SnI_4. In 2006, Seddon et al. tried to make ionic liquids with that high refractive indices.[235] However, only those based on the polyiodides $[I_7]^-$ and $[I_9]^-$ reached that threshold value. In a theoretical study, it was proposed to exchange the cation in $[C_2mim][I_x]$ with ethylammonium to decrease the polyiodides to $[I_3]^-$.[263] Notwithstanding, the map in Fig. 7.6 opens a new path for achieving ILs with remarkably high refractive index by exploiting extensive charge delocalization on the cations. According to Eq. (7.14), the refractive index threshold of 2.0 can also be achieved by long
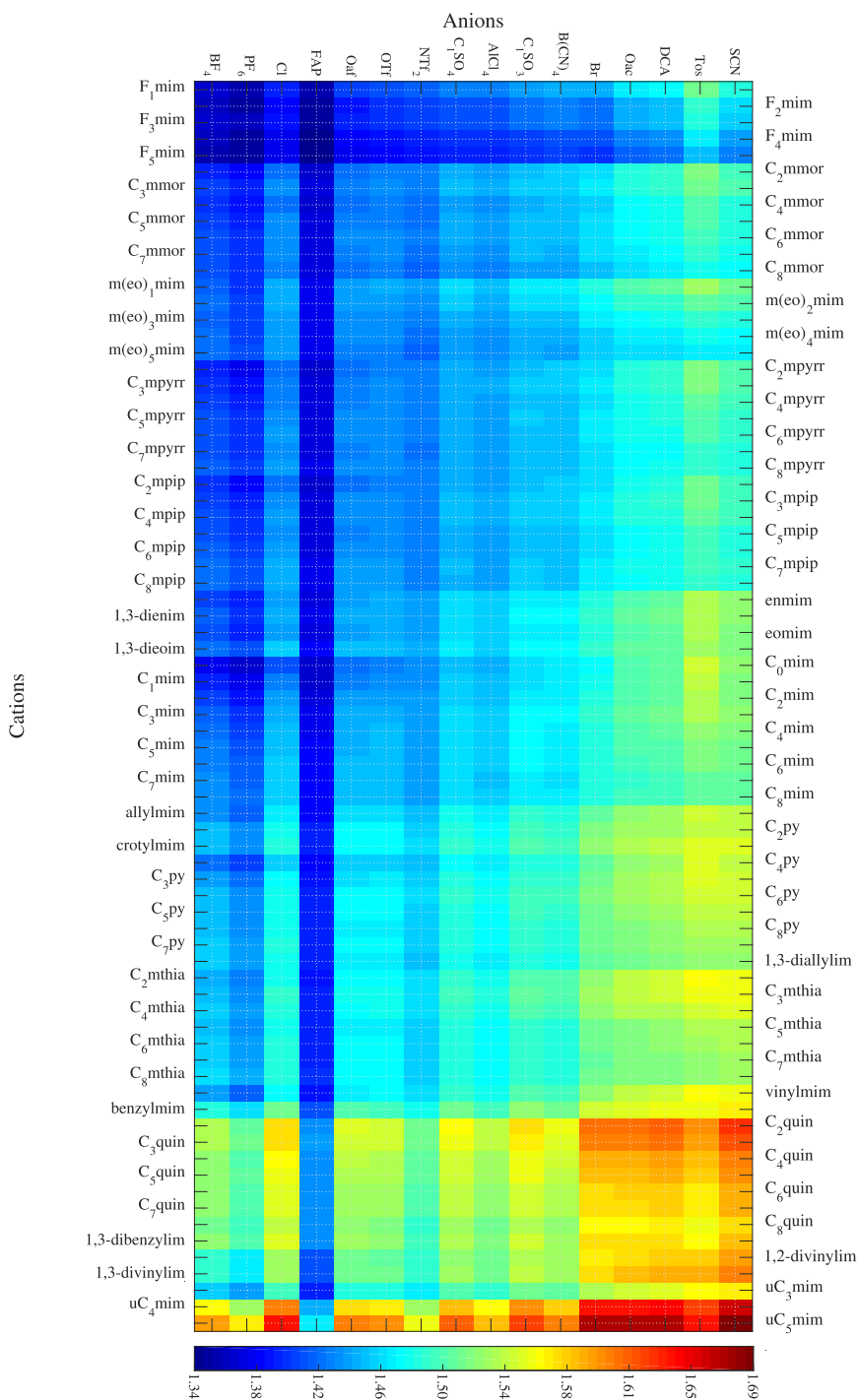
Figure 7.6: Map of the predicted refractive index of the combinations of the different ions at $\lambda = 589$ nm. Meaning of abbreviations can be found in the Tables of the supplementary material.
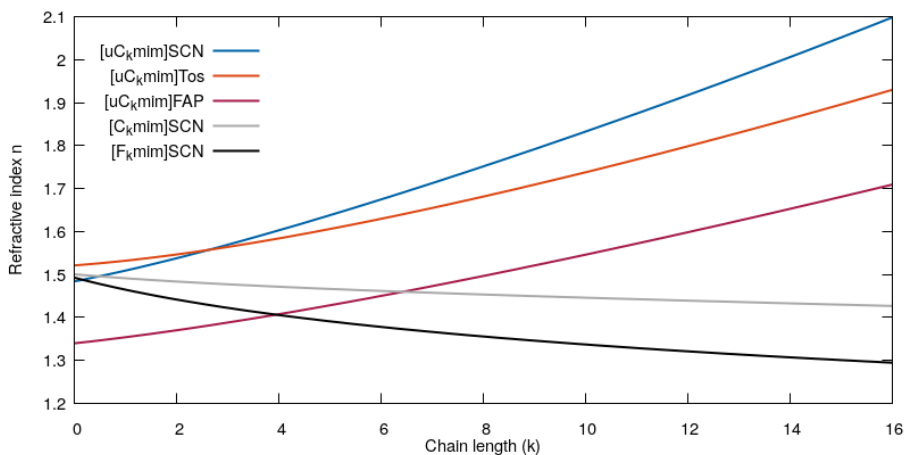
Figure 7.7: Prediction of the refractive index as a function of the cationic alkyl chain length k.

conjugated chain imidazoliums with $[SCN]^-$ or $[Tos]^-$ as visible in Fig. 7.7. The ionic liquid combinations proposed here have the advantage that the anions are stable. Polyiodides are not transparent in the visible range, and, moreover, they tend to decompose into $[I_2]^-$ and smaller iodide anions. For the $[uC_k mim]^+$ cations, the molar volume is a linear function with the chain length, but the electronic polarizability is not. In consequence, the refractive index increases with increasing chain length k. However, it was experimentally found that unsaturated systems also reach a saturation regime when the number of repetition units is large enough,[309] which is not taken into account in Fig. 7.7. Interestingly, very high refractive indices are even possible with hydrophobic $[FAP]^-$ anions using the cation's charge delocalization effect. On the other hand, in imidazoliums with saturated side chains, the number of CH_2 units should be as low as possible to have significant refractive indices.

7.12 Conclusions

In this chapter, we discuss the effect that the presence of delocalized electrons in conjugated systems on the molecular structures of ionic liquid-forming ions induces in their electronic polarizability. The usual assumption of uniform, additive contributions of atoms or molecular groups in the molecules is seen to be invalid for this particular case, because of the practical impossibility to define electronically independent intramolecular groups. Moreover, we modified the conventional treatment of quantum-mechanical volumes derived from the electron density evaluation, leading to significantly improved predictions of volume-based properties of large ionic liquid ions. We applied these more accurate volumes to the prediction of the refractive index, but also other volume-based properties such as density can also be predicted with increased precision.

On the other hand, in the past, most notable efforts to deliver ionic liquids with high refractive indices have focused on the design of optimal anions with highly polarizable atoms. However, in the present chapter, we showed that increasing the fraction of delocalized electrons in the ionic liquid molecular species (e.g. including imidazolium cations with long, unsaturated side chains) high refractive indices can be also achieved. Indeed, the carbon polarizability in unsaturated carbon side chains is not uniform as predicted by former theories, but exhibits a parabolic behavior. Here, carbons in the middle of the side chain may have atomic polarizabilities that are more than twice that of the corresponding terminal carbons, and the charge delocalization effect also extends to the aromatic ring. Finally, a map of the refractive index of the 1216 combinations of anions and cations studied in this work is provided, depicting the high polarizability regions in the geography of the ionic liquid world.

7.13 Acknowledgments

7.14 Supporting material

List of ions

In this chapter, a large set of IL-forming ions distributed in three groups of cations, as well as one group of anions, were considered. The group of anions is shown in Table 7.S1 and it includes some of the most commonly used anions in the field of ionic liquids.

The first group of cations is shown in Table 7.S2, and it includes seven different families of cationic heterocycles with a variable alkyl length chain. The second group of cations is shown in Table 7.S3, and it includes diverse singly and doubly substituted imidazolium species.

Table 7.S1: List of anions studied in this work.

Compound	Abbreviation	α_i /Å^3	V_i /Å^3
4-methylbenzenesulfonate	[Tos]$^-$	18.530	198.40
Acetate	[Oac]$^-$	7.108	85.06
Bis(trifluoromethylsulfonyl)imide	[NTf$_2$]$^-$	14.466	206.35
Bromide	[Br]$^-$	4.367	58.95
Chloride	[Cl]$^-$	2.604	52.66
Dicyanamide	[DCA]$^-$	7.635	88.95
Hexafluorophosphate	[PF$_6$]$^-$	4.289	97.38
Methylsulfate	[C$_1$SO$_4$]$^-$	8.001	114.36
Methylsulfonate	[C$_1$SO$_3$]$^-$	7.767	107.04
Tetracyanoborate	[B(CN)$_4$]$^-$	11.630	153.89
Tetrafluoroborate	[BF$_4$]$^-$	3.110	73.18
Thiocyanate	[SCN]$^-$	7.165	79.22
Trifluoroacetate	[Oaf]$^-$	6.007	98.62
Trifluoromethanesulfonate	[OTf]$^-$	7.526	116.37
Trifluorotris(perfluoroethyl)phosphate	[FAP]$^-$	16.939	289.72

Table 7.S2: List of families of cationic heterocycles studied in this chapter.

Compound	Abbreviation	$\alpha_i(k=2)$ /Å^3	$V_i(k=2)$ /Å^3
1-alkyl-3-methylimidazolium	[C$_k$mim]$^+$	11.758	157.91
1-alkylpyridinium	[C$_k$py]$^+$	12.243	156.38
1-alkyl-1-methylpyrrolidinium	[C$_k$mpyrr]$^+$	12.354	173.00
1-alkyl-1-methylpiperidinium	[C$_k$mpip]$^+$	14.132	195.40
1-alkyl-1-methylmorpholinium	[C$_k$mmor]$^+$	13.020	181.45
1-alkyl-3-methylthiazolium	[C$_k$mthia]$^+$	13.433	163.44
1-alkylquinolinium	[C$_k$quin]$^+$	20.303	209.32

Finally, the last group of cations is shown in Table 7.S4, and it includes imidazolium-based cations with different kinds of functionalized chains attached to them. Specifically perfluorinated, oxygenated and alkyl unsaturated (polyenyl) chains are considered together with a standard alkyl chain which serves as a reference.

Table 7.S3: List of substituted imidazoliums with π bonds in the side chain.

Compound	Abbreviation	α_i /Å^3	V_i /Å^3
1-allyl-3-methylimidazolium	[allylmim]$^+$	13.749	173.42
1,3-diallylimidazolium	[1,3-diallylim]$^+$	17.251	211.32
1-benzyl-3-methylimidazolium	[benzylmim]$^+$	20.364	233.38
1,3-dibenzylimidazolium	[1,3-dibenzylim]$^+$	31.111	332.90
1-crotyl-3-methylimidazolium	[crotylmim]$^+$	15.968	194.37
1-ethoxy-3-methylimidazolium	[eomim]$^+$	12.855	171.11
1,3-diethoxyimidazolium	[1,3-dieoim]$^+$	15.853	205.28
1-ethylnitrile-3-methylimidazolium	[enmim]$^+$	11.931	159.79
1,3-diethylnitrileimidazolium	[1,3-dienim]$^+$	13.921	182.69
1-methyl-3-vinylimidazolium	[vinylmim]$^+$	12.262	150.89
1,2-divinylimidazolium	[1,2-divinylim]$^+$	16.561	184.69
1,3-divinylimidazolium	[1,3-divinylim]$^+$	15.040	166.07

Table 7.S4: List of imidazolium-based cation families with functionalized chains.

Compound	Abbreviation	$\alpha_i(k=2)$ /Å^3	$V_i(k=2)$ /Å^3
1-alkyl-3-methylimidazolium	[C$_k$mim]$^+$	11.758	157.91
1-meth(oxyethyl)$_k$-3-methylimidazolium	[m(eo)$_k$mim]$^+$	19.144	251.59
1-methyl-3-perfluoroalkylimidazolium	[F$_k$mim]$^+$	11.836	182.46
1-polyenyl-3-methylimidazolium	[uC$_k$mim]$^+$	12.262	150.89

Evaluation of the refractive indices

We performed an evaluation of the predictive performance of our model by comparing our ion pair calculations with experimental refractive indices of ILs at 298 K. However, we only found available experimental measurements of 71 different ILs, most of them based on imidazolium, pyrrolidinium and pyridinium cations.[26,44,159–161,164,166,167,171,173,174,232,233,235,245,254,255,257,258,324–403] [40,41,43,45,46,95–98,100,151,154,155,163,165,168,169,172,231,260,404–443] For ILs with more than one available value, we took the average of reported values.
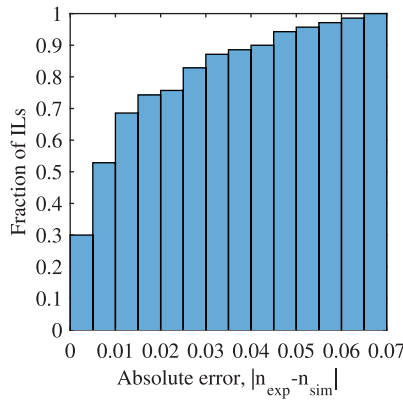
Figure 7.S1: Cumulative frequency histogram of the absolute deviations $|n_{sim} - n_{exp}|$ between the simulated refractive indices and experimental measurements for 71 different ILs at λ = 589 nm and T = 298 K.

Table 7.S5: Values of the simulated refractive index for each ion combination.

	BF$_4$	PF$_6$	Cl	FAP	Oaf	OTf	NTf$_2$	C$_1$SO$_4$	AlCl$_4$	C$_1$SO$_3$	B(CN)$_4$	Br	Oac	DCA	Tos	SCN
F$_1$mim	1.37	1.36	1.39	1.36	1.40	1.41	1.42	1.43	1.43	1.43	1.44	1.44	1.47	1.47	1.51	1.48
F$_2$mim	1.36	1.35	1.38	1.35	1.39	1.40	1.40	1.41	1.41	1.42	1.43	1.42	1.44	1.45	1.49	1.46
F$_3$mim	1.37	1.36	1.39	1.35	1.39	1.40	1.40	1.41	1.41	1.42	1.42	1.42	1.44	1.45	1.48	1.45
F$_4$mim	1.36	1.35	1.38	1.34	1.38	1.39	1.39	1.40	1.40	1.40	1.41	1.41	1.43	1.43	1.46	1.44
F$_5$mim	1.36	1.35	1.37	1.34	1.38	1.38	1.39	1.39	1.39	1.40	1.40	1.40	1.42	1.42	1.45	1.43
C$_2$mmor	1.39	1.38	1.42	1.37	1.42	1.43	1.43	1.44	1.44	1.45	1.45	1.46	1.48	1.48	1.51	1.49
C$_3$mmor	1.40	1.39	1.43	1.37	1.43	1.43	1.43	1.45	1.44	1.45	1.45	1.47	1.48	1.49	1.51	1.50
C$_4$mmor	1.40	1.39	1.42	1.37	1.42	1.43	1.42	1.44	1.43	1.45	1.45	1.46	1.47	1.47	1.50	1.48
C$_5$mmor	1.41	1.39	1.43	1.37	1.43	1.43	1.42	1.44	1.44	1.45	1.45	1.46	1.47	1.48	1.50	1.48
C$_6$mmor	1.41	1.40	1.43	1.37	1.43	1.43	1.42	1.44	1.44	1.45	1.45	1.46	1.47	1.48	1.49	1.48
C$_7$mmor	1.41	1.40	1.43	1.37	1.43	1.43	1.42	1.44	1.43	1.45	1.44	1.46	1.47	1.47	1.49	1.48
C$_8$mmor	1.41	1.40	1.43	1.37	1.42	1.42	1.42	1.43	1.43	1.44	1.44	1.45	1.46	1.46	1.48	1.47
m(eo)$_1$mim	1.41	1.40	1.44	1.38	1.44	1.44	1.44	1.46	1.45	1.47	1.47	1.48	1.50	1.50	1.52	1.51
m(eo)$_2$mim	1.42	1.41	1.44	1.38	1.44	1.44	1.43	1.45	1.45	1.46	1.46	1.47	1.48	1.49	1.50	1.50
m(eo)$_3$mim	1.42	1.41	1.44	1.37	1.43	1.43	1.42	1.44	1.44	1.45	1.45	1.46	1.47	1.47	1.49	1.48
m(eo)$_4$mim	1.42	1.41	1.44	1.37	1.43	1.43	1.42	1.44	1.43	1.44	1.44	1.46	1.46	1.47	1.48	1.47
m(eo)$_5$mim	1.42	1.41	1.44	1.37	1.43	1.43	1.42	1.44	1.43	1.44	1.44	1.45	1.46	1.46	1.47	1.47
C$_2$mpyrr	1.39	1.38	1.42	1.36	1.42	1.43	1.43	1.44	1.44	1.45	1.45	1.46	1.48	1.49	1.52	1.50
C$_3$mpyrr	1.40	1.39	1.43	1.37	1.43	1.43	1.43	1.45	1.44	1.45	1.45	1.46	1.48	1.49	1.51	1.50
C$_4$mpyrr	1.40	1.39	1.43	1.37	1.43	1.43	1.43	1.44	1.44	1.45	1.45	1.46	1.48	1.48	1.50	1.49
C$_5$mpyrr	1.41	1.40	1.43	1.37	1.43	1.43	1.43	1.44	1.44	1.45	1.45	1.46	1.48	1.48	1.50	1.49
C$_6$mpyrr	1.41	1.40	1.43	1.37	1.43	1.43	1.43	1.44	1.44	1.45	1.45	1.46	1.47	1.48	1.50	1.49
C$_7$mpyrr	1.41	1.40	1.43	1.37	1.43	1.43	1.42	1.44	1.44	1.45	1.45	1.46	1.47	1.47	1.49	1.48
C$_8$mpyrr	1.42	1.41	1.44	1.37	1.43	1.43	1.42	1.44	1.44	1.45	1.45	1.46	1.47	1.47	1.49	1.48
C$_2$mpip	1.40	1.38	1.42	1.37	1.42	1.43	1.43	1.44	1.44	1.45	1.45	1.46	1.48	1.48	1.51	1.49
C$_3$mpip	1.41	1.39	1.43	1.37	1.43	1.43	1.43	1.45	1.44	1.45	1.45	1.47	1.48	1.48	1.51	1.49
C$_4$mpip	1.41	1.40	1.44	1.37	1.43	1.43	1.43	1.45	1.44	1.45	1.45	1.47	1.48	1.48	1.50	1.49

170

C$_5$mpip	1.41	1.40	1.43	1.37	1.43	1.43	1.42	1.44	1.44	1.45	1.45	1.46	1.47	1.48	1.49	1.48
C$_6$mpip	1.41	1.40	1.44	1.37	1.43	1.43	1.42	1.44	1.44	1.45	1.45	1.46	1.47	1.47	1.49	1.48
C$_7$mpip	1.42	1.41	1.44	1.38	1.43	1.44	1.43	1.45	1.44	1.45	1.45	1.46	1.47	1.48	1.49	1.48
C$_8$mpip	1.42	1.41	1.44	1.38	1.44	1.44	1.43	1.45	1.44	1.45	1.45	1.46	1.47	1.47	1.49	1.48
enmim	1.40	1.39	1.44	1.37	1.44	1.44	1.44	1.46	1.45	1.47	1.47	1.48	1.50	1.51	1.53	1.52
1,3-dienim	1.42	1.40	1.45	1.38	1.44	1.45	1.44	1.46	1.45	1.47	1.47	1.48	1.50	1.51	1.53	1.52
eomim	1.41	1.39	1.44	1.37	1.44	1.44	1.44	1.46	1.45	1.47	1.47	1.48	1.50	1.50	1.53	1.52
1,3-dieoim	1.42	1.41	1.45	1.38	1.45	1.45	1.44	1.46	1.46	1.47	1.47	1.49	1.50	1.51	1.52	1.52
C$_0$mim	1.38	1.36	1.41	1.36	1.42	1.43	1.43	1.45	1.45	1.46	1.46	1.47	1.50	1.51	1.54	1.52
C$_1$mim	1.39	1.38	1.42	1.37	1.43	1.43	1.43	1.45	1.45	1.46	1.47	1.47	1.50	1.50	1.54	1.52
C$_2$mim	1.40	1.39	1.43	1.37	1.43	1.44	1.44	1.46	1.45	1.47	1.47	1.48	1.50	1.51	1.53	1.52
C$_3$mim	1.41	1.40	1.44	1.38	1.44	1.45	1.44	1.46	1.45	1.47	1.47	1.48	1.50	1.51	1.53	1.52
C$_4$mim	1.42	1.41	1.45	1.38	1.44	1.45	1.44	1.46	1.45	1.47	1.47	1.48	1.50	1.50	1.52	1.51
C$_5$mim	1.42	1.41	1.45	1.38	1.44	1.45	1.44	1.46	1.45	1.47	1.47	1.48	1.50	1.50	1.52	1.51
C$_6$mim	1.43	1.41	1.45	1.38	1.45	1.45	1.44	1.46	1.45	1.47	1.47	1.48	1.49	1.50	1.51	1.51
C$_7$mim	1.43	1.42	1.45	1.38	1.45	1.45	1.44	1.46	1.45	1.47	1.46	1.48	1.49	1.49	1.51	1.50
C$_8$mim	1.43	1.42	1.46	1.38	1.45	1.45	1.44	1.46	1.45	1.47	1.46	1.48	1.49	1.49	1.50	1.50
allylmim	1.43	1.41	1.46	1.38	1.46	1.46	1.45	1.48	1.47	1.49	1.48	1.50	1.52	1.52	1.54	1.54
1,3-diallylim	1.45	1.43	1.48	1.39	1.47	1.47	1.46	1.48	1.47	1.49	1.49	1.51	1.52	1.53	1.54	1.54
crotylmim	1.45	1.43	1.48	1.39	1.47	1.47	1.46	1.49	1.48	1.50	1.49	1.52	1.53	1.53	1.55	1.55
C$_2$py	1.42	1.41	1.46	1.38	1.45	1.46	1.45	1.47	1.46	1.48	1.48	1.50	1.52	1.52	1.55	1.54
C$_3$py	1.44	1.42	1.47	1.39	1.46	1.46	1.45	1.48	1.47	1.49	1.49	1.51	1.52	1.53	1.54	1.54
C$_4$py	1.45	1.43	1.48	1.39	1.47	1.47	1.46	1.49	1.47	1.49	1.49	1.52	1.53	1.53	1.54	1.54
C$_5$py	1.45	1.43	1.48	1.39	1.47	1.47	1.46	1.48	1.47	1.49	1.49	1.51	1.52	1.53	1.54	1.54
C$_6$py	1.45	1.43	1.48	1.39	1.47	1.47	1.45	1.48	1.47	1.49	1.48	1.51	1.52	1.52	1.53	1.53
C$_7$py	1.45	1.44	1.48	1.39	1.47	1.47	1.45	1.48	1.47	1.49	1.48	1.51	1.51	1.52	1.52	1.53
C$_8$py	1.45	1.44	1.48	1.39	1.47	1.47	1.45	1.48	1.47	1.49	1.48	1.50	1.51	1.51	1.52	1.52
C$_2$mthia	1.44	1.42	1.48	1.39	1.47	1.47	1.46	1.49	1.48	1.50	1.50	1.52	1.54	1.54	1.56	1.56
C$_3$mthia	1.45	1.43	1.48	1.39	1.47	1.48	1.46	1.49	1.48	1.50	1.50	1.52	1.54	1.54	1.55	1.55
C$_4$mthia	1.45	1.44	1.48	1.39	1.47	1.47	1.46	1.49	1.48	1.50	1.49	1.52	1.53	1.53	1.54	1.54
C$_5$mthia	1.45	1.43	1.48	1.39	1.47	1.47	1.45	1.48	1.47	1.49	1.48	1.51	1.52	1.52	1.53	1.53
C$_6$mthia	1.45	1.44	1.48	1.39	1.47	1.47	1.45	1.48	1.47	1.49	1.48	1.51	1.52	1.52	1.53	1.53
C$_7$mthia	1.45	1.44	1.48	1.40	1.47	1.47	1.45	1.48	1.47	1.49	1.48	1.51	1.51	1.52	1.52	1.53
C$_8$mthia	1.46	1.44	1.48	1.40	1.47	1.47	1.45	1.48	1.47	1.49	1.48	1.51	1.51	1.52	1.52	1.53
vinylmim	1.44	1.42	1.47	1.39	1.46	1.47	1.46	1.49	1.48	1.50	1.49	1.52	1.53	1.54	1.56	1.55
benzylmim	1.48	1.46	1.51	1.41	1.50	1.49	1.47	1.51	1.49	1.52	1.51	1.54	1.55	1.55	1.55	1.56
C$_2$quin	1.53	1.51	1.57	1.43	1.55	1.54	1.51	1.56	1.54	1.57	1.55	1.61	1.61	1.61	1.60	1.63
C$_3$quin	1.53	1.51	1.57	1.44	1.54	1.54	1.51	1.55	1.53	1.57	1.55	1.60	1.60	1.61	1.59	1.62
C$_4$quin	1.52	1.50	1.56	1.43	1.53	1.53	1.50	1.54	1.53	1.55	1.54	1.58	1.59	1.59	1.58	1.60
C$_5$quin	1.52	1.50	1.55	1.43	1.53	1.53	1.50	1.54	1.52	1.55	1.54	1.58	1.58	1.59	1.57	1.60
C$_6$quin	1.52	1.50	1.55	1.43	1.53	1.52	1.50	1.54	1.52	1.54	1.53	1.57	1.57	1.58	1.57	1.59
C$_7$quin	1.52	1.50	1.55	1.43	1.53	1.52	1.50	1.54	1.52	1.54	1.53	1.57	1.57	1.57	1.56	1.58
C$_8$quin	1.51	1.49	1.54	1.43	1.52	1.52	1.49	1.53	1.51	1.53	1.52	1.56	1.56	1.56	1.55	1.57
1.3-dibenzylim	1.52	1.50	1.54	1.43	1.52	1.52	1.49	1.53	1.52	1.54	1.53	1.57	1.57	1.57	1.56	1.58
1,2-divinylim	1.49	1.46	1.52	1.41	1.51	1.51	1.48	1.52	1.51	1.53	1.52	1.56	1.57	1.58	1.58	1.59
1,3-divinylim	1.49	1.46	1.53	1.41	1.51	1.51	1.49	1.53	1.51	1.54	1.53	1.57	1.58	1.58	1.58	1.60
uC$_3$mim	1.45	1.44	1.49	1.40	1.48	1.48	1.47	1.50	1.48	1.51	1.50	1.53	1.54	1.55	1.56	1.56
uC$_4$mim	1.56	1.53	1.60	1.44	1.57	1.57	1.53	1.58	1.56	1.60	1.58	1.64	1.64	1.65	1.62	1.66
uC$_5$mim	1.59	1.56	1.64	1.46	1.60	1.60	1.55	1.61	1.58	1.63	1.60	1.68	1.67	1.68	1.64	1.69

8. Hyperpolarizability and nonlinear optical response in ionic liquids

[a] Grupo de Nanomateriais, Fotónica e Materia Branda, Departamentos de Física Aplicada e de Física de Partículas, Universidade de Santiago de Compostela.

[b] Department of Computational Biological Chemistry, University of Vienna.

As other organic molecules, ILs can show different nonlinear (NL) optical phenomena. However, the number of works devoted to experimentally determine NL optical magnitudes in ILs is still scarce.[88,120–123,127,444–451] In contrast, several characterization techniques based on NL optics were successfully applied to ILs for studying their ultra-fast dynamics,[129,130,132,133] bulk[123,134] or interface structure.[135–140,452,453] Recently, some computational works have shed light on the magnitude of the NL optical response of ILs by calculating the first and second hyperpolarizabilities of some ILs, as well as of their forming ions.[123–126,451,454,455] However, despite these pioneering works, further investigation on the origins of this NL response is required to determine reliable rules to design ILs with tailored NL optical properties. In this regard, it is well-known that charge delocalization induced by π-orbitals largely increases the NL response of organic molecules.[456,457] Recent works, such as those of Refs. [458] and [459], deal with the influence of structure and/or charge delocalization in the NL response of families of organic molecules different from those yielding ILs.

The purpose of this chapter is to determine the role that delocalized

electronic charge in π-orbitals plays in the NL optical response of a variety of IL-forming ions. For this reason, the molecular volume, first and second hyperpolarizabilities of 92 ions were systematically calculated at the B3LYP/6-311++G(d,p) level of theory for two NL processes, Second Harmonic Generation, SHG, $\beta(-2\omega; \omega, \omega)$, and Electro-Optical Kerr-Effect, EOKE, $\gamma(-\omega; \omega, 0, 0)$. The results are discussed in terms of the hyperpolarizability and molecular volume ratio of each species, and the most interesting ions for enhancing the nonlinear response of ILs are identified. Additionally, the hypothesis of additive hyperpolarizability in ILs is revisited and exploited to provide a complete map of the EOKE susceptibilities in the IL world, comprised by 1496 ion combinations. This map is intended to be a valuable tool to guide the future research on the nonlinear optical properties of ILs.

8.1 Materials

The name, abbreviation and structure of all the ions can be consulted in the Supplementary Material section of this chapter. The considered ions include a set of anions that are commonly found in literature, Table 8.S1, together with cations specially chosen to study the influence of the presence of π-orbitals in their NL response. The cations can be classified into three different groups.

The first one comprises nine different families of cations, including ammonium and phosphonium based-cations and seven different cationic heterocycles, all of them bearing an alkyl chain of variable length, see Table 8.S2. While the ammonium-based cations, $[N_{0,0,0,k}]^+$ and $[N_{1,1,1,k}]^+$, and phosphonium-based cations, $[P_{4,4,4,k}]^+$, $[P_{8,8,8,8}]^+$ and $[P_{6,6,6,14}]^+$, present a purely saturated character, the heterocyclic cations present different extents of charge delocalization, ranging from those clearly aromatic such as 1-alkylpyridinium, $[C_k py]^+$, or 1-alkyl-3-methylthiazolium, $[C_k mthia]^+$, to those clearly aliphatic, such as 1-alkyl-1-methylpiperidinium, $[C_k mpip]^+$, or 1-alkyl-1-methylpyrrolidinium, $[C_k mpyrr]^+$.

The second set of cations are singly and doubly substituted imidazolium derivatives incorporating π-bonds into different extents and in various positions, Table 8.S3. Some examples of the attached substituents are allyl, benzyl, crotyl or vinyl groups.

The third set of cations is composed by four different families of imidazolium-based cations that differ in the functionalization and extension of their side chains, Table 8.S4. It includes a family bearing a perfluorinated alkyl chain, 1-methyl-3-perfluoroalkylimidazolium, $[F_k\text{mim}]^+$, a family with a side chain incorporating oxygen, 1-meth(oxyethyl)$_k$-3-methylimidazolium, $[m(eo)_k\text{mim}]^+$ and a polyenyl side-chain, $[uC_k\text{mim}]^+$, which provides direct access to a charge delocalization region of variable extension. Furthermore, the conventional imidazolium cation bearing an alkyl chain of variable length is also considered, 1-alkyl-3-methylimidazolium, $[C_k\text{mim}]^+$.

8.2 Hyperpolarizabilities

Electronic polarizability, α, SHG first hyperpolarizability, $\beta(-2\omega, \omega, \omega)$, and EOKE second hyperpolarizability, $\gamma(-\omega, \omega, 0, 0,)$, at $\lambda = 1100$ nm were calculated, except indicated otherwise, for isolated ions in gas phase. The employed level of theory was the B3LYP/6-311++G(d,p), chosen in accordance with recent works dealing with the NL optical properties of ILs, which rely on the same level of theory[451] or combinations of the B3LYP functional with related basis sets.[124,125]

As hyperpolarizabilities are tensors whose elements depend on the molecular direction, all the magnitudes provided in this chapter correspond to those more easily accessible from the experimental point of view when dealing with liquid samples. Assuming that all the fields involved in the nonlinear process are parallel polarized, these magnitudes are: i) first hyperpolarizability in the direction of the molecular dipole, $\beta_{||}$, and, ii) the isotropic average of the second

hyperpolarizability, $\langle\gamma\rangle$:[456,460–462]

$$\beta_{||} = 1/5 \sum_j (\beta_{ijj} + \beta_{jij} + \beta_{jji}), \qquad (8.1)$$

and

$$\langle\gamma\rangle = 1/15 \sum_{i,j} (\gamma_{iijj} + \gamma_{ijij} + \gamma_{ijji}). \qquad (8.2)$$

Hyperpolarizabilities are magnitudes that increase with the molecular size. Since ionic species of very different sizes and features are compared in this chapter, we decided to discuss them in terms of their hyperpolarizability and molecular volume ratio, magnitude we will refer as molecular hyperpolarizability density. Since both first and second hyperpolarizabilities are considered, we defined both Molecular First Hyperpolarizability Density, M1HD = $\frac{\beta_{||}}{V}$, and Molecular Second Hyperpolarizability Density, M2HD = $\frac{\langle\gamma\rangle}{V}$.

8.3 Calculation of nonlinear susceptibilities

The nonlinear susceptibilities corresponding to the effective hyperpolarizabilities defined in Eqs. (8.1) and (8.2) are:

$$\chi_{IL}^{(2)}(-\omega_a; \omega_b, \omega_c) \approx f(\bar{\omega})^3 \frac{\beta_{||}^{IL}}{\varepsilon_0 V_{IL}}, \qquad (8.3)$$

and

$$\chi_{IL}^{(3)}(-\omega_a; \omega_b, \omega_c, \omega_d) \approx f(\bar{\omega})^4 \frac{\langle\gamma^{IL}\rangle}{\varepsilon_0 V_{IL}}, \qquad (8.4)$$

where V_{IL}, $\beta_{||}^{IL}$ and $\langle\gamma^{IL}\rangle$ are the molecular volume and hyperpolarizabilities of the IL, and the Lorentz field factors were approximated by an average field factor at $\lambda = 1100$ nm, $f(\bar{\omega})$.[463,464]

8.4 The effect of charge delocalization

The influence of charge delocalization in the hyperpolarizability of molecules can be depicted using different quantum-mechanical models.[303,465–467] In one of the simplest approximations, the delocalized π electrons are described as an electron gas of 2N electrons inside a potential well of length L under the perturbation of an external electric field. The second hyperpolarizability of this system can be calculated by summing up the fourth derivative of the energy E_ξ of each excited state ξ in the system with respect to the electric field F:[303]

$$\gamma = -2\sum_{\xi=1}^{N}\frac{1}{6}\frac{\partial^4 E_\xi}{\partial F^4} = \frac{128L^{10}}{a_0^3 e^2}\sum_{\xi=1}^{N}\left(\frac{-2}{9\pi^6\xi^6} + \frac{140}{3\pi^8\xi^8} - \frac{440}{\pi^{10}\xi^{10}}\right),$$
(8.5)

where e is the electron charge and a_0 the Bohr radius. According to Eq. (8.5), the second hyperpolarizability presents a tenth-power dependence on the size of the region where the electrons are delocalized, L. This distance can be just the length of a σ or a π bond, or that of conjugated systems of coupled π orbitals. As for second hyperpolarizability, a power dependence on L is also expected for first hyperpolarizability.[466,467] However, additionally, first hyperpolarizability also presents a strong dependence on the geometry of the considered system, since it must be zero in the presence of inversion symmetry.[456,468] Furthermore, some recent studies also reported that, for a specific one dimensional potential well, it is possible to predict a maximum theoretical value for first hyperpolarizability,[469] as well as both a minimum and a maximum value of the second hyperpolarizability.[470]

In order to evaluate the extent of charge delocalization of the ions considered in this chapter, we used as a reference the absolute value of the charge-delocalization estimator known as Multi-Center Bond Order (MCBO) index.[318] This parameter was calculated by means of the Multiwfn 3.8 program.[319] The MCBO index of each ion was

calculated in the two possible directions of the regions where charge delocalization was evaluated. Furthermore, as in our case these regions include different numbers of atoms, we worked with the normalized version of the MCBO parameter.[320]

8.5 Charge delocalization and hyperpolarizability on the anion

Anions commonly used in ILs generally do not present extensive conjugated systems. However, they have π orbitals because they often present double and triple bonds. Some examples of families of anions having double bonds are acetates, triflates or sulfates while triple bonds are present in all anions with the nitrile group such as dicyanamide or thiocyanate. The π orbitals participating in these double and triple bonds often form part of small resonant structures that cover an important part of the anions. Hence, despite most of the commonly used anions do not have large conjugated systems, some of them present charge delocalization on considerably large fractions of their molecular structures. The MCBO index, M1HD and M2HD of the studied IL-forming anions are shown in Table 8.1.

MCBO indices of the anions range from 0.17 to 0.73 due to their large structural and compositional differences. Anions with MCBO index ranging from 0.17 to 0.31 show, in general, the lowest M1HD and M2HDs. The M1HDs are very low in magnitude and of negative sign for $[OTf]^-$ and $[NTf_2]^-$, and even negligible, for the more symmetric $[B(CN)_4]^-$ anion. The highest M1HD within this group is found for $[C_1SO_4]^-$, which also shows the largest MCBO index. Anions with MCBO indices in the range $0.40 - 0.49$ show higher hyperpolarizability densities than those of lower MCBO indices. The exception is $[N(CN)_2]^-$, which shows slightly lower values for both M1HD and M2HD than $[C_1SO_4]^-$, despite having a larger MCBO index. In this case, the M1HD is negative but of greater magnitude than those shown by $[OTf]^-$ or $[NTf_2]^-$. For the other anions in this MCBO index range, the increase of hyperpolarizability density is evident. The

Table 8.1: MCBO index, M1HD and M2HD of selected anions.

Anion	$|MCBO|$	M1HD $/10^{-23}$ C^3J^{-2}	M2HD $/10^{-33}$ C^4mJ^{-3}
$[OTf]^-$	0.17	-0.56	6.01
$[NTf_2]^-$	0.23	-0.34	5.02
$[B(CN)_4]^-$	0.26	$\simeq$ -0	5.65
$[C_1SO_4]^-$	0.31	5.07	9.55
$[Tos]^-$	0.40	9.27	15.87
$[C_1SO_3]^-$	0.47	11.44	17.31
$[N(CN)_2]^-$	0.49	-3.48	9.26
$[Oac]^-$	0.51	53.59	72.72
$[SCN]^-$	0.73	13.41	27.14

anions with MCBO index values comprised between 0.51 and 0.73 show the highest hyperpolarizability densities, being the highest ones those of ILs with the $[Oac]^-$ anion. The M1HDs and M2HDs of all the studied anions are shown in Fig. 8.1.

As expected, symmetric anions such as $[BF_4]^-$, $[PF_6]^-$, $[AlCl_4]^-$, $[FAP]^-$ or the above mentioned $[B(CN)_4]^-$ present a vanishing first hyperpolarizability density, which is also true for monoatomic anions such as $[Cl]^-$ or $[Br]^-$. Highly fluorinated anions tend to provide small but negative first hyperpolarizabilities as it is the case of $[Oaf]^-$, $[OTf]^-$ or $[NTf_2]^-$, while asymmetric anions without fluorine provide positive first hyperpolarizability and higher M1HDs as it is the case of $[C_1SO_3]^-$, $[C_1SO_4]^-$, $[Tos]^-$, $[SCN]^-$ or $[Oac]^-$. It is interesting how the fluorination of the $[Oac]^-$ to yield $[Oaf]^-$, apart from changing the hyperpolarizability sign, produces a strong reduction of its magnitude, already observed by Bardak et al.[455] Decrease of the M1HD also happens upon introduction of a new O atom in $[C_1SO_3]^-$ to produce $[C_1SO_4]^-$, indicating that the introduction of highly electronegative atoms could be inconvenient if not used properly. In this regard,
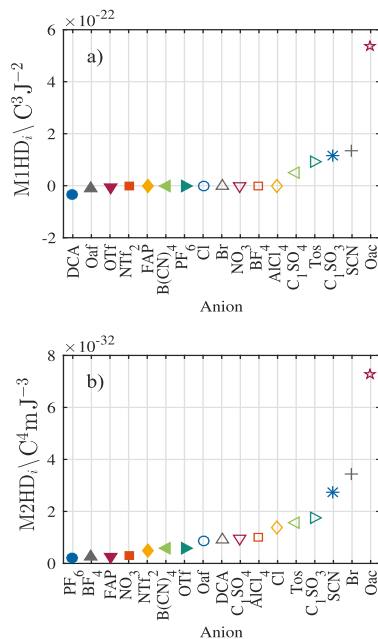
Figure 8.1:   a) M1HD and b) M2HD for the studied anions.

it is well known that combining donor and acceptor regions in a molecule linked by extended conjugated systems greatly enhances hyperpolarizabilities.[456]

The trend for the first hyperpolarizabilities used to calculate the M1HD values (see Supplementary material section of this chapter) matches that of isolated anions in other computational works,[125,455] which also predict negligible first hyperpolarizability for symmetric anions and good responses for anions showing charge delocalization such as [Oaf]⁻, [Tos]⁻ or [Oac]⁻. At the quantitative level agreement is not so good, since very different levels of theory were used in the calculations. Our values are up to three times higher than those at the M06-2X/6-311++G(d,p) level of theory shown in Ref. [455].

Regarding M2HDs, the smallest values are shown by anions containing a large amount of fluorine atoms such as $[BF_4]^-$, $[PF_6]^-$

or also [FAP]$^-$, which again shows that the introduction of fluorine is inconvenient to achieve large hyperpolarizabilities. Other organic anions containing fluorine such as [OTf]$^-$ or [NTf$_2$]$^-$ present slightly higher M2HD values. Monoatomic halogen anions show relatively good M2HDs, which seem to be larger the larger their atomic numbers. Introduction of metal atoms by means of metal complexes such as [AlCl$_4$]$^-$, produces moderate responses, at least as far as closed-shell metal cations are involved. However, the largest responses are those of organic anions without fluorine atoms, such as [C$_1$SO$_3$]$^-$, [C$_1$SO$_4$]$^-$, [Tos]$^-$, [SCN]$^-$ or [Oac]$^-$. Again, fluorination of [Oac]$^-$ to yield [Oaf]$^-$ decreases the M2HDs, as well as the introduction of a fourth oxygen atom in [C$_1$SO$_3$]$^-$ to produce [C$_1$SO$_4$]$^-$. Curiously, despite the extensive conjugated system in [Tos]$^-$, its M2HD is not the highest one, possibly due to a cyclic arrangement of this moiety. The large values of M1HDs and M2HDs of [SCN]$^-$ and [Oac]$^-$ make them the most promising anions to achieve strong NL responses in ILs.

The second hyperpolarizability used to calculate the M2HD values (see Supplementary material section of this chapter) shows a trend almost identical to that provided in Ref. [455] for isolated anions at the M06-2X/6-311++G(d,p) level of theory. However, the numerical agreement is not good because of the differences in the chosen functionals. Our values are one order of magnitude smaller than those presented in that work, just the opposite to the behavior found for the first hyperpolarizabilities. Interestingly, the trend we predict for anions is also close to that shown in Ref. [455] for ILs sharing different anions with the same cation, which points to the large influence of anions in the second hyperpolarizabilities of ILs.

8.6 Influence of the cationic core

A large number of IL-forming cations are derivatives of ammonium and phosphonium cations, or cationic heterocycles bearing alkyl chains of variable length, k. In Table 8.2, the MCBO index, M1HD and M2HD

of different IL-forming cations with a butyl side chain ($k = 4$) are shown.

Table 8.2: MCBO index, M1HD and M2HD of ammonium, phosphonium and heterocycle-based cations bearing the same alkyl chain length (k = 4). For the [C_4quin]$^+$ cation the MCBO index was calculated on the perimeter involving both cycles.

Cation	|MCBO|	M1HD $/10^{-23}$ C^{3}J^{-2}	M2HD $/10^{-33}$ C^{4}mJ^{-3}
[$N_{0,0,0,4}$]$^+$	0.26	3.61	4.98
[$P_{4,4,4,4}$]$^+$	0.30	0.90	5.85
[C_4mpyrr]$^+$	0.28	1.26	4.00
[C_4mpip]$^+$	0.30	0.66	4.19
[C_4mmor]$^+$	0.31	1.42	4.22
[C_4mim]$^+$	0.58	2.68	5.64
[C_4mthia]$^+$	0.59	4.39	7.33
[C_4py]$^+$	0.59	6.96	8.22
[C_4quin]$^+$	0.63	1.54	5.99

The considered heterocycles can be separated into two groups according to their MCBO index values. The first group is formed by aliphatic cations with MCBO index values ranging from 0.26 to 0.31, and it includes ammonium and phosphonium derivatives as well as non conjugated heterocyclic cations. The M1HD and M2HD values in this group are, respectively, within the range of $0.66 - 3.61 \cdot 10^{-23}$ C^{3}J^{-2} and $4.00 - 5.85 \cdot 10^{-33}$ C^{4}mJ^{-3}. While [C_4mmor]$^+$, [C_4mpip]$^+$ and [C_4mpyrr]$^+$ heterocyclic cations present similar M2HDs, the M1HD is slightly lower for [C_4mpip]$^+$. On the other hand, the ammonium and phosphonium-based cations, [$N_{0,0,0,4}$]$^+$ and [$P_{4,4,4,4}$]$^+$, present the highest M2HDs, behavior that could be related to their lack of cycles and linear arrangement of their alkyl chains, as discussed later in the text. Since symmetry plays a major role in molecular first hyperpolarizability,[456,468] the M1HD of the very asymmetric [$N_{0,0,0,4}$]$^+$ cation is high whereas the M1HD of the centrosymmetric [$P_{4,4,4,4}$]$^+$ cation could be expected to be negligible. Nevertheless, it presents a

low but non negligible value, which, according to Ref. [126], could be explained by a certain symmetry distortion originated by the Janh-Teller effect arising from the lack of an electron in the phosphorus atom.

The second group of cations is composed by those that show a certain degree of charge delocalization, their MCBO index values range from 0.58 to 0.63, and their M1HD and M2HD are, respectively, within the range of $1.54 - 6.96 \cdot 10^{-23}$ C^3J^{-2} and $5.64 - 8.22 \cdot 10^{-33}$ C^4mJ^{-3}. Both the M1HD and M2HD of the cations bearing a single ring in this group grow in this order: $[C_4mim]^+ < [C_4mthia]^+ < [C_4py]^+$. With regard to the $[C_4quin]^+$ cation, it does not lead to particularly high hyperpolarizability densities, maybe because of the presence of the second cycle in its structure.

8.7 Influence of the alkyl chain length

The cations considered up to now are often tailored by modifying the length of their alkyl chains. Fig. 8.2, shows the evolution of $\beta_{||}$, M1HD, $\langle \gamma \rangle$ and M2HD as a function of the alkyl chain length for the cationic cores considered in the previous section.

The first, $\beta_{||}$, and second hyperpolarizability, $\langle \gamma \rangle$, increase with the chain length for all the cations. In both cases increasing the number of CH_2 units produces a net contribution to the hyperpolarizabilities, and, for the first hyperpolarizability case, the increase of the asymmetry of the molecule with the chain length may also play a role. With regard to the slopes, it is similar for the aliphatic cations and lower than that of the cations with aromatic heterocycles. For the aromatic cations the first and second hyperpolarizabilities increase in the same order found for the species with $k = 4$, $[C_kmim]^+ < [C_kmthia]^+ < [C_kpy]^+$. Again, an exception to this trend is $[C_kquin]^+$, which behaves similarly to an aliphatic cation, maybe, again, due to the second ring. The difference in slopes as a function of the heterocycle conjugation was already observed by Castellanos-Águila et al.,[124] when comparing the first hyperpolarizability of pyridinium and imidazolium cations as a function

USC
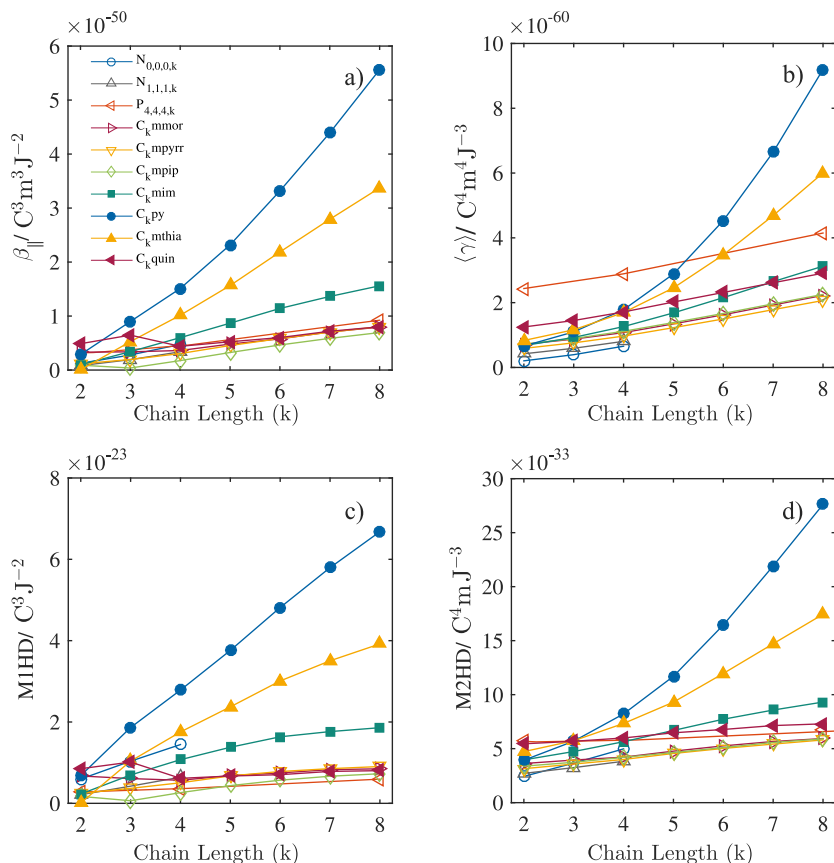
Figure 8.2: (a) First hyperpolarizability, $\beta_{||}$, (b) second hyperpolarizability $\langle\gamma\rangle$, (c) M1HD, and (d) M2HD as a function of the alkyl chain length for several ammonium, phosphonium and heterocycle-based cations.

of the chain length. In that work, the slope differences were proposed to be originated by changes in the conjugation of the heterocycles produced by the steric effects associated to the increase of the alkyl chain.

The increase of first and second hyperpolarizabilities with the

alkyl chain length is in agreement with the results reported in recent computational works for $[N_{2,k,k,k}]^+$ based cations[126] as well as imidazolium and pyridinium based cations.[124,125,451] With regard to the numerical agreement of first hyperpolarizability, our figures are slightly higher but compatible with those given in the above mentioned works, specially taken into account that we are comparing with static calculations, sometimes involving smaller basis sets and using different definitions of first hyperpolarizability. For instance, for the imidazolium cation with $k = 4 - 8$, our first hyperpolarizability (see Supplementary material section) is in the range of $1.6 - 4.2 \cdot 10^{-30}$ esu while in Ref. [124] it is approximately in the range of $1.2 - 3.2 \cdot 10^{-30}$ esu. For the pyridinium cation, at the same k interval, we obtained first hyperpolarizability values of $4.1 - 15.0 \cdot 10^{-30}$ esu and, in Ref. [124], an approximate value of $2.3 - 4.9 \cdot 10^{-30}$ esu was reported. Moreover, for the $[C_4mim]^+$ cation, our first hyperpolarizability value is slightly higher than that given by Bardak et al.[455] using the M06-2X functional, while, our second hyperpolarizability value, is almost one order of magnitude smaller, showing the strong functional dependence of these magnitudes. Additionally to computational evidences, available experimental measurements of the first hyperpolarizability of imidazolium-based ILs also point to a small increase of this magnitude with the chain length for the $[C_kmim]^+$ family.[123]

With respect to the hyperpolarizability densities, values shown by aliphatic cations are smaller than those of the aromatic ones, which increase in the order $[C_kmim]^+ < [C_kmthia]^+ < [C_kpy]^+$. The introduction of the molecular volume compensates the large hyperpolarizabilities of the bulkiest cation families, such as $[P_{4,4,4,k}]^+$, as well as reduces the impact of increasing the alkyl chain length. For long alkyl chains, all aliphatic cations (and $[C_kquin]^+$), reach a saturation regime with similar hyperpolarizability densities, which is not the case for aromatic cations that benefit to a larger extent of increasing the alkyl chain length.

From these results, the importance of using aromatic heterocycles to improve the NL optical response of ILs is clear. Specifically, it seems

USC
UNIVERSIDADE
DE SANTIAGO
DE COMPOSTELA

that among the considered cations, the ones derived from the thiazolium or pyridinium heterocycles are the most suitable to be used to design ILs with enhanced NL optical response.

8.8 Influence of substituents

A recurrent mechanism for tuning the properties of IL forming cations consists in incorporating functionalized side chains. For this reason, we calculated the hyperpolarizability densities of an imidazolium cation bearing one or two substituents with different number of π bonds and degrees of charge delocalization. The MCBO index, M1HD and M2HD of these cations are shown in Table 8.3.

Table 8.3: MCBO index, M1HD and M2HD of imidazolium-based cations having different substituents.

Cation	|MCBO|	M1HD $/10^{-23}$ C^{3}J^{-2}	M2HD $/10^{-33}$ C^{4}mJ^{-3}
$[C_3mim]^+$	0.33	1.74	4.73
$[C_4mim]^+$	0.34	2.68	5.64
$[eomim]^+$	0.33	1.83	4.14
$[1,3\text{-dieoim}]^+$	0.34	0.78	4.67
$[enmim]^+$	0.34	0.36	3.70
$[1,3\text{-dienim}]^+$	0.32	0.26	3.90
$[allylmim]^+$	0.35	1.12	5.34
$[1,3\text{-diallylim}]^+$	0.37	0.14	6.33
$[crotylmim]^+$	0.32	3.60	6.42
$[benzylmim]^+$	0.36	3.28	7.32
$[1,3\text{-dibenzylim}]^+$	0.35	1.19	9.67
$[vinylmim]^+$	0.40	1.26	5.84
$[1,2\text{-divinylmim}]^+$	0.39	-1.17	7.55
$[1,3\text{-divinylim}]^+$	0.48	0.67	11.39

Singly substituted imidazolium-based cations present higher hyperpolarizability densities the higher the MCBO index value of the substituent. Doubling the substituent leads to different behaviors for M1HD and M2HD. While the M1HD always decreases, since the symmetry of the cation increases, the M2HD always increases, behavior in accordance with Eq. (8.5), which ensures that each new bond contributes to increasing the overall M2HD value. The substituted cations can be distributed in three categories according to their MCBO index values.

The first group contains imidazolium rings with alkyl, ethoxy and ethylnitrile substituents. The first two lack any π bonds, while the third one presents a sp hybridized carbon linked to an N atom. These cations show the lowest hyperpolarizability densities, and their MCBO index values range from 0.32 to 0.34. Among them, the highest values are those of molecules with the butyl group, which also has the largest number of atoms. Comparing propyl, ethoxy and ethylnitrile substituents suggests that substituting C atoms by N or O atoms does not significantly increase the NL response.

The second group includes carbon-based substituents incorporating π bonds in different positions and MCBO index values ranging from 0.32 to 0.37. The presence of isolated π bonds seems to increase the hyperpolarizability density with respect to σ bonds. It can be observed in the higher value of M2HD for [allylmim]$^+$ and [crotylmim]$^+$ cations with respect to their saturated equivalents, [C$_3$mim]$^+$ and [C$_4$mim]$^+$. Curiously, this trend is not totally true for M1HD since the [allylmim]$^+$ cation shows a slightly lower value than [C$_3$mim]$^+$. The benzyl group presents an extensive π conjugated system and, for this reason, it is expected to present large hyperpolarizability densities. Indeed, according to Eq. (8.5), the effective L for the benzene ring is larger than that of the rest of substituents within this group.

The third group comprises imidazolium-based cations with different number of vinyl groups attached at different positions. This category is the one showing the highest MCBO index values, ranging

from 0.39 to 0.48. The high values of the MCBO indices suggest that the electrons in the vinyl group participate to a certain extent in the charge delocalization throughout the imidazolium ring.[471] The M1HDs in this category are not very large due to the large degree of symmetry of the considered cations. As expected, introducing a second vinyl group in the second N of the imidazolium ring produces an important decrease of the overall M1HD. However, interestingly, introducing it in the C between both N atoms ([1,2-divinylmim]$^+$) yields a much limited reduction of M1HD, and specially, leads to change in the sign of the first hyperpolarizability value, which becomes negative. The negative sign in [1,2-divinylmim]$^+$ suggests a net electron flow from the imidazolium ring to the vinyl group, which is playing an electron acceptor role.[472] On the other hand, the M2HD of the vinyl-substituted imidazolium is large and doubling it produces the largest M2HD of the studied substituents.

Another important fact is that the increase of hyperpolarizability densities due to aromatic rings is not as high as expected when comparing it with that of linear chains. Focusing on M2HDs to discard strong symmetry effects, aromatic cyclic substituents, such as the benzyl group, which contains a cycle of 6 conjugated carbon atoms, present NL responses not much higher than those of much shorter linear conjugated substituents, such as those of the vinyl group. Similar evidences of the influence of linear and cyclic arrangements of atoms in the hyperpolarizabilities of cations were also observed for the ammonium, phosphonium and quinolinium charged moieties of the previous section. The differences between the intensity in the NL response of linear and cyclic charge distributions are related to the existence of a dimensional effect,[473] which is widely supported by available experimental measurements.[457,474]

8.9 Influence of functionalized chains

Atomic arrangement and charge delocalization by means of delocalized π bonds play a decisive role in the NL response of cations. For this reason, four families of imidazolium cations bearing functionalized side chains of variable length were simulated. The side chains considered are i) a perfluorinated alkyl chain where the H atoms are replaced by F atoms, ii) an oxygenated chain where the repetition unit is an oxyethyl group, iii) a polyenylic chain where there is an alternance of single and double bonds between carbons, and iv) a common alkyl chain. The first two are interesting since they contain chemical elements beyond H and C. The last two include totally opposite characters, since the alkyl chain only contains highly localized σ bonds, while the polyenyl chain contains resonant π bonds that delocalize the charge throughout all the chain length. Fig. 8.3 shows the M1HD and M2HD of the different types of side chains as a function of their length.

Increasing the chain length leads to an increase of the M1HD values, which present a minimum at the chain length providing cations with the highest symmetry. Alkyl, perfluorinated and oxyethyl chains yield moderate increases of M1HD with the chain length. Among them, the alkyl chain is the one which potentially provides the larger NL response by increasing the chain length. However, these responses are much weaker than that of the polyenylic chain, which produces a huge increase of the M1HD of the cation.

The cations bearing alkyl, perfluorinated and oxyethyl chains show moderate increases of M2HD with k, but much smaller than those of cations with polyenylic chains. The comparison of the alkyl chain with those containing heteroatoms suggests that neither the introduction of F or O in the molecular moieties is favorable for achieving larger NL responses. Interestingly, the introduction of the first unit of the perfluorinated chain is inconvenient for the NL response of the imidazolium ring, since the latter decreases from $k = 0$ to $k = 1$, and

USC
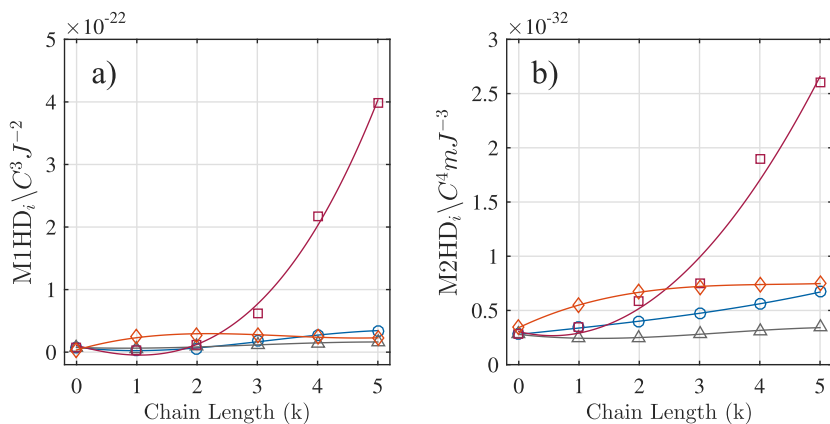
Figure 8.3: M1HDs and M2HDs of imidazolium cations with side chains of variable length. Marker legend: CH_2 ($\circ$), CF_2 ($\triangle$), -CH= (or =CH-) ($\square$) and CH_2-O-CH_2 ($\diamond$). Solid lines only mean to be a guide to the eye.

monotonically increases for larger k values. Moreover, the M2HD of the oxygenated chain seems to reach saturation for relatively low k values. Indeed, for $k = 5$ the alkyl chain length reaches the NL response of the oxygenated chain, even if the latter contains two carbon atoms and one oxygen atom per carbon in the alkyl chain.

8.10 Influence of charge delocalization regions of variable length

In order to obtain a deeper insight into the origins of the differences found for both M1HDs and M2HDs in chains containing only σ bonds and extended π conjugated systems, the molecular volume, V, first hyperpolarizability, $\beta_{||}$, and second hyperpolarizability, $\langle\gamma\rangle$, of an imidazolium cation bearing a saturated alkyl chain or an unsaturated (conjugated) polyenyl chain are shown in Fig. 8.4.

Molecular volume is linear upon increase of both alkyl chains,
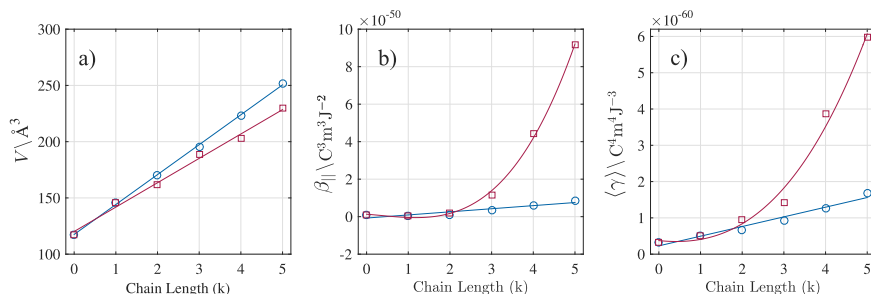
Figure 8.4: a) Molecular volume, V, b) first hyperpolarizability for SHG, $\beta_{||}$, and, c) average second hyperpolarizability for EOKE, $\langle\gamma\rangle$, of a saturated alkyl chain (○) and a polyenyl (conjugated) chain (□) of variable length, k. Solid lines are guides to the eye.

but the slope is larger in the saturated case than for the unsaturated case, which is explained by the shorter bond distance and the lack of a hydrogen atom in its basic unit. This volume inspection reveals that even if the basic units of both chains had the same contribution to hyperpolarizability, the unsaturated one would present larger M1HDs and M2HDs values due to its smaller volume. Nevertheless, conjugated chains also present larger contributions to hyperpolarizabilities than saturated alkyl chains, whose increase is roughly linear with k. Leaving aside geometrical effects, the different behaviors can be qualitatively explained by means of the simple model of Eq. (8.5). In a saturated chain, each σ bond is an independent region of highly localized charge of length L with an independent contribution to the overall molecular hyperpolarizability. This explains the approximately linear increase of $\beta_{||}$ and $\langle\gamma\rangle$ with k, which was also experimentally observed for other families of molecules.[460,475,476] Oppositely, in the polyenylic chain, each new π bond contributes to expand the π conjugated system, thus, there is an effective increase of the length L in Eq. (8.5), where the delocalized electrons are allowed to move. This effect yields a NL increase of the hyperpolarizability due to the power dependence on L. The resulting difference of contributions of alkyl and polyenyl chains

191

to hyperpolarizabilities is huge. For instance, for $k = 5$, the values of $\beta_{||}$ and $\langle\gamma\rangle$ of the cation bearing the polyenyl chain are respectively about 10.5 and 3.5 times larger than those of the saturated chain. Hence, the introduction of linear conjugated regions is a promising mechanism to enhance the NL optical response of specific IL-forming cations.

8.11 Additivity of hyperpolarizabilities

The nonlinear susceptibilities of ILs can be estimated by means of Eqs. (8.3) and (8.4). However, in order to do that, the hyperpolarizability of the ionic pair must be known. The most common procedure to calculate it is performing joint simulations of ionic pairs,[124–126,455] or even considering a higher number of ionic dimers.[123] We have simulated the first and second hyperpolarizability of 36 different ionic pairs together and compared the results with those obtained from the linear addition of the contributions of the i ions they are made of, $\beta_{IL} = \sum_i^N \beta_{||,i}$ and $\gamma_{IL} = \sum_i^N \langle\gamma_i\rangle$. The considered pairs were combinations of ions with different extents of conjugation and symmetries: three cationic heterocycles, $[C_k\text{mpyrr}]^+$, $[C_k\text{mim}]^+$ and $[C_k\text{py}]^+$, with three different alkyl chain lengths, $k = 2, 4, 8$, and four anions, $[\text{SCN}]^-$, $[\text{Oaf}]^-$, $[\text{NTf}_2]^-$ and $[\text{BF}_4]^-$. The results are shown in Fig.8.5.

First hyperpolarizabilities are largely non additive, in perfect agreement with Refs. [124], [125], [126] and [455], but second hyperpolarizabilities present a region where additivity holds, behavior that was already noted in Ref. [455]. The strong differences in the additivity of both hyperpolarizabilities could be related to the important dependence on geometry shown by the first hyperpolarizability, largely affected by the differences in the symmetry of isolated ions and ionic pairs. With respect to second hyperpolarizability, linearity seems to hold for most of the tested ion combinations, but it partially breaks down when dealing with ILs containing highly resonant anions such as $[\text{SCN}]^-$, and in minor extent, $[\text{Oaf}]^-$. This fact could indicate that nonlinearities are stronger in the presence of highly delocalized charges

but also a limitation of the chosen functional to properly describe these interactions. Further research is required to shed more light on this point. Nevertheless, even in the cases where the linear behavior is less evident, the differences between the second hyperpolarizability calculated by both methods are, in general, below a factor of 2.

8.12 Nonlinear susceptibilities of ILs

Using Eqs. (8.3) and (8.4), the nonlinear susceptibility of any IL can be calculated. The field factor can be estimated using the refractive index of the IL at $\lambda = 1100$ nm and molecular volumes can be easily obtained from that of the isolated ions following the procedure described in the previous chapter. On the other hand, the hyperpolarizability of the IL, at least the second order one, can be approximately calculated as the sum of contributions of its ions. This assumption provides a computationally affordable and time-saving strategy to identify the most interesting susceptibilities for NL optics in the IL world. Since additivity is not ensured for the first hyperpolarizability, the rest of this section is focused on third order susceptibility, but a similar discussion for second order susceptibility was included in the Supplementary material section of this chapter.

Under the additivity assumption of second order hyperpolarizability, the third order susceptibility of an IL, $\chi^{(3)}$, can be expressed in terms of the M2HDs of its composing ions:

$$\chi^{(3)} \propto \frac{\gamma_{IL}}{V_{IL}} \leq \sum_{i}^{N} \text{M2HD}_i \cdot \phi_i, \qquad (8.6)$$

being $\phi_i = V_i / \sum_i V_i$ the volume fraction of each species. The inequality mean that the IL susceptibility would be lower than that of the ideal mixture, since the effective volume of the IL is larger than the sum of the ions. According to Eq. (8.6), it could seem that the third order NL susceptibilities of ILs are governed by the commonly bulky cations. Nevertheless, it is important to note that small anions can

USC
UNIVERSIDADE
DE SANTIAGO
DE COMPOSTELA

193
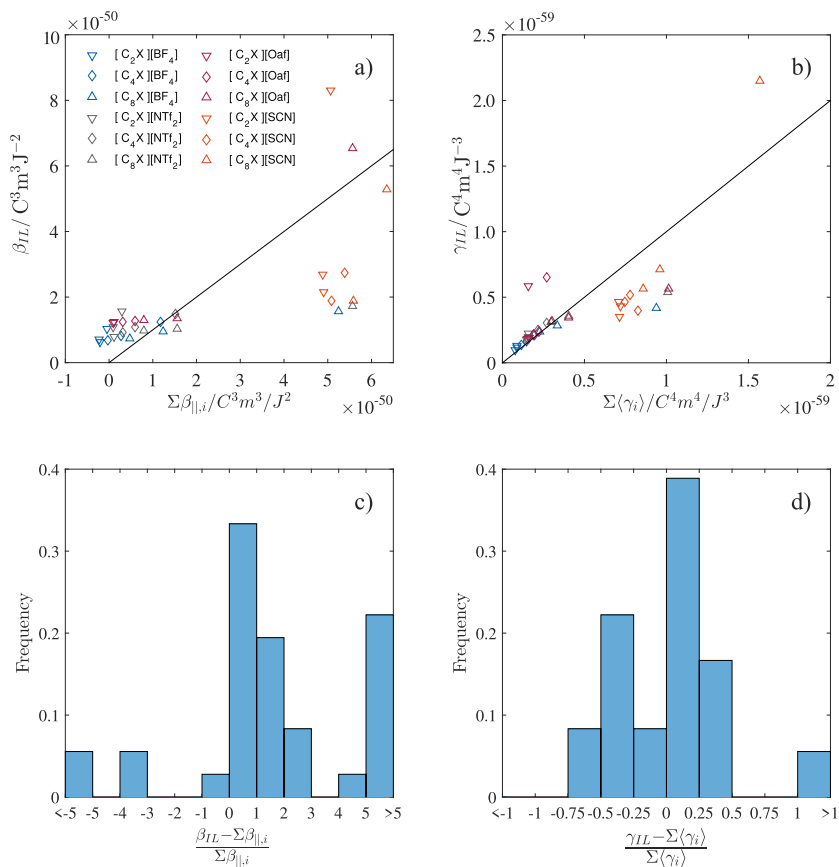
Figure 8.5: Comparison between first hyperpolarizability (a) and second hyperpolarizability (b) of 36 ILs calculated as the sum of the hyperpolarizabilities of the ions, $\beta(-2\omega,\omega,\omega)(\sum_i \beta_i)$ and $\gamma(-\omega,\omega,0,0)(\sum_i \gamma_i)$, and those given by DFT calculations over the ionic pairs, β_{IL} and γ_{IL}. Relative frequency histograms show the relative deviation of both methods in the calculation of (c) first hyperpolarizability and (d) second hyperpolarizability as a function of the number of ILs showing that relative deviation.

present much higher hyperpolarizability densities, counterbalancing the cationic dominance in terms of volume, see Table 8.4.

Table 8.4: M2HD of selected anions and cations.

Anion	M2HD $/10^{-33}$ C^4mJ^{-3}	Cation	M2HD $/10^{-33}$ C^4mJ^{-3}
$[PF_6]^-$	1.91	$[F_5mim]^+$	3.42
$[BF_4]^-$	2.58	$[C_4mpip]^+$	4.19
$[NTf_2]^-$	5.02	$[C_4mim]^+$	5.64
$[OTf]^-$	6.01	$[vinylmim]^+$	5.84
$[N(CN)_2]^-$	9.26	$[m(eo)_5mim]^+$	7.47
$[Tos]^-$	15.87	$[C_4py]^+$	8.22
$[SCN]^-$	27.14	$[1,3\text{-divinylim}]^+$	11.39
$[Oac]^-$	72.72	$[uC_5mim]^+$	26.47

Indeed, the third order NL susceptibility of an IL is given by a delicate interplay between the contributions of its constituent ions. For instance, commonly used inorganic anions such as $[PF_6]^-$ or $[BF_4]^-$ present lower values than those of widely used cations such as $[C_4mim]^+$, $[C_4mpip]^+$ or $[C_4py]^+$. However, other frequent anions such as $[OTf]^-$ or $[NTf_2]^-$ present responses similar to those of these cations, and other anions such as $[Tos]^-$, $[SCN]^-$ or $[Oac]^-$, show much higher M2HDs. In general, a large number of ion combinations yield M2HDs higher than that of the urea, molecule often taken as reference in the NL optics field, whose M2HD is $4.07 \cdot 10^{-33}$ C^4mJ^{-3}.[477] The $\chi^3(-\omega; \omega, 0, 0)$ susceptibilities for the EOKE process at $\lambda = 1100$ nm, for all the combinations of the ions considered in this chapter, is shown in the color map of Fig. 8.6. The corresponding values can be seen in the Supplementary material section of the chapter.

The figure shows that, combinations including the most common IL-forming anions such as $[BF_4]^-$ $[OTf]^-$ or $[NTf_2]^-$, are inconvenient to obtain high third order susceptibilities. Nevertheless, combinations involving anions and cations with large degrees of charge delocalization, i.e., those including aromatic or resonant anions such as $[Tos]^-$, $[SCN]^-$ or $[Oac]^-$ together with strongly aromatic heterocyclic cations such
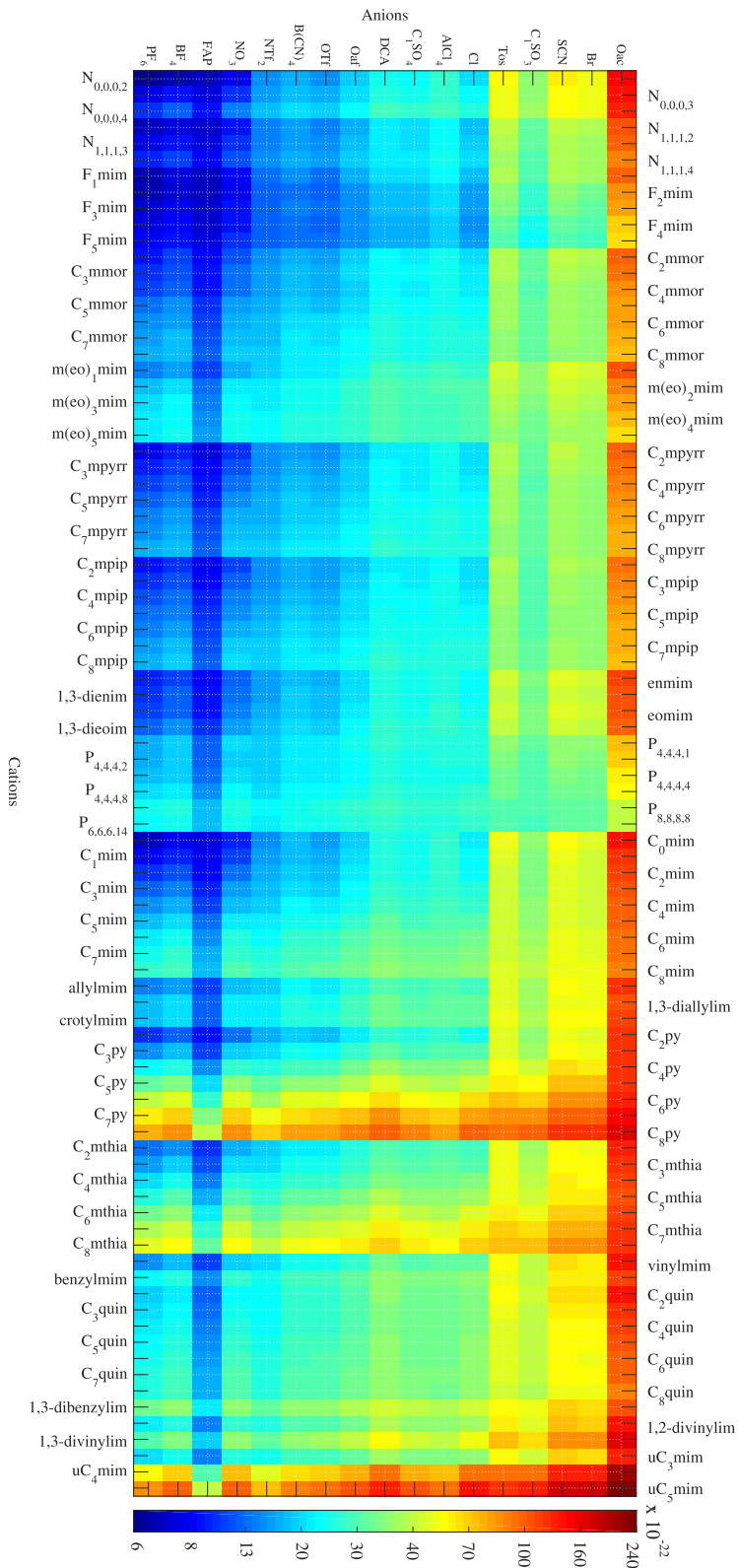
Figure 8.6: Color map of the third order susceptibility $\chi^3(-\omega;\omega,0,0)$ for EOKE at $\lambda = 1100$ nm for the combinations of all the studied ions.

as $[C_4thia]^+$, $[C_4py]^+$ produce the highest third order susceptibilities. Further tailoring of the cation, such as the introduction of an conjugated chain, as in the $[uC_kmim]^+$ family, produces a great increase of the final third susceptibility of the IL, reaching values for $k = 5$ as high as $277 \cdot 10^{-22}$ m^2/V^2. However, further research on these combinations of highly delocalized ions are required, since our additive model is less accurate in this region of the susceptibility map. In this regard, some works suggest that long range charge transfer[478] and thus, accurate predictions of hyperpolarizabilities,[479] can only be properly achieved by the employment of long-range corrected functionals[480] such as CAM-B3LYP[481] or LC-ωPBE.[482]

Comparison of our results with those of other theoretical works can be done in terms of the second hyperpolarizability since susceptibilities are not frequently simulated. For ILs based on combinations of the $[C_4mim]^+$ cation with different anions, we predict a trend of second hyperpolarizability, which is in qualitative agreement with that of the calculations of Ref. [455] at the M06-2X/6-311++G(d,p) level of theory. The most important discrepancies are found for the $[C_4mim][Br]$ and $[C_4mim][Oac]$ ILs, since we predict for this last IL the highest second hyperpolarizability of the series, while this place is occupied by $[C_4mim][Br]$ in Ref. [455]. At the quantitative level, our values are approximately one order magnitude lower than those presented in that work. Nevertheless, this is not surprising since this offset was already noted for isolated ions. Higher quantitative agreement is found for the second hyperpolarizability of the $[C_4mim][Oaf]$ given in Ref. [451], which is just a 20% larger than the one in this chapter. In relation to experimental measurements, available data indicate that our simulations of second order susceptibility overestimate that of the experiments in one order of magnitude. For instance, using the simulated refractive indices of Ref. [471] and the experimental measurements of Ref. [122], we estimate an experimental third order susceptibility for $[m(eo)_1mim][NTf_2]$ of $0.15 \cdot 10^{-21}$ m^2/V^2, while the value simulated in this chapter is $1.7 \cdot 10^{-21}$ m^2/V^2. This trend can also be seen in $[C_4mim][OTf]$, where the experimental third order

susceptibility[451] is $2.3 \cdot 10^{-22}$ m^2/V^2 whereas our estimation yields $22.12 \cdot 10^{-22}$ m^2/V^2. In this last work, from the experimental third order susceptibility, the experimental second hyperpolarizability was extracted, which also was one order of magnitude smaller than our estimations. Indeed, our calculations were in agreement with those carried out in that work, which also overestimated the experimental second hyperpolarizability in one order of magnitude. The generalized overestimation of the second hyperpolarizability of the B3LYP functional suggests that further investigation of the influence of DFT functionals on the hyperpolarizability of ILs is required.

8.13 Conclusions

ILs are highly versatile materials that can be tailored to produce important nonlinear optical responses. The two key factors for designing ILs with enhanced nonlinear responses are charge delocalization and molecular symmetry. While charge delocalization is important both for second and third order responses, the symmetry is more relevant for second order responses, since the more symmetric a molecule is, the less elements in its first hyperpolarizability tensor are different from zero. First hyperpolarizabilities of ILs cannot be obtained by simple addition of those of their constituent ions. However, the second hyperpolarizability exhibits a certain degree of additivity, specifically for ions with low degrees of charge delocalization, which can be exploited to perform efficient calculations of the hyperpolarizability of a large number of ILs. In this regard, we present in this chapter a map of third order nonlinear susceptibilities of ILs, which is expected to be a valuable tool to guide future works on the nonlinear optical properties of these materials. This map indicates that the best option to enhance the nonlinear susceptibility of ILs is keeping small resonant anions and tailoring high aromatic cations, decorating them, for instance, with substituents including aromatic cycles or long linear conjugated regions.

8.14 Acknowledgments

8.15 Supporting material

List of ions

The considered ions could be distributed in three groups of cations and one group of anions. The anions consist on a set of commonly IL-forming anions found in literature, Table 8.S1.

Table 8.S1: List of anions studied in this work.

Compound	Abbreviation	$\beta_i(-2\omega,\omega,\omega)$ /10^{-50}C^{3}m^{3}J^{-2}	$\gamma_i(-\omega,\omega,0,0)$ / 10^{-60}/C^{4}m^{4}J^{-3}	V_i /Å^3
4-methylbenzenesulfonate	[Tos]$^-$	2.00	3.43	198.40
Acetate	[Oac]$^-$	4.78	6.49	85.06
Bis(trifluoromethylsulfonyl)imide	[NTf$_2$]$^-$	-0.08	1.13	206.35
Bromide	[Br]$^-$	0.00	2.12	58.95
Chloride	[Cl]$^-$	0.00	0.76	52.66
Dicyanamide	[DCA]$^-$	-0.32	0.86	88.95
Hexafluorophosphate	[PF$_6$]$^-$	0.00	0.20	97.38
Methylsulfate	[C$_1$SO$_4$]$^-$	0.61	1.16	114.36
Methylsulfonate	[C$_1$SO$_3$]$^-$	1.30	1.96	107.04
Nitrate	[NO$_3$]$^-$	0.00	0.26	80.22
Tetracyanoborate	[B(CN)$_4$]$^-$	0.00	0.93	153.89
Tetrafluoroborate	[BF$_4$]$^-$	0.00	0.20	73.18

Thiocyanate	[SCN]$^-$	1.11	2.25	79.22
Trifluoroacetate	[Oaf]$^-$	-0.13	0.90	98.62
Trifluoromethanesulfonate	[OTf]$^-$	-0.07	0.74	116.37
Trifluorotris(perfluoroethyl)phosphate	[FAP]$^-$	-0.01	0.81	289.72

The first group of cations includes nine different families of cationic cores, with a variable alkyl length chain, Table 8.S2.

Table 8.S2: List of families of cationic cores studied in this work.

Compound	Abbreviation	$\beta_i\,(-2\omega,\omega,\omega)$ $(k=4)$ $/10^{-50}\mathrm{C^3m^3J^{-2}}$	$\gamma_i(-\omega,\omega,0,0)$ $(k=4)$ $/10^{-60}\mathrm{C^4m^4J^{-3}}$	V_i $(k=4)$ $/\mathrm{Å}^3$
1-alkyl-3-methylimidazolium	[C$_k$mim]$^+$	0.60	1.26	204.46
1-alkylpyridinium	[C$_k$py]$^+$	1.51	1.78	198.77
1-alkyl-1-methylpyrrolidinium	[C$_k$mpyrr]$^+$	0.30	0.97	220.07
1-alkyl-1-methylpiperidinium	[C$_k$mpip]$^+$	0.17	1.12	240.43
1-alkyl-1-methylmorpholinium	[C$_k$mmor]$^+$	0.36	1.08	231.44
1-alkyl-3-methylthiazolium	[C$_k$mthia]$^+$	1.014	1.69	210.91
1-alkylquinolinium	[C$_k$quin]$^+$	0.44	1.71	257.17
Alkylamonnium	[N$_{0,0,0,k}$]$^+$	0.48	0.66	123.72
Alkyl(Trimethyl)Ammonium	[N$_{1,1,1,k}$]$^+$	0.34	0.80	193.15
Alkyl(Tributyl)phosphonium	[P$_{4,4,4,k}$]$^+$	0.44	2.89	420.92
Tetraoctylphosphonium	[P$_{8,8,8,8}$]$^+$	0.92	4.15	514.76
Tetradecyl(trihexyl)phosphonium	[P$_{6,6,6,14}$]$^+$	0.79	8.05	791.37

The second group of cations is shown in Table 8.S3, and it includes diverse singly and doubly substituted imidazolium-based cations. Considered substituents present double and triple bonds with different extents of conjugation.

Table 8.S3: List of imidazolium-based cations with delocalized π-systems in the side chain.

Compound	Abbreviation	$\beta_i(-2\omega,\omega,\omega)$ $/10^{-50}\mathrm{C^3m^3J^{-2}}$	$\gamma_i(-\omega,\omega,0,0)$ $/10^{-60}\mathrm{C^4m^4J^{-3}}$	V_i $/\mathrm{Å}^3$
1-allyl-3-methylimidazolium	[allylmim]$^+$	0.21	1.00	173.42
1,3-diallylimidazolium	[1,3-diallylim]$^+$	0.03	1.46	211.32
1-benzyl-3-methylimidazolium	[benzylmim]$^+$	0.84	1.89	233.38
1,3-dibenzylimidazolium	[1,3-dibenzylim]$^+$	0.45	3.67	332.90

1-crotyl-3-methylimidazolium	[crotylmim]$^+$	0.76	1.36	194.37
1-ethoxy-3-methylimidazolium	[eomim]$^+$	0.34	0.77	171.11
1,3-diethoxyimidazolium	[1,3-dieoim]$^+$	0.17	1.05	205.28
1-ethylnitrile-3-methylimidazolium	[enmim]$^+$	0.06	0.77	159.79
1,3-diethylnitrileimidazolium	[1,3-dienim]$^+$	0.05	0.77	182.69
1-methyl-3-vinylimidazolium	[vinylmim]$^+$	0.20	0.95	150.89
1,2-divinylimidazolium	[1,2-divinylim]$^+$	-0.24	1.51	184.69
1,3-divinylimidazolium	[1,3-divinylim]$^+$	0.12	2.04	166.07

The last group of cations includes imidazolium-based cations with functionalized chains of variable length, Table 8.S4.

Table 8.S4: List of imidazolium-based cation families with functionalized chains.

Compound	Abbreviation	$\beta_i(-2\omega,\omega,\omega)$ (k=4) /10^{-50}C^{3}m^{3}J^{-2}	$\gamma_i(-\omega,\omega,0,0)$ (k=4) /10^{-60}C^{4}m^{4}J^{-3}	V_i (k=4) /Å^3
1-alkyl-3-methylimidazolium	[C$_k$mim]$^+$	0.60	1.26	204.46
1-meth(oxyethyl)$_k$-3-methylimidazolium	[m(eo)$_k$mim]$^+$	1.04	3.15	369.71
1-methyl-3-perfluoroalkylimidazolium	[F$_k$mim]$^+$	0.39	0.86	247.57
1-polyenyl-3-methylimidazolium	[uC$_k$mim]$^+$	4.42	3.86	186.72

Tables of computed magnitudes

Molecular volume, first and second hyperpolarizabilities at a wavelength of $\lambda = 1000$ nm of the considered ions are respectively shown in Table 8.S5. Third order susceptibility for the EOKE process at λ=1100 nm, $\chi^3(-\omega;\omega,0,0)$, is given for the different ILs in Table 8.S6.

Table 8.S5: Electronic polarizability, α (SI units, Å^3), first hyperpolarizability, $\beta(-2\omega;\omega,\omega)$ for SHG (SI, esu units), second hyperpolarizability $\gamma(-\omega;\omega,0,0)$ for the EOKE (SI, esu units), all of them at λ=1100 nm, and volume of the considered ions.

	α	α	$\beta(-2\omega;\omega,\omega)$	$\beta(-2\omega;\omega,\omega)$	$\gamma(-\omega;\omega,0,0)$	$\gamma(-\omega;\omega,0,0)$	V
	$/10^{-39}\mathrm{C^2m^2J^{-1}}$	$/\mathrm{\AA}^3$	$/10^{-50}\mathrm{C^3m^3J^{-2}}$	$/10^{-30}$ esu	$/10^{-60}\mathrm{C^4m^4J^{-3}}$	$/10^{-35}$ esu	$/\mathrm{\AA}^3$
Anions							

Anions							
	α	α	$\beta(-2\omega;\omega,\omega)$	$\beta(-2\omega;\omega,\omega)$	$\gamma(-\omega;\omega,0,0)$	$\gamma(-\omega;\omega,0,0)$	V
	$/10^{-39}\mathrm{C^2m^2J^{-1}}$	$/\mathrm{\AA}^3$	$/10^{-50}\mathrm{C^3m^3J^{-2}}$	$/10^{-30}$ esu	$/10^{-60}\mathrm{C^4m^4J^{-3}}$	$/10^{-35}$ esu	$/\mathrm{\AA}^3$
BF_4	0.35	3.11	0.00	0.00	0.20	0.16	73.18
PF_6	0.48	4.29	0.00	0.00	0.20	0.16	97.38
Cl	0.29	2.60	0.00	0.00	0.76	0.62	52.66
NO_3	0.49	4.42	0.00	0.00	0.26	0.21	80.22
FAP	1.88	16.94	-0.01	-0.03	0.81	0.66	289.72
Oaf	0.67	6.01	-0.13	-0.36	0.90	0.73	98.62
OTf	0.84	7.53	-0.07	-0.19	0.74	0.60	116.37
NTf_2	1.61	14.47	-0.08	-0.21	1.13	0.92	206.35
C_1SO_4	0.89	8.00	0.61	1.66	1.16	0.94	114.36
$AlCl_4$	1.26	11.36	0.00	0.00	1.76	1.42	159.30
C_1SO_3	0.86	7.77	1.29	3.50	1.96	1.58	107.04
$B(CN)_4$	1.29	11.63	0.00	0.00	0.93	0.76	153.89
Br	0.49	4.37	0.00	0.00	2.12	1.71	58.95
Oac	0.79	7.11	4.79	12.92	6.49	5.24	85.06
DCA	0.85	7.63	-0.33	-0.88	0.87	0.70	88.95
Tos	2.06	18.53	2.01	5.42	3.44	2.78	198.40
SCN	0.80	7.17	1.11	3.01	2.25	1.82	79.22
Cations							
	α	α	$\beta(-2\omega;\omega,\omega)$	$\beta(-2\omega;\omega,\omega)$	$\gamma(-\omega;\omega,0,0)$	$\gamma(-\omega;\omega,0,0)$	V
	$/10^{-39}\mathrm{C^2m^2J^{-1}}$	$/\mathrm{\AA}^3$	$/10^{-50}\mathrm{C^3m^3J^{-2}}$	$/10^{-30}$ esu	$/10^{-60}\mathrm{C^4m^4J^{-3}}$	$/10^{-35}$ esu	$/\mathrm{\AA}^3$
$N_{0,0,0,2}$	0.52	4.67	0.13	0.34	0.20	0.16	80.11
$N_{0,0,0,3}$	0.72	6.51	0.28	0.75	0.39	0.32	101.85
$N_{0,0,0,4}$	0.93	8.39	0.48	1.28	0.66	0.53	123.72
$N_{1,1,1,2}$	1.07	9.58	0.08	0.22	0.42	0.34	145.16
$N_{1,1,1,3}$	1.27	11.45	0.19	0.52	0.59	0.48	168.65
$N_{1,1,1,4}$	1.48	13.34	0.34	0.91	0.81	0.65	193.15
F_1mim	1.12	10.09	0.09	0.24	0.40	0.33	150.74
F_2mim	1.32	11.84	0.18	0.48	0.48	0.38	182.46
F_3mim	1.56	14.06	0.28	0.75	0.67	0.54	212.26
F_4mim	1.79	16.04	0.39	1.05	0.86	0.69	247.57
F_5mim	2.01	18.02	0.51	1.39	1.07	0.86	278.94
C_2mmor	1.45	13.02	0.33	0.89	0.71	0.58	181.45
C_3mmor	1.66	14.91	0.34	0.91	0.87	0.71	202.86
C_4mmor	1.87	16.79	0.36	0.98	1.08	0.87	231.44
C_5mmor	2.08	18.74	0.48	1.30	1.34	1.09	253.73
C_6mmor	2.30	20.66	0.58	1.56	1.62	1.31	276.12
C_7mmor	2.51	22.60	0.70	1.90	1.93	1.56	301.47
C_8mmor	2.73	24.53	0.80	2.15	2.22	1.80	329.03
$m(eo)_1mim$	1.61	14.51	0.51	1.38	1.14	0.92	191.92
$m(eo)_2mim$	2.13	19.14	0.78	2.11	1.89	1.52	251.59
$m(eo)_3mim$	2.64	23.74	0.99	2.67	2.54	2.05	312.21
$m(eo)_4mim$	3.15	28.34	1.04	2.81	3.15	2.54	369.71
$m(eo)_5mim$	3.66	32.93	1.13	3.05	3.73	3.01	425.05
C_2mpyrr	1.37	12.35	0.12	0.31	0.59	0.48	173.00
C_3mpyrr	1.58	14.24	0.20	0.53	0.76	0.61	194.84
C_4mpyrr	1.79	16.13	0.31	0.83	0.97	0.78	220.07
C_5mpyrr	2.01	18.07	0.45	1.23	1.23	0.99	243.41
C_6mpyrr	2.22	19.99	0.58	1.57	1.50	1.21	267.03
C_7mpyrr	2.44	21.92	0.70	1.89	1.78	1.44	292.34
C_8mpyrr	2.65	23.85	0.80	2.17	2.07	1.67	314.05
C_2mpip	1.57	14.13	0.09	0.24	0.72	0.58	195.40
C_3mpip	1.78	16.04	0.04	0.10	0.89	0.72	217.27
C_4mpip	2.00	17.96	0.17	0.47	1.12	0.90	240.43
C_5mpip	2.22	19.91	0.33	0.88	1.39	1.12	267.45
C_6mpip	2.43	21.86	0.46	1.25	1.67	1.35	290.39

C_7mpip	2.65	23.80	0.59	1.58	1.96	1.59	311.18
C_8mpip	2.86	25.73	0.69	1.87	2.25	1.82	334.51
enmim	1.33	11.93	0.06	0.17	0.64	0.51	159.79
1,3-dienim	1.55	13.92	0.05	0.14	0.77	0.62	182.69
eomim	1.43	12.86	0.34	0.91	0.77	0.62	171.11
1,3-dieoim	1.76	15.85	0.17	0.47	1.05	0.85	205.28
$P_{4,4,4,1}$	3.01	27.08	0.28	0.75	2.36	1.91	350.11
$P_{4,4,4,2}$	3.21	28.85	0.30	0.80	2.44	1.97	371.58
$P_{4,4,4,4}$	3.64	32.70	0.44	1.20	2.89	2.33	420.92
$P_{4,4,4,8}$	4.50	40.49	0.92	2.49	4.15	3.35	514.76
$P_{8,8,8,8}$	7.13	64.05	0.79	2.14	8.05	6.50	791.37
$P_{6,6,6,14}$	7.11	63.92	0.91	2.45	7.64	6.17	784.17
C_0mim	0.87	7.85	0.09	0.25	0.33	0.26	111.05
C_1mim	1.10	9.90	0.04	0.12	0.50	0.40	136.18
C_2mim	1.31	11.76	0.10	0.26	0.67	0.54	157.91
C_3mim	1.53	13.73	0.34	0.92	0.93	0.75	180.52
C_4mim	1.74	15.67	0.60	1.62	1.26	1.02	204.46
C_5mim	1.96	17.64	0.87	2.34	1.68	1.36	228.49
C_6mim	2.18	19.58	1.14	3.08	2.15	1.74	251.15
C_7mim	2.40	21.53	1.36	3.68	2.65	2.14	276.04
C_8mim	2.61	23.47	1.56	4.21	3.13	2.52	297.71
allylmim	1.53	13.75	0.21	0.57	1.00	0.81	173.42
1,3-diallylim	1.92	17.25	0.03	0.09	1.46	1.18	211.33
crotylmim	1.78	15.97	0.76	2.06	1.36	1.10	194.37
C_2py	1.36	12.24	0.29	0.77	0.66	0.53	156.39
C_3py	1.59	14.29	0.90	2.43	1.10	0.89	177.96
C_4py	1.81	16.28	1.51	4.08	1.78	1.44	198.77
C_5py	2.04	18.31	2.32	6.26	2.88	2.33	224.07
C_6py	2.26	20.31	3.32	8.96	4.53	3.66	248.45
C_7py	2.48	22.32	4.39	11.86	6.65	5.37	271.31
C_8py	2.70	24.30	5.56	15.02	9.20	7.43	295.80
C_2mthia	1.49	13.43	0.00	0.01	0.83	0.67	163.44
C_3mthia	1.72	15.47	0.53	1.42	1.16	0.94	186.48
C_4mthia	1.94	17.45	1.01	2.74	1.69	1.37	210.91
C_5mthia	2.17	19.46	1.56	4.22	2.46	1.98	238.64
C_6mthia	2.39	21.44	2.19	5.90	3.48	2.81	260.93
C_7mthia	2.61	23.43	2.79	7.54	4.69	3.79	283.94
C_8mthia	2.82	25.39	3.37	9.11	6.00	4.85	304.74
vinylmim	1.36	12.26	0.20	0.55	0.95	0.76	150.89
benzylmim	2.27	20.36	0.84	2.28	1.89	1.52	233.38
C_2quin	2.26	20.30	0.49	1.32	1.25	1.01	209.32
C_3quin	2.48	22.29	0.65	1.75	1.45	1.17	231.19
C_4quin	2.70	24.30	0.44	1.19	1.71	1.38	257.17
C_5quin	2.92	26.29	0.52	1.41	2.02	1.63	278.67
C_6quin	3.14	28.27	0.60	1.62	2.31	1.87	302.48
C_7quin	3.36	30.23	0.72	1.94	2.61	2.11	322.32
C_8quin	3.58	32.19	0.80	2.16	2.91	2.35	348.00
1.3-dibenzylim	3.46	31.11	0.45	1.22	3.67	2.96	332.90
1,2-divinylim	1.84	16.56	-0.24	-0.64	1.51	1.22	184.69
1,3-divinylim	1.67	15.04	0.12	0.32	2.04	1.65	166.07
uC_3mim	1.63	14.62	1.15	3.10	1.42	1.15	173.99
uC_4mim	2.13	19.10	4.42	11.92	3.86	3.12	186.72
uC_5mim	2.51	22.57	9.15	24.69	5.97	4.82	209.68

Table 8.S6: Values of the simulated third order susceptibilities $\chi^3(-\omega;\omega,0,0)$ for the EOKE process at $\lambda=1100$ nm. SI units, 10^{-22} m^2/V^2.

	BF$_4$	PF$_6$	Cl	NO$_3$	FAP	Oaf	OTf	NTf2	C$_1$SO$_4$	AlCl$_4$	C$_1$SO$_3$	B(CN)$_4$	Br	Oac	DCA	Tos	SCN
N$_{0,0,0,2}$	5.5	6.6	6.9	8.0	14.5	16.6	14.6	18.1	24.0	22.5	26.2	19.6	55.7	38.1	59.6	52.9	146.1
N$_{0,0,0,3}$	7.7	9.1	7.8	10.4	15.5	17.8	16.2	19.6	25.3	23.6	26.7	21.6	53.6	38.0	57.2	51.8	135.3
N$_{0,0,0,4}$	10.5	12.2	9.1	13.6	17.0	19.8	18.5	21.9	27.6	25.5	27.9	24.4	52.6	38.9	56.5	52.0	127.4
N$_{1,1,1,2}$	6.8	7.8	7.2	8.9	13.5	15.1	13.7	16.5	20.2	19.6	22.6	17.7	44.1	31.1	44.4	40.9	106.4
N$_{1,1,1,3}$	8.1	9.2	7.7	10.2	14.0	15.6	14.5	17.1	20.6	19.9	22.6	18.5	42.2	30.5	42.4	39.4	98.6
N$_{1,1,1,4}$	9.5	10.8	8.4	11.7	14.6	16.4	15.5	17.9	21.3	20.5	22.8	19.5	40.7	30.2	40.9	38.4	91.7
F$_1$mim	6.5	7.5	7.0	8.5	13.1	14.6	13.2	15.9	19.4	19.0	22.0	17.1	43.0	30.3	43.0	39.7	103.7
F$_2$mim	6.3	7.1	6.7	8.0	12.1	13.2	12.0	14.3	16.9	16.9	19.7	15.1	37.5	26.3	36.2	33.6	86.7
F$_3$mim	7.4	8.3	7.2	9.1	12.5	13.6	12.7	14.8	17.2	17.1	19.5	15.6	35.5	25.6	34.2	32.1	79.1
F$_4$mim	7.8	8.7	7.4	9.4	12.1	13.2	12.4	14.2	16.3	16.2	18.3	15.0	32.1	23.5	30.5	28.8	68.6
F$_5$mim	8.5	9.4	7.7	10.0	12.2	13.3	12.6	14.3	16.1	16.0	17.9	15.1	30.2	22.6	28.8	27.3	62.5
C$_2$mmor	9.3	10.7	8.4	11.7	14.8	16.7	15.7	18.4	22.1	21.2	23.5	20.1	42.8	31.7	43.8	41.0	99.3
C$_3$mmor	10.4	11.8	8.9	12.8	15.3	17.3	16.4	19.0	22.5	21.6	23.7	20.9	41.6	31.5	42.6	40.2	94.3
C$_4$mmor	11.1	12.5	9.2	13.3	15.3	17.2	16.5	18.8	21.9	21.1	22.9	20.5	38.8	29.8	39.4	37.4	84.6
C$_5$mmor	12.7	14.2	10.1	15.1	16.3	18.3	17.8	20.1	23.3	22.2	23.7	22.0	38.6	30.5	39.6	37.8	81.7
C$_6$mmor	14.2	15.8	11.0	16.6	17.2	19.4	19.0	21.3	24.4	23.2	24.4	23.4	38.4	31.0	39.7	38.1	79.0
C$_7$mmor	15.4	17.1	11.7	17.8	17.9	20.1	19.9	22.1	25.1	23.8	24.8	24.2	37.7	31.0	39.0	37.7	75.0
C$_8$mmor	16.2	17.8	12.2	18.5	18.2	20.4	20.3	22.3	25.1	23.9	24.7	24.4	36.5	30.5	37.8	36.6	70.4
m(eo)$_1$mim	13.7	15.7	10.6	16.8	18.2	20.9	20.3	23.3	27.9	25.9	27.5	26.0	46.8	36.7	49.9	47.2	104.9
m(eo)$_2$mim	17.7	19.9	12.9	20.8	20.3	23.4	23.2	25.8	30.0	27.9	28.6	28.8	44.2	36.7	47.2	45.4	90.5
m(eo)$_3$mim	19.5	21.6	14.1	22.3	21.0	23.9	23.9	26.3	29.8	27.9	28.3	29.0	41.0	35.1	43.6	42.3	78.5
m(eo)$_4$mim	20.6	22.6	14.9	23.2	21.5	24.2	24.4	26.4	29.5	27.8	27.9	29.1	38.7	34.0	41.2	40.2	70.6
m(eo)$_5$mim	21.3	23.2	15.6	23.7	21.7	24.3	24.6	26.5	29.3	27.6	27.6	29.0	36.9	33.1	39.3	38.6	64.8
C$_2$mpyrr	8.3	9.5	7.8	10.5	14.2	15.9	14.8	17.5	21.1	20.4	23.0	19.1	42.8	31.2	43.6	40.7	101.2
C$_3$mpyrr	9.5	10.8	8.4	11.8	14.7	16.6	15.6	18.3	21.7	20.9	23.2	19.9	41.6	31.0	42.4	39.9	95.7
C$_4$mpyrr	10.6	12.0	9.0	12.9	15.1	17.0	16.3	18.7	21.9	21.1	23.1	20.4	39.8	30.3	40.5	38.3	88.3
C$_5$mpyrr	12.2	13.7	9.8	14.6	16.0	18.1	17.5	19.9	23.1	22.0	23.7	21.8	39.2	30.7	40.1	38.3	84.2
C$_6$mpyrr	13.6	15.2	10.6	16.0	16.8	19.0	18.5	20.8	24.0	22.8	24.2	22.9	38.6	30.9	39.7	38.1	80.4
C$_7$mpyrr	14.8	16.4	11.3	17.1	17.5	19.7	19.4	21.6	24.6	23.3	24.4	23.6	37.7	30.8	39.0	37.6	76.2
C$_8$mpyrr	16.1	17.8	12.1	18.5	18.3	20.6	20.4	22.6	25.6	24.2	25.1	24.8	37.7	31.4	39.2	37.9	74.2
C$_2$mpip	9.0	10.2	8.1	11.2	14.3	16.0	15.1	17.6	20.9	20.2	22.6	19.2	40.8	30.2	41.3	38.8	93.9
C$_3$mpip	10.1	11.4	8.7	12.3	14.8	16.6	15.8	18.3	21.5	20.7	22.8	20.0	39.7	30.1	40.4	38.2	89.2
C$_4$mpip	11.4	12.9	9.4	13.7	15.5	17.4	16.8	19.2	22.3	21.4	23.1	21.0	38.9	30.1	39.6	37.8	84.6
C$_5$mpip	12.6	14.1	10.1	14.9	16.0	18.0	17.5	19.7	22.7	21.7	23.2	21.6	37.5	29.7	38.3	36.6	78.7
C$_6$mpip	14.0	15.6	10.9	16.3	16.9	19.0	18.7	20.8	23.8	22.6	23.8	22.8	37.2	30.1	38.3	36.9	75.9
C$_7$mpip	15.6	17.3	11.8	18.0	17.9	20.2	20.0	22.2	25.1	23.9	24.8	24.3	37.5	31.1	39.0	37.7	74.6
C$_8$mpip	16.7	18.4	12.5	19.1	18.6	20.9	20.9	23.0	25.9	24.5	25.2	25.2	37.1	31.3	38.8	37.6	72.0
enmim	9.5	11.0	8.5	12.2	15.6	17.8	16.7	19.8	24.2	22.9	25.3	21.9	47.0	34.9	49.4	46.2	113.0
1,3-dienim	10.4	11.9	8.9	13.0	15.8	18.0	17.1	20.0	24.0	22.8	25.0	22.1	44.9	33.9	47.0	44.2	105.2
eomim	10.6	12.2	9.0	13.4	16.2	18.5	17.5	20.6	25.0	23.5	25.7	22.8	46.4	35.1	48.9	45.9	109.4
1,3-dieoim	12.5	14.3	10.0	15.3	17.0	19.5	18.8	21.6	25.7	24.2	25.9	24.0	44.3	34.5	46.7	44.3	100.0
P$_{4,4,4,1}$	16.8	18.5	12.6	19.1	18.6	20.8	20.8	22.8	25.6	24.3	25.0	25.0	36.4	30.8	37.9	36.9	69.8
P$_{4,4,4,2}$	16.4	18.0	12.3	18.6	18.1	20.2	20.2	22.1	24.6	23.4	24.1	24.1	34.8	29.6	36.2	35.3	66.2
P$_{4,4,4,4}$	17.0	18.5	12.8	19.0	18.2	20.2	20.3	22.1	24.3	23.2	23.7	24.0	33.1	28.6	34.4	33.6	60.5
P$_{4,4,4,8}$	19.6	21.2	14.7	21.6	19.9	22.0	22.3	23.8	25.9	24.7	24.8	25.8	32.3	29.1	34.0	33.5	54.8
P$_{8,8,8,8}$	22.9	24.2	17.6	24.4	21.9	23.8	24.4	25.5	27.0	25.9	25.5	27.3	29.8	28.7	31.8	31.8	44.0
P$_{6,6,6,14}$	22.2	23.5	17.1	23.7	21.3	23.2	23.7	24.9	26.3	25.3	24.9	26.6	29.3	28.1	31.3	31.2	43.7
C$_0$mim	7.0	8.2	7.4	9.6	14.9	17.0	15.4	18.9	24.2	22.8	26.0	20.9	52.5	37.4	56.3	51.4	135.6
C$_1$mim	8.5	9.9	8.1	11.2	15.4	17.6	16.3	19.5	24.3	23.0	25.7	21.6	49.5	36.1	52.4	48.5	122.5
C$_2$mim	10.0	11.6	8.8	12.7	16.0	18.3	17.2	20.4	25.0	23.5	25.9	22.6	47.7	35.6	50.4	47.1	114.4
C$_3$mim	12.1	13.9	9.8	15.1	17.2	19.7	18.9	22.0	26.5	24.8	26.7	24.5	46.9	36.1	49.8	47.0	108.3
C$_4$mim	14.6	16.6	11.1	17.7	18.6	21.5	20.9	23.9	28.4	26.4	27.8	26.7	46.3	36.8	49.5	47.1	102.4
C$_5$mim	17.5	19.8	12.7	20.8	20.5	23.7	23.4	26.3	31.0	28.6	29.5	29.5	46.6	38.3	50.3	48.2	98.4
C$_6$mim	20.6	23.1	14.4	24.1	22.6	26.2	26.2	29.1	33.9	31.1	31.5	32.7	47.5	40.3	51.8	50.0	96.2

C_7mim	23.1	25.8	16.0	26.8	24.3	28.1	28.3	31.2	36.0	33.0	32.9	35.0	47.7	41.5	52.4	50.8	92.8
C_8mim	25.6	28.5	17.5	29.4	26.1	30.2	30.6	33.4	38.3	35.1	34.6	37.5	48.6	43.2	53.8	52.4	91.6
allylmim	13.8	15.9	10.6	17.2	18.7	21.8	21.1	24.4	29.8	27.4	29.0	27.7	50.4	39.6	55.1	52.1	117.9
1,3-diallylim	17.3	19.8	12.4	20.9	20.7	24.1	23.8	27.1	32.3	29.6	30.5	30.8	49.4	40.6	54.4	52.2	109.2
crotylmim	17.2	19.8	12.3	21.1	21.0	24.6	24.3	27.7	33.5	30.5	31.4	31.8	51.7	42.2	57.6	55.0	116.8
C_2py	10.3	12.0	8.9	13.2	16.4	18.9	17.9	21.2	26.1	24.4	26.8	23.8	49.4	37.2	53.1	49.8	120.5
C_3py	14.8	17.1	11.1	18.3	19.4	22.7	22.1	25.5	31.0	28.4	29.8	29.0	51.0	40.5	56.2	53.3	118.3
C_4py	21.5	24.7	14.6	26.0	24.1	28.6	28.6	32.2	38.9	34.9	35.0	37.2	55.2	46.6	62.7	60.2	120.1
C_5py	30.7	35.0	19.6	36.4	30.8	36.8	37.5	41.4	49.3	43.6	42.2	47.9	61.0	54.7	71.2	69.0	122.0
C_6py	43.7	49.4	26.9	50.9	40.6	48.7	50.3	54.7	64.4	56.5	53.1	63.4	70.8	67.2	85.0	83.1	130.3
C_7py	59.4	66.8	35.9	68.4	52.7	63.2	65.9	70.9	82.8	72.3	66.6	82.2	83.7	83.0	102.7	101.2	143.7
C_8py	75.8	84.7	45.7	86.4	65.6	78.5	82.2	87.7	101.5	88.7	80.9	101.4	97.1	99.3	120.6	119.4	157.1
C_2mthia	12.7	14.8	10.0	16.1	18.2	21.3	20.4	24.0	29.6	27.2	29.1	27.4	51.9	40.4	57.4	54.2	125.9
C_3mthia	15.6	18.1	11.5	19.3	19.9	23.4	22.9	26.4	32.0	29.3	30.5	30.2	51.5	41.5	57.3	54.6	119.4
C_4mthia	20.0	22.9	13.8	24.1	22.8	26.8	26.8	30.2	36.2	32.8	33.2	34.7	52.4	44.0	58.9	56.6	114.5
C_5mthia	25.2	28.6	16.8	29.8	26.4	31.1	31.5	34.9	41.2	37.1	36.6	39.9	54.1	47.3	61.3	59.4	109.8
C_6mthia	32.9	37.1	21.1	38.3	32.1	38.0	38.9	42.6	49.8	44.5	42.8	48.9	59.4	54.4	68.9	67.3	113.4
C_7mthia	41.1	46.1	25.9	47.3	38.3	45.4	46.9	50.8	58.9	52.4	49.5	58.3	65.2	61.9	77.0	75.6	117.7
C_8mthia	49.8	55.6	31.0	56.8	45.0	53.3	55.4	59.6	68.6	60.9	56.8	68.4	71.8	70.3	86.1	85.0	124.0
vinylmim	14.5	17.0	10.9	18.4	19.8	23.4	22.6	26.4	33.0	29.8	31.3	30.5	55.3	43.6	62.3	58.7	133.4
benzylmim	21.7	24.8	14.6	26.0	23.8	28.1	28.2	31.8	37.7	34.1	34.2	36.6	52.7	45.2	59.9	58.0	113.8
C_2quin	18.2	21.2	12.5	22.5	21.8	25.9	25.9	29.9	36.3	32.8	33.5	35.2	54.9	46.1	64.0	61.9	131.5
C_3quin	19.3	22.3	13.1	23.5	22.2	26.3	26.4	30.2	36.1	32.8	33.3	35.3	53.1	45.1	61.3	59.6	123.0
C_4quin	20.2	23.2	13.7	24.2	22.5	26.4	26.6	30.2	35.5	32.4	32.7	34.8	50.6	43.4	57.6	56.1	112.1
C_5quin	22.0	25.1	14.7	26.1	23.6	27.7	28.0	31.5	36.7	33.5	33.5	36.3	50.2	43.9	57.2	56.0	107.6
C_6quin	23.1	26.1	15.5	27.0	24.1	28.2	28.7	31.9	36.8	33.8	33.6	36.5	49.0	43.3	55.5	54.4	101.4
C_7quin	24.7	27.8	16.4	28.6	25.1	29.3	29.9	33.1	38.0	34.8	34.4	37.9	49.0	43.9	55.7	54.8	99.0
C_8quin	25.0	28.0	16.8	28.8	25.2	29.2	29.8	32.8	37.3	34.3	33.9	37.2	47.2	42.7	53.2	52.4	92.5
1.3-dibenzylim	33.0	37.1	21.0	38.0	31.5	37.0	38.2	41.8	47.9	43.3	41.6	48.1	55.9	52.5	65.5	64.7	106.9
1,2-divinylim	21.2	24.7	14.1	26.2	24.3	29.1	29.2	33.4	40.9	36.3	36.4	39.3	58.9	49.8	69.1	66.4	136.1
1,3-divinylim	29.7	34.9	18.1	36.8	30.8	38.0	38.7	43.8	54.9	46.9	45.2	52.8	70.1	62.1	86.8	83.6	158.9
uC$_3$mim	19.5	22.7	13.4	24.1	23.1	27.6	27.4	31.3	38.5	34.3	34.8	36.4	57.2	47.4	65.8	62.8	131.4
uC$_4$mim	57.0	67.6	30.3	69.9	50.0	63.4	67.1	74.8	93.4	77.1	69.3	93.4	95.4	94.7	129.6	127.8	202.5
uC$_5$mim	85.6	101.1	43.4	103.7	69.7	89.2	95.8	105.7	130.7	106.9	93.4	133.1	119.0	125.8	168.4	168.0	236.4

Second order susceptibilities of ILs considering additive first hyperpolarizability

In the limit of additive first hyperpolarizability, second order susceptibility $\chi^2(-2\omega; \omega, \omega)$ of an IL is related to the M1HD of its constituent ions on the same way that third order susceptibility is related to the M2HD of its constituent ions. It is important to note that this magnitude as also the first hyperpolarizability, is highly dependent on the microscopic symmetry of each system, and, specifically, it vanishes for centrosymmetric materials. For this reason, it must be zero in the

205

bulk of most of ILs since, at the optical scale, they are isotropic liquids. However, it must be emphasized that oriented ionic liquid crystals or ILs at solid state are materials suitable to show important second-order NL responses. In addition, it is worth to mention that, even in an isotropic liquid, NL processes leaded by second order susceptibility can be found arising from regions where isotropy is broken, such as interfaces. In fact, NL processes related to second order susceptibility, such as SHG or Sum Frequency Generation (SFG), have been used to probe and extract valuable information about the distribution and orientation of organic molecules,[483–485] including ILs,[135–138,452] at interfaces. Additionally, certain incoherent NL processes driven by second order susceptibility such as Hyper Rayleigh Scattering (HRS), can also be observed in the bulk of ILs.[123]

As second order susceptibility is related to the M1HD of the ions forming the IL, some design clues can be extracted from data on Table 8.S7.

Table 8.S7: Comparison of M1HD of selected anions and cations.

Anion	M1HD $/10^{-23}$ C^3J^{-2}	Cation	M1HD $/10^{-23}$ C^3J^{-2}
$[PF_6]^-$	$\simeq 0$	$[F_5mim]^+$	1.65
$[BF_4]^-$	$\simeq 0$	$[C_4mpip]^+$	0.66
$[NTf_2]^-$	-0.34	$[C_4mim]^+$	2.68
$[OTf]^-$	-0.56	$[vinylmim]^+$	1.26
$[N(CN)_2]^-$	-3.48	$[m(eo)_5mim]^+$	2.29
$[Tos]^-$	9.27	$[C_4py]^+$	6.96
$[SCN]^-$	13.41	$[1,3\text{-divinylim}]^+$	0.67
$[Oac]^-$	53.59	$[uC_5mim]^+$	39.83

Several of the most commonly used anions in ILs, such as $[BF_4]^-$ or $[PF_6]^-$, are centrosymmetric and, in consequence, have almost zero M1HDs. On the opposite, most common cations present low but non negligible M1HDs. This difference of hyperpolarizability between cationic and anionic species could be exploited to selectively monitor cations at interfaces by means of their second order NL response. On

the other hand, some anions show negative first hyperpolarizabilities, such as $[\text{NTf}_2]^-$, $[\text{OTf}]^-$ or $[\text{N(CN)}_2]^-$. In this case, it should be possible to combine these anions with cations with negative or low M1HD responses so, the final IL would present also negative first hyperpolarizability. Other option is to counterbalance the negative and positive contributions of anions and cations to yield ILs with closely zero first order NL responses, even at interfaces. Nevertheless, maximizing the first order NL response of ILs is also possible by selecting anions with high M1HD, such as $[\text{Tos}]^-$, $[\text{SCN}]^-$ or $[\text{Oac}]^-$. In particular, these anions present much higher NL response than the urea molecule, which is taken as a reference of molecular NL responses and whose M1HD value is $1.55 \cdot 10^{-23}$ C^3J^{-2}.[477] Unfortunately, the low M1HD responses and bulky size of the most common cations limit, in practice, the NL performance of the anions in ILs. This response can be enhanced by using highly aromatic cations such as $[\text{C}_4\text{mthia}]^+$ or $[\text{C}_4\text{py}]^+$ in combination with the proper anions. Further increase of the NL response could be obtained by tailoring cations to present even larger degrees of conjugation. For instance, cations belonging to the $[\text{uC}_k\text{mim}]^+$ family provide ILs with M1HDs 15-30 times greater than that of urea. In Fig. 8.S1 the $\chi^2(-2\omega;\omega,\omega)$ at λ=1100 nm for all the possible combinations of the anions and cations considered in this work are shown in a color map. The corresponding values can be found in Table 8.S8.

Fig. 8.S1 shows that most ion combinations lead to a region with relatively similar second order susceptibilities, but also that particularly high values can be achieved by properly choosing the ions to combine. In this regard, in agreement with the previous discussion, highly aromatic heterocycles such as $[\text{C}_4\text{mthia}]^+$ or $[\text{C}_4\text{py}]^+$ are the most interesting commonly used cations to combine with highly responsive anions such as $[\text{Tos}]^-$, $[\text{SCN}]^-$ or $[\text{Oac}]^-$. Notwithstanding, the best responses are those using the highly conjugated family of cations $[\text{uC}_k\text{mim}]^+$, which, with $k = 5$, provide values of $193 \cdot 10^{-12}$ m/V. Furthermore, as first hyperpolarizability can be negative, highly negative responses can be tailored by combining anions and cations
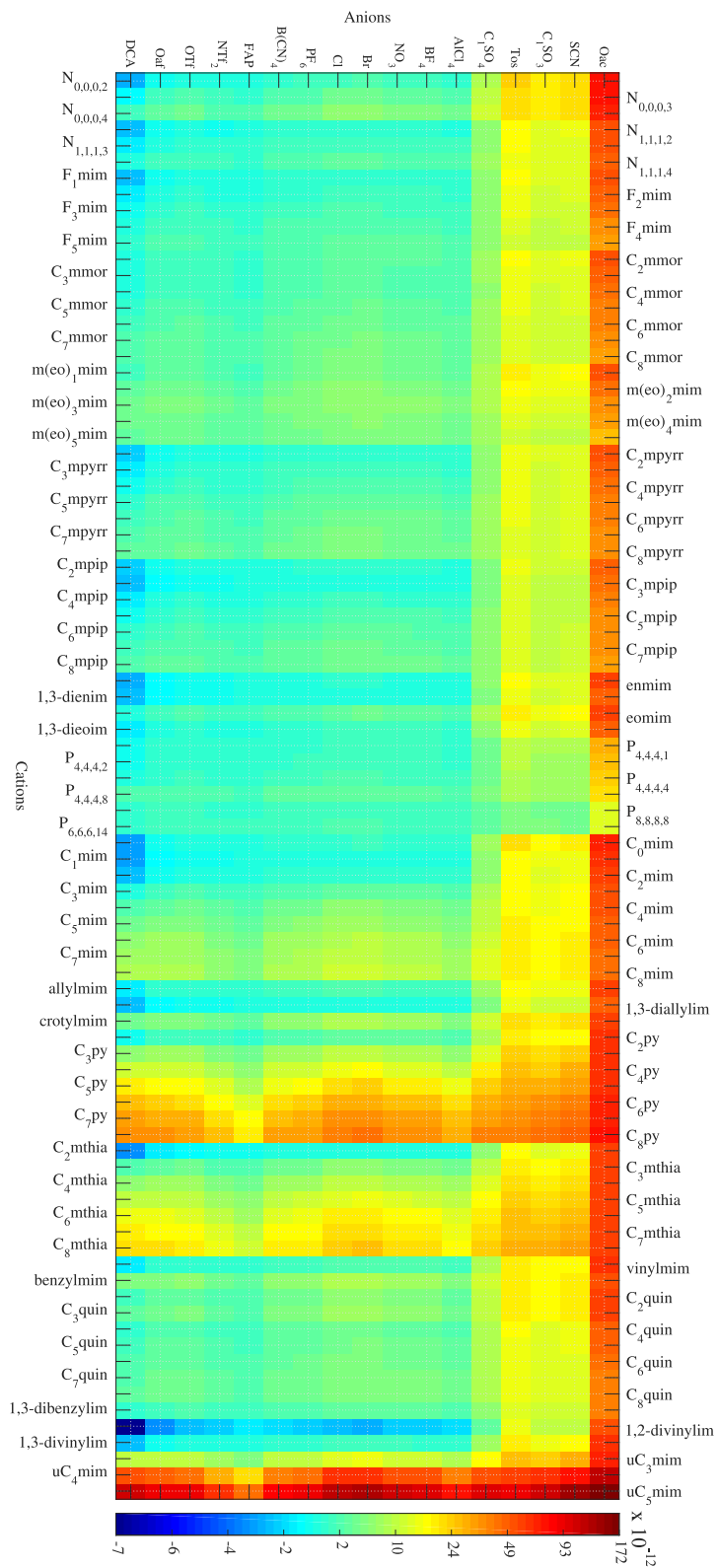
Figure 8.S1: Color map of the second order susceptibility $\chi^2(-2\omega;\omega,\omega)$ for SHG at λ=1100 nm for the combinations of all the studied ions supposing additivity.

of negative hyperpolarizabilities, particularly the $[1,2\text{-divinylim}]^+$ cation with the $[N(CN)_2]^-$ anion yield a second order susceptibility of $-6.91 \cdot 10^{-12}$ m/V.

Available simulations on first hyperpolarizability of ILs, show that both $[C_k\text{mim}][NO_3]$ and $[C_k\text{py}][NO_3]$ families increase their first hyperpolarizability with the chain length,[124] as well as $[C_k\text{mim}][BF_4]$ and $[C_k\text{mim}][\text{Oaf}]$,[125] whereas the $[C_k\text{mim}][PF_6]$ family presents a decreasing tendency. These trends, with the exception of that of the $[C_k\text{mim}][PF_6]$ family, are in accordance with our simulations on hyperpolarizability, which are also coincident with the trend observed for the second order susceptibility in Fig. 8.S1. This increasing trend is compatible with the available experimental evidences,[123] which point to a small increment of the second susceptibility with the chain length for the $[C_k\text{mim}][NTf_2]$ family of ILs. However, this small increment is in practice overshadowed by the influence of molecular orientation in the first order NL response of ILs.[135] Both second order susceptibility and its increase with the chain length is overestimated in our model compared with experimental results. However, this mismatch was also observed in Ref. [123] for simulations taking into account ionic pairs, and not isolated ions as in our case. In that work it was shown that only when considering up to eight ionic pairs in the simulation box the experimental results were quantitatively close to that of the simulations. Other theoretical works compare the same cation with different anions and provide trends for the hyperpolarizability of ILs[125,455] which are different from those of second order susceptibilities shown here. These discrepancies are already found at the hyperpolarizability level, and could be attributed to the assumption of additivity in first hyperpolarizability and the usage of different levels of theory.

Table 8.S8: Values of the simulated second order susceptibilities $\chi^2(-2\omega;\omega,\omega)$ for the SHG process at λ=1100 nm. SI units 10^{-12} m/V.

	BF_4	PF_6	Cl	NO_3	FAP	Oaf	OTf	NTf2	C_1SO_4	$AlCl_4$	C_1SO_3	$B(CN)_4$	Br	Oac	DCA	Tos	SCN
$N_{0,0,0,2}$	-3.2	-0.1	0.7	0.4	0.6	1.3	1.4	2.0	2.2	1.7	1.7	1.3	9.2	22.8	18.8	21.7	78.7
$N_{0,0,0,3}$	-0.7	1.7	2.3	1.5	1.4	2.8	2.9	4.0	4.3	3.5	3.4	2.6	10.2	22.3	18.9	21.6	72.6
$N_{0,0,0,4}$	2.0	3.6	4.0	2.8	2.2	4.3	4.6	6.3	6.6	5.4	5.3	4.1	11.4	22.3	19.4	22.1	68.0
$N_{1,1,1,2}$	-2.8	-0.5	0.1	0.0	0.3	0.7	0.7	0.9	1.0	0.8	0.8	0.6	6.5	16.9	13.4	14.4	54.9
$N_{1,1,1,3}$	-1.4	0.5	1.0	0.7	0.8	1.5	1.5	2.0	2.1	1.8	1.7	1.4	6.9	16.4	13.2	14.1	50.7
$N_{1,1,1,4}$	0.1	1.6	2.0	1.5	1.3	2.4	2.5	3.2	3.3	2.8	2.8	2.2	7.4	16.0	13.3	14.1	47.2
F_1mim	-2.6	-0.4	0.2	0.1	0.3	0.7	0.8	1.0	1.1	0.9	0.9	0.7	6.4	16.7	13.2	14.1	53.7
F_2mim	-1.4	0.3	0.8	0.6	0.7	1.2	1.3	1.7	1.7	1.5	1.5	1.2	6.2	15.1	12.0	12.6	45.8
F_3mim	-0.4	1.0	1.4	1.0	1.0	1.8	1.9	2.3	2.4	2.1	2.1	1.7	6.3	14.3	11.5	12.0	41.6
F_4mim	0.5	1.6	1.9	1.5	1.3	2.2	2.3	2.8	2.9	2.5	2.5	2.1	6.2	13.1	10.7	11.0	36.3
F_5mim	1.2	2.1	2.4	1.9	1.6	2.6	2.7	3.3	3.4	3.0	3.0	2.5	6.2	12.5	10.3	10.6	33.1
C_2mmor	0.1	1.7	2.1	1.5	1.4	2.5	2.6	3.4	3.5	3.0	3.0	2.3	7.9	17.0	14.2	15.3	51.1
C_3mmor	0.1	1.6	2.0	1.5	1.3	2.4	2.5	3.2	3.3	2.9	2.8	2.2	7.5	16.0	13.3	14.1	47.4
C_4mmor	0.3	1.6	2.0	1.5	1.3	2.3	2.4	3.0	3.1	2.7	2.7	2.2	6.8	14.6	12.0	12.6	41.9
C_5mmor	1.2	2.3	2.6	2.0	1.7	2.9	3.0	3.8	3.9	3.4	3.4	2.7	7.2	14.4	12.1	12.6	39.9
C_6mmor	1.8	2.8	3.0	2.3	2.0	3.2	3.4	4.2	4.3	3.8	3.8	3.1	7.4	14.1	11.9	12.5	37.9
C_7mmor	2.5	3.3	3.5	2.7	2.3	3.7	3.9	4.7	4.8	4.3	4.3	3.5	7.5	13.7	11.8	12.3	35.7
C_8mmor	2.8	3.5	3.7	2.9	2.4	3.8	4.1	4.9	5.0	4.4	4.4	3.7	7.4	13.1	11.3	11.7	33.0
$m(eo)_1mim$	1.9	3.2	3.5	2.6	2.1	3.8	4.0	5.2	5.4	4.6	4.5	3.6	9.3	18.1	15.6	17.0	52.3
$m(eo)_2mim$	3.6	4.5	4.7	3.5	2.8	4.7	5.1	6.3	6.5	5.7	5.6	4.5	9.4	16.5	14.5	15.5	43.4
$m(eo)_3mim$	4.2	4.9	5.0	3.9	3.2	5.0	5.4	6.5	6.6	5.9	5.9	4.8	8.9	14.8	13.1	13.8	36.6
$m(eo)_4mim$	3.9	4.4	4.6	3.6	3.0	4.6	4.9	5.8	5.9	5.3	5.3	4.4	7.9	13.0	11.5	11.9	31.2
$m(eo)_5mim$	3.8	4.3	4.4	3.5	3.0	4.4	4.7	5.4	5.5	5.0	5.0	4.3	7.3	11.8	10.4	10.8	27.5
C_2mpyrr	-2.2	-0.2	0.4	0.2	0.4	0.9	0.9	1.2	1.3	1.1	1.1	0.8	6.3	15.9	12.7	13.5	50.7
C_3mpyrr	-1.2	0.5	1.0	0.7	0.8	1.4	1.5	1.9	2.0	1.7	1.7	1.3	6.5	15.4	12.5	13.2	47.5
C_4mpyrr	-0.2	1.3	1.7	1.2	1.1	2.0	2.1	2.7	2.8	2.4	2.4	1.9	6.8	14.9	12.2	12.8	43.7
C_5mpyrr	1.0	2.2	2.5	1.9	1.6	2.8	3.0	3.7	3.8	3.3	3.3	2.7	7.3	14.7	12.4	13.0	41.5
C_6mpyrr	1.9	2.9	3.2	2.4	2.0	3.3	3.6	4.4	4.5	4.0	3.9	3.2	7.6	14.5	12.3	12.9	39.2
C_7mpyrr	2.5	3.4	3.6	2.8	2.3	3.7	4.0	4.9	5.0	4.4	4.4	3.6	7.7	14.1	12.1	12.7	36.8
C_8mpyrr	3.0	3.8	4.0	3.1	2.6	4.1	4.3	5.2	5.4	4.8	4.8	3.9	7.9	13.8	12.0	12.6	35.3
C_2mpip	-2.2	-0.3	0.2	0.1	0.3	0.6	0.7	0.9	0.9	0.8	0.8	0.6	5.6	14.6	11.5	12.0	46.0
C_3mpip	-2.5	-0.7	-0.2	-0.2	0.1	0.3	0.3	0.3	0.4	0.3	0.3	0.2	4.9	13.3	10.3	10.6	42.2
C_4mpip	-1.2	0.3	0.7	0.5	0.6	1.1	1.2	1.5	1.5	1.3	1.3	1.0	5.5	13.2	10.6	10.9	39.9
C_5mpip	0.0	1.2	1.6	1.2	1.1	1.9	2.0	2.4	2.5	2.2	2.2	1.8	5.9	13.0	10.6	10.9	37.1
C_6mpip	0.9	2.0	2.3	1.7	1.5	2.5	2.7	3.2	3.3	2.9	2.9	2.4	6.4	12.9	10.8	11.1	35.5
C_7mpip	1.7	2.6	2.8	2.2	1.9	3.0	3.2	3.9	4.0	3.5	3.5	2.9	6.8	12.9	10.9	11.3	34.4
C_8mpip	2.2	3.0	3.2	2.5	2.1	3.4	3.6	4.3	4.4	3.9	3.9	3.2	6.9	12.7	10.9	11.2	32.8
enmim	-3.0	-0.7	-0.1	-0.1	0.2	0.5	0.5	0.7	0.8	0.6	0.6	0.5	6.3	16.7	13.3	14.2	55.0
1,3-dienim	-2.9	-0.7	-0.2	-0.2	0.2	0.4	0.4	0.5	0.6	0.5	0.5	0.4	5.7	15.4	12.1	12.8	50.0
eomim	0.1	1.9	2.3	1.6	1.4	2.7	2.8	3.8	3.9	3.3	3.2	2.5	8.5	18.1	15.3	16.6	55.3
1,3-dieoim	-1.4	0.3	0.8	0.6	0.7	1.2	1.3	1.7	1.8	1.5	1.5	1.2	6.3	15.1	12.2	12.9	47.0
$P_{4,4,4,1}$	-0.3	0.7	1.0	0.8	0.8	1.3	1.4	1.6	1.7	1.5	1.5	1.2	4.5	10.3	8.2	8.3	29.0
$P_{4,4,4,2}$	-0.2	0.8	1.1	0.8	0.8	1.3	1.4	1.7	1.7	1.5	1.5	1.3	4.4	9.9	7.9	7.9	27.5
$P_{4,4,4,4}$	0.6	1.3	1.6	1.2	1.2	1.7	1.8	2.2	2.2	2.0	2.0	1.7	4.5	9.3	7.6	7.6	24.7
$P_{4,4,4,8}$	2.3	2.8	2.9	2.4	2.1	3.0	3.2	3.6	3.7	3.4	3.4	2.9	5.3	9.2	7.9	7.9	21.7
$P_{8,8,8,8}$	1.1	1.4	1.5	1.3	1.2	1.6	1.7	1.9	1.9	1.8	1.8	1.6	3.0	5.5	4.5	4.4	12.7
$P_{6,6,6,14}$	1.3	1.7	1.8	1.5	1.4	1.9	2.0	2.2	2.2	2.1	2.1	1.8	3.3	5.8	4.9	4.8	13.2
C_0mim	-3.4	-0.5	0.2	0.1	0.4	0.9	1.0	1.3	1.4	1.1	1.1	0.8	8.0	20.3	16.6	18.6	69.6
C_1mim	-3.6	-0.9	-0.2	-0.2	0.1	0.4	0.4	0.6	0.6	0.5	0.5	0.4	6.7	18.0	14.4	15.6	60.7
C_2mim	-2.6	-0.3	0.3	0.1	0.4	0.8	0.9	1.2	1.2	1.0	1.0	0.8	6.7	17.1	13.7	14.8	55.8
C_3mim	0.2	1.8	2.3	1.6	1.4	2.6	2.8	3.7	3.8	3.2	3.2	2.5	8.3	17.7	14.9	16.1	53.5
C_4mim	2.6	3.8	4.1	3.0	2.4	4.3	4.6	5.9	6.1	5.2	5.1	4.1	9.7	18.1	15.8	17.1	50.9
C_5mim	4.7	5.5	5.7	4.3	3.4	5.7	6.1	7.7	8.0	6.9	6.8	5.5	10.9	18.4	16.5	18.0	48.8
C_6mim	6.5	7.1	7.1	5.4	4.2	7.0	7.5	9.4	9.7	8.4	8.4	6.8	12.1	18.9	17.4	18.8	47.3
C_7mim	7.6	8.0	8.0	6.1	4.8	7.8	8.3	10.3	10.5	9.3	9.2	7.5	12.5	18.8	17.4	18.9	44.9

C$_8$mim	8.5	8.7	8.7	6.7	5.3	8.5	9.0	11.1	11.3	10.0	10.0	8.1	13.0	18.8	17.7	19.1	43.5
allylmim	-1.3	0.7	1.2	0.8	0.9	1.7	1.8	2.4	2.5	2.1	2.1	1.6	7.6	17.5	14.5	15.7	55.6
1,3-diallylim	-2.8	-0.8	-0.3	-0.3	0.1	0.2	0.2	0.3	0.3	0.3	0.3	0.2	5.3	14.3	11.3	11.7	46.6
crotylmim	4.6	5.6	5.8	4.2	3.3	5.9	6.3	8.3	8.6	7.3	7.2	5.6	12.0	20.7	18.7	20.8	57.9
C$_2$py	-0.5	1.5	2.0	1.4	1.3	2.5	2.6	3.5	3.7	3.1	3.0	2.3	8.8	19.1	16.2	17.8	60.5
C$_3$py	6.3	7.1	7.3	5.2	4.0	7.2	7.7	10.2	10.6	8.9	8.8	6.8	13.8	22.7	20.9	23.5	62.5
C$_4$py	12.2	12.0	11.9	8.7	6.4	11.4	12.2	16.0	16.6	14.0	13.9	10.8	18.1	25.8	25.0	28.3	64.3
C$_5$py	18.4	17.4	16.9	12.6	9.3	16.1	17.2	22.1	22.8	19.6	19.4	15.3	22.8	29.1	29.3	33.2	65.2
C$_6$py	25.1	23.3	22.6	17.1	12.7	21.3	22.8	28.8	29.6	25.7	25.6	20.4	28.2	33.1	34.3	38.9	67.8
C$_7$py	31.6	29.1	28.1	21.5	16.1	26.4	28.4	35.3	36.2	31.7	31.6	25.4	33.5	37.3	39.5	44.6	71.1
C$_8$py	37.4	34.4	33.1	25.7	19.4	31.2	33.4	41.1	42.0	37.1	37.0	30.0	38.3	41.1	44.0	49.6	73.7
C$_2$mthia	-3.9	-1.3	-0.6	-0.5	0.0	0.0	0.0	0.1	0.1	0.0	0.0	0.0	6.1	16.8	13.4	14.3	57.5
C$_3$mthia	2.2	3.6	4.0	2.8	2.3	4.2	4.5	6.0	6.2	5.2	5.1	4.0	10.3	19.6	17.2	19.0	57.9
C$_4$mthia	6.8	7.4	7.5	5.5	4.2	7.4	8.0	10.3	10.7	9.1	9.0	7.1	13.4	21.4	19.9	22.0	56.9
C$_5$mthia	10.8	10.8	10.7	8.0	6.1	10.4	11.1	14.1	14.5	12.5	12.5	9.9	16.1	22.9	22.0	24.4	55.1
C$_6$mthia	15.0	14.5	14.2	10.8	8.2	13.6	14.6	18.3	18.8	16.4	16.3	13.0	19.4	25.2	25.0	27.8	56.1
C$_7$mthia	18.4	17.6	17.1	13.1	10.0	16.3	17.5	21.6	22.1	19.5	19.4	15.6	22.0	27.1	27.4	30.4	56.5
C$_8$mthia	21.5	20.3	19.7	15.3	11.6	18.7	20.1	24.6	25.2	22.3	22.2	18.0	24.4	28.8	29.6	32.9	57.3
vinylmim	-1.5	0.7	1.3	0.9	0.9	1.8	2.0	2.7	2.8	2.3	2.3	1.7	8.4	19.2	16.1	17.7	62.7
benzylmim	4.9	5.8	6.0	4.4	3.4	6.0	6.4	8.3	8.5	7.3	7.3	5.7	11.6	19.4	17.7	19.4	52.9
C$_2$quin	1.9	3.4	3.8	2.7	2.2	4.0	4.4	5.9	6.0	5.1	5.0	3.8	10.4	19.6	17.5	19.3	60.0
C$_3$quin	3.4	4.6	4.8	3.5	2.7	4.9	5.4	7.1	7.3	6.2	6.2	4.7	11.0	19.4	17.6	19.4	56.5
C$_4$quin	1.1	2.5	2.8	2.0	1.7	3.1	3.3	4.3	4.4	3.8	3.8	2.9	8.3	16.3	14.2	15.1	48.4
C$_5$quin	1.7	2.9	3.2	2.4	2.0	3.4	3.7	4.7	4.8	4.2	4.2	3.3	8.4	15.9	13.9	14.8	45.6
C$_6$quin	2.2	3.3	3.5	2.6	2.2	3.7	4.0	5.0	5.1	4.4	4.4	3.5	8.3	15.2	13.3	14.1	42.4
C$_7$quin	2.9	3.9	4.1	3.1	2.5	4.2	4.5	5.6	5.7	5.0	5.0	4.0	8.6	15.1	13.4	14.2	40.9
C$_8$quin	3.2	4.1	4.2	3.2	2.7	4.3	4.6	5.7	5.8	5.1	5.1	4.1	8.4	14.4	12.8	13.5	37.9
1.3-dibenzylim	0.9	2.0	2.3	1.8	1.5	2.5	2.8	3.4	3.5	3.1	3.1	2.5	6.7	13.3	11.3	11.7	37.7
1,2-divinylim	-6.6	-3.6	-2.8	-2.1	-1.1	-2.0	-2.1	-2.9	-3.0	-2.5	-2.5	-1.9	3.6	14.3	10.6	10.9	53.0
1,3-divinylim	-2.6	-0.1	0.5	0.3	0.5	1.1	1.2	1.6	1.7	1.4	1.4	1.0	7.6	18.4	15.4	16.8	62.4
uC$_3$mim	9.6	9.9	9.9	7.1	5.2	9.6	10.3	13.8	14.4	12.0	11.9	9.1	16.8	25.6	24.4	27.9	68.7
uC$_4$mim	53.0	46.2	43.7	30.6	21.2	40.0	44.0	60.4	62.6	51.5	51.1	37.8	52.7	55.7	62.9	76.3	118.8
uC$_5$mim	109.2	93.9	88.0	62.0	43.0	79.8	88.3	120.2	124.0	102.9	102.3	75.7	98.5	92.8	110.5	134.9	172.0

211

9. Doping ionic liquids with transition metals

Grupo de Nanomateriais, Fotónica e Materia Branda, Departamentos de Física Aplicada e de Física de Partículas, Universidade de Santiago de Compostela.

Throughout the previous chapters of this thesis, different optical properties of neat ionic liquids were studied from experimental and computational perspectives. It was shown that tailoring of cations and anions provides a path to smartly design refractive indices, nonlinear response and even mesogenic character in the world of ILs.

However, further tailoring of the IL properties can be obtained by considering mixtures of ILs with solvents,[486–488] other ionic liquids[32,489] or by the introduction of nanoparticles.[50,490] Another way to tune the properties of ILs is by doping them with metals,[280,491–496] procedure widely used in the design of ILs for electrochemical[191,497–499] or separation applications.[47,500–502] Among the different metals, those known as transition metals have turned to be of special interest in the field of photonics,[503–509] since they are able to induce interesting optical responses including electroluminescence,[505,506] photoluminescence[507,508] or nonlinear absorption and refraction.[88,127]

Despite the interesting optical properties of these systems, only a bunch of studies on transition metal doped ILs are currently available.[110,113,114,356,494,510] For instance, the ionic liquid 1-butyl-3-methylimidazolium thiocyanate, $[C_4mim][SCN]$, doped with Co^{2+} presents an important thermochromic effect as a consequence of the dependence on temperature of the coordination of the metal cation

with the thiocyanate anions.[113,114] Thermochromism was also observed in the same IL when doping it with Ni^{2+},[510] and other properties of this IL were studied in a recent article when doping them with other metals.[356] However, precisely because of the large number of possible combinations of ILs with metals, experimental probing of properties is not the most practical way to gain insight in these systems. On the opposite, computer simulations emerge as a highly convenient alternative.

Molecular Dynamics (MD) and Density Functional Theory (DFT) simulations have been widely used to reproduce, explain and predict different properties of ILs,[245,271,511–514] as well as to study their microscopic structure.[190,515–519] ILs doped with metals were also successfully addressed both by MD and DFT in previous studies.[103,500,520–522] These theoretical approaches were extensively used to study ILs containing Li^+ in the field of battery design[499,523–526] as well as other metal cations that could also potentially provide efficient energy storage, such as Al^{3+}, Mg^{2+}, K^+ or Na^+.[65,191,498,527,528]

In this chapter, we study the introduction of transition metals as a mechanism to tailor the properties of ILs, and specially, their absorption spectrum. We carry out a complete computational study of the 1-butyl-3-methylimidazolium thiocyanate IL, [C_4mim][SCN], doped with aluminum and different transition metals. The properties of these ILs are tightly related to those of the octahedral metal-thiocyanate complexes that are stabilized within their bulk.

9.1 Materials

We considered six different ILs, one is the [C_4mim][SCN], and the other five are derivations obtained by doping it with different metals. The stoichiometry of the doped ILs is $[C_4mim]^+_{6-q}M^{q+}[SCN]^-_6$, where M^{q+} are the metal cations: Al^{3+}, Cr^{3+}, Fe^{3+}, Mn^{2+} or Ni^{2+}, which are stabilized in the bulk of the liquid forming octahedral complexes with the thiocyanate anions.

9.2 Force field, molecular parametrization and simulation details

In the MD simulations of this chapter, the chemical species were parametrized according to the OPLS-AA force field.[197] The parameters for the $[C_4mim]^+$ cation were taken from Ref. [201], while for the $[SCN]^-$ anion were taken from Ref. [202]. The parametrization of the metal cations was inspired by the values provided in Ref. [529] for divalent cations, Ni^{2+} and Mn^{2+}, and in Ref. [530] for trivalent cations, Cr^{3+}, Al^{3+}, and Fe^{3+}. The LJ parameters calculated in these publications, Table 9.1, yield a precise reproduction of the coordination number of the complexes formed in our ILs.

Table 9.1: LJ parameters employed for each metal cation.

Cation	σ/ nm	ϵ/ kJ mol^{-1}
Al^{3+}	0.2594	0.0197
Cr^{3+}	0.2688	0.0355
Mn^{2+}	0.2814	0.0706
Fe^{3+}	0.2772	0.0567
Ni^{2+}	0.2510	0.0110

In the simulation box of each doped IL, the total number of metal cations was 100 and the number of ILs ions was set accordingly with this figure. For divalent metals, 600 $[SCN]^-$ anions and 400 $[C_4mim]^+$ cations were included, while, for trivalent metals, 600 $[SCN]^-$ anions and 300 $[C_4mim]^+$ cations were introduced. MD simulations were run at a reference temperature of 298 K and a pressure of 1 atm in a cubic box of 55.27 Å of side length. Further information about the MD simulation details can be found in the methodology chapter. Exceptionally, production runs of 250 ns long and a time step of 1 fs were performed to calculate the velocity auto correlation function (VACF) and the vibrational density of states (vDOS) of the systems,

since high frequency sampling is required to properly evaluate these magnitudes.

9.3 Density Functional Theory

DFT and TD-DFT simulations were performed to calculate the absorption and vibrational (Raman) spectra of the thiocyanate-transition metal complexes stabilized in the bulk of the studied ILs. The level of theory for the Al^{3+}, Cr^{3+}, Mn^{2+}, and Ni^{2+} complexes was B3LYP/6-311++G(d,p) while for the Fe^{3+} complex, a functional with corrected long-range exchange interaction was required to properly reproduce the available experimental data. In consequence, the calculation for this complex was carried out with the CAM-B3LYP functional in combination with two different basis sets, the 6-311++G(d,p) for the [SCN]$^-$ anions and the LanL2DZ for the metal center. In the absorption spectra of some complexes, some of the lowest energy transitions are predicted with a zero oscillator strength. However, in order to illustrate Laporte-forbidden transitions, all the oscillator strengths were artificially increased by an amount of 0.01.

9.4 Experimental details

Absorption spectra in the range from 320 nm to 1000 nm were measured by means of our RISBI device operating in the spectrophotometer configuration. Since these ILs present strong colorations, they had to be diluted in a solvent in order to be measured. The solutions were prepared by mixing the metal doped ILs with acetone. The election of acetone was made after studying the effect of different solvents in the absorption spectrum since an important solvatochromic effect was detected for solutions in ethanol and acetonitrile. The mass percentage of IL in the solutions was always below 0.05% and the samples were measured in a QS Hellma quartz cell of 1 cm of

optical path length. XRD patterns of the Ni^{2+} and Fe^{3+} doped ILs were measured in a Bruker Kappa-APEX-II diffractometer. Other magnitudes used as experimental references were extracted from our previous publication.[356]

9.5 Basic test of the simulations

The first magnitude to analyze is the simulated density, since it provides a reference value to check if the packing of the liquid structure in the simulation is close to that of the real system, Table 9.2. We obtained a very good agreement between both simulated and experimental values that guarantees our simulation results are suitable to be analyzed in deeper detail. The registered deviations in density are within the regular range of MD simulations, being always below 4.0% except for the Mn^{2+} IL, which presents a slightly higher deviation of 6.1%. In addition, they all have the same sign since the simulated densities were always higher than the experimental ones. The considerably important change in density observed in the pure IL upon metal addition is a first evidence of the influence of the metals in the IL structure.

Table 9.2: Comparison of simulated and experimental density[356] at 298.15 K for the $[C_4 mim]^+_{6-q} M^{q+} [SCN]^-_6$ ILs with M= Al^{3+}, Cr^{3+}, Fe^{3+}, Mn^{2+}, and Ni^{2+} and pure IL.

IL	ρ_{sim}/ g cm^{-3}	ρ_{exp}/ g cm^{-3}	$S(\rho_{exp})$/ g cm^{-3}	Deviation
Fe^{3+}	1.252	1.21	$1 \cdot 10^{-2}$	3.6%
Cr^{3+}	1.248	1.2120	$5 \cdot 10^{-4}$	3.0%
Ni^{2+}	1.243	solid	−	−
Mn^{2+}	1.231	1.16	$1 \cdot 10^{-2}$	6.1%
Al^{3+}	1.218	1.1762	$5 \cdot 10^{-4}$	3.6%
Pure	1.109	1.068	$5 \cdot 10^{-4}$	3.8%

9.6 Nanosegregation in the bulk

Deeper insights in the changes suffered by the structure of the pure liquid because of the introduction of the metals can be obtained by means of the radial distribution functions (RDF) of the different ionic species in the bulk of the liquids, Fig. 9.1. The reference for establishing the $[C_4mim]^+$ cation position was taken at the center of mass of the imidazolium ring, while the reference for the $[SCN]^-$ anion was set in the C atom. In the pure IL, the $[SCN]^- - [C_4mim]^+$,
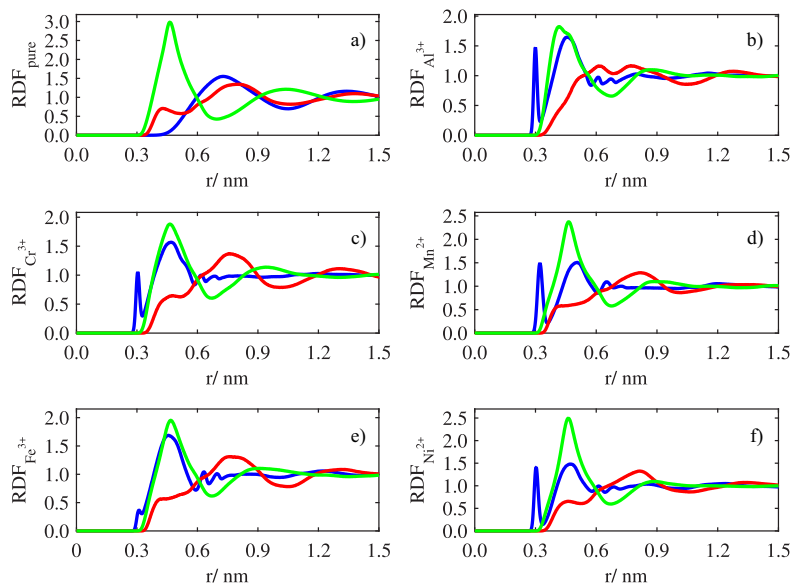
Figure 9.1: $[C_4mim]^+$ - $[C_4mim]^+$ (red), $[SCN]^-$ - $[SCN]^-$ (blue) and $[C_4mim]^+$ - $[SCN]^-$ (green) RDFs for a) the pure IL and their mixtures with b) Al^{3+}, c) Cr^{3+}, d) Mn^{2+}, e) Fe^{3+}, and f) Ni^{2+}.

$[C_4mim]^+ - [C_4mim]^+$ and $[SCN]^- - [SCN]^-$ RDFs evidence

218

the typical nanosegregated bulk of ILs, which shows a highly amphiphilically driven nanoscopic order. Once the metal cations are introduced, the ionic species in the bulk of the material are redistributed as a result of the formation of the coordination complexes of the $[SCN]^-$ with the divalent and trivalent metal cations, as observed in the appearance of new and well-defined peaks in the $[SCN]^- - [SCN]^-$ RDFs of the doped ILs. At least two peaks are clearly observed, a sharp peak at about 0.30 nm and a broader one at around 0.49 nm, being the exact positions dependent on the specific metal cation. These peaks reflect the relative distance of each $[SCN]^-$ anion with respect to the others inside its coordination sphere. Regarding the $[C_4mim]^+ - [C_4mim]^+$ and the $[SCN]^- - [C_4mim]^+$ RDFs, both reveal that the $[C_4mim]^+$ spatial distribution is only slightly distorted upon the introduction of the metal cations as the pseudoreticular charge alternation pattern of the pure ILs is still present to a certain extent. This result points to that the main effect of the introduction of the metals in the pure IL structure is to reorganize the $[SCN]^-$ around the metal cations by forming complexes that are embedded in the polar regions of the IL. This effect is known as nanostructurated solvation and it has been observed in different ILs.[523]

The structure factor of the different ILs were simulated and compared with experimental XRD data and the results are shown in Fig. 9.2. The structure factor of the pure IL shows a clear peak at q $\sim$ 16.5 nm^{-1}, which is associated to an adjacency distance of 3.8 Å between nearest neighbor atoms[299] and lacks of a charge-alternation peak at lower q values, usually present in molten salts. The absence of this peak is likely produced by the cancellation of different atomic contributions in the overall structure function $S(q)$ of the IL, or by limitations imposed by the size of our simulation box.

The doped ILs also show the adjacency peak but their structure factor significantly differ from that of the pure IL in the charge-alternation region. At slightly larger q values than from adjacency, the simulations of the ILs containing Mn^{2+} and Ni^{2+} show intense peaks while ILs containing Al^{3+}, Cr^{3+} or Fe^{3+} show diffuse structures. The

219
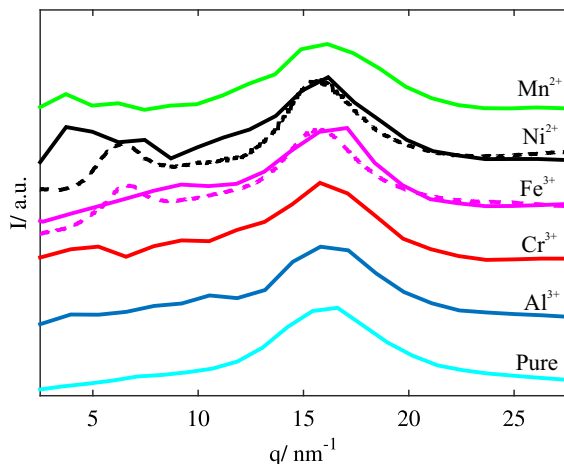
Figure 9.2: Simulated X-ray diffraction patterns of the different ILs (solid line) and comparison with available experimental values (dashed lines).

absence of clearer features in this regions is likely produced by the limited resolution for the simulations at low q values. The experimental measurements show the presence of a broad charge alternation peak both for the Ni^{2+} and Fe^{3+} ILs. These peaks correspond to a characteristic distance of $d_{Ni^{2+}} \sim 9.8$ Å in the case of the Ni^{2+} IL and of $d_{Fe^{3+}} \sim 9.3$ Å for the Fe^{3+} IL. On the other hand, DFT geometries for those complexes provided a diameter of 10.01 Å for $Ni[SCN]_6^{-4}$ and 9.53 Å for $Fe[SCN]_6^{-3}$, suggesting that the experimental peaks are caused by the complexes inside the doped ILs. In addition, the observed $d_{Fe^{3+}} < d_{Ni^{2+}}$ trend can be expected according to the larger size of the Ni^{2+} cation. These results point towards the existence of a highly nanosegregated bulk in the doped ILs. The polar domains would be composed by the metal complexes and the polar heads of the $[C_4mim]^+$ cations and the nonpolar domains would be mainly composed by their alkylic chains.

220

9.7 The structure of the coordination complexes

The structure of the metal-thiocyanate complexes was further analyzed by calculating the RDFs and the coordination number (CN) of all the species with respect to the metals, M, Figs. 9.3 and 9.4.
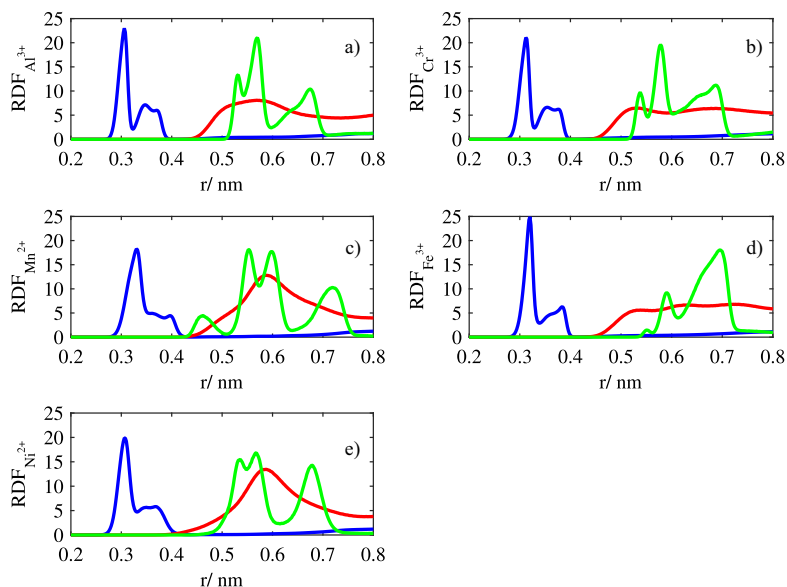
Figure 9.3: M - $[SCN]^-$ (blue), M - $[C_4mim]^+$ (red) and M - M (green) RDFs for $[C_4mim]_{6-q}^+ M^{q+} [SCN]_6^-$ ILs. a) Al^{3+}, b) Cr^{3+}, c) Mn^{2+}, d) Fe^{3+}, and e) Ni^{2+}, doped ILs.

The distribution of the IL species doped with metal cations is qualitatively similar for all the ILs. The $[C_4mim]^+$ cations are poorly coordinated with the metals, in accordance with the previous observation that their distribution is scarcely perturbed upon metal addition. Hence, the $[C_4mim]^+$ cations are largely excluded from the
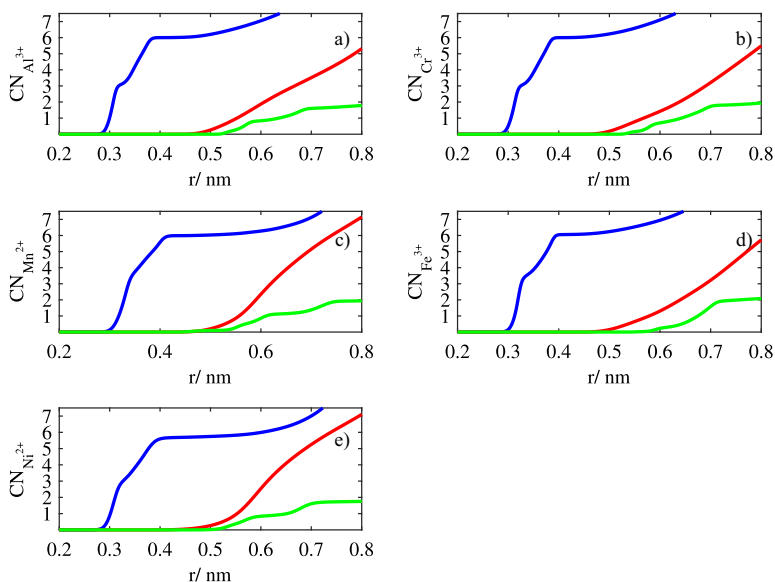
Figure 9.4: Coordination number (CN) of M - [SCN]$^-$ (blue), M - [C$_4$mim]$^+$ (red) and M - M (green) for [C$_4$mim]$^+_{6-q}$ M^{q+} [SCN]$^-_6$ ILs. a) Al^{3+}, b) Cr^{3+}, c) Mn^{2+}, d) Fe^{3+}, and e) Ni^{2+}.

metal coordination sphere despite they surround the complexes in the polar nanoregions of the bulk. On the other hand, the coordination number (CN) of the metals with respect to the [SCN]$^-$ anions is 6, Fig. 9.4, which indicates that they are octahedrally coordinated. The RDF of the [SCN]$^-$ presents a sharp and well-defined peak at around 0.3 nm and a complex structure at longer distances where two peaks can be observed around 0.37 nm, being the exact values dependent on the considered metal. The existence of two separate families of peaks indicates that not all the SCN anions are placed at the same distance from the metal they are coordinating. In order to obtain a deeper insight in this phenomenon, the RDF and CN of the N and the S of the [SCN]$^-$

anions with respect to the metal cations were calculated and the results are shown in Table 9.3.

Table 9.3: Position of the first maximum in the RDFs of M - $[SCN]^-$ when the reference is N(R_N) or S(R_S). Coordination numbers for N(CN_N), S(CN_S) and their sum CN_{N+S}.

IL	R_N/ nm	R_S/ nm	CN_N	CN_S	CN_{N+S}
Al^{3+}	0.203	0.220	3.114	2.885	5.999
Cr^{3+}	0.203	0.220	3.134	2.866	6.000
Mn^{2+}	0.222	0.240	3.814	2.169	5.983
Fe^{3+}	0.204	0.222	3.554	2.503	6.057
Ni^{2+}	0.200	0.220	3.112	2.559	5.671

The $[SCN]^-$ anions present an ambidentate coordination with the metals, i.e., they are able to coordinate them by both their N or S extremes. The relative coordination number with respect to each one of the RDF peaks can be used as an indicative of the relative abundance of both coordination modes. Without exception, the coordination via N is the most probable. However, the specific ratio between both types of coordination depends on the metal. The maximum fraction of N coordination is found in the IL with Mn^{2+} where the 64% of $[SCN]^-$ anions present this coordination. On the other hand, the minimum ratio is found for both Al^{3+} and Cr^{3+}, where the coordination via N reaches only the 52%. In addition, the N or S coordination of the $[SCN]^-$ induces differences in the coordination distance of the anions which go beyond the expected ones, given the intrinsic asymmetry of the $[SCN]^-$ molecule. The $[SCN]^-$ anions place closer to the metal cations when the coordination is via N than when the coordination is via S, as can be deduced from the values of the position of the first maximum of the RDF of the N (R_N) and S (R_S) extremes of the $[SCN]^-$ in Table 9.3.

The existence of two different populations of $[SCN]^-$ anions not only affects the coordination distance of the ligands with respect to the metals, but it also affects their orientation. The relative orientation of the

[SCN]$^-$ anions with respect to the metals, can be analyzed studying the angle θ subtended by the vector pointing from the metal to the C atom of the [SCN]$^-$ and by the vector colinear to the [SCN]$^-$ molecule (pointing from the S atom to the N atom). The value of $\cos\theta$ was calculated for all the ILs and a frequency histogram was made as a function of the distance of the C atom in [SCN]$^-$ to the metals, Fig. 9.5.
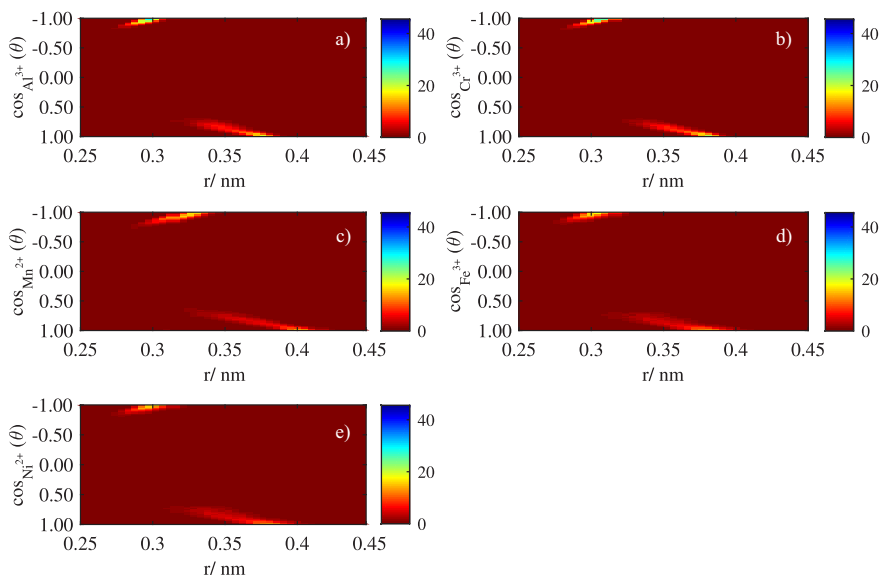
Figure 9.5: Frequency histogram of the $\cos\theta$ as a function of the distance of the M to the C of the [SCN]$^-$ anions. a) Al^{3+}, b) Cr^{3+}, c) Mn^{2+}, d) Fe^{3+}, and e) Ni^{2+}.

When the [SCN]$^-$ anions coordinate via N, their orientation is mostly parallel to the radius that links the metal and the anion, and their position with respect to the metal is relatively fixed. On the other hand, when the coordination is via S, both the position and the angle θ are much more labile than in the case of N. Interestingly, for both N and S coordinations, the larger is the distance [SCN]$^-$ is placed from the

metal, the more parallel it aligns in the radial direction. Regarding the differences between ILs, there are subtle distinguishing features among them. For the N coordination, the Mn^{2+} presents a wider distribution of highly probable locations and angles of $[SCN]^-$ anions than the rest of ILs. However, the most important differences are found for the S coordination. For ILs with Al^{3+} and Cr^{3+} the S coordination presents a small high probability region where the orientation of the $[SCN]^-$ anions is markedly oriented in the radial direction embedded in an extensive and continuous region where the angle is not fixed. For the rest of ILs, this high probability region is absent and only diffuse location and angle orientation is found.

Figs. 9.3 and 9.4 not only provide information about the distribution of $[SCN]^-$ anions around metal cations, but also about the correlation between the metal cations themselves. The $M-M$ RDFs show that in a certain range of distances, from 0.5 nm to 0.7 nm, it is highly probable to find metal centers of the neighbor complexes. This range coincides with the expected distance between two metal cations if they are separated by a $[SCN]^-$ anion. This fact suggests that there is a certain extent of bridging of ligands, i.e., there are $[SCN]^-$ anions that form part, at the same time, of two coordination spheres belonging to neighbor metals. Additionally, the complex peak structure of these $M-M$ RDFs is related to the differences observed in the coordination when it happens via N or via S.

From the $M-M$ coordination number, the average number of bridged metal neighbors in each IL can be obtained, Table 9.4, and it varies in the range from 1.6 to 2. According to these values, there is a strong tendence to form bridges as, on average, each complex is linked at least to another one. For Mn^{2+} and Fe^{3+} each complex is linked to other two complexes, while for the rest of ILs this number is slightly lower. In these ILs, the non integer CN points to the possibility of the existence of several kinds of complexes according to the number of bridging ligands in their coordination sphere. The wide presence of bridging mechanisms in these metal-doped ILs could be related to the need of decreasing the neat charge of the complexes in a highly-charged

environment of weakly coordinating cations. Bridging reduces the effective negative charge of the complexes by sharing some $[SCN]^-$ molecules with the neighbor metal cations, and it facilitates the charge screening by the $[C_4mim]^+$ cations. Furthermore, this process provides an excess of "free" ion pairs that could act as an extra polar solvent for accommodating the complexes.

Table 9.4: Coordination number for M - M (CN_M) in each IL.

IL	CN_M
Al^{3+}	1.621
Cr^{3+}	1.800
Mn^{2+}	1.925
Fe^{3+}	1.965
Ni^{2+}	1.724

9.8 Dynamics of the metals and complexes

The single-particle dynamics was studied by means of the velocity auto correlation function (VACF) of the different ionic species. The VACF for the $[C_4mim]^+$ and the $[SCN]^-$ are plotted in Fig. 9.6. In all the ILs, the $[C_4mim]^+$ diffuses freely. This free diffusion was expected since the $[C_4mim]^+$ cation is not playing any significant role in the direct complexation of the metals, but in the charge compensation of the complexes. Regarding the $[SCN]^-$, the VACF curves reveal some rattling motion associated to caging effects of the metal cations inside their coordination sphere. The fast motion of the anions to the free diffusion regime indicates a relatively weak interaction. $[SCN]^-$ anions are able to coordinate the metal cations usually on an octahedral configuration, but they are easily exchanged by free $[SCN]^-$ originated from the bridging of neighbour metals in the bulk IL. While the VACFs of the $[C_4mim]^+$ and $[SCN]^-$ provide valuable information of the
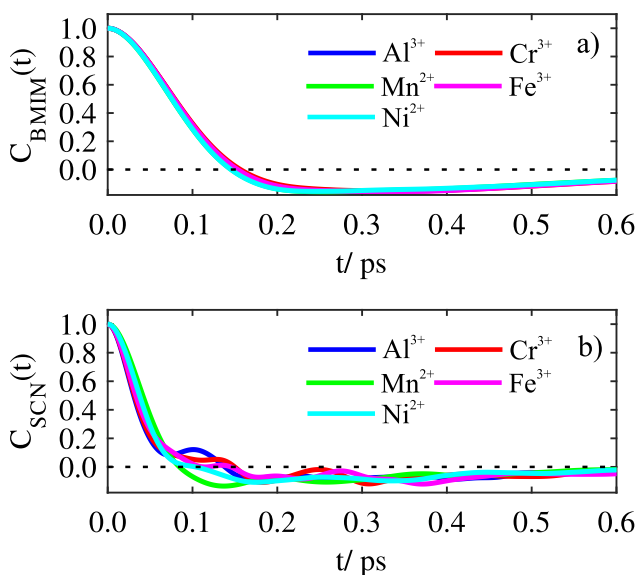
Figure 9.6: Velocity auto correlation function (VACF), C(t) for the a) $[C_4mim]^+$ cation and the b) $[SCN]^-$ anion in the different ILs. Color code: blue Al^{3+}, green Cr^{3+}, red Mn^{3+}, cyan Fe^{3+} and purple Ni^{3+}.

dynamics inside IL, the VACF of the metal provides a more accurate description of the dynamics of the complexes. The VACFs of the different metal cations and their associated vibrational spectra are shown in Fig. 9.7. The VACFs register long correlation times for all the metals, which are associated to the formation of stable complexes as, in some cases, it takes up to 1 ps to reach the free diffusion regime. Nevertheless, since we are not using polarizable force fields, caution is required with regard the provided correlation times. Despite all the complexes are considerably stable, some of them are markedly more stable than the others. It is possible to distribute the metal cations in two groups according to their effect on the VACF correlation time. Metal cations with a trivalent charge, Al^{3+}, Cr^{3+}, and Fe^{3+} present the longest correlation times and thus, they seem to form more stable
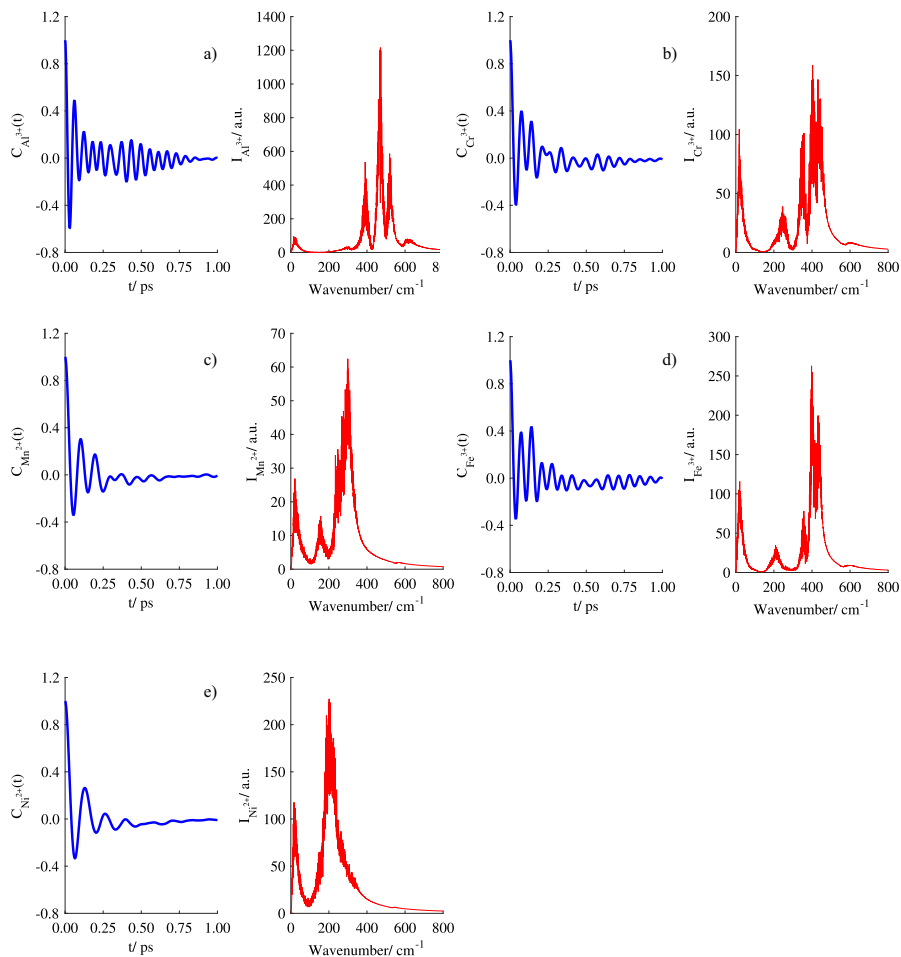
Figure 9.7: Velocity auto correlation function (VACF) C(t) (in blue) and the respective vibrational spectrum (in red) of the metal cations inside the ILs. a) Al^{3+}, b) Cr^{3+}, c) Mn^{2+}, d) Fe^{3+}, and e) Ni^{2+}.

complexes. On the other hand, complexes formed by divalent metal cations, Mn^{2+} and Ni^{2+}, present shorter correlation times and, hence, slightly lower stability than that of trivalent cation complexes.

In order to shed more light on this, the vibrational density of states (vDOS) of the metal cations was calculated from the VACFs by taking the Fourier transform. The resulting spectra were multiplied by a shift factor that was determined by comparison with experimental spectra, as explained below in more detail. In octahedral complexes the active stretching frequencies are $\nu_1(A_{1g})$, $\nu_2(E_g)$ and $\nu_3(F_{1u})$ which are placed at higher wavenumbers (higher frequencies) than the active bending frequencies $\nu_4(F_{1u})$, $\nu_5(F_{2g})$.[531] The position of the metal-ligand stretching frequency, ν_1, can be used as a quantitative indicator of the order of the stretching metal-ligand force constants because the metal center is not moving in this mode.

The ν_1 stretching mode is assigned to the first intense band placed at the highest frequency for all the metal cations, as it is expected to be the band placed at highest energy. These bands are at 523 cm^{-1} for Al^{3+}, 445 cm^{-1} for Cr^{3+}, 430 cm^{-1} for Fe^{3+} and at much lower frequencies for the divalent cations, 297 cm^{-1} for Mn^{2+} and approximately 225 cm^{-1} for Ni^{2+}. The higher frequency of the ν_1 stretching frequency in the trivalent cations in comparison with divalent cations can be interpreted as the result of an interaction between the trivalent metal cations and the ligands more intense than in the case of the divalent metals. This enhanced interaction is ultimately observed in the formation of more stable complexes that present longer correlation times. The increase of the metal-ligand stretching frequencies with increasing number of the metal oxidation state in octahedral complexes has been reported before, and it is a well known trend for complexes sharing the same ligand.[531] Furthermore, for cations in the same oxidation state, the frequency of the ν_1 decreases as the mass of the cation increases, as observed here both for the studied trivalent and divalent cations as $\nu_1(\text{Al}^{3+}) > \nu_1(\text{Cr}^{3+}) > \nu_1(\text{Fe}^{3+})$ and $\nu_1(\text{Mn}^{2+}) > \nu_1(\text{Ni}^{2+})$.

The rest of the metal-ligand stretching bands (ν_2 and ν_3) are easily assigned once ν_1 has been identified, ν_2 is the strong band closest to ν_1 while, ν_3 is the strong band that lies at slightly lower frequencies. In the case of divalent metals, these bands are very close making harder the individual assignation. The bending modes ν_4 and ν_5 are placed at

2

Carlos Damián Rodríguez Fernández

about 300 cm^{-1} for Al^{3+}, 250 cm^{-1} for Cr^{3+}, and at 210 cm^{-1} for Fe^{3+} while these modes appear at lower frequencies in divalent metals, at 154 cm^{-1} for Mn^{2+} and for the case of Ni^{2+} they are not well-resolved.
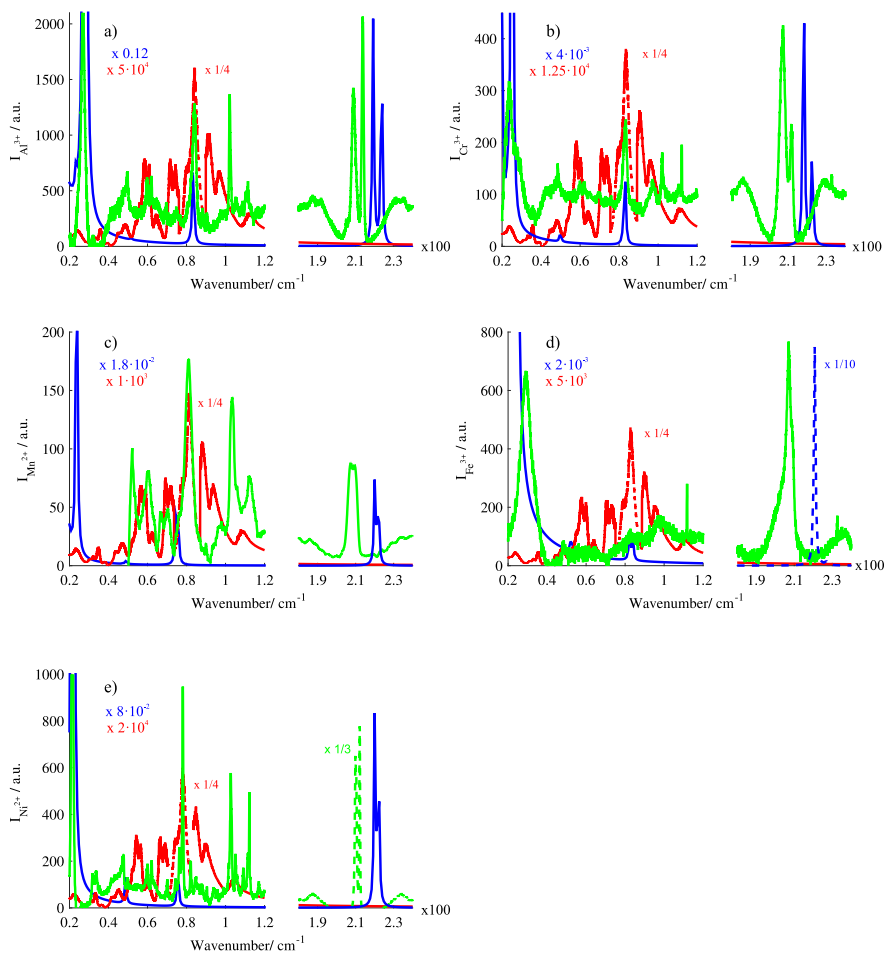
Figure 9.8: Raman spectra calculated via MD (red) and DFT (blue) and comparison with the experimental Raman spectrum (green) for the different metal containing ILs. a) Al^{3+}, b) Cr^{3+}, c) Mn^{2+}, d) Fe^{3+}, and e) Ni^{2+}.

2

230

The vibrational spectra of the complete ILs were simulated by means of MD in the same way as that of the metals in the previous section. The spectra of each IL was multiplied by a shift factor to center the most intense simulated peak in the experimental position of the ν_{CS} stretching peak of the [SCN]$^-$ anion. The low frequency vibrations of the system predicted by the MD simulations were completed with DFT vibrational (Raman) calculations, which provides access to higher frequency vibrational regions. DFT Raman spectra were calculated for N coordinated complexes via standard procedures.[532] It is important to stress that the complexes were simulated in the N coordination mode as it was the most stable geometry while MD simulations indicate the presence of bridging and the existence of some extent of S coordination. The apparent discrepancy between the DFT and MD results, suggests that it is the energy of the highly charged bulk of these ILs what stabilizes the bridging and the existence of coordination via S.

The DFT and the MD spectra were superimposed and compared with experimental Raman spectra taken from our previous work[356] in Fig. 9.8. The experimental spectra were filtered and baseline corrected by means of a Savitzky-Golay filter. The theoretical spectra are qualitatively similar to those of the experiments, being the major difference the absence in the simulations of several peaks in the region from 1100 cm^{-1} to approximately 1700 cm^{-1}, which are associated to the C-H bonding in the [C$_4$mim]$^+$ cations. These peaks lie at too high frequencies to be properly described by MD and they cannot appear in the DFT calculations since, in those simulations, only the metal-thiocyanate complexes were considered. For clarity purposes, this region was not presented in Fig. 9.8.

From the available vibrational data, the [SCN]$^-$ stretching frequencies provide very important information about the complex structure, as these stretching frequencies have been widely used to identify the coordination mode of the [SCN]$^-$ anion with different metals.[356,510,533]

The ν_{CN} stretching frequency is usually placed at $2100-2050\,\mathrm{cm}^{-1}$

for N coordination, at $2130 - 2085$ cm^{-1} for S coordination and at $2165 - 2065$ cm^{-1} for the bridging case. In this wavenumber range, only the DFT predicted bands are available and they are blue-shifted for all the ILs in comparison with the experimental bands. From the experimental point of view, the overlapping ranges of the precise signatures of the different coordination modes prevent doing any meaningful assignation based on this stretching mode.

The ν_{CS} stretching goes from $870 - 820$ cm^{-1} in the case of N coordination, from $760 - 700$ cm^{-1} in the case of S coordination and from $800 - 750$ cm^{-1} in the case of bridging. The DFT predicts the ν_{CS} contribution of the simulated N coordinated complexes very accurately as the agreement with experimental data is excellent. The experimental Raman spectra of all the ILs show important peaks in the range from 840-812 cm^{-1}, which suggest a predominance of N-coordination in these ILs, in agreement with MD predictions. Furthermore, the experimental Raman spectra of all the ILs, with exception of the one containing Cr^{3+}, show also low intensity shoulders and even peaks (in the case of Ni^{2+}) in a range that could be compatible with the presence of a certain extent of bridging. In addition, the experimental spectra is qualitatively compatible with the simulated MD Raman spectra, which contains bridging [SCN]$^-$ anions. It is worth to note that the MD simulations showed that only a reduced number of the [SCN]$^-$ anions in the IL mixtures participate in the bridging. Hence, bridging signals are expected to be weak in comparison with the predominant N coordination mode.

The third most exploited window to study the coordination of the [SCN]$^-$ is the ν_{NCS} stretching, from $486 - 440$ cm^{-1}. However, this range also contains the frequencies of the already discussed vibrational modes of the metal atoms, which makes the peak identification difficult. As a consequence, the predicted existence of a certain extent of bridging in these ILs is not confirmed by the available experimental data but also it cannot be discarded. Further experimental work is needed in order to provide new insights on this topic.

9.9 Absorption spectra
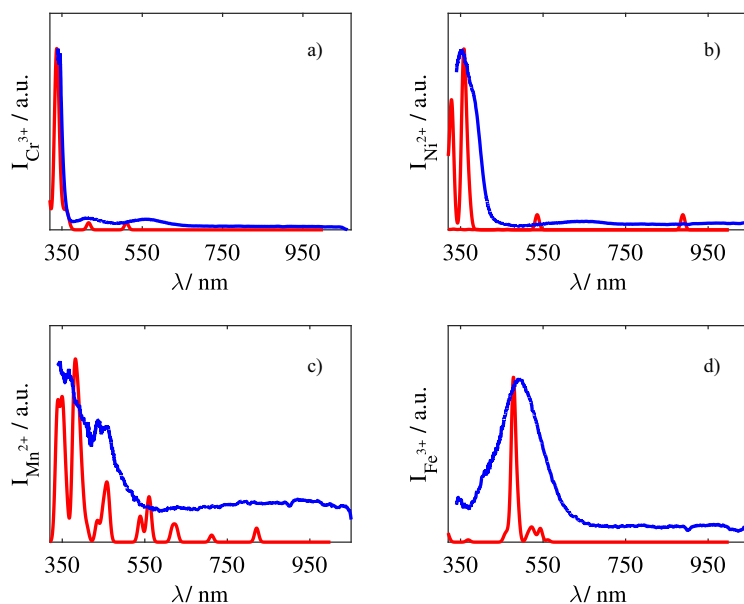
Figure 9.9: Experimental (blue) and simulated (red) absorption spectra for the different metal containing ILs. a) Cr^{3+}, b) Ni^{2+}, c) Mn^{2+}, and d) Fe^{3+}

The absorption spectra of these systems was calculated for the coordination complexes in the gas phase by means of TD-DFT and compared with experimental measurements of diluted samples. Further details about the calculations and experimental procedure are described in the methodology chapter. The employment of the gas phase approach for simulating the absorption spectrum of these ILs is justified by the secondary role that the $[C_4mim]^+$ cations play in the coordination of the metals by the $[SCN]^-$ anions, a behavior that has been highlighted by the results of the structural and dynamical MD calculations. The d-d

233

transitions in a complex of octahedral symmetry are always Laporte-forbidden, and thus the associated oscillator strength is expected to be zero. In order to visualize them, all transitions were provided with an strength of 0.01 by adding this amount to the predicted values. Experimental and simulated absorption spectra for Cr^{3+}, Mn^{2+}, Fe^{3+}, and Ni^{2+} containing ILs are shown in Fig. 9.9.

The spectra for the Al^{3+} IL is not shown because it is a $2s^2\ 2p^6$ closed shell cation, so, it is not expected to present absorption at frequencies within the visible or near UV range. In other words, this IL is expected to be optically transparent, as confirmed by the simulations, which placed the first absorption peak at about 285 nm.

In the experimental spectrum of the Cr^{3+} based IL, we observe three absorption bands, two weak bands centered at 562 nm, and 419 nm, and the third one, much stronger than the others, centered at 342 nm. The first two bands correspond to the typical spin-allowed transitions for a d^3 transition metal complex $^4A_{2g}(^4F) \longrightarrow {}^4T_{2g}(^4F)$ and $^4A_{2g}(^4F) \longrightarrow {}^4T_{1g}(^4F)$.[534–538] The third band is much more intense than the others, discarding an origin similar to those of the previous bands. Indeed, the next expected d-d transition, the $^4A_{2g}(^4F) \longrightarrow {}^4T_{1g}(^4P)$ one, usually falls at considerably lower wavelengths than the measured range.[535] According to the intensity of this band, it is produced by an doubly allowed transition whose origin could be charge transfer (CT) between the metal and the ligands or perturbed intra-ligand transitions in the $[SCN]^-$ anions.[539] The same bands of the experimental spectrum are reproduced in the simulated spectrum at the positions 511 nm, 417 nm and 337 nm.

In the case of Ni^{2+} based mixtures, three bands are observed in the experimental spectrum, one weak band around 970 nm, another weak and broad band centered at 645 nm and a strong peak at 352 nm with a shoulder at 380 nm. As in the case of Cr^{3+}, the first two bands are produced by the well-known d-d spin-allowed transitions of a d^8 transition metal: $^3A_{2g}(^3F) \longrightarrow {}^3T_{2g}(^3F)$ and $^3A_{2g}(^3F) \longrightarrow {}^3T_{1g}(^3F)$.[535,537] The peak produced by the third d-d

spin-allowed transition for Ni^{2+}, $^3A_{2g}(^3F) \longrightarrow {}^1T_{1g}(^3P)$ is expected to lie close to the position of the most intense peak.[535,537] However, the peak intensity suggests that the observed band is not produced by a d-d transition but, as in the case of the Cr^{3+} IL, it is likely produced by CT or intra-ligand transitions. Hence, the d-d transition $^3A_{2g}(^3F) \longrightarrow {}^1T_{1g}(^3P)$ is expected to be hidden beneath this peak. In the simulated spectrum, the first two bands are easily recognized and are predicted at 890 nm and 535 nm, while the third band at 352 nm is predicted as produced by the combination of two transitions. The high intensity of these transitions in relation to that of the d-d ones supports the assignment of these bands to CT or intraligand interactions.

Regarding the Mn^{2+}, the absorption spectrum was simulated both for high and low spin configurations of the complex. The agreement obtained between experimental and simulated data in the low spin case suggests that the Mn^{2+} cation is found in an unusual low-spin configuration.[540] The absorption spectrum of the Mn^{2+} IL is much more complex than those of the Ni^{2+} and Cr^{3+}. There are two important peaks we have tentatively identified; the one at 355 nm which we attributed to the transition between $^2T_{2g}(^2I) \longrightarrow {}^2E_{2g}(^2I)$, and the peak at 445 nm which is attributed to the transition between the almost degenerated levels $^2T_{2g}(^2I) \longrightarrow {}^2A_{2g}(^2I)$ and $^2T_{2g}(^2I) \longrightarrow {}^2T_{1g}(^2I)$. The assigned peaks are easily found in the simulated spectrum. Both experimental and computationally calculated peaks present a slight splitting that could be originated by the weak Jahn-Teller effect that could be present in a d^5 low spin metal cation.[541] In addition, a large amount of weak bands are observable, which we associate to d-d spin-forbidden transitions.

The IL doped with Fe^{3+} is in a d^5 configuration and, as in the case of the Mn^{2+} containing IL, the spin state was studied comparing the predicted absorption spectrum with the experimental one. In this case, the best agreement was obtained for the high spin configuration. The most relevant feature of the Fe^{3+} experimental spectrum is a broad peak at 491 nm that covers a large part of the spectral window. The high intensity of this peak, as well as the intense coloration of this IL,

indicates that the observed band is produced by ligand to metal charge transfer (LMCT) transitions since d-d transitions are weaker. The broadness and intensity of this band hides the rest of low intensity d-d transitions. The appearance of LMCT bands in the visible region is a common feature for Fe^{3+} complexes.[539,542–544] The simulated spectrum shows the existence of several low intensity peaks which are related to the d-d transitions, as well as the very intense LMCT band that dominates the spectrum at 478 nm, in very good agreement with the experimental results.

In order to obtain a deeper insight in the character of the near UV absorption bands found in Ni^{2+} and Cr^{3+} ILs, we plotted the energy (in eV) of the lowest energy spin and Laporte allowed TD-DFT transition of each IL against the reduction potential of each metal cation, Fig. 9.10. In the case that more than one band was registered in less than 10 nm, the one with the highest intensity was chosen. The reduction potentials were extracted from Ref. [545]. As can be seen, there is
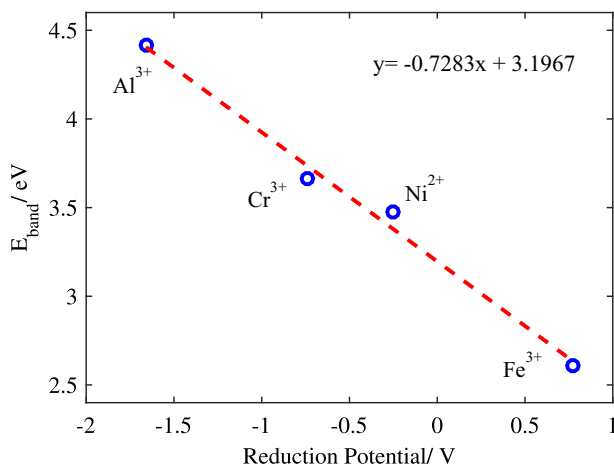
Figure 9.10: Energy of the first spin and Laporte allowed absorption band of each IL with respect to the reduction potential of their metal cation.

a closely linear relationship between the reduction potential of each

metal and the position of the first spin and Laporte allowed absorption band. The absorption band of the Fe^{3+} IL was assigned to LMCT, and, hence, the linear behavior observed for the rest of ILs suggests that the intense absorption bands in the Ni^{2+} and Cr^{3+} ILs are also produced by LMCT.[539] The predicted bands for Al^{3+} and Mn^{2+} ILs are not observed in their experimental spectra because their are placed in an UV region which was not accessible for our experimental technique. For the Al^{3+} this prediction implies that the first absorption peak observed in the simulations, at 285 nm, is produced by LMCT, while for the Mn^{2+} based IL, this result suggest the existence of an important LMCT absorption band at 305.5 nm which is neither experimentally or computationally observed as it falls outside of both our measurement and prediction range.

From the agreement achieved between the experimental and the simulated absorption bands it is possible to conclude that the near UV-Vis absorption of the system is mostly ruled by the inner structure of the $M - [SCN]^-$ complexes. The $[C_4mim]^+$ cations play a secondary role in the absorption of the complexes, since they were not included in the DFT calculations and the experimental results were reasonably reproduced. This result is in agreement with the behavior expected for a highly nanosegregated IL where the complexes are formed and confined in highly polar areas isolated in extensive nonpolar regions.

9.10 Conclusions

The introduction of metal cations, specifically of transition metals, provides a relevant mechanism for tailoring the structural and optical properties of ILs. Upon their addition, the microscopic structure of ILs unavoidably evolves in order to accommodate the metal cations within the polar regions of the nanosegregated bulk, as proved by experimental XRD patterns and MD simulations. The accommodation of the metal cations takes place by octahedral complexation with the thiocyanate anions, whose distribution within the polar regions is deeply modified

by the metals. Nevertheless, as a consequence of the intense charge screening of the metal cations, the organic cation distribution is roughly unaltered. The complexation of metal cations in these highly charged environments is, according to our observations, the result of a delicate interplay between ambidentation and bridging of thiocyanate anions. The existence of these coordination modes is compatible with a mechanism to reduce the charge of the metal-ligand complexes at the same time that their embedding within the polar regions is facilitated. Dynamic properties of these ILs are also dependent on the doping transition metal, both VACF and vibrational spectra suggest that trivalent metal cations lead to far more stable complexes than divalent ones. Nevertheless, the most notable changes induced by the different transition metals are found in the absorption spectra of the ILs. The important shift in the absorption bands produced by the different metals yield very different colorations for each IL, mostly governed by d-d Laporte-forbidden transitions within the complexes. However, a relevant ligand-metal charge transfer (LMCT) band, whose position is a function of the reduction potential of the metal cation was also found, and it was identified as the dominant transition in the case of the $[C_4mim]_3Fe[SCN]_6$ IL. The agreement of the experimental data with the calculated gas-phase absorption spectra suggests that the $[C_4mim]^+$ cations are mostly spectators of the electronic transitions within the metal-ligand complexes behind the UV-VIS spectra, providing an additional evidence of the strong nanosegregation within the polar regions of these IL mixtures.

9.11 Acknowledgments

Part IV

Conclusions

10. Conclusions and Future Perspectives

10.1 Conclusions

Throughout the different chapters of this thesis, we have traveled through the wide world of ionic liquids from the novel perspective of optics and photonics. During this trip, the relation of refractive, nonlinear and spectroscopic properties of ionic liquids with their structure at different characteristic scales was addressed from both experimental and computational points of view. Before ending, I summarize the most relevant reached conclusions:

1. Material dispersion of ionic liquids was for first time measured with high accuracy, $S(n) < 2.0 \cdot 10^{-4}$, within a broad spectral range, from 300 nm to 1550 nm using Refractive Index Spectroscopy by Broadband Interferometry (RISBI).

2. Anions were seem to determine the material dispersion with a precision of 10^{-2} while the length of the alkyl chain length of cations contributes only to 10^{-3}. Combining the effect of the anions with that of the alkyl chain of cations allows a precise tuning of the material dispersion which is interesting for applications from wave-guiding to refractive index fluids.

3. The modeling of material dispersion with Sellmeier formulas depends on the spectral range upon consideration. One-resonance models work well in the 400 nm to 1000 nm range, but three-resonance models are required for wider spectral ranges, such as that spanning from 300 nm to 1550 nm.

4. The wider is the spectral range upon consideration, further information is retrieved from the Sellmeier models. A single-resonance describes the temperature dependence, but three-

243

resonances also describe structural variations such as changes in the length of alkyl chains.

5. Within the framework of Sellmeier models and for imidazolium-based ionic liquids, the resonance positions are governed by the imidazolium ring, while the resonator strengths are linear functions of temperature and alkyl chain length.

6. The thermo-optical coefficient is a weakly dispersive magnitude with variations in the order of $1 \cdot 10^{-5} \ \mathrm{K}^{-1}$. The subtle spectral dependence arises from a residual dependence of electronic polarizability on temperature.

7. Material dispersion of ionic liquids can be rationalized in two basically independent contributions: molar refraction dispersion, responsible of the dependence on wavelength, and molar volume, responsible of the dependence on temperature.

8. Polarizability of ionic liquids is obtained by the addition of that of its composing ions, discarding charge transfer between them. However, additivity in terms of atomic polarizabilities is only ensured in the absence of charge delocalization.

9. Rational design of charge delocalized regions in conjunction with proper ion combination could deliver ionic liquids with refractive indices higher than 1.8, which are useful, for instance, for immersion liquids.

10. Second hyperpolarizability in ionic liquids is largely that of the sum of the contributions of their composing ions. However, first hyperpolarizability does not absolutely obey the superposition principle possibly because of its strong dependence on symmetry.

11. Charge delocalization is a key structural feature to produce relevant hyperpolarizabilities. Appropriate tailoring yields ionic liquids with third order susceptibilities about 10 times larger than that of the urea molecule, which is useful for triggering nonlinear optical phenomena.

12. Ionic liquids crystals can be macroscopically aligned by mechanical procedures and their birefringence measured. We demonstrated it by measuring the achromatic and temperature-independent birefringence of $[C_2mim][C_{10}SO_4]$, $\overline{\Delta n_{T,\lambda}} = 4.08(12) \cdot 10^{-3}$. Hence, in common applications, they offer a greener alternative to standard liquid crystals.

13. Transition metal doping is a promising strategy to tune the optical properties of ionic liquids, namely absorption spectra. The optical response is exclusively determined by the interaction of metals and anions within complexes and it could be used to design highly efficient spectral filters.

10.2 Future perspectives

On the basis of the results and conclusions exposed here, new research lines are currently under development or are expected to be addressed in the following years:

- a) Developing a MD model for ionic liquid crystals, and specifically, for the $[C_2mim][C_{10}SO_4]$ to study the interactions that lead to the mesophase stabilization and self-assembly processes.

- b) Synthesizing and experimentally characterize the material dispersion of ionic liquids with long conjugated chains, specifically, those candidates to present refractive indices higher than 1.8. Afterwards, characterizing their first and second order nonlinear optical response.

- c) Further improving our Sellmeier models for material dispersion of ionic liquids by explicitly considering cations beyond imidazolium and the role of charge delocalization.

USC
UNIVERSIDADE
DE SANTIAGO
DE COMPOSTELA

- d) Going a step forward and characterizing the optical responses of ionic liquids and their mixtures with active salts close to surfaces. The description and interpretation of the interactions in this 2D limit is essential to develop photonic sensors based on ionic liquids, which could be used, for instance, for in operando evaluation of the state of electrodes within batteries.

Bibliography

[1]   P. Walden and U. Molekulargr: Ueber die Molekulargrösse und elektrische Leitfähigkeit einiger geschmolzenen Salze, *Bull. l'Académie Impériale des Sci. St.-pétersbg.*, **8** (6), 405–422, 1914.

[2]   C. Nanjundiah, K. Shimizu, and R. A. Osteryoung: Electrochemical Studies of Fe(II) and Fe(III) in an Aluminum Chloride-Butylpyridinium Chloride Ionic Liquid, *J. Electrochem. Soc.*, **129** (11), 2474–2480, 1982.

[3]   T. M. Laher and C. L. Hussey: Electrochemical Studies of Chloro Complex Formation in Low-Temperature Chloroaluminate Melts. 2. Silver(I), *Inorg. Chem.*, **22** (9), 1279–1283, 1983.

[4]   T. M. Laher and C. L. Hussey: Copper(I) and Copper(II) Chloro Complexes in the Basic Aluminum Chloride-l-Methyl-3-ethylimidazolium Chloride Ionic Liquid, *Inorg. Chem.*, **22** (22), 3247–3251, 1983.

[5]   T. B. Scheffler and C. Hussey: Electrochemical study of tungsten chloro complex chemistry in the basic aluminum chloride-1-methyl-3-ethylimidazolium chloride ionic liquid, *Inorg. Chem.*, **23** (13), 1926–1932, 1984.

[6]   C. L. Hussey: Room temperature haloaluminate ionic liquids. Novel solvents for transition metal solution chemistry, *Pure Appl. Chem.*, **60** (12), 1763–1772, 1988.

[7]   J. S. Wilkes and M. J. Zaworotko: Air and water stable 1-ethyl-3-methylimidazolium based ionic liquids, *J. Chem. Soc. Chem. Commun.*, (13), 965–967, 1992.

[8]   L. P. N. Rebelo, J. N. Canongia Lopes, J. M. S. S. Esperança, and E. Filipe: On the Critical Temperature, Normal Boiling Point,

and Vapor Pressure of Ionic Liquids, *J. Phys. Chem. B*, **109** (13), 6040–6043, 2005.

[9] M. J. Earle, J. M. Esperança, M. A. Gilea, J. N. Canongia Lopes, L. P. Rebelo, et al.: The distillation and volatility of ionic liquids, *Nature*, **439**, 831–834, 2006.

[10] J. M. S. S. Esperança, J. N. Canongia Lopes, M. Tariq, L. M. N. B. F. Santos, J. W. Magee, et al.: Volatility of Aprotic Ionic Liquids — A Review, *J. Chem. Eng. Data*, **55** (1), 3–12, 2010.

[11] H. L. Ngo, K. LeCompte, L. Hargens, and A. B. McEwen: Thermal properties of imidazolium ionic liquids, *Thermochim. Acta*, **357-358**, 97–102, 2000.

[12] D. M. Fox, W. H. Awad, J. W. Gilman, P. H. Maupin, H. C. De Long, et al.: Flammability, thermal stability, and phase change characteristics of several trialkylimidazolium salts, *Green Chem.*, **5** (6), 724, 2003.

[13] K. J. Baranyai, G. B. Deacon, D. R. MacFarlane, J. M. Pringle, and J. L. Scott: Thermal Degradation of Ionic Liquids at Elevated Temperatures, *Aust. J. Chem.*, **57** (2), 145, 2004.

[14] U. Domańska: Thermophysical properties and thermodynamic phase behavior of ionic liquids, *Thermochim. Acta*, **448** (1), 19–30, 2006.

[15] H.-J. Liaw, C.-C. Chen, Y.-C. Chen, J.-R. Chen, S.-K. Huang, et al.: Relationship between flash point of ionic liquids and their thermal decomposition, *Green Chem.*, **14** (7), 2001, 2012.

[16] E. Gómez, N. Calvar, and Á. Domínguez: Thermal Behaviour of Pure Ionic Liquids, in *Ion. Liq. - Curr. State Art*, InTech, 2015.

[17] T. Welton: Room-Temperature Ionic Liquids. Solvents for Synthesis and Catalysis, *Chem. Rev.*, **99** (8), 2071–2084, 1999.

[18] C. Wheeler, K. N. West, C. A. Eckert, and C. L. Liotta: Ionic liquids as catalytic green solvents for nucleophilic displacement reactions, *Chem. Commun.*, (10), 887–888, 2001.

[19] R. D. Rogers and K. R. Seddon: Ionic Liquids–Solvents of the Future?, *Science*, **302** (5646), 792–793, 2003.

[20] J. Wilkes: Properties of ionic liquid solvents for catalysis, *J. Mol. Catal. A Chem.*, **214** (1), 11–17, 2004.

[21] C. Chiappe and D. Pieraccini: Ionic liquids: solvent properties and organic reactivity, *Journal of Physical Organic Chemistry*, **18**, 275–297, 2005.

[22] L. Galán Sánchez, G. Meindersma, and A. de Haan: Solvent Properties of Functionalized Ionic Liquids for CO_2 Absorption, *Chem. Eng. Res. Des.*, **85** (1), 31–39, 2007.

[23] Y. Pu, N. Jiang, and A. J. Ragauskas: Ionic Liquid as a Green Solvent for Lignin, *J. Wood Chem. Technol.*, **27** (1), 23–33, 2007.

[24] T. Sato, G. Masuda, and K. Takagi: Electrochemical properties of novel ionic liquids for electric double layer capacitor applications, *Electrochim. Acta*, **49** (21), 3603–3611, 2004.

[25] M. Armand, F. Endres, D. R. MacFarlane, H. Ohno, and B. Scrosati: Ionic-liquid materials for the electrochemical challenges of the future, *Nat. Mater.*, **8** (8), 621–629, 2009.

[26] K. S. Kim: Physical and electrochemical properties of lithium-doped 1-butyl-3-methylimidazolium salts, *Korean J. Chem. Eng.*, **26** (3), 770–774, 2009.

[27] J. Salgado, J. Parajó, M. Villanueva, J. Rodríguez, O. Cabeza, et al.: Liquid range of ionic liquid – metal salt mixtures for electrochemical applications, *The Journal of Chemical Thermodynamics*, **134**, 164–174, 2019.

[28]   H. Wang, S. Gu, Y. Bai, S. Chen, N. Zhu, et al.: Anion-effects on electrochemical properties of ionic liquid electrolytes for rechargeable aluminum batteries, *J. Mater. Chem. A*, **3** (45), 22677–22686, 2015.

[29]   A. E. Visser, R. P. Swatloski, W. M. Reichert, J. H. Davis Jr., R. D. Rogers, et al.: Task-specific ionic liquids for the extraction of metal ions from aqueous solutions, *Chem. Commun.*, (1), 135–136, 2001.

[30]   E. D. Bates, R. D. Mayton, I. Ntai, and J. H. Davis: CO_2 capture by a task-specific ionic liquid, *J. Am. Chem. Soc.*, **124** (6), 926–927, 2002.

[31]   X. Wang, M. Sternberg, F. T. U. Kohler, B. U. Melcher, P. Wasserscheid, et al.: Long-alkyl-chain-derivatized imidazolium salts and ionic liquid crystals with tailor-made properties, *RSC Adv.*, **4** (24), 12476–12481, 2014.

[32]   J. S. Moreno, S. Jeremias, A. Moretti, S. Panero, S. Passerini, et al.: Ionic liquid mixtures with tunable physicochemical properties, *Electrochim. Acta*, **151**, 599–608, 2015.

[33]   W. Liu, C. Ye, Q. Gong, H. Wang, and P. Wang: Tribological performance of room-temperature ionic liquids as lubricant, *Tribol. Lett.*, **13** (2), 81–85, 2002.

[34]   H. Wang, Q. Lu, C. Ye, W. Liu, and Z. Cui: Friction and wear behaviors of ionic liquid of alkylimidazolium hexafluorophosphates as lubricants for steel/steel contact, *Wear*, **256** (1-2), 44–48, 2004.

[35]   H. Kamimura, T. Kubo, I. Minami, and S. Mori: Effect and mechanism of additives for ionic liquids as new lubricants, *Tribol. Int.*, **40** (4), 620–625, 2007.

[36] M. Palacio and B. Bhushan: A Review of Ionic Liquids for Green Molecular Lubrication in Nanotechnology, *Tribol. Lett.*, **40** (2), 247–268, 2010.

[37] A. E. Somers, P. C. Howlett, D. R. MacFarlane, and M. Forsyth: A review of ionic liquid lubricants, *Lubricants*, **1** (1), 3–21, 2013.

[38] M. D. Avilés, C. Sánchez, R. Pamies, J. Sanes, and M. D. Bermúdez: Ionic liquid crystals in tribology, *Lubricants*, **7** (9), 72, 2019.

[39] L. Chen, L. Ge, L. Fan, and R. Guo: Microstructure and Tribological Properties of Lamellar Liquid Crystals Formed by Ionic Liquids as Cosurfactants, *Langmuir*, **35** (11), 4037–4045, 2019.

[40] A. Arce, H. Rodríguez, and A. Soto: Effect of anion fluorination in 1-ethyl-3-methylimidazolium as solvent for the liquid extraction of ethanol from ethyl tert-butyl ether, *Fluid Phase Equilib.*, **242** (2), 164–168, 2006.

[41] L. Alonso, A. Arce, M. Francisco, and A. Soto: Extraction ability of nitrogen-containing compounds involved in the desulfurization of fuels by using ionic liquids, *J. Chem. Eng. Data*, **55** (9), 3262–3267, 2010.

[42] C. F. Poole and S. K. Poole: Extraction of organic compounds with room temperature ionic liquids, *J. Chromatogr. A*, **1217** (16), 2268–2286, 2010.

[43] I. Domínguez, E. J. González, R. González, and Á. Domínguez: Extraction of benzene from aliphatic compounds using commercial ionic liquids as solvents: Study of the liquid-liquid equilibrium at T = 298.15 k, *J. Chem. Eng. Data*, **56** (8), 3376–3383, 2011.

[44] S. Corderí, B. González, N. Calvar, and E. Gómez: Ionic liquids as solvents to separate the azeotropic mixture hexane/ethanol, *Fluid Phase Equilib.*, **337**, 11–17, 2013.

[45] B. Rodríguez-Cabo, A. Arce, and A. Soto: Desulfurization of fuels by liquid-liquid extraction with 1-ethyl-3-methylimidazolium ionic liquids, *Fluid Phase Equilib.*, **356**, 126–135, 2013.

[46] J. Saien, M. M. S. Badieh, M. Norouzi, and S. Salehzadeh: Ionic liquid 1-hexyl-3-methylimidazolium hexafluorophosphate, an efficient solvent for extraction of acetone from aqueous solutions, *J. Chem. Thermodyn.*, **91**, 404–413, 2015.

[47] W. Wei, C.-W. Cho, S. Kim, M.-H. Song, J. K. Bediako, et al.: Selective recovery of Au(III), Pt(IV), and Pd(II) from aqueous solutions by liquid–liquid extraction using ionic liquid Aliquat-336, *J. Mol. Liq.*, **216**, 18–24, 2016.

[48] A. Berthod, M. J. Ruiz-Ángel, and S. Carda-Broch: Recent advances on ionic liquid uses in separation techniques, *J. Chromatogr. A*, **1559**, 2–16, 2018.

[49] S. Park and R. J. Kazlauskas: Biocatalysis in ionic liquids – advantages beyond green technology, *Curr. Opin. Biotechnol.*, **14** (4), 432–437, 2003.

[50] K. L. Luska, P. Migowski, and W. Leitner: Ionic liquid-stabilized nanoparticles as catalysts for the conversion of biomass, *Green Chem.*, **17** (6), 3195–3206, 2015.

[51] F. Maier, I. Niedermaier, and H. P. Steinrück: Perspective: Chemical reactions in ionic liquids monitored through the gas (vacuum)/liquid interface, *J. Chem. Phys.*, **146** (17), 2017.

[52] R. L. Vekariya: A review of ionic liquids: Applications towards catalytic organic transformations, *J. Mol. Liq.*, **227**, 44–60, 2017.

[53] J. Claus, F. O. Sommer, and U. Kragl: Ionic liquids in biotechnology and beyond, *Solid State Ionics*, **314**, 119–128, 2018.

[54] A. Taubert: CuCl nanoplatelets from an ionic liquid-crystal precursor, *Angew. Chemie - Int. Ed.*, **43** (40), 5380–5382, 2004.

[55] W. Dobbs, J.-M. Suisse, L. Douce, and R. Welter: Electrodeposition of Silver Particles and Gold Nanoparticles from Ionic Liquid-Crystal Precursors, *Angew. Chemie*, **118** (25), 4285–4288, 2006.

[56] M. Brettholle, O. Höfft, L. Klarhöfer, S. Mathes, W. Maus-Friedrichs, et al.: Plasma electrochemistry in ionic liquids: Deposition of copper nanoparticles, *Phys. Chem. Chem. Phys.*, **12** (8), 1750–1755, 2010.

[57] H. Wender, L. F. De Oliveira, P. Migowski, A. F. Feil, E. Lissner, et al.: Ionic liquid surface composition controls the size of gold nanoparticles prepared by sputtering deposition, *J. Phys. Chem. C*, **114** (27), 11764–11768, 2010.

[58] E. Vanecht, K. Binnemans, J. W. Seo, L. Stappers, and J. Fransaer: Growth of sputter-deposited gold nanoparticles in ionic liquids, *Phys. Chem. Chem. Phys.*, **13** (30), 13565–13571, 2011.

[59] J. F. Brennecke and B. E. Gurkan: Ionic liquids for CO_2 capture and emission reduction, *J. Phys. Chem. Lett.*, **1** (24), 3459–3464, 2010.

[60] M. Hasib-ur Rahman, M. Siaj, and F. Larachi: Ionic liquids for CO_2 capture—Development and progress, *Chem. Eng. Process. Process Intensif.*, **49** (4), 313–322, 2010.

[61] M. Ramdin, T. W. De Loos, and T. J. Vlugt: State-of-the-art of CO_2 capture with ionic liquids, *Ind. Eng. Chem. Res.*, **51** (24), 8149–8177, 2012.

[62]   T. Su, Z. Tang, C. Yin, Y. Yang, H. Wang, et al.: Insights into quaternary ammonium-based ionic liquids series with tetrafluoroborate anion for CO_2 capture, *J. Mol. Liq.*, **327**, 114857, 2021.

[63]   G. B. Appetecchi, M. Montanino, A. Balducci, S. F. Lux, M. Winterb, et al.: Lithium insertion in graphite from ternary ionic liquid-lithium salt electrolytes. I. Electrochemical characterization of the electrolytes, *J. Power Sources*, **192** (2), 599–605, 2009.

[64]   G. A. Elia, J. Hassoun, W.-J. Kwak, Y.-K. Sun, B. Scrosati, et al.: An Advanced Lithium–Air Battery Exploiting an Ionic Liquid-Based Electrolyte, *Nano Lett.*, **14** (11), 6572–6577, 2014.

[65]   M. Kar, Z. Ma, L. M. Azofra, K. Chen, M. Forsyth, et al.: Ionic liquid electrolytes for reversible magnesium electrochemistry, *Chem. Commun.*, **52** (21), 4033–4036, 2016.

[66]   R. Sasi, S. Sarojam, and S. J. Devaki: High Performing Biobased Ionic Liquid Crystal Electrolytes for Supercapacitors, *ACS Sustain. Chem. Eng.*, **4** (6), 3535–3543, 2016.

[67]   R. Mangaiyarkarasi, S. Selvam, V. Ganesh, and S. Umadevi: A cholesterol based imidazolium ionic liquid crystal: synthesis, characterisation and its dual application as an electrolyte and electrode material, *New J. Chem.*, **43** (2), 1063–1071, 2019.

[68]   X. Chen, Y. Xie, Y. Ling, J. Zhao, Y. Xu, et al.: Ionic liquid crystal induced morphological control of solid composite polymer electrolyte for lithium-ion batteries, *Mater. Des.*, **192**, 2020.

[69]   R. Kawano, M. K. Nazeeruddin, A. Sato, M. Grätzel, and M. Watanabe: Amphiphilic ruthenium dye as an ideal sensitizer in conversion of light to electricity using ionic liquid crystal electrolyte, *Electrochem. commun.*, **9** (5), 1134–1138, 2007.

[70] N. Yamanaka, R. Kawano, W. Kubo, N. Masaki, T. Kitamura, et al.: Dye-sensitized TiO$_2$ solar cells using imidazolium-type ionic liquid crystal systems as effective electrolytes, *J. Phys. Chem. B*, **111** (18), 4763–4769, 2007.

[71] X. Pan, M. Wang, X. Fang, C. Zhang, Z. Huo, et al.: Ionic liquid crystal-based electrolyte with enhanced charge transport for dye-sensitized solar cells, *Sci. China Chem.*, **56** (10), 1463–1469, 2013.

[72] R. Atasiei, M. Raicopol, C. Andronescu, A. Hanganu, A. L. Alexe-Ionescu, et al.: Investigation of the conduction properties of ionic liquid crystal electrolyte used in dye sensitized solar cells, *J. Mol. Liq.*, **267**, 81–88, 2018.

[73] M. Deetlefs, K. R. Seddon, and M. Shara: Neoteric optical media for refractive index determination of gems and minerals, *New J. Chem.*, **30** (3), 317, 2006.

[74] X. Wu, M. Muntzeck, T. de los Arcos, G. Grundmeier, R. Wilhelm, et al.: Determination of the refractive indices of ionic liquids by ellipsometry, and their application as immersion liquids, *Appl. Opt.*, **57** (31), 9215, 2018.

[75] X. Hu, S. Zhang, C. Qu, Q. Zhang, L. Lu, et al.: Ionic liquid based variable focus lenses, *Soft Matter*, **7** (13), 5941, 2011.

[76] X. Hu, S. Zhang, Y. Liu, C. Qu, L. Lu, et al.: Electrowetting based infrared lens using ionic liquids, *Appl. Phys. Lett.*, **99** (21), 213505, 2011.

[77] S. Calixto, M. Rosete-Aguilar, F. J., O. L., E. M. Martinez Prado, et al.: Optofluidic Compound Lenses Made with Ionic Liquids, in S. Handy, editor, *Appl. Ion. Liq. Sci. Technol.*, chapter 23, InTech, 2011.

[78]   A. Shahini, J. Xia, Z. Zhou, Y. Zhao, and M. M. C. Cheng: Versatile Miniature Tunable Liquid Lenses Using Transparent Graphene Electrodes, *Langmuir*, **32** (6), 1658–1665, 2016.

[79]   J. Guo, M. Zhou, Y.-G. Liu, K. Di, R. Li, et al.: An all-optical controlled attenuation effect in an all-fiber system based on ionic liquid-filled photonic bandgap fiber, *Phys. Scr.*, **94** (11), 115508, 2019.

[80]   X. He, Q. Shao, P. Cao, W. Kong, J. Sun, et al.: Electro-optical phenomena based on ionic liquids in an optofluidic waveguide, *Lab Chip*, **15** (5), 1311–1319, 2015.

[81]   A. Abate, A. Petrozza, G. Cavallo, G. Lanzani, F. Matteucci, et al.: Anisotropic ionic conductivity in fluorinated ionic liquid crystals suitable for optoelectronic applications, *J. Mater. Chem. A*, **1** (22), 6572–6578, 2013.

[82]   L. Gao, X. Yang, Y. Shu, X. Chen, and J. Wang: Ionic liquid-based slab optical waveguide sensor for the detection of ammonia in human breath, *J. Colloid Interface Sci.*, **512**, 819–825, 2018.

[83]   O. Cabeza, E. Rilo, L. Segade, M. Domínguez-Pérez, S. García-Garabal, et al.: Imidazolium decyl sulfate: a very promising selfmade ionic hydrogel, *Mater. Chem. Front.*, **2** (3), 505–513, 2018.

[84]   K. Tanabe, Y. Suzui, M. Hasegawa, and T. Kato: Full-Color Tunable Photoluminescent Ionic Liquid Crystals Based on Tripodal Pyridinium, Pyrimidinium, and Quinolinium Salts, *J. Am. Chem. Soc.*, **134** (12), 5652–5661, 2012.

[85]   C. Yang, Q. Sun, T. Qiao, and Y. Li: Ionic Liquid Doped Polymer Light-Emitting Electrochemical Cells, *J. Phys. Chem. B*, **107** (47), 12981–12988, 2003.

256

[86]   J. Huang, C. A. Tao, Q. An, W. Zhang, Y. Wu, et al.: 3D-ordered macroporous poly(ionic liquid) films as multifunctional materials, *Chem. Commun.*, **46** (6), 967–969, 2010.

[87]   R. E. Del Sesto, D. S. Dudis, F. Ghebremichael, N. E. Heimer, T. K. Low, et al.: Nonlinear optical ionic liquids, in *ACS Symp. Ser.*, volume 902, pages 144–158, 2005.

[88]   J. A. Nóvoa-López, E. López Lago, J. A. Seijas, M. Pilar Vázquez-Tato, J. Troncoso, et al.: Nonlinear absorption in ionic liquids with transition metallic atoms in the anion, *Opt. Mater. (Amst).*, **52**, 144–149, 2016.

[89]   E. F. Borra, O. Seddiki, R. Angel, D. Eisenstein, P. Hickson, et al.: Deposition of metal films on an ionic liquid as a basis for a lunar telescope, *Nature*, **447**, 979–981, 2007.

[90]   R. D. Rogers: Materials science: Reflections on ionic liquids, *Nature*, **447** (7147), 917–918, 2007.

[91]   A. P. Fröba, H. Kremer, and A. Leipertz: Density, Refractive Index, Interfacial Tension, and Viscosity of Ionic Liquids [EMIM][EtSO$_4$], [EMIM][NTf$_2$], [EMIM][N(CN)$_2$], and [OMA][NTf$_2$] in Dependence on Temperature at Atmospheric Pressure, *J. Phys. Chem. B*, **112** (39), 12420–12430, 2008.

[92]   S. Calixto, M. E. Sánchez-Morales, F. J. Sánchez-Marin, M. Rosete-Aguilar, A. M. Richa, et al.: Optofluidic variable focus lenses, *Applied Optics*, **48**, 2308, 2009.

[93]   B. Hasse, J. Lehmann, D. Assenbaum, P. Wasserscheid, A. Leipertz, et al.: Viscosity, Interfacial Tension, Density, and Refractive Index of Ionic Liquids [EMIM][MeSO$_3$], [EMIM][MeOHPO$_2$], [EMIM][OcSO$_4$], and [BBIM][NTf$_2$] in Dependence on Temperature at Atmospheric Pressure, *J. Chem. Eng. Data*, **54** (9), 2576–2583, 2009.

257

[94]   C. Chiappe, P. Margari, A. Mezzetta, C. S. Pomelli, S. Koutsoumpos, et al.: Temperature effects on the viscosity and the wavelength-dependent refractive index of imidazolium-based ionic liquids with a phosphorus-containing anion, *Phys. Chem. Chem. Phys.*, **19** (12), 8201–8209, 2017.

[95]   B. Mokhtarani, M. M. Mojtahedi, H. R. Mortaheb, M. Mafi, F. Yazdani, et al.: Densities, Refractive Indices, and Viscosities of the Ionic Liquids 1-Methyl-3-octylimidazolium Tetrafluoroborate and 1-Methyl-3-butylimidazolium Perchlorate and Their Binary Mixtures with Ethanol at Several Temperatures, *J. Chem. Eng. Data*, **53** (3), 677–682, 2008.

[96]   I. Bandrés, F. M. Royo, I. Gascón, M. Castro, and C. Lafuente: Anion influence on thermophysical properties of ionic liquids: 1-Butylpyridinium tetrafluoroborate and 1-butylpyridinium triflate, *J. Phys. Chem. B*, **114** (10), 3601–3607, 2010.

[97]   S. Seki, S. Tsuzuki, K. Hayamizu, Y. Umebayashi, N. Serizawa, et al.: Comprehensive Refractive Index Property for Room-Temperature Ionic Liquids, *J. Chem. Eng. Data*, **57** (8), 2211–2216, 2012.

[98]   G. Vakili-Nezhaad, M. Vatani, M. Asghari, and I. Ashour: Effect of temperature on the physical properties of 1-butyl-3-methylimidazolium based ionic liquids with thiocyanate and tetrafluoroborate anions, and 1-hexyl-3-methylimidazolium with tetrafluoroborate and hexafluorophosphate anions, *J. Chem. Thermodyn.*, **54**, 148–154, 2012.

[99]   M. G. Montalbán, C. L. Bolívar, F. G. Díaz Baños, and G. Víllora: Effect of Temperature, Anion, and Alkyl Chain Length on the Density and Refractive Index of 1-Alkyl-3-methylimidazolium-Based Ionic Liquids, *J. Chem. Eng. Data*, **60** (7), 1986–1996, 2015.

[100] Z. Vaid, U. More, S. P. Ijardar, and N. I. Malek: Investigation on thermophysical and excess properties of binary mixtures of imidazolium based ionic liquids at temperatures (293.15 to 323.15) K: III [$C_n$mim][PF_6] (n = 4, 6, 8) + THF, *J. Chem. Thermodyn.*, **86**, 143–153, 2015.

[101] A. Paul, P. K. Mandal, and A. Samanta: On the optical properties of the imidazolium ionic liquids, *J. Phys. Chem. B*, **109** (18), 9148–9153, 2005.

[102] I. Billard, G. Moutiers, A. Labet, A. El Azzi, C. Gaillard, et al.: Stability of Divalent Europium in an Ionic Liquid: Spectroscopic Investigations in 1-Methyl-3-butylimidazolium Hexafluorophosphate, *Inorg. Chem.*, **42** (5), 1726–1733, 2003.

[103] C. Gaillard, I. Billard, A. Chaumont, S. Mekki, A. Ouadi, et al.: Europium(III) and Its Halides in Anhydrous Room-Temperature Imidazolium-Based Ionic Liquids: A Combined TRES, EXAFS, and Molecular Dynamics Study, *Inorg. Chem.*, **44** (23), 8355–8367, 2005.

[104] P. Nockemann, E. Beurer, K. Driesen, R. Van Deun, K. Van Hecke, et al.: Photostability of a highly luminescent europium β-diketonate complex in imidazolium ionic liquids, *Chem. Commun.*, (34), 4354, 2005.

[105] S. Tang, A. Babai, and A.-V. Mudring: Europium-Based Ionic Liquids as Luminescent Soft Materials, *Angew. Chemie Int. Ed.*, **47** (40), 7631–7634, 2008.

[106] T. Cardinaels, K. Lava, K. Goossens, S. V. Eliseeva, and K. Binnemans: 1,10-Phenanthrolinium Ionic Liquid Crystals, *Langmuir*, **27** (5), 2036–2043, 2011.

[107] N. Lei, D. Shen, X. Wang, J. Wang, Q. Li, et al.: Enhanced full color tunable luminescent lyotropic liquid crystals from P123 and ionic liquid by doping lanthanide complexes and AIEgen, *J. Colloid Interface Sci.*, **529**, 122–129, 2018.

[108] I. Sánchez, C. Cuerva, G. Marcelo, E. Oliveira, H. M. Santos, et al.: Designing Eu-β-diketonate complexes as a support of ionic liquid crystals (ILCs) with additional luminescent properties, *Dye. Pigment.*, **159** (June), 395–405, 2018.

[109] C. V. Rao, A. Rout, and K. Venkatesan: Europium(III) complexation behaviour in an alkyl ammonium ionic liquid medium containing neutral extractants, *Sep. Purif. Technol.*, **213** (December 2018), 545–552, 2019.

[110] A. Babai and A.-V. Mudring: Anhydrous Praseodymium Salts in the Ionic Liquid [bmpyr][Tf$_2$N]: Structural and Optical Properties of [bmpyr]$_4$ [PrI$_6$][Tf$_2$N] and [bmyr]$_2$[Pr(Tf$_2$N)$_5$], *Chem. Mater.*, **17** (25), 6230–6238, 2005.

[111] J.-H. Olivier, F. Camerel, J. Barberá, P. Retailleau, and R. Ziessel: Ionic Liquid Crystals Formed by Self-Assembly around an Anionic Anthracene Core, *Chem. - A Eur. J.*, **15** (33), 8163–8174, 2009.

[112] J.-H. Olivier, F. Camerel, G. Ulrich, J. Barberá, and R. Ziessel: Luminescent Ionic Liquid Crystals from Self-Assembled BODIPY Disulfonate and Imidazolium Frameworks, *Chem. - A Eur. J.*, **16** (24), 7134–7142, 2010.

[113] S. J. Osborne, S. Wellens, C. Ward, S. Felton, R. M. Bowman, et al.: Thermochromism and switchable paramagnetism of cobalt(ii) in thiocyanate ionic liquids, *Dalt. Trans.*, **44** (25), 11286–11289, 2015.

[114] B. May, M. Hönle, B. Heller, F. Greco, R. Bhuin, et al.: Surface-Induced Changes in the Thermochromic Transformation of an Ionic Liquid Cobalt Thiocyanate Complex, *J. Phys. Chem. Lett.*, **8** (6), 1137–1141, 2017.

[115] A. Brazier, G. B. Appetecchi, S. Passerini, A. Surca Vuk, B. Orel, et al.: Ionic liquids in electrochromic devices, *Electrochim. Acta*, **52** (14), 4792–4797, 2007.

[116] S. Yazaki, M. Funahashi, and T. Kato: An electrochromic nanostructured liquid crystal consisting of π-conjugated and ionic moieties, *J. Am. Chem. Soc.*, **130** (40), 13206–13207, 2008.

[117] A. Branco, L. C. Branco, and F. Pina: Electrochromic and magnetic ionic liquids, *Chem. Commun.*, **47** (8), 2300–2302, 2011.

[118] A. Kavanagh, K. J. Fraser, R. Byrne, and D. Diamond: An electrochromic ionic liquid: Design, characterization, and performance in a solid-state platform, *ACS Appl. Mater. Interfaces*, **5** (1), 55–62, 2013.

[119] L. C. Branco and F. Pina: Intrinsically photochromic ionic liquids, *Chem. Commun.*, (41), 6204–6206, 2009.

[120] F. I. López, J. M. Domínguez, A. D. Miranda, M. Trejo-Durán, E. Alvarado-Méndez, et al.: Synthesis of symmetric ionic liquids and their evaluation of nonlinear optical properties, *Opt. Mater. (Amst).*, **96**, 109276, 2019.

[121] M. Trejo-Durán, E. Alvarado-Méndez, and J. M. Estudillo-Ayala: Nonlinear optical properties in ionic liquids, *Nonlinear Opt. Fundam. Appl. Technol. Adv.*, pages 179–201, 2014.

[122] V. C. Ferreira, G. Marin, J. Dupont, and R. R. B. Correia: Nonlinear and thermo-optical characterisation of bare imidazolium ionic liquids, *J. Phys. Condens. Matter*, **33** (9), 095101, 2020.

[123] V. Rodriguez, J. Grondin, F. Adamietz, and Y. Danten: Local Structure in Ionic Liquids Investigated by Hyper-Rayleigh Scattering, *J. Phys. Chem. B*, **114** (46), 15057–15065, 2010.

[124] J. Castellanos-Águila, M. Olea-Amezcua, H. Hernández-Cocoletzi, and M. Trejo-Durán: Tuning the nonlinear optical properties of the $[alkyl-Py]^{+}[NO_3]^{-}$ and $[alkyl-MIM]^{+}[NO_3]^{-}$ ionic liquids, *J. Mol. Liq.*, **285** (3), 803–810, 2019.

USC
UNIVERSIDADE
DE SANTIAGO
DE COMPOSTELA

[125] J. Castellanos Águila and M. Trejo-Durán: Theoretical study of the second-order nonlinear optical properties of ionic liquids, *J. Mol. Liq.*, **269**, 833–838, 2018.

[126] M. Olea-Amezcua, J. Castellanos-Águila, H. Hernández-Cocoletzi, E. Ferreira, M. Trejo-Durán, et al.: Effect of the side-chain length and NLO properties of the N-ethyl-N,N,N-trialkylammonium ionic liquids – A DFT study, *J. Mol. Liq.*, **337**, 116251, 2021.

[127] J. Nóvoa-López, E. López Lago, M. Domínguez-Pérez, J. Troncoso, L. Varela, et al.: Thermal refraction in ionic liquids induced by a train of femtosecond laser pulses, *Opt. Laser Technol.*, **61**, 1–7, 2014.

[128] M. C. Schlick, N. Kapernaum, M. M. Neidhardt, T. Wöhrle, Y. Stöckl, et al.: Large Electro-Optic Kerr Effect in Ionic Liquid Crystals: Connecting Features of Liquid Crystals and Polyelectrolytes, *ChemPhysChem*, **19** (18), 2305–2312, 2018.

[129] B.-R. Hyun, S. V. Dzyuba, R. A. Bartsch, and E. L. Quitevis: Intermolecular Dynamics of Room-Temperature Ionic Liquids: Femtosecond Optical Kerr Effect Measurements on 1-Alkyl-3-methylimidazolium Bis((trifluoromethyl)sulfonyl)imides, *J. Phys. Chem. A*, **106** (33), 7579–7585, 2002.

[130] G. Giraud, C. M. Gordon, I. R. Dunkin, and K. Wynne: The effects of anion and cation substitution on the ultrafast solvent dynamics of ionic liquids: A time-resolved optical Kerr-effect spectroscopic study, *J. Chem. Phys.*, **119** (1), 464–477, 2003.

[131] H. Shirota, A. M. Funston, J. F. Wishart, and E. W. Castner: Ultrafast dynamics of pyrrolidinium cation ionic liquids, *J. Chem. Phys.*, **122** (18), 184512, 2005.

[132] D. Xiao, J. R. Rajian, A. Cady, S. Li, R. A. Bartsch, et al.: Nanostructural Organization and Anion Effects on the

Temperature Dependence of the Optical Kerr Effect Spectra of Ionic Liquids, *J. Phys. Chem. B*, **111** (18), 4669–4677, 2007.

[133] D. Xiao, J. R. Rajian, L. G. Hines, S. Li, R. A. Bartsch, et al.: Nanostructural Organization and Anion Effects in the Optical Kerr Effect Spectra of Binary Ionic Liquid Mixtures, *J. Phys. Chem. B*, **112** (42), 13316–13325, 2008.

[134] A. Pardon, O. Bonhomme, C. Gaillard, P.-F. Brevet, and E. Benichou: Nonlinear optical signature of nanostructural transition in ionic liquids, *J. Mol. Liq.*, **322**, 114976, 2021.

[135] R. Costa, C. M. Pereira, A. F. Silva, P.-F. Brevet, and E. Benichou: Ordering and Nonideality of Air–Ionic Liquid Interfaces in Surface Second Harmonic Generation, *J. Phys. Chem. B*, **124** (19), 3954–3961, 2020.

[136] C. Romero and S. Baldelli: Sum Frequency Generation Study of the Room-Temperature Ionic Liquids/Quartz Interface, *J. Phys. Chem. B*, **110** (12), 6213–6223, 2006.

[137] C. Romero, H. J. Moore, T. R. Lee, and S. Baldelli: Orientation of 1-Butyl-3-methylimidazolium Based Ionic Liquids at a Hydrophobic Quartz Interface Using Sum Frequency Generation Spectroscopy, *J. Phys. Chem. C*, **111** (1), 240–247, 2007.

[138] S. Baldelli: Probing Electric Fields at the Ionic Liquid−Electrode Interface Using Sum Frequency Generation Spectroscopy and Electrochemistry, *J. Phys. Chem. B*, **109** (27), 13049–13051, 2005.

[139] S. Baldelli: Surface Structure at the Ionic Liquid−Electrified Metal Interface, *Acc. Chem. Res.*, **41** (3), 421–431, 2008.

[140] S. Baldelli, J. Bao, W. Wu, and S.-s. Pei: Sum frequency generation study on the orientation of room-temperature ionic liquid at the graphene–ionic liquid interface, *Chem. Phys. Lett.*, **516** (4-6), 171–173, 2011.

[141] K. Binnemans: Ionic Liquid Crystals, *Chem. Rev.*, **105** (11), 4148–4204, 2005.

[142] K. V. Axenov and S. Laschat: Thermotropic Ionic Liquid Crystals, *Materials (Basel).*, **4** (1), 206–259, 2011.

[143] A. Alvarez Fernandez and P. Kouwer: Key Developments in Ionic Liquid Crystals, *Int. J. Mol. Sci.*, **17** (5), 731, 2016.

[144] K. Goossens, K. Lava, C. W. Bielawski, and K. Binnemans: Ionic Liquid Crystals: Versatile Materials, *Chem. Rev.*, **116** (8), 4643–4807, 2016.

[145] C. M. Gordon, J. D. Holbrey, A. R. Kennedy, and K. R. Seddon: Ionic liquid crystals: hexafluorophosphate salts, *J. Mater. Chem.*, **8** (12), 2627–2636, 1998.

[146] J. D. Holbrey and K. R. Seddon: The phase behaviour of 1-alkyl-3-methylimidazolium tetrafluoroborates; ionic liquids and ionic liquid crystals, *J. Chem. Soc. Dalt. Trans.*, (13), 2133–2140, 1999.

[147] A. E. Bradley, C. Hardacre, J. D. Holbrey, S. Johnston, S. E. J. McMath, et al.: Small-Angle X-ray Scattering Studies of Liquid Crystalline 1-Alkyl-3-methylimidazolium Salts, *Chem. Mater.*, **14** (2), 629–635, 2002.

[148] K. Goossens, P. Nockemann, K. Driesen, B. Goderis, C. Görller-Walrand, et al.: Imidazolium ionic liquid crystals with pendant mesogenic groups, *Chem. Mater.*, **20** (1), 157–168, 2008.

[149] W. Li, J. Zhang, B. Li, M. Zhang, and L. Wu: Branched quaternary ammonium amphiphiles: Nematic ionic liquid crystals near room temperature, *Chem. Commun.*, (35), 5269–5271, 2009.

[150] M. Tariq, P. Forte, M. C. Gomes, J. C. Lopes, and L. Rebelo: Densities and refractive indices of imidazolium- and

phosphonium-based ionic liquids: Effect of temperature, alkyl chain length, and anion, *J. Chem. Thermodyn.*, **41** (6), 790–798, 2009.

[151] W. G. Xu, L. Li, X. X. Ma, J. Wei, W.-B. Duan, et al.: Density, Surface Tension, and Refractive Index of Ionic Liquids Homologue of 1-Alkyl-3-methylimidazolium Tetrafluoroborate [C$_n$mim][BF$_4$] (n = 2,3,4,5,6), *J. Chem. Eng. Data*, **57** (8), 2177–2184, 2012.

[152] M. M. Akbar and T. Murugesan: Thermophysical properties of 1-hexyl-3-methylimidazolium tetrafluoroborate [hmim][BF$_4$] +N-methyldiethanolamine (MDEA) at temperatures (303.15 to 323.15) K, *J. Mol. Liq.*, **177**, 54–59, 2013.

[153] A. Muhammad, M. I. Abdul Mutalib, C. D. Wilfred, T. Murugesan, and A. Shafeeq: Thermophysical properties of 1-hexyl-3-methyl imidazolium based ionic liquids with tetrafluoroborate, hexafluorophosphate and bis(trifluoromethylsulfonyl)imide anions, *J. Chem. Thermodyn.*, **40** (9), 1433–1438, 2008.

[154] S. P. Ijardar and N. I. Malek: Experimental and theoretical excess molar properties of imidazolium based ionic liquids with molecular organic solvents – I. 1-Hexyl-3-methylimidazlouim tetraflouroborate and 1-octyl-3-methylimidazlouim tetraflouroborate with cyclic ethers, *J. Chem. Thermodyn.*, **71**, 236–248, 2014.

[155] A. A. Miran Beigi, M. Abdouss, M. Yousefi, S. M. Pourmortazavi, and A. Vahid: Investigation on physical and electrochemical properties of three imidazolium based ionic liquids (1-hexyl-3-methylimidazolium tetrafluoroborate, 1-ethyl-3-methylimidazolium bis(trifluoromethylsulfonyl) imide and 1-butyl-3-methylimidazolium methylsulfate), *J. Mol. Liq.*, **177**, 361–368, 2013.

[156] H. Lv, Y. Guo, X. An, and W. Shen: Liquid−Liquid Coexistence Curves of { x 1-Butyl-3-methylimidazolium Tetrafluoroborate + (1 − x) 1,3-Propanediol} and { x 1-Butyl-3-methylimidazolium Tetrafluoroborate + (1 − x) 1,4-Butanediol}, *J. Chem. Eng. Data*, **55** (7), 2482–2488, 2010.

[157] Z. Hao, Z. Cui, T. Yin, P. Zheng, J. Zhao, et al.: Liquid–liquid phase equilibria of ionic liquid solutions in the critical region: 1-Methyl-3-octylimidazolium tetrafluoroborate with 1-pentanol or 1-hexanol, *Fluid Phase Equilib.*, **380**, 58–66, 2014.

[158] P. Navarro, M. Larriba, S. García, J. García, and F. Rodríguez: Physical Properties of Binary and Ternary Mixtures of 2-Propanol, Water, and 1-Butyl-3-methylimidazolium Tetrafluoroborate Ionic Liquid, *J. Chem. Eng. Data*, **57** (4), 1165–1173, 2012.

[159] Q. Zhang, Z. Li, J. Zhang, S. Zhang, L. Zhu, et al.: Physicochemical Properties of Nitrile-Functionalized Ionic Liquids, *J. Phys. Chem. B*, **111** (11), 2864–2872, 2007.

[160] S. Govardhana Rao, T. Madhu Mohan, T. Vijaya Krishna, K. Narendra, and B. Subba Rao: Thermophysical properties of 1-butyl-3-methylimidazolium tetrafluoroborate and N-methyl-2-pyrrolidinone as a function of temperature, *J. Mol. Liq.*, **211**, 1009–1017, 2015.

[161] K. S. Kim, B. K. Shin, and H. Lee: Physical and electrochemical properties of 1-butyl-3-methylimidazolium bromide, 1-butyl-3-methylimidazolium iodide, and 1-butyl-3-methylimidazolium tetrafluoroborate, *Korean J. Chem. Eng.*, **21** (5), 1010–1014, 2004.

[162] K. S. Kim, B. K. Shin, H. Lee, and F. Ziegler: Refractive index and heat capacity of 1-butyl-3-methylimidazolium bromide and 1-butyl-3-methylimidazolium tetrafluoroborate, and vapor pressure of binary systems for 1-butyl-3-methylimidazolium

bromide + trifluoroethanol and 1-butyl-3-methylimidazolium tetrafluoroborate+trifluoroethanol, *Fluid Phase Equilib.*, **218** (2), 215–220, 2004.

[163] M. M. Taib and T. Murugesan: Density, refractive index, and excess properties of 1-butyl-3- methylimidazolium tetrafluoroborate with water and monoethanolamine, *J. Chem. Eng. Data*, **57** (1), 120–126, 2012.

[164] A. N. Soriano, B. T. Doma, and M. H. Li: Measurements of the density and refractive index for 1-n-butyl-3-methylimidazolium-based ionic liquids, *J. Chem. Thermodyn.*, **41** (3), 301–307, 2009.

[165] A. Kumar: Estimates of internal pressure and molar refraction of imidazolium based ionic liquids as a function of temperature, *J. Solution Chem.*, **37** (2), 203–214, 2008.

[166] E. Vercher, F. J. Llopis, V. González-Alfaro, P. J. Miguel, V. Orchillés, et al.: Volumetric properties, viscosities and refractive indices of binary liquid mixtures of tetrafluoroborate-based ionic liquids with methanol at several temperatures, *J. Chem. Thermodyn.*, **90**, 174–184, 2015.

[167] M. Srinivasa Reddy, S. M. Nayeem, K. T. S. S. Raju, and B. Hari Babu: The study of solute–solvent interactions in 1-ethyl-3-methylimidazolium tetrafluoroborate + 2-ethoxyethanol from density, speed of sound, and refractive index measurements, *J. Therm. Anal. Calorim.*, **124** (2), 959–971, 2016.

[168] O. Ciocirlan, O. Croitoru, and O. Iulian: Density and Refractive Index of Binary Mixtures of Two 1-Alkyl-3-methylimidazolium Ionic Liquids with 1,4-Dioxane and Ethylene Glycol, *J. Chem. Eng. Data*, **59** (4), 1165–1174, 2014.

[169] X. He, Q. Shao, W. Kong, L. Yu, X. Zhang, et al.: A simple method for estimating mutual diffusion coefficients of ionic liquids-water based on an optofluidic chip, *Fluid Phase Equilib.*, **366**, 9–15, 2014.

[170] M. Shamsipur, A. A. M. Beigi, M. Teymouri, S. M. Pourmortazavi, and M. Irandoust: Physical and electrochemical properties of ionic liquids 1-ethyl-3-methylimidazolium tetrafluoroborate, 1-butyl-3-methylimidazolium trifluoro-methanesulfonate and 1-butyl-1-methylpyrrolidinium bis(trifluoromethylsulfonyl)imide, *J. Mol. Liq.*, **157** (1), 43–50, 2010.

[171] C. M. S. S. Neves, K. A. Kurnia, J. A. P. Coutinho, I. M. Marrucho, J. N. C. Lopes, et al.: Systematic Study of the Thermophysical Properties of Imidazolium-Based Ionic Liquids with Cyano-Functionalized Anions, *J. Phys. Chem. B*, **117** (35), 10271–10283, 2013.

[172] M. A. Iglesias-Otero, J. Troncoso, E. Carballo, and L. Romaní: Density and Refractive Index for Binary Systems of the Ionic Liquid [Bmim][BF$_4$] with Methanol, 1,3-Dichloropropane, and Dimethyl Carbonate, *J. Solution Chem.*, **36** (10), 1219–1230, 2007.

[173] L. Alonso, A. Arce, M. Francisco, and A. Soto: Solvent extraction of thiophene from n-alkanes (C7, C12, and C16) using the ionic liquid [C$_8$mim][BF$_4$], *J. Chem. Thermodyn.*, **40** (6), 966–972, 2008.

[174] M. Wagner, O. Stanga, and W. Schröer: The liquid–liquid coexistence of binary mixtures of the room temperature ionic liquid 1-methyl-3-hexylimidazolium tetrafluoroborate with alcohols, *Phys. Chem. Chem. Phys.*, **6** (18), 4421–4431, 2004.

[175] G. Pérez-Sánchez, J. Troncoso, P. Losada-Pérez, P. Méndez-Castro, and L. Romaní: Highly precise (liquid+liquid) equilibrium and heat capacity measurements near the critical point for [Bmim][BF$_4$]+1H, 1H, 2H, 2H perfluoroctanol, *J. Chem. Thermodyn.*, **65**, 131–137, 2013.

[176] P. Brocos, Á. Piñeiro, R. Bravo, and A. Amigo: Refractive indices, molar volumes and molar refractions of binary liquid mixtures: Concepts and correlations, *Phys. Chem. Chem. Phys.*, **5** (3), 550–557, 2003.

[177] P. Nockemann, K. Binnemans, and K. Driesen: Purification of imidazolium ionic liquids for spectroscopic applications, *Chem. Phys. Lett.*, **415** (1-3), 131–136, 2005.

[178] L. Valerio., P. Kai-Erik, J. J. Saarinen, and V. Erik M.: *Kramers-Kronig Relations in Optical Materials Research*, volume 110 of *Springer Series in Optical Sciences*, Springer-Verlag, Berlin/Heidelberg, 2005.

[179] Y. Arosa, E. L. Lago, L. M. Varela, and R. de la Fuente: Spectrally resolved white light interferometry to measure material dispersion over a wide spectral band in a single acquisition, *Opt. Express*, **24** (15), 17303, 2016.

[180] Y. Arosa, E. López-Lago, and R. de la Fuente: Spectrally resolved white light interferometer for measuring dispersion in the visible and near infrared range, *Measurement*, **122**, 6–13, 2018.

[181] Y. Arosa, E. López-Lago, and R. de la Fuente: Refractive index retrieval in the UV range using white light spectral interferometry, *Opt. Mater. (Amst).*, **82**, 88–92, 2018.

[182] Y. Arosa, C. D. Rodríguez-Fernández, A. Doval, E. L. Lago, and R. de la Fuente: Accuracy of refractive index spectroscopy by broadband interferometry, *Measurement*, **187**, 110225, 2022.

[183] P. Hlubina and J. Olszewski: Phase retrieval from spectral interferograms including a stationary-phase point, *Opt. Commun.*, **285** (24), 4733–4738, 2012.

[184] L. M. Smith and C. C. Dobson: Absolute displacement measurements using modulation of the spectrum of white light in a Michelson interferometer, *Appl. Opt.*, **28** (16), 3339, 1989.

[185] M. Yoshio, T. Kato, T. Mukai, M. Yoshizawa, and H. Ohno: Self- Assembly of an Ionic Liquid and a Hydroxyl-Terminated Liquid Crystal: Anisotropic Ionic Conduction in Layered Nanostructures, *Mol. Cryst. Liq. Cryst.*, **413** (1), 99–108, 2004.

[186] Y. Iinuma, K. Kishimoto, Y. Sagara, M. Yoshio, T. Mukai, et al.: Uniaxially Parallel Alignment of a Smectic A Liquid-Crystalline Rod−Coil Molecule and Its Lithium Salt Complexes Using Rubbed Polyimides, *Macromolecules*, **40** (14), 4874–4878, 2007.

[187] J. N. Canongia Lopes, J. Deschamps, and A. A. Pádua: Modeling Ionic Liquids Using a Systematic All-Atom Force Field, *J. Phys. Chem. B*, **108** (6), 2038–2047, 2004.

[188] C. J. Margulis: Computational study of imidazolium-based ionic solvents with alkyl substituents of different lengths, *Mol. Phys.*, **102** (9-10), 829–838, 2004.

[189] J. N. A. Canongia Lopes and A. A. H. Pádua: Nanostructural Organization in Ionic Liquids, *J. Phys. Chem. B*, **110** (7), 3330–3335, 2006.

[190] B. Docampo-Álvarez, V. Gómez-González, H. Montes-Campos, J. M. Otero-Mato, T. Méndez-Morales, et al.: Molecular dynamics simulation of the behaviour of water in nano-confined ionic liquid–water mixtures, *J. Phys. Condens. Matter*, **28** (46), 464001, 2016.

[191] V. Gómez-González, B. Docampo-Álvarez, H. Montes-Campos, J. C. Otero, E. L. Lago, et al.: Solvation of Al $^{3+}$ cations in bulk and confined protic ionic liquids: a computational study, *Phys. Chem. Chem. Phys.*, **20** (28), 19071–19081, 2018.

270

[192] M. J. Quevillon and J. K. Whitmer: Charge transport and phase behavior of imidazolium-based ionic liquid crystals from fully atomistic simulations, *Materials (Basel).*, **11** (1), 64, 2018.

[193] H. Berendsen, D. van der Spoel, and R. van Drunen: GROMACS: A message-passing parallel molecular dynamics implementation, *Comput. Phys. Commun.*, **91** (1-3), 43–56, 1995.

[194] D. Van Der Spoel, E. Lindahl, B. Hess, G. Groenhof, A. E. Mark, et al.: GROMACS: Fast, flexible, and free, *J. Comput. Chem.*, **26** (16), 1701–1718, 2005.

[195] M. J. Abraham, T. Murtola, R. Schulz, S. Páll, J. C. Smith, et al.: Gromacs: High performance molecular simulations through multi-level parallelism from laptops to supercomputers, *SoftwareX*, **1-2**, 19–25, 2015.

[196] W. L. Jorgensen and J. Tirado-Rives: The OPLS Potential Functions for Proteins. Energy Minimizations for Crystals of Cyclic Peptides and Crambin, *J. Am. Chem. Soc.*, **110** (6), 1657–1666, 1988.

[197] W. L. Jorgensen, D. S. Maxwell, and J. Tirado-Rives: Development and Testing of the OPLS All-Atom Force Field on Conformational Energetics and Properties of Organic Liquids, *J. Am. Chem. Soc.*, **118** (45), 11225–11236, 1996.

[198] B. R. Brooks, R. E. Bruccoleri, B. D. Olafson, D. J. States, S. Swaminathan, et al.: CHARMM: A program for macromolecular energy, minimization, and dynamics calculations, *J. Comput. Chem.*, **4** (2), 187–217, 1983.

[199] W. F. van Gunsteren and H. J. C. Berendsen: Groningen Molecular Simulation (GROMOS) Library Manual, 1987.

[200] S. J. Weiner, P. A. Kollman, U. C. Singh, D. A. Case, C. Ghio, et al.: A New Force Field for Molecular Mechanical Simulation

of Nucleic Acids and Proteins, *J. Am. Chem. Soc.*, **106** (3), 765–784, 1984.

[201] S. V. Sambasivarao and O. Acevedo: Development of OPLS-AA Force Field Parameters for 68 Unique Ionic Liquids, *J. Chem. Theory Comput.*, **5** (4), 1038–1050, 2009.

[202] B. Doherty, X. Zhong, S. Gathiaka, B. Li, and O. Acevedo: Revisiting OPLS Force Field Parameters for Ionic Liquid Simulations, *J. Chem. Theory Comput.*, **13** (12), 6131–6145, 2017.

[203] L. Martínez, R. Andrade, E. G. Birgin, and J. M. Martínez: PACKMOL: A package for building initial configurations for molecular dynamics simulations, *J. Comput. Chem.*, **30** (13), 2157–2164, 2009.

[204] T. Darden, D. York, and L. Pedersen: Particle mesh Ewald: An N·log(N) method for Ewald sums in large systems, *J. Chem. Phys.*, **98** (12), 10089–10092, 1993.

[205] B. Hess, H. Bekker, H. J. C. Berendsen, and J. G. E. M. Fraaije: LINCS: A linear constraint solver for molecular simulations, *J. Comput. Chem.*, **18** (12), 1463–1472, 1997.

[206] M. J. Frisch, G. W. Trucks, H. B. Schlegel, G. E. Scuseria, M. A. Robb, et al.: Gaussian 16, Revision C.01, 2016.

[207] D. G. Truhlar and V. McKoy: Computational chemistry, in *Comput. Sci. Eng.*, volume 2, pages 19–21, Elsevier, 2000.

[208] P. Hohenberg and W. Kohn: Inhomogeneous electron gas, *Phys. Rev.*, **136** (3B), B864–B871, 1964.

[209] A. D. Becke: A new mixing of Hartree-Fock and local density-functional theories, *J. Chem. Phys.*, **98** (2), 1372–1377, 1993.

[210] P. J. Stephens, F. J. Devlin, C. F. Chabalowski, and M. J. Frisch: Ab Initio calculation of vibrational absorption and circular dichroism spectra using density functional force fields, *J. Phys. Chem.*, **98** (45), 11623–11627, 1994.

[211] A. D. Becke: Density-functional exchange-energy approximation with correct asymptotic behavior, *Phys. Rev. A*, **38** (6), 3098–3100, 1988.

[212] C. Lee, W. Yang, and R. G. Parr: Development of the Colle-Salvetti correlation-energy formula into a functional of the electron density, *Phys. Rev. B*, **37** (2), 785–789, 1988.

[213] S. H. Vosko, L. Wilk, and M. Nusair: Accurate spin-dependent electron liquid correlation energies for local spin density calculations: a critical analysis, *Can. J. Phys.*, **58** (8), 1200–1211, 1980.

[214] W. J. Hehre, R. F. Stewart, and J. A. Pople: Self-consistent molecular-orbital methods. i. use of gaussian expansions of slater-type atomic orbitals, *The Journal of Chemical Physics*, **51**, 2657–2664, 1969.

[215] R. Ditchfield, W. J. Hehre, and J. A. Pople: Self-consistent molecular-orbital methods. ix. an extended gaussian-type basis for molecular-orbital studies of organic molecules, *The Journal of Chemical Physics*, **54**, 724–728, 1971.

[216] T. H. Dunning: Gaussian basis sets for use in correlated molecular calculations. i. the atoms boron through neon and hydrogen, *The Journal of Chemical Physics*, **90**, 1007–1023, 1989.

[217] P. J. Hay and W. R. Wadt: Ab initio effective core potentials for molecular calculations. potentials for k to au including the outermost core orbitals, *The Journal of Chemical Physics*, **82**, 299–310, 1985.

273

[218] P. J. Hay and W. R. Wadt: Ab initio effective core potentials for molecular calculations. potentials for the transition metal atoms sc to hg, *The Journal of Chemical Physics*, **82**, 270–283, 1985.

[219] W. R. Wadt and P. J. Hay: Ab initio effective core potentials for molecular calculations. potentials for main group elements na to bi, *The Journal of Chemical Physics*, **82**, 284–298, 1985.

[220] M. D. Hanwell, D. E. Curtis, D. C. Lonie, T. Vandermeersch, E. Zurek, et al.: Avogadro: an advanced semantic chemical editor, visualization, and analysis platform, *Journal of Cheminformatics*, **4**, 17, 2012.

[221] X. Li and M. J. Frisch: Energy-represented direct inversion in the iterative subspace within a hybrid geometry optimization method, *Journal of Chemical Theory and Computation*, **2**, 835–839, 2006.

[222] D. S. Sholl and J. A. Steckel: Dft calculations of vibrational frequencies, 2009.

[223] J. Dodds, R. McWeeny, W. Raynes, and J. Riley: SCF theory for multiple perturbations, *Mol. Phys.*, **33** (3), 611–617, 1977.

[224] R. F. W. Bader, M. T. Carroll, J. R. Cheeseman, and C. Chang: Properties of atoms in molecules: atomic volumes, *J. Am. Chem. Soc.*, **109** (26), 7968–7979, 1987.

[225] D. F. Parsons and B. W. Ninham: Ab Initio Molar Volumes and Gaussian Radii, *J. Phys. Chem. A*, **113** (6), 1141–1150, 2009.

[226] J. Liu and W. Liang: Analytical approach for the excited-state hessian in time-dependent density functional theory: Formalism, implementation, and performance, *The Journal of Chemical Physics*, **135**, 184111, 2011.

[227] J. Liu and W. Liang: Analytical hessian of electronic excited states in time-dependent density functional theory with tamm-dancoff approximation, *The Journal of Chemical Physics*, **135**, 014113, 2011.

USC

[228] E. Runge and E. K. U. Gross: Density-functional theory for time-dependent systems, *Physical Review Letters*, **52**, 997–1000, 1984.

[229] M. Deetlefs, M. Shara, and K. Seddon: Ch. 17, in *Ion. Liq. III A Fundam. Progress, Challenges, Oppor.*, chapter 17, pages 219–233, 2005.

[230] K. Kieu, Y. Merzlyak, L. Schneebeli, J. Hales, J. Perry, et al.: Integrated liquid-core optical fiber for nonlinear liquid photonics, in *Adv. Photonics Congr.*, page NTh2A.2, OSA, Washington, D.C., 2012.

[231] E. Rilo, M. Domínguez-Pérez, J. Vila, L. Segade, M. García, et al.: Easy prediction of the refractive index for binary mixtures of ionic liquids with water or ethanol, *J. Chem. Thermodyn.*, **47**, 219–222, 2012.

[232] A. B. Pereiro, E. Tojo, A. Rodríguez, J. Canosa, and J. Tojo: Properties of ionic liquid $HMIMPF_6$ with carbonates, ketones and alkyl acetates, *J. Chem. Thermodyn.*, **38** (6), 651–661, 2006.

[233] A. B. Pereiro and A. Rodríguez: Thermodynamic properties of ionic liquids in organic solvents from (293.15 to 303.15) K, *J. Chem. Eng. Data*, **52** (2), 600–608, 2007.

[234] W. G. Scaife and C. G. Lyons: Density and Dielectric Polarizability of n-Alkane Liquids, *Berichte der Bunsengesellschaft für Phys. Chemie*, **94** (7), 758–765, 1990.

[235] M. Deetlefs, K. R. Seddon, and M. Shara: Predicting physical properties of ionic liquids, *Phys. Chem. Chem. Phys.*, **8** (5), 642–649, 2006.

[236] J. A. Novoa López, H. Michinel, and E. López Lago: Optical properties of Ionic Liquids, in A. P. De los Ríos and F. J. Hernández Fernández, editors, *Ion. Liq. Sep. Technol.*, chapter 1.3, pages 24–33, elsevier edition, 2014.

[237] Y. Arosa, C. D. Rodríguez Fernández, E. López Lago, A. Amigo, L. M. Varela, et al.: Refractive index measurement of imidazolium based ionic liquids in the Vis-NIR, *Opt. Mater. (Amst).*, **73**, 647–657, 2017.

[238] Y. Sanmamed, D. González-Salgado, J. Troncoso, C. Cerdeiriña, and L. Romaní: Viscosity-induced errors in the density determination of room temperature ionic liquids using vibrating tube densitometry, *Fluid Phase Equilib.*, **252** (1-2), 96–102, 2007.

[239] C. A. Nieto de Castro, E. Langa, A. L. Morais, M. L. M. Lopes, M. J. Lourenço, et al.: Studies on the density, heat capacity, surface tension and infinite dilution diffusion with the ionic liquids $[C_4mim][NTf_2]$, $[C_4mim][dca]$, $[C_2mim][EtOSO_3]$ and [Aliquat][dca], *Fluid Phase Equilib.*, **294** (1-2), 157–179, 2010.

[240] A. J. L. Costa, J. M. S. S. Esperança, I. M. Marrucho, and L. P. N. Rebelo: Densities and Viscosities of 1-Ethyl-3-methylimidazolium n -Alkyl Sulfates, *J. Chem. Eng. Data*, **56** (8), 3433–3441, 2011.

[241] J. Klomfar, M. Součková, and J. Pátek: Temperature Dependence Measurements of the Density at 0.1 MPa for 1-Alkyl-3-methylimidazolium-Based Ionic Liquids with the Trifluoro-methanesulfonate and Tetrafluoroborate Anion, *J. Chem. Eng. Data*, **55** (9), 4054–4057, 2010.

[242] M. Tariq, A. P. Serro, J. L. Mata, B. Saramago, J. M. Esperança, et al.: High-temperature surface tension and density measurements of 1-alkyl-3-methylimidazolium bistriflamide ionic liquids, *Fluid Phase Equilib.*, **294** (1-2), 131–138, 2010.

[243] D. Song and J. Chen: Density and Viscosity Data for Mixtures of Ionic Liquids with a Common Anion, *J. Chem. Eng. Data*, **59** (2), 257–262, 2014.

USC

[244] E. I. Izgorodina, M. Forsyth, and D. R. MacFarlane: On the components of the dielectric constants of ionic liquids: ionic polarization?, *Phys. Chem. Chem. Phys.*, **11** (14), 2452, 2009.

[245] K. Bica, M. Deetlefs, C. Schröder, and K. R. Seddon: Polarisabilities of alkylimidazolium ionic liquids, *Phys. Chem. Chem. Phys.*, **15** (8), 2703, 2013.

[246] J. P. Laib and D. M. Mittleman: Temperature-Dependent Terahertz Spectroscopy of Liquid n-alkanes, *J. Infrared, Millimeter, Terahertz Waves*, **31** (9), 1015–1021, 2010.

[247] E. Stoumbou, I. Stavrakas, G. Hloupis, A. Alexandridis, D. Triantis, et al.: A comparative study on the use of the extended-Cauchy dispersion equation for fitting refractive index data in crystals, *Opt. Quantum Electron.*, **45** (8), 837–859, 2013.

[248] S. B. Capelo, T. Méndez-Morales, J. Carrete, E. López Lago, J. Vila, et al.: Effect of Temperature and Cationic Chain Length on the Physical Properties of Ammonium Nitrate-Based Protic Ionic Liquids, *J. Phys. Chem. B*, **116** (36), 11302–11312, 2012.

[249] W. Sellmeier: Ueber die durch die Aetherschwingungen erregten Mitschwingungen der Körpertheilchen und deren Rückwirkung auf die ersteren, besonders zur Erklärung der Dispersion und ihrer Anomalien, *Ann. der Phys. und Chemie*, **223** (11), 386–403, 1872.

[250] B. Tatian: Fitting refractive-index data with the Sellmeier dispersion formula, *Appl. Opt.*, **23** (24), 4477, 1984.

[251] G. Ghosh, M. Endo, and T. Iwasaki: Temperature-dependent Sellmeier coefficients and chromatic dispersions for some optical fiber glasses, *J. Light. Technol.*, **12** (8), 1338–1342, 1994.

[252] M. F. C. Gomes, J. N. C. Lopes, and A. A. H. Padua: Thermodynamics and Micro Heterogeneity of Ionic Liquids, in *Top. Curr. Chem.*, volume 290, pages 161–183, 2009.

[253] M. Brehm, H. Weber, M. Thomas, O. Hollóczki, and B. Kirchner: Domain Analysis in Nanostructured Liquids: A Post-Molecular Dynamics Study at the Example of Ionic Liquids, *ChemPhysChem*, **16** (15), 3271–3277, 2015.

[254] A. Bhattacharjee, P. J. Carvalho, and J. A. Coutinho: The effect of the cation aromaticity upon the thermophysical properties of piperidinium- and pyridinium-based ionic liquids, *Fluid Phase Equilib.*, **375**, 80–88, 2014.

[255] X. X. Ma, J. Wei, W. Guan, Y. Pan, L. Zheng, et al.: Ionic parachor and its application to pyridinium-based ionic liquids of $\{[C_npy][DCA]$ (n = 2, 3, 4, 5, 6)\}, *J. Chem. Thermodyn.*, **89**, 51–59, 2015.

[256] S. Li, J. L. Bañuelos, J. Guo, L. Anovitz, G. Rother, et al.: Alkyl chain length and temperature effects on structural properties of pyrrolidinium-based ionic liquids: A combined atomistic simulation and small-angle x-ray scattering study, *J. Phys. Chem. Lett.*, **3** (1), 125–130, 2012.

[257] M. Musiał, K. Malarz, A. Mrozek-Wilczkiewicz, R. Musiol, E. Zorebski, et al.: Pyrrolidinium-Based Ionic Liquids as Sustainable Media in Heat-Transfer Processes, *ACS Sustain. Chem. Eng.*, **5** (11), 11024–11033, 2017.

[258] E. J. González, B. González, and E. A. Macedo: Effect of the relative humidity and isomeric structure on the physical properties of pyridinium based-ionic liquids, *J. Chem. Thermodyn.*, **86** (8), 96–105, 2015.

[259] J. Jiao, B. Han, M. Lin, N. Cheng, L. Yu, et al.: Salt-free catanionic surface active ionic liquids 1-alkyl-3-methylimidazolium alkylsulfate: Aggregation behavior in aqueous solution, *J. Colloid Interface Sci.*, **412**, 24–30, 2013.

[260] N. Mungar Ram, P. Naidoo, T. M. Letcher, and D. Ramjugernath: (Liquid + liquid) equilibria for mixtures of dodecane and ethanol

with alkylsulfate-based ionic liquids, *J. Chem. Thermodyn.*, **81**, 95–100, 2015.

[261] Y. Arosa, B. S. Algnamat, C. D. Rodríguez, E. L. Lago, L. M. Varela, et al.: Modeling the Temperature-Dependent Material Dispersion of Imidazolium-Based Ionic Liquids in the VIS-NIR, *J. Phys. Chem. C*, **122** (51), 29470–29478, 2018.

[262] S. S. Park, S. Lee, J. Y. Bae, and F. Hagelberg: Refractive indices of liquid-forming organic compounds by density functional theory, *Chem. Phys. Lett.*, **511** (4-6), 466–470, 2011.

[263] E. Heid, M. Heindl, P. Dienstl, and C. Schröder: Additive polarizabilities of halides in ionic liquids and organic solvents, *The Journal of Chemical Physics*, **149**, 044302, 2018.

[264] S. Ando: DFT Calculations on Refractive Index Dispersion of Fluoro-compounds in the DUV-UV-Visible Region, *J. Photopolym. Sci. Technol.*, **19** (3), 351–360, 2006.

[265] M. H. Ghatee, M. Zare, F. Moosavi, and A. R. Zolghadr: Temperature-Dependent Density and Viscosity of the Ionic Liquids 1-Alkyl-3-methylimidazolium Iodides: Experiment and Molecular Dynamics Simulation, *J. Chem. Eng. Data*, **55** (9), 3084–3088, 2010.

[266] G. D. Smith, O. Borodin, J. J. Magda, R. H. Boyd, Y. Wang, et al.: A comparison of fluoroalkyl-derivatized imidazolium:TFSI and alkyl-derivatized imidazolium:TFSI ionic liquids: a molecular dynamics simulation study, *Phys. Chem. Chem. Phys.*, **12** (26), 7064, 2010.

[267] M. Sattari, A. Kamari, A. H. Mohammadi, and D. Ramjugernath: Prediction of refractive indices of ionic liquids – A quantitative structure-property relationship based model, *J. Taiwan Inst. Chem. Eng.*, **52**, 165–180, 2015.

USC
UNIVERSIDADE
DE SANTIAGO
DE COMPOSTELA

[268] A. N. Soriano, K. F. P. Ornedo-Ramos, C. A. M. Muriel, A. P. Adornado, V. C. Bungay, et al.: Prediction of refractive index of binary solutions consisting of ionic liquids and alcohols (methanol or ethanol or 1-propanol) using artificial neural network, *J. Taiwan Inst. Chem. Eng.*, **65**, 83–90, 2016.

[269] R. Hayes, G. G. Warr, and R. Atkin: Structure and Nanostructure in Ionic Liquids, *Chem. Rev.*, **115** (13), 6357–6426, 2015.

[270] T. Kato and M. Yoshio: Liquid Crystalline Ionic Liquids, in H. Ohno, editor, *Electrochem. Asp. Ion. Liq.*, chapter 25, pages 375–392, John Wiley & Sons, Inc., Hoboken, NJ, USA, 2011.

[271] W. Xu, T. Wang, N. Cheng, Q. Hu, Y. Bi, et al.: Experimental and DFT Studies on the Aggregation Behavior of Imidazolium-Based Surface-Active Ionic Liquids with Aromatic Counterions in Aqueous Solution, *Langmuir*, **31** (4), 1272–1282, 2015.

[272] O. Cabeza, J. Vila, E. Rilo, M. Domínguez-Pérez, L. Otero-Cernadas, et al.: Physical properties of aqueous mixtures of the ionic 1-ethl-3-methyl imidazolium octyl sulfate: A new ionic rigid gel, *J. Chem. Thermodyn.*, **75**, 52–57, 2014.

[273] M. A. Firestone, J. A. Dzielawa, P. Zapol, L. A. Curtiss, S. Seifert, et al.: Lyotropic Liquid-Crystalline Gel Formation in a Room-Temperature Ionic Liquid, *Langmuir*, **18** (20), 7258–7260, 2002.

[274] K. Lava, Y. Evrard, K. V. Hecke, L. V. Meervelt, and K. Binnemans: Quinolinium and isoquinolinium ionic liquid crystals, *RSC Adv.*, **2** (21), 8061, 2012.

[275] P. H. J. Kouwer and T. M. Swager: Synthesis and Mesomorphic Properties of Rigid-Core Ionic Liquid Crystals, *J. Am. Chem. Soc.*, **129** (45), 14042–14052, 2007.

[276] J.-M. Suisse, S. Bellemin-Laponnaz, L. Douce, A. Maisse-François, and R. Welter: A new liquid crystal compound based on

an ionic imidazolium salt, *Tetrahedron Lett.*, **46** (25), 4303–4305, 2005.

[277] M. Biswas, M. Dule, P. N. Samanta, S. Ghosh, and T. K. Mandal: Imidazolium-based ionic liquids with different fatty acid anions: phase behavior, electronic structure and ionic conductivity investigation, *Phys. Chem. Chem. Phys.*, **16** (30), 16255, 2014.

[278] T. Singh, M. Drechsler, A. H. E. Müeller, I. Mukhopadhyay, and A. Kumar: Micellar transitions in the aqueous solutions of a surfactant-like ionic liquid: 1-butyl-3-methylimidazolium octylsulfate, *Phys. Chem. Chem. Phys.*, **12** (37), 11728, 2010.

[279] J. Jiao, B. Dong, H. Zhang, Y. Zhao, X. Wang, et al.: Aggregation Behaviors of Dodecyl Sulfate-Based Anionic Surface Active Ionic Liquids in Water, *J. Phys. Chem. B*, **116** (3), 958–965, 2012.

[280] J. Jiao, Y. Zhang, L. Fang, L. Yu, L. Sun, et al.: Electrolyte effect on the aggregation behavior of 1-butyl-3-methylimidazolium dodecylsulfate in aqueous solution, *J. Colloid Interface Sci.*, **402**, 139–145, 2013.

[281] T. Mukai, M. Yoshio, T. Kato, and H. Ohno: Effect of Methyl Groups onto Imidazolium Cation Ring on Liquid Crystallinity and Ionic Conductivity of Amphiphilic Ionic Liquids, *Chem. Lett.*, **33** (12), 1630–1631, 2004.

[282] G. Cavallo, G. Terraneo, A. Monfredini, M. Saccone, A. Priimagi, et al.: Superfluorinated Ionic Liquid Crystals Based on Supramolecular, Halogen-Bonded Anions, *Angew. Chemie Int. Ed.*, **55** (21), 6300–6304, 2016.

[283] T. Ichikawa, M. Yoshio, A. Hamasaki, T. Mukai, H. Ohno, et al.: Self-Organization of Room-Temperature Ionic Liquids Exhibiting Liquid-Crystalline Bicontinuous Cubic Phases: Formation of Nano-Ion Channel Networks, *J. Am. Chem. Soc.*, **129** (35), 10662–10663, 2007.

[284] T. S. Jo, H. Han, P. K. Bhowmik, B. Heinrich, and B. Donnio: Thermotropic Liquid-Crystalline and Light-Emitting Properties of Poly(pyridinium) Salts Containing Various Diamine Connectors and Hydrophilic Macrocounterions, *Polymers (Basel).*, **11** (5), 851, 2019.

[285] N.-N. Shen, M.-L. Cai, Y. Song, Z.-P. Wang, F.-Q. Huang, et al.: Supramolecular Organization of [TeCl 6] 2– with Ionic Liquid Cations: Studies on the Electrical Conductivity and Luminescent Properties, *Inorg. Chem.*, **57** (9), 5282–5291, 2018.

[286] Y. Funasako, H. Okada, and M. Inokuchi: Photochromic Ionic Liquids Containing Cationic Spiropyran Derivatives, *ChemPhotoChem*, **3** (1), 28–30, 2019.

[287] L. Vicari: *Optical applications of liquid crystals*, Institute of Physics Publishing, Bristol and Philadelphia, 2003.

[288] S. Venkatesh, P. K. Yadav, M. G. Kolambe, and M. Ramana: Ionic liquid crystals derived from dl-Phenylalanine: Mesomorphism, optical behavior and evaluation of toxicological profile, *J. Mol. Liq.*, **289**, 111061, 2019.

[289] J. Parajó, M. Villanueva, P. Sánchez, and J. Salgado: Liquid window of some biologically-active ionic liquids, *J. Chem. Thermodyn.*, **126**, 1–10, 2018.

[290] V. V. Matveev, A. V. Ievlev, M. A. Vovk, O. Cabeza, J. Salgado-Carballo, et al.: NMR investigation of the structure and single-particle dynamics of inorganic salt solutions in a protic ionic liquid, *J. Mol. Liq.*, **278**, 239–246, 2019.

[291] J. Dai, B. Kharkov, and S. Dvinskikh: Molecular and Segmental Orientational Order in a Smectic Mesophase of a Thermotropic Ionic Liquid Crystal, *Crystals*, **9** (1), 18, 2018.

[292] M. E. Di Pietro, T. Margola, G. Celebre, G. De Luca, and G. Saielli: A combined LX-NMR and molecular dynamics

investigation of the bulk and local structure of ionic liquid crystals, *Soft Matter*, **15** (22), 4486–4497, 2019.

[293] D. Majhi, A. Pabbathi, and M. Sarkar: Probing the Aggregation Behavior of Neat Imidazolium-Based Alkyl Sulfate (Alkyl = Ethyl, Butyl, Hexyl, and Octyl) Ionic Liquids through Time Resolved Florescence Anisotropy and NMR and Fluorescence Correlation Spectroscopy Study, *J. Phys. Chem. B*, **120** (1), 193–205, 2016.

[294] I. Dierking: *Textures of Liquid Crystals*, WILEY-VCH Verlag GmbH & Co. KGaA, Weinheim, 2003.

[295] A. Shah and P. Ghalsasi: Use of interference colours to distinguish between fast and slow axes of a quarter wave plate, *Eur. J. Phys.*, **40** (6), 065301, 2019.

[296] W. Dobbs, L. Douce, L. Allouche, A. Louati, F. Malbosc, et al.: New ionic liquid crystals based on imidazolium salts, *New J. Chem.*, **30** (4), 528, 2006.

[297] M. R. Schenkel, J. B. Hooper, M. J. Moran, L. A. Robertson, D. Bedrov, et al.: Effect of counter-ion on the thermotropic liquid crystal behaviour of bis(alkyl)-tris(imidazolium salt) compounds, *Liq. Cryst.*, **41** (11), 1668–1685, 2014.

[298] R. P. Matthews, T. Welton, and P. A. Hunt: Hydrogen bonding and $\pi-\pi$ interactions in imidazolium-chloride ionic liquid clusters, *Phys. Chem. Chem. Phys.*, **17** (22), 14437–14453, 2015.

[299] J. C. Araque, J. J. Hettige, and C. J. Margulis: Modern Room Temperature Ionic Liquids, a Simple Guide to Understanding Their Structure and How It May Relate to Dynamics, *J. Phys. Chem. B*, **119** (40), 12727–12740, 2015.

[300] C. D. Rodríguez Fernández, Y. Arosa, B. Algnamat, E. López Lago, and R. de la Fuente: An experimental and computational

study on the material dispersion of 1-alkyl-3-methylimidazolium tetrafluoroborate ionic liquids, *Phys. Chem. Chem. Phys.*, **22** (25), 14061–14076, 2020.

[301] C. E. Bernardes, K. Shimizu, J. N. C. Lopes, P. Marquetand, E. Heid, et al.: Additive polarizabilities in ionic liquids, *Phys. Chem. Chem. Phys.*, **18** (3), 1665–1670, 2016.

[302] P. Díaz-Rodríguez, J. C. Cancilla, N. V. Plechkova, G. Matute, K. R. Seddon, et al.: Estimation of the refractive indices of imidazolium-based ionic liquids using their polarisability values, *Phys. Chem. Chem. Phys.*, **16** (1), 128–134, 2014.

[303] K. Rustagi and J. Ducuing: Third-order optical polarizability of conjugated organic molecules, *Opt. Commun.*, **10** (3), 258–261, 1974.

[304] B. Shanker and J. Applequist: Atom monopole-dipole interaction model with limited delocalization length for polarizabilities of polyenes, *J. Phys. Chem.*, **100** (26), 10834–10836, 1996.

[305] Y. K. Lee, S. J. Jeon, and M. Cho: Molecular polarizability and first hyperpolarizability of octupolar molecules: Donor-substituted triphenylmethane dyes, *J. Am. Chem. Soc.*, **120** (42), 10921–10927, 1998.

[306] C. Van Dyck, T. J. Marks, and M. A. Ratner: Chain Length Dependence of the Dielectric Constant and Polarizability in Conjugated Organic Thin Films, *ACS Nano*, **11** (6), 5970–5981, 2017.

[307] S. Dähne and K. D. Nolte: The electronic polarizability of polymethines, *J. Chem. Soc. Chem. Commun.*, **0** (19), 1056–1057, 1972.

[308] M. T. Zhao, B. P. Singh, and P. N. Prasad: A systematic study of polarizability and microscopic third-order optical nonlinearity in thiophene oligomers, *J. Chem. Phys.*, **89** (9), 5535–5541, 1988.

[309] H. Thienpont, G. L. Rikken, E. W. Meijer, W. Ten Hoeve, and H. Wynberg: Saturation of the hyperpolarizability of oligothiophenes, *Phys. Rev. Lett.*, **65** (17), 2141–2144, 1990.

[310] F. Momicchioli, G. Ponterini, and D. Vanossi: First- and second-order polarizabilities of simple merocyanines. An experimental and theoretical reassessment of the two-level model, *J. Phys. Chem. A*, **112** (46), 11861–11872, 2008.

[311] E. Heid, A. Szabadi, and C. Schröder: Quantum mechanical determination of atomic polarizabilities of ionic liquids, *Phys. Chem. Chem. Phys.*, **20** (16), 10992–10996, 2018.

[312] M. W. Wong, K. B. Wiberg, and M. J. Frisch: Ab initio calculation of molar volumes: Comparison with experiment and use in solvation models, *Journal of Computational Chemistry*, **16**, 385–394, 1995.

[313] H. C. Bolton: The electrical polarizability of conjugated molecules: The use of free-electron orbitals, *Trans. Faraday Soc.*, **50**, 1265–1269, 1954.

[314] P. L. Davies: Polarizabilities of long chain conjugated molecules, *Trans. Faraday Soc.*, **48** (C), 789–795, 1952.

[315] E. Heid, P. A. Hunt, and C. Schröder: Evaluating excited state atomic polarizabilities of chromophores, *Physical Chemistry Chemical Physics*, **20**, 8554–8563, 2018.

[316] A. J. Stone: Distributed multipole analysis: Stability for large basis sets, *Journal of Chemical Theory and Computation*, **1**, 1128–1132, 2005.

[317] A. J. Misquitta and A. J. Stone: Distributed polarizabilities obtained using a constrained density-fitting algorithm, *The Journal of Chemical Physics*, **124**, 024111, 2006.

[318] M. Giambiagi, M. S. de Giambiagi, and K. C. Mundim: Definition of a multicenter bond index, *Struct. Chem.*, **1** (5), 423–427, 1990.

[319] T. Lu and F. Chen: Multiwfn: A multifunctional wavefunction analyzer, *J. Comput. Chem.*, **33** (5), 580–592, 2012.

[320] E. Matito: An electronic aromaticity index for large rings, *Phys. Chem. Chem. Phys.*, **18** (17), 11839–11846, 2016.

[321] R. Ponec, P. Bultinck, and A. G. Saliner: Multicenter bond indices as a new means for the quantitative characterization of homoaromaticity, *J. Phys. Chem. A*, **109** (29), 6606–6609, 2005.

[322] N. Weiß, C. H. Schmidt, G. Thielemann, E. Heid, C. Schröder, et al.: The physical significance of the kamlet–taft $\pi*$ parameter of ionic liquids, *Physical Chemistry Chemical Physics*, **23**, 1616–1626, 2021.

[323] H. Meier, U. Stalmach, and H. Kolshorn: Effective conjugation length and UV/vis spectra of oligomers, *Acta Polym.*, **48** (9), 379–384, 1997.

[324] S. K. Tadikonda, K. T. Raju, M. Gowrisankar, A. K. Nain, and B. Munibhadrayya: Volumetric, ultrasonic and spectroscopic studies of molecular interactions in binary mixtures of 1-butyl-3-methylimidazolium hexafluorophosphate with 2-propoxyethanol at temperatures from 298.15 to 323.15 K, *J. Mol. Liq.*, **216**, 484–495, 2016.

[325] H. Shekaari, M. T. Zafarani-Moattar, and N. Jabbarvand Behrooz: Volumetric, acoustic, and refractometric properties of (thiophene + hexane/cyclohexane) solutions in the presence of some imidazolium based ionic liquids at T = 298.15 K, *J. Chem. Thermodyn.*, **86**, 188–195, 2015.

[326] H. Jin, B. O'Hare, J. Dong, S. Arzhantsev, G. A. Baker, et al.: Physical properties of ionic liquids consisting of the 1-butyl-3- methylimidazolium cation with various anions and the bis(trifluoromethylsulfonyl)imide anion with various cations, *J. Phys. Chem. B*, **112** (1), 81–92, 2008.

[327] K. Kaneko, Y. Yoshimura, and A. Shimizu: Water concentration dependence of the refractive index of various ionic liquid-water mixtures, *J. Mol. Liq.*, **250**, 283–286, 2018.

[328] P. Suneetha, T. Srinivasa Krishna, M. Gowrisankar, and D. Ramachandran: Volumetric, acoustic and spectroscopic study of 1-butyl-3-methylimidazolium trifluoromethanesulfonate with alkoxyalkanols at different temperatures, *J. Mol. Liq.*, **238**, 170–183, 2017.

[329] H. Shekaari and S. S. Mousavi: Volumetric properties of ionic liquid 1,3-dimethylimidazolium methyl sulfate + molecular solvents at T = (298.15-328.15) K, *Fluid Phase Equilib.*, **291** (2), 201–207, 2010.

[330] M. T. Zafarani-Moattar and R. Majdan-Cegincara: Viscosity, density, speed of sound, and refractive index of binary mixtures of organic solvent + Ionic liquid, 1-Butyl-3-methylimidazolium hexafluorophosphate at 298.15 K, *J. Chem. Eng. Data*, **52** (6), 2359–2364, 2007.

[331] I. Bou Malham and M. Turmine: Viscosities and refractive indices of binary mixtures of 1-butyl-3-methylimidazolium tetrafluoroborate and 1-butyl-2,3-dimethylimidazolium tetrafluoroborate with water at 298 K, *J. Chem. Thermodyn.*, **40** (4), 718–723, 2008.

[332] H. Patel, Z. S. Vaid, U. U. More, S. P. Ijardar, and N. I. Malek: Thermophysical, acoustic and optical properties of binary mixtures of imidazolium based ionic liquids + polyethylene glycol, *J. Chem. Thermodyn.*, **99**, 40–53, 2016.

[333] F. J. Deive, M. A. Rivas, and A. Rodríguez: Thermophysical properties of two ionic liquids based on benzyl imidazolium cation, *J. Chem. Thermodyn.*, **43** (3), 487–491, 2011.

[334] J. C. Gonçalves and A. E. Rodrigues: Thermodynamic equilibrium of xylene isomerization in the liquid phase, *J. Chem. Eng. Data*, **58** (6), 1440–1448, 2013.

[335] H. F. Almeida, H. Passos, J. A. Lopes-Da-Silva, A. M. Fernandes, M. G. Freire, et al.: Thermophysical properties of five acetate-based ionic liquids, *J. Chem. Eng. Data*, **57** (11), 3005–3013, 2012.

[336] E. Vercher, V. González-Alfaro, F. J. Llopis, A. V. Orchillés, P. J. Miguel, et al.: Thermophysical properties of binary mixtures of 1-butyl-1-methylpyrrolidinium trifluoromethanesulfonate ionic liquid with alcohols at several temperatures, *J. Chem. Thermodyn.*, **118**, 292–301, 2018.

[337] M. Nduli and N. Deenadayalu: Thermophysical properties of binary mixtures of (methanol or 1-ethyl-3-methylimidazolium acetate + furfural or furfuryl alcohol) at various temperatures, *J. Mol. Liq.*, **241**, 407–421, 2017.

[338] I. Bandrés, M. Carmen López, M. Castro, J. Barberá, and C. Lafuente: Thermophysical properties of 1-propylpyridinium tetrafluoroborate, *J. Chem. Thermodyn.*, **44** (1), 148–153, 2012.

[339] N. M. Yunus, M. I. Abdul Mutalib, Z. Man, M. A. Bustam, and T. Murugesan: Thermophysical properties of 1-alkylpyridinum bis(trifluoromethylsulfonyl)imide ionic liquids, *J. Chem. Thermodyn.*, **42** (4), 491–495, 2010.

[340] M. A. Rocha, F. M. Ribeiro, A. I. Ferreira, J. A. Coutinho, and L. M. Santos: Thermophysical properties of $[C_{N-1}C_1im][PF_6]$ ionic liquids, *J. Mol. Liq.*, **188**, 196–202, 2013.

[341] M. G. Freire, A. R. R. Teles, M. A. Rocha, B. Schröder, C. M. Neves, et al.: Thermophysical characterization of ionic liquids able to dissolve biomass, *J. Chem. Eng. Data*, **56** (12), 4813–4822, 2011.

[342] M. García-Andreu, M. Castro, I. Gascón, and C. Lafuente: Thermophysical characterization of 1-ethylpyridinium triflate and comparison with similar ionic liquids, *J. Chem. Thermodyn.*, **103**, 395–402, 2016.

[343] R. Anantharaj and T. Banerjee: Thermodynamic properties of 1-ETHYL-3-methylimidazolium methanesulphonate with aromatic sulphur, nitrogen compounds at T=298.15-323.15K and P=1bar, *Can. J. Chem. Eng.*, **91** (2), 245–256, 2013.

[344] H. Shekaari, M. T. Zafarani-Moattar, and M. Niknam: Thermodynamic evaluation of imidazolium based ionic liquids with thiocyanate anion as effective solvent to thiophene extraction, *J. Mol. Liq.*, **219**, 975–984, 2016.

[345] M. Srinivasa Reddy, I. Khan, K. T. S. Raju, P. Suresh, and B. Hari Babu: The study of molecular interactions in 1-ethyl-3-methylimidazolium trifluoromethanesulfonate + 1-pentanol from density, speed of sound and refractive index measurements, *J. Chem. Thermodyn.*, **98**, 298–308, 2016.

[346] D. Zhang, W. Jiang, L. Liu, K. Yu, M. Hong, et al.: The molar surface Gibbs energy and polarity of ether-functionalized ionic liquids, *J. Chem. Thermodyn.*, **138**, 313–320, 2019.

[347] J. Benito, M. García-Mardones, V. Pérez-Gregorio, I. Gascón, and C. Lafuente: Physicochemical study of n-ethylpyridinium bis(trifluoromethylsulfonyl) imide ionic liquid, *J. Solution Chem.*, **43** (4), 696–710, 2014.

[348] A. S. Rodrigues, H. F. Almeida, M. G. Freire, J. A. Lopes-da Silva, J. A. Coutinho, et al.: The effect of n vs. iso isomerization

289

on the thermophysical properties of aromatic and non-aromatic ionic liquids, *Fluid Phase Equilib.*, **423**, 190–202, 2016.

[349] M. Barzegar-Jalali, A. Jouyban, H. Shekaari, F. Martinez, and S. N. Mirheydari: The effect of 1-hexyl-3-methylimidazolium bromide ionic liquid as a co-solvent on the aqueous solubility of lamotrigine at T = (293.2–313.2) K, *J. Chem. Thermodyn.*, **133**, 261–271, 2019.

[350] F. J. Hernández-Fernández, A. P. de los Ríos, D. Gómez, M. Rubio, F. Tomás-Alonso, et al.: Ternary liquid-liquid equilibria for mixtures of an ionic liquid + n-hexane + an organic compound involved in the kinetic resolution of rac-1-phenyl ethanol (rac-1-phenyl ethanol, vinyl propionate, rac-1-phenylethyl propionate or propionic acid) at 298.2 , *Fluid Phase Equilib.*, **263** (2), 190–198, 2008.

[351] A. B. Pereiro and A. Rodríguez: Ternary liquid-liquid equilibria ethanol + 2-butanone + 1-butyl-3-methylimidazolium hexafluorophosphate, 2-propanol + 2-butanone + 1-butyl-3-methylimidazolium hexafluorophosphate, and 2-butanone + 2-propanol + 1,3-dimethylimidazolium methyl sulfate at 298.15 K, *J. Chem. Eng. Data*, **52** (6), 2138–2142, 2007.

[352] A. B. Pereiro and A. Rodríguez: Ternary (liquid + liquid) equilibria of the azeotrope (ethyl acetate + 2-propanol) with different ionic liquids at T = 298.15 K, *J. Chem. Thermodyn.*, **39** (12), 1608–1613, 2007.

[353] M. S. Altuwaim, K. H. Alkhaldi, A. S. Al-Jimaz, and A. A. Mohammad: Temperature dependence of physicochemical properties of imidazolium-, pyroldinium-, and phosphonium-based ionic liquids, *J. Chem. Eng. Data*, **59** (6), 1955–1963, 2014.

[354] A. B. Pereiro, F. Santamarta, E. Tojo, A. Rodríguez, and J. Tojo: Temperature dependence of physical properties of ionic liquid

1,3-dimethylimidazolium methyl sulfate, *J. Chem. Eng. Data*, **51** (3), 952–954, 2006.

[355] R. G. Seoane, S. Corderí, E. Gómez, N. Calvar, E. J. González, et al.: Temperature dependence and structural influence on the thermophysical properties of eleven commercial ionic liquids, *Ind. Eng. Chem. Res.*, **51** (5), 2492–2504, 2012.

[356] O. Cabeza, L. M. Varela, E. Rilo, L. Segade, M. Domínguez-Pérez, et al.: Synthesis, microstructure and volumetry of novel metal thiocyanate ionic liquids with [BMIM] cation, *J. Mol. Liq.*, **283**, 638–651, 2019.

[357] M. Yousefi, A. Naseri, M. Abdouss, and A. A. Miran Beigi: Synthesis and characterization of eight hydrophilic imidazolium-based ionic liquids and their application on enhanced oil recovery, *J. Mol. Liq.*, **248**, 370–377, 2017.

[358] G. Reyes, M. Cartes, C. Rey-Castro, H. Segura, and A. Mejía: Surface tension of 1-ethyl-3-methylimidazolium ethyl sulfate or 1-butyl-3-methylimidazolium hexafluorophosphate with argon and carbon dioxide, *J. Chem. Eng. Data*, **58** (5), 1203–1211, 2013.

[359] N. I. Malek, A. Singh, R. Surati, and S. P. Ijardar: Study on thermo physical and excess molar properties of binary systems of ionic liquids. I: $[C_n \text{mim}][PF_6]$ (n = 6, 8) and alkyl acetates, *J. Chem. Thermodyn.*, **74**, 103–118, 2014.

[360] A. S. Al-Jimaz, K. H. Alkhaldi, M. H. Al-Rashed, M. S. Fandary, and M. S. AlTuwaim: Study on the separation of propylbenzene from alkanes using two methylsulfate-based ionic liquids at (313 and 333) K, *Fluid Phase Equilib.*, **354**, 29–37, 2013.

[361] A. B. Pereiro and A. Rodríguez: Study on the phase behaviour and thermodynamic properties of ionic liquids containing imidazolium cation with ethanol at several temperatures, *J. Chem. Thermodyn.*, **39** (6), 978–989, 2007.

[362] M. Srinivasa Reddy, S. M. Nayeem, C. Soumini, K. Thomas, and B. Hari Babu: Study of molecular interactions in binary liquid mixtures of [Emim][BF$_4$] with 2-methoxyethanol using thermo acoustic, volumetric and optical properties, *Thermochim. Acta*, **630**, 37–49, 2016.

[363] F. Yebra, K. Zemánková, and J. Troncoso: Speed of sound in ionic liquids with a common ion as a function of pressure and temperature, *J. Chem. Thermodyn.*, **116**, 235–240, 2018.

[364] E. Vercher, F. J. Llopis, V. González-Alfaro, P. J. Miguel, and A. Martínez-Andreu: Refractive indices and deviations in refractive indices of trifluoromethanesulfonate-based ionic liquids in water, *J. Chem. Eng. Data*, **56** (12), 4499–4504, 2011.

[365] A. S. Branco, M. S. Calado, J. M. Fareleira, Z. P. Visak, and J. N. Canongia Lopes: Refraction index and molar refraction in ionic liquid/PEG200 solutions, *J. Solution Chem.*, **44** (3-4), 431–439, 2015.

[366] M. R. Shah, R. Anantharaj, T. Banerjee, and G. D. Yadav: Quaternary (liquid + liquid) equilibria for systems of imidazolium based ionic liquid + thiophene + pyridine + cyclohexane at 298.15 K: Experiments and quantum chemical predictions, *J. Chem. Thermodyn.*, **62**, 142–150, 2013.

[367] X. X. Ma, J. Wei, Q. B. Zhang, F. Tian, Y. Y. Feng, et al.: Prediction of thermophysical properties of acetate-based ionic liquids using semiempirical methods, *Ind. Eng. Chem. Res.*, **52** (27), 9490–9496, 2013.

[368] O. A. Al-Rashed, M. A. Fahim, and M. Shaaban: Prediction and measurement of phase equilibria for the extraction of BTX from naphtha reformate using BMIMPF$_6$ ionic liquid, *Fluid Phase Equilib.*, **363**, 248–262, 2014.

[369] S. Bansal, N. Kaur, G. R. Chaudhary, S. K. Mehta, and A. S. Ahluwalia: Physiochemical properties of new formulations of

1-ethyl-3-methylimidazolium bis(trifluoromethylsulfonyl)imide with Tritons, *J. Chem. Eng. Data*, **59** (12), 3988–3999, 2014.

[370] Z. Song, Q. Yan, M. Xia, X. Qi, Z. Zhang, et al.: Physicochemical properties of N-alkylpyridine trifluoroacetate ionic liquids [C$_n$Py][TFA] (n = 2–6), *J. Chem. Thermodyn.*, **155**, 106366, 2021.

[371] Z. Chen, Y. Huo, J. Cao, L. Xu, and S. Zhang: Physicochemical Properties of Ether-Functionalized Ionic Liquids: Understanding Their Irregular Variations with the Ether Chain Length, *Ind. Eng. Chem. Res.*, **55** (44), 11589–11596, 2016.

[372] A. E. Andreatta, A. Arce, E. Rodil, and A. Soto: Physico-chemical properties of binary and ternary mixtures of ethyl acetate + ethanol + 1-butyl-3-methyl-imidazolium bis(trifluoromethylsulfonyl)imide at 298.15 K and atmospheric pressure, *J. Solution Chem.*, **39** (3), 371–383, 2010.

[373] X. J. Yan, S. N. Li, Q. G. Zhai, Y. C. Jiang, and M. C. Hu: Physicochemical properties for the binary systems of ionic liquids [C$_n$mim]Cl + N,N-dimethylformamide, *J. Chem. Eng. Data*, **59** (5), 1411–1422, 2014.

[374] B. González, E. Gómez, A. Domínguez, M. Vilas, and E. Tojo: Physicochemical characterization of new sulfate ionic liquids, *J. Chem. Eng. Data*, **56** (1), 14–20, 2011.

[375] B. González, N. Calvar, E. Gómez, and Á. Domínguez: Physical properties of the ternary system (ethanol + water + 1-butyl-3-methylimidazolium methylsulphate) and its binary mixtures at several temperatures, *J. Chem. Thermodyn.*, **40** (8), 1274–1281, 2008.

[376] B. González and E. J. González: Physical properties of the pure 1-methyl-1-propylpyrrolidinium bis(trifluoromethylsulfonyl)imide ionic liquid and its binary mixtures with alcohols, *J. Chem. Thermodyn.*, **68**, 109–116, 2014.

[377] E. J. González, L. Alonso, and A. Domínguez: Physical properties of binary mixtures of the ionic liquid 1-methyl-3-octylimidazolium chloride with methanol, ethanol, and 1-propanol at T = (298.15, 313.15, and 328.15) K and at P = 0.1 MPa, *J. Chem. Eng. Data*, **51** (4), 1446–1452, 2006.

[378] A. E. Andreatta, A. Arce, E. Rodil, and A. Soto: Physical properties of binary and ternary mixtures of ethyl acetate, ethanol, and 1-octyl-3-methyl-imidazolium bis(trifluoromethylsulfonyl)imide at 298.15 K, *J. Chem. Eng. Data*, **54** (3), 1022–1028, 2009.

[379] H. Shekaari and E. Armanfar: Physical properties of aqueous solutions of ionic liquid, 1-propyl-3-methylimidazolium methyl sulfate, at T = (298.15 to 328.15) K, *J. Chem. Eng. Data*, **55** (2), 765–772, 2010.

[380] A. E. Andreatta, A. Arce, E. Rodil, and A. Soto: Physical properties and phase equilibria of the system isopropyl acetate + isopropanol + 1-octyl-3-methyl-imidazolium bis(trifluoromethylsulfonyl)imide, *Fluid Phase Equilib.*, **287** (2), 84–94, 2010.

[381] E. J. González, Á. Domínguez, and E. A. MacEdo: Physical and excess properties of eight binary mixtures containing water and ionic liquids, *J. Chem. Eng. Data*, **57** (8), 2165–2176, 2012.

[382] T. Singh and A. Kumar: Physical and excess properties of a room temperature ionic liquid (1-methyl-3-octylimidazolium tetrafluoroborate) with n-alkoxyethanols (C_1E_m, m = 1 to 3) at T = (298.15 to 318.15) K, *J. Chem. Thermodyn.*, **40** (3), 417–423, 2008.

[383] A. Arce, E. Rodil, and A. Soto: Physical and excess properties for binary mixtures of 1-methyl-3- octylimidazolium tetrafluoroborate, [Omim][BF_4], ionic liquid with different alcohols, *J. Solution Chem.*, **35** (1), 63–78, 2006.

[384] J. Saien, M. Razi Asrami, and S. Salehzadeh: Phase equilibrium measurements and thermodynamic modelling of water + phenol + [Hmim][NTf$_2$] ionic liquid system at several temperatures, *J. Chem. Thermodyn.*, **119**, 76–83, 2018.

[385] R. Anantharaj and T. Banerjee: Phase behaviour of 1-ethyl-3-methylimidazolium thiocyanate ionic liquid with catalytic deactivated compounds and water at several temperatures: Experiments and theoretical predictions, *Int. J. Chem. Eng.*, **2011**, 1–13, 2011.

[386] I. Domínguez, E. J. González, J. Palomar, and Á. Domínguez: Phase behavior of ternary mixtures {aliphatic hydrocarbon + aromatic hydrocarbon + ionic liquid}: Experimental LLE data and their modeling by COSMO-RS, *J. Chem. Thermodyn.*, **77**, 222–229, 2014.

[387] J. M. Araújo, A. B. Pereiro, F. Alves, I. M. Marrucho, and L. P. Rebelo: Nucleic acid bases in 1-alkyl-3-methylimidazolium acetate ionic liquids: A thermophysical and ionic conductivity analysis, *J. Chem. Thermodyn.*, **57**, 1–8, 2013.

[388] A. Andresová, M. Bendová, J. Schwarz, Z. Wagner, and J. Feder-Kubis: Influence of the alkyl side chain length on the thermophysical properties of chiral ionic liquids with a (1R,2S,5R)-(−)-menthol substituent and data analysis by means of mathematical gnostics, *J. Mol. Liq.*, **242**, 336–348, 2017.

[389] M. C. Castro, H. Rodríguez, A. Arce, and A. Soto: Mixtures of ethanol and the ionic liquid 1-ethyl-3-methylimidazolium acetate for the fractionated solubility of biopolymers of lignocellulosic biomass, *Ind. Eng. Chem. Res.*, **53** (29), 11850–11861, 2014.

[390] L. Alonso, A. Arce, M. Francisco, and A. Soto: Measurement and correlation of liquid-liquid equilibria of two imidazolium ionic liquids with thiophene and methylcyclohexane, *J. Chem. Eng. Data*, **52** (6), 2409–2412, 2007.

[391] S. Corderí, E. Gómez, N. Calvar, and Á. Domínguez: Measurement and correlation of liquid-liquid equilibria for ternary and quaternary systems of heptane, cyclohexane, toluene, and [EMim][OAc] at 298.15 K, *Ind. Eng. Chem. Res.*, **53** (22), 9471–9477, 2014.

[392] F. Mohammed, M. Qasim, A. A. Aidan, and N. A. Darwish: Measurement and correlation of isobaric binary vapor-liquid equilibria for water and 2-propanol each with 1-butyl-1-methypyrrolidinium chloride and 1-butyl-1-methylpyrrolidinium trifluoromethanesulfonate, *J. Mol. Liq.*, **264**, 534–542, 2018.

[393] M. Bendová and Z. Wagner: Liquid-liquid equilibrium in binary system [bmim][PF$_6$] + 1-butanol, *J. Chem. Eng. Data*, **51** (6), 2126–2131, 2006.

[394] Y. Y. Choi, I. C. Hwang, S. H. Shin, and S. J. Park: Liquid-liquid equilibria, excess molar volume and deviations of the refractive indices at 298.15K for mixtures of solvents used in the molybdenum extraction process, *Fluid Phase Equilib.*, **354**, 59–65, 2013.

[395] M. C. Castro, A. Arce, A. Soto, and H. Rodríguez: Thermophysical characterization of the mixtures of the ionic liquid 1-ethyl-3-methylimidazolium acetate with 1-propanol or 2-propanol, *J. Chem. Eng. Data*, **61** (7), 2299–2310, 2016.

[396] A. Cháfer, J. De La Torre, A. Font, and E. Lladosa: Liquid-Liquid Equilibria of Water + Ethanol + 1-Butyl-3-methylimidazolium Bis(trifluoromethanesulfonyl)imide Ternary System: Measurements and Correlation at Different Temperatures, *J. Chem. Eng. Data*, **60** (8), 2426–2433, 2015.

[397] F. Espiau, J. Ortega, L. Fernández, and J. Wisniak: Liquid-liquid equilibria in binary solutions formed by [pyridinium-derived] [F4B] ionic liquids and alkanols: New experimental data and

validation of a multiparametric model for correlating LLE data, *Ind. Eng. Chem. Res.*, **50** (21), 12259–12270, 2011.

[398] L. Alonso, A. Arce, M. Francisco, O. Rodríguez, and A. Soto: Liquid-liquid equilibria for systems composed by 1-methyl-3- octylimidazolium tetrafluoroborate ionic liquid, thiophene, and n-hexane or cyclohexane, *J. Chem. Eng. Data*, **52** (5), 1729–1732, 2007.

[399] N. Mungar Ram, I. Bahadur, T. M. Letcher, P. Naidoo, and D. Ramjugernath: Liquid-liquid equilibria for mixtures of hexadecane and ethanol with imidazolium-based ionic liquids, *J. Solution Chem.*, **44** (3-4), 593–605, 2015.

[400] L. Alonso, A. Arce, M. Francisco, and A. Soto: Liquid-liquid equilibria for $[C_8mim][NTf_2]$ + thiophene + 2,2,4-trimethylpentane or + toluene, *J. Chem. Eng. Data*, **53** (8), 1750–1755, 2008.

[401] H. D. Kim, I. C. Hwang, and S. J. Park: Isothermal vapor-liquid equilibrium data at T = 333.15 K and excess molar volumes and refractive indices at T = 298.15 K for the dimethyl carbonate + methanol and isopropanol + water with ionic liquids, *J. Chem. Eng. Data*, **55** (7), 2474–2481, 2010.

[402] M. Teodorescu: Isothermal vapor + liquid equilibrium and thermophysical properties for 1-butyl-3-methylimidazolium bromide + 1-butanol binary system, *Ind. Eng. Chem. Res.*, **53** (34), 13522–13528, 2014.

[403] A. E. Andreatta, M. Francisco, E. Rodil, A. Soto, and A. Arce: Isobaric vapour-liquid equilibria and physical properties for isopropyl acetate+isopropanol+1-butyl-3-methyl-imidazolium bis(trifluoromethylsulfonyl)imide mixtures, *Fluid Phase Equilib.*, **300** (1-2), 162–171, 2011.

[404] F. S. Oliveira, L. P. Rebelo, and I. M. Marrucho: Influence of different inorganic salts on the ionicity and thermophysical

properties of 1-ethyl-3-methylimidazolium acetate ionic liquid, *J. Chem. Eng. Data*, **60** (3), 781–789, 2015.

[405] S. Lago, H. Rodríguez, A. Arce, and A. Soto: Improved concentration of citrus essential oil by solvent extraction with acetate ionic liquids, *Fluid Phase Equilib.*, **361**, 37–44, 2014.

[406] A. B. Pereiro and A. Rodríguez: Experimental liquid-liquid equilibria of 1-alkyl-3-methylimidazolium hexafluorophosphate with 1-alcohols, *J. Chem. Eng. Data*, **52** (4), 1408–1412, 2007.

[407] N. Calvar, E. Gómez, B. González, and Á. Domínguez: Experimental determination, correlation, and prediction of physical properties of the ternary mixtures ethanol + water with 1-octyl-3- methylimidazolium chloride and 1-ethyl-3-methylimidazolium ethylsulfate, *J. Chem. Eng. Data*, **52** (6), 2529–2535, 2007.

[408] A. Cháfer, J. De La Torre, J. B. Montón, and E. Lladosa: Experimental Determination and Correlation of Liquid-Liquid Equilibria Data for a System of Water + Ethanol + 1-Butyl-3-methylimidazolium Hexafluorophosphate at Different Temperatures, *J. Chem. Eng. Data*, **62** (2), 773–779, 2017.

[409] S. N. Mirheydari, M. Barzegar-Jalali, H. Shekaari, F. Martinez, and A. Jouyban: Experimental determination and correlation of lamotrigine solubility in aqueous mixtures of 1-octyl-3-methylimidazolium bromide ionic liquid at various temperatures, *J. Chem. Thermodyn.*, **135** (3), 75–85, 2019.

[410] A. Pal, R. Gaba, T. Singh, and A. Kumar: Excess thermodynamic properties of binary mixtures of ionic liquid (1-butyl-3-methylimidazolium hexafluorophosphate) with alkoxyalkanols at several temperatures, *J. Mol. Liq.*, **154** (1), 41–46, 2010.

[411] E. Gómez, B. González, N. Calvar, and Á. Domínguez: Excess molar properties of ternary system (ethanol + water + 1,3-dimethylimidazolium methylsulphate) and its binary mixtures at

several temperatures, *J. Chem. Thermodyn.*, **40** (8), 1208–1216, 2008.

[412] S. Corderí and B. González: Ethanol extraction from its azeotropic mixture with hexane employing different ionic liquids as solvents, *J. Chem. Thermodyn.*, **55**, 138–143, 2012.

[413] P. F. Requejo, E. J. González, E. A. Macedo, and Á. Domínguez: Effect of the temperature on the physical properties of the pure ionic liquid 1-ethyl-3-methylimidazolium methylsulfate and characterization of its binary mixtures with alcohols, *J. Chem. Thermodyn.*, **74**, 193–200, 2014.

[414] E. Gómez, N. Calvar, E. A. MacEdo, and Á. Domínguez: Effect of the temperature on the physical properties of pure 1-propyl 3-methylimidazolium bis(trifluoromethylsulfonyl)imide and characterization of its binary mixtures with alcohols, *J. Chem. Thermodyn.*, **45** (1), 9–15, 2012.

[415] A. B. Pereiro, H. I. Veiga, J. M. Esperança, and A. Rodríguez: Effect of temperature on the physical properties of two ionic liquids, *J. Chem. Thermodyn.*, **41** (12), 1419–1423, 2009.

[416] E. Gómez, B. González, Á. Domínguez, E. Tojo, and J. Tojo: Dynamic viscosities of a series of 1-alkyl-3-methylimidazolium chloride ionic liquids and their binary mixtures with water at several temperatures, *J. Chem. Eng. Data*, **51** (2), 696–701, 2006.

[417] S. Lago, H. Rodríguez, A. Soto, and A. Arce: Deterpenation of citrus essential oil by liquid-liquid extraction with 1-alkyl-3-methylimidazolium bis(trifluoromethylsulfonyl)amide ionic liquids, *J. Chem. Eng. Data*, **56** (4), 1273–1281, 2011.

[418] Q. Zhang, S. Cai, W. Zhang, Y. Lan, and X. Zhang: Density, viscosity, conductivity, refractive index and interaction study of binary mixtures of the ionic liquid 1–ethyl–3–methylimidazolium acetate with methyldiethanolamine, *J. Mol. Liq.*, **233**, 471–478, 2017.

[419] E. Vercher, F. J. Llopis, M. V. González-Alfaro, and A. Martínez-Andreu: Density, speed of sound, and refractive index of 1-ethyl-3- methylimidazolium trifluoromethanesulfonate with acetone, methyl acetate, and ethyl acetate at temperatures from (278.15 to 328.15) K, *J. Chem. Eng. Data*, **55** (3), 1377–1388, 2010.

[420] G. R. Sunkara, M. M. Tadavarthi, V. K. Tadekoru, S. K. Tadikonda, and S. R. Bezawada: Density, refractive index, and speed of sound of the binary mixture of 1-butyl-3-methylimidazolium tetrafluoroborate + N -vinyl-2-pyrrolidinone from T = (298.15 to 323.15) K at atmospheric pressure, *J. Chem. Eng. Data*, **60** (3), 886–894, 2015.

[421] A. N. Soriano, B. T. Doma, and M. H. Li: Density and refractive index measurements of 1-ethyl-3-methylimidazolium-based ionic liquids, *J. Taiwan Inst. Chem. Eng.*, **41** (1), 115–121, 2010.

[422] M. A. Iglesias-Otero, J. Troncoso, E. Carballo, and L. Romaní: Density and refractive index in mixtures of ionic liquids and organic solvents: Correlations and predictions, *J. Chem. Thermodyn.*, **40** (6), 949–956, 2008.

[423] S. Seki, N. Serizawa, S. Ono, K. Takei, K. Hayamizu, et al.: Densities, Viscosities, and Refractive Indices of Binary Room-Temperature Ionic Liquids with Common Cations/Anions, *J. Chem. Eng. Data*, **64** (2), 433–441, 2019.

[424] S. Singh, M. Aznar, and N. Deenadayalu: Densities, speeds of sound, and refractive indices for binary mixtures of 1-butyl-3-methylimidazolium methyl sulphate ionic liquid with alcohols at T = (298.15, 303.15, 308.15, and 313.15) K, *J. Chem. Thermodyn.*, **57**, 238–247, 2013.

[425] A. Nazet, S. Sokolov, T. Sonnleitner, S. Friesen, and R. Buchner: Densities, Refractive Indices, Viscosities, and Conductivities of Non-Imidazolium Ionic Liquids [Et$_3$S][TFSI], [Et$_2$MeS][TFSI],

[BuPy][TFSI], [N$_{8881}$][TFA], and [P$_{14}$][DCA], *J. Chem. Eng. Data*, **62** (9), 2549–2561, 2017.

[426] Z. Vaid, U. U. More, R. L. Gardas, N. I. Malek, and S. P. Ijardar: Composition and temperature dependence of excess properties of binary mixtures of imidazolium based ionic liquids: II ([C$_n$mim][PF$_6$]) + propylamine, *J. Solution Chem.*, **44** (3-4), 718–741, 2015.

[427] K. H. Alkhaldi, A. S. Al-Jimaz, and M. S. AlTuwaim: Comparative study of physical properties of binary mixtures of halogen free ionic liquids with alcohols, *J. Chem. Thermodyn.*, **110**, 175–185, 2017.

[428] M. Dzida, M. Musiał, E. Zorebski, M. Zorebski, J. Jacquemin, et al.: Comparative study of effect of alkyl chain length on thermophysical characteristics of five N-alkylpyridinium bis(trifluoromethylsulfonyl)imides with selected imidazolium-based ionic liquids, *J. Mol. Liq.*, **278**, 401–412, 2019.

[429] J. G. Huddleston, A. E. Visser, W. M. Reichert, H. D. Willauer, G. A. Broker, et al.: Characterization and comparison of hydrophilic and hydrophobic room temperature ionic liquids incorporating the imidazolium cation, *Green Chem.*, **3** (4), 156–164, 2001.

[430] B. González and S. Corderí: Capacity of two 1-butyl-1-methylpyrrolidinium-based ionic liquids for the extraction of ethanol from its mixtures with heptane and hexane, *Fluid Phase Equilib.*, **354**, 89–94, 2013.

[431] A. B. Pereiro and A. Rodríguez: Binary mixtures containing OMIM PF$_6$: Density, speed of sound, refractive index and LLE with hexane, heptane and 2-propanol at several temperatures, *Phys. Chem. Liq.*, **46** (2), 162–174, 2008.

[432] L. Fernández, D. Montaño, J. Ortega, and F. J. Toledo: Binary liquid-liquid equilibria for systems of mono- or disubstituted

haloalkanes (Cl, Br) and pyridinium-based ionic liquids. Advances in the experimentation and interpretation of results, *Ind. Eng. Chem. Res.*, **52** (33), 11758–11766, 2013.

[433] S. Corderí, E. J. González, N. Calvar, and Á. Domínguez: Application of [HMim][NTf$_2$], [HMim][TfO] and [BMim][TfO] ionic liquids on the extraction of toluene from alkanes: Effect of the anion and the alkyl chain length of the cation on the LLE, *J. Chem. Thermodyn.*, **53**, 60–66, 2012.

[434] H. Shekaari and E. Armanfar: Apparent molar volumes and expansivities of aqueous solutions of ionic liquids, l-alkyl-3-methylimidazolium alkyl sulfate at T=(298.15-328.15)K, *Fluid Phase Equilib.*, **303** (2), 120–125, 2011.

[435] W. David, T. M. Letcher, D. Ramjugernath, and J. D. Raal: Activity coefficients of hydrocarbon solutes at infinite dilution in the ionic liquid, 1-methyl-3-octyl-imidazolium chloride from gas-liquid chromatography, *J. Chem. Thermodyn.*, **35** (8), 1335–1341, 2003.

[436] M. Geppert-Rybczyńska and M. Sitarek: Acoustic and volumetric properties of binary mixtures of ionic liquid 1-butyl-3-methylimidazolium bis(trifluoromethylsulfonyl)imide with acetonitrile and tetrahydrofuran, *J. Chem. Eng. Data*, **59** (4), 1213–1224, 2014.

[437] A. B. Pereiro and A. Rodríguez: A study on the liquid-liquid equilibria of 1-alkyl-3-methylimidazolium hexafluorophosphate with ethanol and alkanes, *Fluid Phase Equilib.*, **270** (1-2), 23–29, 2008.

[438] R. Wang, X. Qi, S. Liu, Y. He, and Y. Deng: A comparison study on the properties of 1,3-dialkylimidazolium tetrafluoroborate salts prepared by halogen-free and traditional method, *J. Mol. Liq.*, **221**, 339–345, 2016.

USC

[439] R. G. Seoane, E. J. González, and B. González: 1-Alkyl-3-methylimidazolium bis(trifluoromethylsulfonyl)imide ionic liquids as solvents in the separation of azeotropic mixtures, *J. Chem. Thermodyn.*, **53**, 152–157, 2012.

[440] S. Corderí, E. Gómez, Á. Domínguez, and N. Calvar: (Liquid + liquid) equilibrium of ternary and quaternary systems containing heptane, cyclohexane, toluene and the ionic liquid [EMim][N(CN)$_2$]. Experimental data and correlation, *J. Chem. Thermodyn.*, **94**, 16–23, 2016.

[441] I. Domínguez, P. F. Requejo, J. Canosa, and Á. Domínguez: (Liquid + liquid) equilibrium at T = 298.15 K for ternary mixtures of alkane + aromatic compounds + imidazolium-based ionic liquids, *J. Chem. Thermodyn.*, **74**, 138–143, 2014.

[442] L. Alonso, A. Arce, M. Francisco, and A. Soto: (Liquid + liquid) equilibria of [C$_8$mim][NTf$_2$] ionic liquid with a sulfur-component and hydrocarbons, *J. Chem. Thermodyn.*, **40** (2), 265–270, 2008.

[443] R. G. Seoane, E. Gómez, E. J. González, and Á. Domínguez: (Liquid + liquid) equilibria for the ternary mixtures (alkane + toluene + ionic liquid) at T = 298.15 K: Influence of the anion on the phase equilibria, *J. Chem. Thermodyn.*, **47**, 402–407, 2012.

[444] R. F. Souza, M. A. R. C. Alencar, M. R. Meneghetti, J. Dupont, and J. M. Hickmann: Nonlocal optical nonlinearity of ionic liquids, *J. Phys. Condens. Matter*, **20** (15), 155102, 2008.

[445] C. E. Santos, M. A. Alencar, P. Migowski, J. Dupont, and J. M. Hickmann: Anionic and cationic influence on the nonlocal nonlinear optical response of ionic liquids, *Chem. Phys.*, **403**, 33–36, 2012.

[446] C. E. Santos, M. A. Alencar, P. Migowski, J. Dupont, and J. M. Hickmann: Nonlocal nonlinear optical response of ionic liquids under violet excitation, *Adv. Mater. Sci. Eng.*, **2013**, 1–6, 2013.

[447] N. F. Corrêa, C. E. A. Santos, D. R. B. Valadão, L. F. de Oliveira, J. Dupont, et al.: Third-order nonlinear optical responses of colloidal Ag nanoparticles dispersed in BMIBF$_4$ ionic liquid, *Opt. Mater. Express*, **6** (1), 244, 2016.

[448] M. Trejo-Durán, E. Alvarado-Méndez, K. A. Barrera-Rivera, and V. M. Castaño: Nonlinear optical phenomena in Bi-ionic Liquids, *Optik (Stuttg).*, **130**, 895–899, 2017.

[449] I. Severiano-Carrillo, E. Alvarado-Méndez, K. Barrera-Rivera, M. Vázquez, M. Ortiz-Gutierrez, et al.: Studies of optical nonlinear properties of asymmetric ionic liquids, *Opt. Mater. (Amst).*, **84**, 166–171, 2018.

[450] J. Zhou, S.-K. Dong, Z.-H. He, and Y.-H. Zhang: Refractive index of ionic liquids under electric field: Methyl propyl imidazole iodide and several derivatives, *Chinese Phys. B*, **29** (4), 047801, 2020.

[451] V. C. Ferreira, L. Zanchet, W. F. Monteiro, L. G. da Trindade, M. O. de Souza, et al.: Theoretical and experimental comparative study of nonlinear properties of imidazolium cation based ionic liquids, *J. Mol. Liq.*, **328**, 115391, 2021.

[452] S. Rivera-Rubero and S. Baldelli: Surface Spectroscopy of Room-temperature Ionic Liquids on a Platinum Electrode: A Sum Frequency Generation Study, *J. Phys. Chem. B*, **108** (39), 15133–15140, 2004.

[453] N. Nishi, R. Ishimatsu, M. Yamamoto, and T. Kakiuchi: Orientation of 1-Dodecyl-4-phenylpyridinium Ions Constituting an Ionic Liquid at the Ionic Liquid|Water Interface Studied by Second Harmonic Generation, *J. Phys. Chem. C*, **111** (33), 12461–12466, 2007.

[454] C. Bardak, A. Atac, and F. Bardak: Effect of the external electric field on the electronic structure, spectroscopic features, NLO

properties, and interionic interactions in ionic liquids: A DFT approach, *J. Mol. Liq.*, **273**, 314–325, 2019.

[455] F. Bardak, C. Bardak, C. Karaca, E. Kose, S. Bilgili, et al.: Anionic dependency of electronic and nonlinear optical properties of ionic liquids, *J. Mol. Liq.*, (xxxx), 117030, 2021.

[456] J. L. Bredas, C. Adant, P. Tackx, A. Persoons, and B. M. Pierce: Third-Order Nonlinear Optical Response in Organic Materials: Theoretical and Experimental Aspects, *Chem. Rev.*, **94** (1), 243–278, 1994.

[457] J. P. Hermann and J. Ducuing: Third-order polarizabilities of long-chain molecules, *J. Appl. Phys.*, **45** (11), 5100–5102, 1974.

[458] A. Migalska-Zalas, K. EL Korchi, and T. Chtouki: Enhanced nonlinear optical properties due to electronic delocalization in conjugated benzodifuran derivatives, *Opt. Quantum Electron.*, **50** (11), 389, 2018.

[459] A. Kumar, A. K. Srivastava, S. N. Tiwari, N. Misra, and D. Sharma: Evolution of Anisotropy, First Order Hyperpolarizability and Electronic Parameters in p-Alkyl-p'-Cynobiphenyl Series of Liquid Crystals: Odd-Even Effect Revisited, *Mol. Cryst. Liq. Cryst.*, **681** (1), 23–31, 2019.

[460] B. F. Levine and C. G. Bethea: Second and third order hyperpolarizabilities of organic molecules, *J. Chem. Phys.*, **63** (6), 2666–2682, 1975.

[461] D. P. Shelton and J. E. Rice: Measurements and calculations of the hyperpolarizabilities of atoms and small molecules in the gas phase, *Chem. Rev.*, **94** (1), 3–29, 1994.

[462] S. J. A. van Gisbergen, J. G. Snijders, and E. J. Baerends: Accurate density functional calculations on frequency-dependent hyperpolarizabilities of small molecules, *J. Chem. Phys.*, **109** (24), 10657–10668, 1998.

[463] C. Valverde, S. A. de Lima e Castro, G. R. Vaz, J. L. de Almeida Ferreira, B. Baseia, et al.: Third-Order Nonlinear Optical Properties of a Carboxylic Acid Derivative, *Acta Chim. Slov.*, **65** (3), 739–749, 2018.

[464] A. V. Vologzhanina, A. A. Golovanov, D. M. Gusev, I. S. Odin, R. A. Apreyan, et al.: Intermolecular Interactions and Second-Harmonic Generation Properties of (E)-1,5-Diarylpentenyn-1-ones, *Cryst. Growth Des.*, **14** (9), 4402–4410, 2014.

[465] G. P. Agrawal, C. Cojan, and C. Flytzanis: Nonlinear optical properties of one-dimensional semiconductors and conjugated polymers, *Phys. Rev. B*, **17** (2), 776–789, 1978.

[466] N. J. Dawson, B. R. Anderson, J. L. Schei, and M. G. Kuzyk: Classical model of the upper bounds of the cascading contribution to the second hyperpolarizability, *Physical Review A*, **84**, 043406, 2011.

[467] M. G. Kuzyk, K. D. Singer, and G. I. Stegeman: Theory of molecular nonlinear optics, *Advances in Optics and Photonics*, **5**, 4, 2013.

[468] M. G. Vivas, D. L. da Silva, C. R. Mendonca, and L. De Boni: First-order hyperpolarizability of organic molecules: hyper-Rayleigh scattering and applications, in *Mol. Laser Spectrosc.*, pages 275–314, Elsevier, 2020.

[469] T. J. Atherton, J. Lesnefsky, G. A. Wiggers, and R. G. Petschek: Maximizing the hyperpolarizability poorly determines the potential, *J. Opt. Soc. Am. B*, **29** (3), 513, 2012.

[470] C. J. Burke, T. J. Atherton, J. Lesnefsky, and R. G. Petschek: Optimizing the second hyperpolarizability with minimally parametrized potentials, *J. Opt. Soc. Am. B*, **30** (6), 1438, 2013.

[471] C. D. Rodríguez-Fernández, E. López Lago, C. Schröder, and L. M. Varela: Non-additive electronic polarizabilities of ionic

liquids: Charge delocalization effects, *J. Mol. Liq.*, (xxxx), 117099, 2021.

[472] J. Zyss and D. Chemla: Quadratic Nonlinear Optics and Optimization of the Second-Order Nonlinear Optical Response of Molecular Crystals, in *Nonlinear Opt. Prop. Org. Mol. Cryst.*, pages 23–191, Elsevier, 1987.

[473] C. Flytzanis: Dimensionality Effects and Scaling Laws in Nonlinear Optical Susceptibilities, in *Nonlinear Opt. Prop. Org. Mol. Cryst.*, volume 1, pages 121–135, Elsevier, 1987.

[474] J. F. Ward and D. S. Elliott: Measurements of molecular hyperpolarizabilities for ethylene, butadiene, hexatriene, and benzene, *J. Chem. Phys.*, **69** (12), 5438–5440, 1978.

[475] J. V. Champion, G. H. Meeten, and C. D. Whittle: Electro-optic Kerr effect in n-alkane liquids, *Trans. Faraday Soc.*, **66**, 2671, 1970.

[476] Z. Błaszczak and P. Gauden: Optical investigation of short-chain n-alkanes, *J. Chem. Soc., Faraday Trans. 2*, **84** (3), 239–245, 1988.

[477] C. Adant, M. Dupuis, and J. L. Bredas: Ab initio study of the nonlinear optical properties of urea: Electron correlation and dispersion effects, *Int. J. Quantum Chem.*, **56** (S29), 497–507, 1995.

[478] C. Adamo and D. Jacquemin: The calculations of excited-state properties with Time-Dependent Density Functional Theory, *Chem. Soc. Rev.*, **42** (3), 845–856, 2013.

[479] A. J. Garza, G. E. Scuseria, S. B. Khan, and A. M. Asiri: Assessment of long-range corrected functionals for the prediction of non-linear optical properties of organic materials, *Chem. Phys. Lett.*, **575**, 122–125, 2013.

[480] H. Iikura, T. Tsuneda, T. Yanai, and K. Hirao: A long-range correction scheme for generalized-gradient-approximation exchange functionals, *The Journal of Chemical Physics*, **115**, 3540–3544, 2001.

[481] T. Yanai, D. P. Tew, and N. C. Handy: A new hybrid exchange–correlation functional using the coulomb-attenuating method (cam-b3lyp), *Chemical Physics Letters*, **393**, 51–57, 2004.

[482] O. A. Vydrov and G. E. Scuseria: Assessment of a long-range corrected hybrid functional, *The Journal of Chemical Physics*, **125**, 234109, 2006.

[483] C. C. Wang: Second-Harmonic Generation of Light at the Boundary of an Isotropic Medium, *Phys. Rev.*, **178** (3), 1457–1460, 1969.

[484] Y. R. Shen: Surface Second Harmonic Generation: A New Technique for Surface Studies, *Annu. Rev. Mater. Sci.*, **16** (1), 69–86, 1986.

[485] R. M. Corn and D. A. Higgins: Optical second harmonic generation as a probe of surface chemistry, *Chem. Rev.*, **94** (1), 107–125, 1994.

[486] K. Hashimoto, K. Fujii, T. Kusano, K. Hirosawa, and M. Shibayama: Small-angle X-ray scattering study on nano-scale structures controlled by water content in a binary water/ionic liquid system, *Phys. Chem. Chem. Phys.*, **20** (27), 18355–18360, 2018.

[487] N. Cheng, Q. Hu, Y. Bi, W. Xu, Y. Gong, et al.: Gels and Lyotropic Liquid Crystals: Using an Imidazolium-Based Catanionic Surfactant in Binary Solvents, *Langmuir*, **30** (30), 9076–9084, 2014.

308

[488] G. García-Miaja, J. Troncoso, and L. Romaní: Excess properties for binary systems ionic liquid+ethanol: Experimental results and theoretical description using the ERAS model, *Fluid Phase Equilib.*, **274** (1-2), 59–67, 2008.

[489] M. T. Clough, C. R. Crick, J. Gräsvik, P. A. Hunt, H. Niedermeyer, et al.: A physicochemical investigation of ionic liquid mixtures, *Chem. Sci.*, **6** (2), 1101–1114, 2015.

[490] S. Shahnazar, S. Bagheri, and S. B. Abd Hamid: Enhancing lubricant properties by nanoparticle additives, *Int. J. Hydrogen Energy*, **41** (4), 3153–3170, 2016.

[491] O. Cabeza, L. Segade, M. Domínguez-Pérez, E. Rilo, D. Ausín, et al.: Mesostructure and physical properties of aqueous mixtures of the ionic liquid 1-ethyl-3-methyl imidazolium octyl sulfate doped with divalent sulfate salts in the liquid and the mesomorphic states, *Phys. Chem. Chem. Phys.*, **20** (13), 8724–8736, 2018.

[492] O. Cabeza, L. Segade, M. Domínguez-Pérez, E. Rilo, S. García-Garabal, et al.: Tuning physical properties and mesomorphic structures in aqueous 1-ethyl-3-methylimidazolium octylsulfate rigid-gel with univalent salt doping, *J. Chem. Thermodyn.*, **112**, 267–275, 2017.

[493] D. Chand, M. Q. Farooq, A. K. Pathak, J. Li, E. A. Smith, et al.: Magnetic ionic liquids based on transition metal complexes with N -alkylimidazole ligands, *New J. Chem.*, **43** (1), 20–23, 2019.

[494] P. Nockemann, B. Thijs, N. Postelmans, K. Van Hecke, L. Van Meervelt, et al.: Anionic Rare-Earth Thiocyanate Complexes as Building Blocks for Low-Melting Metal-Containing Ionic Liquids, *J. Am. Chem. Soc.*, **128** (42), 13658–13659, 2006.

[495] C. Chiappe and M. Malvaldi: Highly concentrated "solutions" of metal cations in ionic liquids: current status and future challenges, *Phys. Chem. Chem. Phys.*, **12** (37), 11191, 2010.

[496] T. Peppel, M. Köckerling, M. Geppert-Rybczyńska, R. V. Ralys, J. K. Lehmann, et al.: Low-Viscosity Paramagnetic Ionic Liquids with Doubly Charged $[Co(NCS)_4]^{2-}$ Ions, *Angew. Chemie Int. Ed.*, **49** (39), 7116–7119, 2010.

[497] S. Seki, Y. Kobayashi, H. Miyashiro, Y. Ohno, A. Usami, et al.: Lithium Secondary Batteries Using Modified-Imidazolium Room-Temperature Ionic Liquid, *J. Phys. Chem. B*, **110** (21), 10228–10230, 2006.

[498] T. Mandai, K. Dokko, and M. Watanabe: Solvate Ionic Liquids for Li, Na, K, and Mg Batteries, *Chem. Rec.*, **19** (4), 708–722, 2019.

[499] Z. Li, G. D. Smith, and D. Bedrov: Li^+ Solvation and Transport Properties in Ionic Liquid/Lithium Salt Mixtures: A Molecular Dynamics Simulation Study, *J. Phys. Chem. B*, **116** (42), 12801–12809, 2012.

[500] A. Chaumont and G. Wipff: Solvation of M^{3+} lanthanide cations in room-temperature ionic liquids. A molecular dynamics investigation, *Phys. Chem. Chem. Phys.*, **5** (16), 3481–3488, 2003.

[501] G.-T. Wei, Z. Yang, and C.-J. Chen: Room temperature ionic liquid as a novel medium for liquid/liquid extraction of metal ions, *Anal. Chim. Acta*, **488** (2), 183–192, 2003.

[502] C. Shi, Y. Jing, and Y. Jia: Solvent extraction of lithium ions by tri-n-butyl phosphate using a room temperature ionic liquid, *J. Mol. Liq.*, **215**, 640–646, 2016.

[503] P. D. Fleischauer and P. Fleischauer: Photoluminescence of transition metal coordination compounds, *Chem. Rev.*, **70** (2), 199–230, 1970.

USC

[504] V. W. W. Yam, V. K. M. Au, and S. Y. L. Leung: Light-Emitting Self-Assembled Materials Based on d8 and d10 Transition Metal Complexes, *Chem. Rev.*, **115** (15), 7589–7728, 2015.

[505] K. Y. Zhang, X. Chen, G. Sun, T. Zhang, S. Liu, et al.: Utilization of Electrochromically Luminescent Transition-Metal Complexes for Erasable Information Recording and Temperature-Related Information Protection, *Adv. Mater.*, **28** (33), 7137–7142, 2016.

[506] J. Wang, S. Tang, A. Sandström, and L. Edman: Combining an Ionic Transition Metal Complex with a Conjugated Polymer for Wide-Range Voltage-Controlled Light-Emission Color, *ACS Appl. Mater. Interfaces*, **7** (4), 2784–2789, 2015.

[507] L. L. Han, T. P. Hu, K. Mei, Z. M. Guo, C. Yin, et al.: Solvent-controlled three families of Zn(ii) coordination compounds: synthesis, crystal structure, solvent-induced structural transformation, supramolecular isomerism and photoluminescence, *Dalt. Trans.*, **44** (13), 6052–6061, 2015.

[508] R. B. Lin, S. Y. Liu, J. W. Ye, X.-Y. Li, and J. P. Zhang: Photoluminescent Metal–Organic Frameworks for Gas Sensing, *Adv. Sci.*, **3** (7), 1500434, 2016.

[509] S. Di Bella: Second-order nonlinear optical properties of transition metal complexes, *Chem. Soc. Rev.*, **30** (6), 355–366, 2001.

[510] E. López Lago, J. A. Seijas, I. de Pedro, J. Rodríguez Fernández, M. P. Vázquez-Tato, et al.: Structural and physical properties of a new reversible and continuous thermochromic ionic liquid in a wide temperature interval: $[BMIM]_4 [Ni(NCS)_6]$, *New J. Chem.*, **42** (19), 15561–15571, 2018.

[511] Z. Hu and C. J. Margulis: A Study of the Time-Resolved Fluorescence Spectrum and Red Edge Effect of ANF in a Room-Temperature Ionic Liquid, *J. Phys. Chem. B*, **110** (23), 11025–11028, 2006.

[512] Y. Zhang and E. J. Maginn: Direct Correlation between Ionic Liquid Transport Properties and Ion Pair Lifetimes: A Molecular Dynamics Study, *J. Phys. Chem. Lett.*, **6** (4), 700–705, 2015.

[513] I. Tanabe, Y. Kurawaki, Y. Morisawa, and Y. Ozaki: Electronic absorption spectra of imidazolium-based ionic liquids studied by far-ultraviolet spectroscopy and quantum chemical calculations, *Phys. Chem. Chem. Phys.*, **18** (32), 22526–22530, 2016.

[514] M. A. Salam, B. Abdullah, A. Ramli, and I. Mujtaba: Structural feature based computational approach of toxicity prediction of ionic liquids: Cationic and anionic effects on ionic liquids toxicity, *J. Mol. Liq.*, **224**, 393–400, 2016.

[515] B. Docampo-Álvarez, V. Gómez-González, T. Méndez-Morales, J. Carrete, J. R. Rodríguez, et al.: Mixtures of protic ionic liquids and molecular cosolvents: A molecular dynamics simulation, *J. Chem. Phys.*, **140** (21), 214502, 2014.

[516] G. Saielli, A. Bagno, and Y. Wang: Insights on the Isotropic-to-Smectic A Transition in Ionic Liquid Crystals from Coarse-Grained Molecular Dynamics Simulations: The Role of Microphase Segregation, *J. Phys. Chem. B*, **119** (9), 3829–3836, 2015.

[517] F. Dommert, K. Wendler, R. Berger, L. Delle Site, and C. Holm: Force Fields for Studying the Structure and Dynamics of Ionic Liquids: A Critical Review of Recent Developments, *ChemPhysChem*, **13** (7), 1625–1637, 2012.

[518] W. Jiang, Y. Wang, and G. A. Voth: Molecular dynamics simulation of nanostructural organization in ionic liquid/water mixtures, *J. Phys. Chem. B*, **111** (18), 4812–4818, 2007.

[519] T. I. Morrow and E. J. Maginn: Molecular Dynamics Study of the Ionic Liquid 1- n -Butyl-3-methylimidazolium Hexafluorophosphate, *J. Phys. Chem. B*, **106** (49), 12807–12813, 2002.

[520] A. Chaumont and G. Wipff: Solvation of Uranyl(II), Europium(III) and Europium(II) Cations in"Basic" Room-Temperature Ionic Liquids: A Theoretical Study, *Chem. - A Eur. J.*, **10** (16), 3919–3930, 2004.

[521] A. Chaumont and G. Wipff: Solvation of Ln(III) Lanthanide Cations in the [BMI][SCN], [MeBu$_3$N][SCN], and [BMI]$_5$[Ln(NCS)$_8$] Ionic Liquids: A Molecular Dynamics Study, *Inorg. Chem.*, **48** (10), 4277–4289, 2009.

[522] M. Busato, P. D'Angelo, and A. Melchior: Solvation of Zn^{2+} ion in 1-alkyl-3-methylimidazolium bis(trifluoromethylsulfonyl)imide ionic liquids: a molecular dynamics and X-ray absorption study, *Phys. Chem. Chem. Phys.*, **21** (13), 6958–6969, 2019.

[523] L. Varela, T. Méndez-Morales, J. Carrete, V. Gómez-González, B. Docampo-Álvarez, et al.: Solvation of molecular cosolvents and inorganic salts in ionic liquids: A review of molecular dynamics simulations, *J. Mol. Liq.*, **210**, 178–188, 2015.

[524] V. Lesch, S. Jeremias, A. Moretti, S. Passerini, A. Heuer, et al.: A Combined Theoretical and Experimental Study of the Influence of Different Anion Ratios on Lithium Ion Dynamics in Ionic Liquids, *J. Phys. Chem. B*, **118** (26), 7367–7375, 2014.

[525] V. Lesch, H. Montes-Campos, T. Méndez-Morales, L. J. Gallego, A. Heuer, et al.: Molecular dynamics analysis of the effect of electronic polarization on the structure and single-particle dynamics of mixtures of ionic liquids and lithium salts, *J. Chem. Phys.*, **145** (20), 204507, 2016.

[526] J.-C. Lassègues, J. Grondin, C. Aupetit, and P. Johansson: Spectroscopic Identification of the Lithium Ion Transporting Species in LiTFSI-Doped Ionic Liquids, *J. Phys. Chem. A*, **113** (1), 305–314, 2009.

[527] V. Gómez-González, B. Docampo-Álvarez, O. Cabeza, M. Fedorov, R. M. Lynden-Bell, et al.: Molecular dynamics simulations of the structure and single-particle dynamics of mixtures of divalent salts and ionic liquids, *J. Chem. Phys.*, **143** (12), 124507, 2015.

[528] O. Borodin, G. A. Giffin, A. Moretti, J. B. Haskins, J. W. Lawson, et al.: Insights into the Structure and Transport of the Lithium, Sodium, Magnesium, and Zinc Bis(trifluoromethansulfonyl)imide Salts in Ionic Liquids, *J. Phys. Chem. C*, **122** (35), 20108–20121, 2018.

[529] P. Li, B. P. Roberts, D. K. Chakravorty, and K. M. Merz: Rational Design of Particle Mesh Ewald Compatible Lennard-Jones Parameters for +2 Metal Cations in Explicit Solvent, *J. Chem. Theory Comput.*, **9** (6), 2733–2748, 2013.

[530] P. Li, L. F. Song, and K. M. Merz: Parameterization of Highly Charged Metal Ions Using the 12-6-4 LJ-Type Nonbonded Model in Explicit Water, *J. Phys. Chem. B*, **119** (3), 883–895, 2015.

[531] K. Nakamoto: Infrared and Raman Spectra of Inorganic and Coordination Compounds, in P. R. Griffiths, editor, *Handb. Vib. Spectrosc.*, volume 156, pages 1872–1892, John Wiley & Sons, Ltd, Chichester, UK, 2006.

[532] K. Chaitanya, C. Santhamma, K. V. Prasad, and V. Veeraiah: Molecular structure, vibrational spectroscopic (FT-IR, FT-Raman), first order hyperpolarizability, NBO analysis, HOMO and LUMO analysis, thermodynamic properties of 3,5-dimethylbenzophenone by ab inito HF and density functional method, *J. At. Mol. Sci.*, **3** (1), 1–22, 2011.

[533] J. Kabesova, M.;Gazo: Structure and classification of thiocyanates and the mutual influence of their ligands, *Chem. Rev.*, **34** (6), 41, 1980.

314

[534] F. Vlahović, M. Perić, M. Gruden-Pavlović, and M. Zlatar: Assessment of TD-DFT and LF-DFT for study of $d-d$ transitions in first row transition metal hexaaqua complexes, *J. Chem. Phys.*, **142** (21), 214111, 2015.

[535] M. Castillo and E. Ramirez: Synthesis and spectral properties of new complexes between glycine and titanium(III), vanadium(III), chromium(III), iron(III), cobalt(II), nickel(II) and copper(II), *Transit. Met. Chem.*, **9** (7), 268–270, 1984.

[536] A. Adamson: Medium and ligand effects on the absorption spectra of some Cr(III) complexes, *J. Inorg. Nucl. Chem.*, **28** (9), 1955–1964, 1966.

[537] S. Lakshmi, T. Endo, and G. Siva: Electronic (Absorption) Spectra of 3d Transition Metal Complexes, in *Adv. Asp. Spectrosc.*, pages 3–48, InTech, 2012.

[538] A. Sanchez Navas, B. Reddy, and F. Nieto: Spectroscopic study of chromium, iron, OH, fluid and mineral inclusions in uvarovite and fuchsite, *Spectrochim. Acta Part A Mol. Biomol. Spectrosc.*, **60** (10), 2261–2268, 2004.

[539] J. C. Barnes and P. Day: 740. Charge-transfer spectra of some inorganic complexes in solution, *J. Chem. Soc.*, (3886), 3886, 1964.

[540] I. Syiemlieh, A. Kumar, S. D. Kurbah, A. K. De, and R. A. Lal: Low-spin manganese(II) and high-spin manganese(III) complexes derived from disalicylaldehyde oxaloyldihydrazone: Synthesis, spectral characterization and electrochemical studies, *J. Mol. Struct.*, **1151**, 343–352, 2018.

[541] D. Sathyanarayana: *Electronic Absorption Spectroscopy and Related Techniques*, Universities Press, 2001.

[542] J. Šima and R. Šípoš: Insights into Coordination, Bioinorganic and Applied Inorganic Chemistry, Iii, chapter Applied Ph, pages

315

306–365, Press of Slovak University of Technology, Bratislava, 2009.

[543] J. Šima and J. Makáňová: Photochemistry of iron (III) complexes, *Coord. Chem. Rev.*, **160**, 161–189, 1997.

[544] A. E. Regazzoni and M. A. Blesa: Reactivity of surface iron(III)-thiocyanate complexes characterized by the dissolution of hematite in acidic thiocyanate solutions, *Langmuir*, **7** (3), 473–478, 1991.

[545] D. C. Harris: *Quantitative chemical analysis; second edition (Harris, Daniel C.)*, volume 65, Craig Bleyer, New York, 7th edition, 1988.

List of publications included in this thesis

- **Refractive index measurement of imidazolium based ionic liquids in the Vis-NIR,** Y. Arosa, C.D. Rodríguez-Fernández, E. López Lago, A. Amigo, L. M. Varela, O. Cabeza and R. de la Fuente, *Optical Materials,* **73**, 647 – 657 (2017).

    – **Journal information:** Impact factor: 2.320. Category: Optics Ranking inside category: 36/94 (Q2).

    – **Author Contribution:** Conceptualization, Methodology, Formal analysis, Validation, Investigation, Writing - Original Draft, Writing - Review & Editing , Visualization.

- **Modeling the Temperature- Dependent Material Dispersion of Imidazolium-Based Ionic Liquids in the VIS-NIR,** Y. Arosa, B. Algnamat, C. D. Rodríguez-Fernández, E. López Lago, L. M. Varela and R. de la Fuente, *J. Phys. Chem. C,* **122**(51), 29470 – 29478 (2018).

    – **Journal information:** Impact factor: 4.309. Category: Materials Science, Multidisciplinary. Ranking inside Category: 60/293 (Q1).

    – **Author Contribution:** This contribution was reprinted in the thesis of Y. Arosa, *Spectroscopic refractometry by broadband interference within the ultraviolet, visible and near infrared ranges* with the purpose of showcasing the performance of the RISBI device whose development is

the cornerstone of that thesis. Here, I partially reprint this contribution with the aim of discussing the relations found in that work about the structure of ionic liquids and their optical properties, relations which are the leitmotiv of this thesis. The author contribution in this publication is: Conceptualization, Methodology, Formal analysis, Validation, Investigation, Writing - Original Draft, Writing - Review & Editing , Visualization.
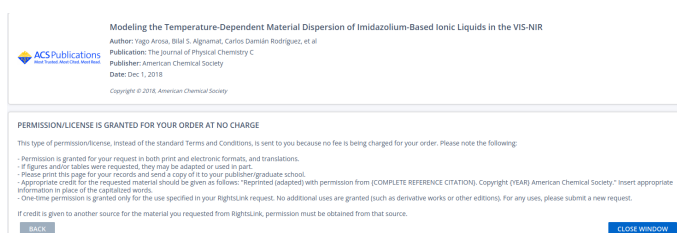
- **An experimental and computational study on the material dispersion of 1-alkyl-3-methylimidazolium tetrafluoroborate ionic liquids,** C.D. Rodríguez-Fernández, Y. Arosa, B. Algnamat, E. López Lago and R. de la Fuente, *Phys. Chem. Chem. Phys.,* **22**, 14061 – 14076 (2020).

  – **Journal information:** Impact factor: 3.676. Category: Physics, Atomic, Molecular & Chemical. Ranking inside Category: 8/37 (Q1).

  – **Author Contribution:** Conceptualization, Methodology, Software, Formal analysis, Validation, Investigation, Data Curation, Writing - Original Draft, Writing - Review & Editing , Visualization.

- **Non-additive electronic polarizabilities of ionic liquids: Charge delocalization effects,** C. D. Rodríguez-Fernández, E. López Lago, C. Schröder and L. M. Varela, *J. Mol. Liq.,* **346**, 117099 (2022).

  – **Journal information (2020):** Impact factor: 6.165. Category: Physics, Atomic, Molecular & Chemical. Ranking inside Category: 4/37 (Q1).

  – **Author Contribution:** Conceptualization, Methodology, Software, Formal analysis, Validation, Investigation, Data Curation, Writing - Original Draft, Writing - Review & Editing , Visualization.
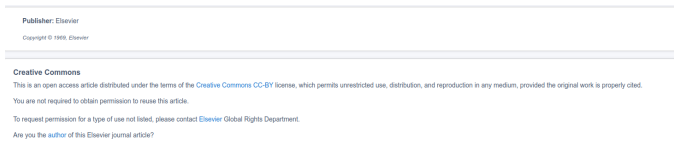
- **Charge delocalization and hyperpolarizability in ionic liquids,** C. D. Rodríguez-Fernández, E. López Lago, C. Schröder and L. M. Varela, *J. Mol. Liq.,* **xx**, DOI: 10.1016/j.molliq.2021.118153 (2021).

  – **Journal information (2020):** Impact factor: 6.165. Category: Physics, Atomic, Molecular & Chemical. Ranking inside Category: 4/37 (Q1).

  – **Author Contribution:** Conceptualization, Methodology, Software, Formal analysis, Validation, Investigation, Data Curation, Writing - Original Draft, Writing - Review & Editing , Visualization.
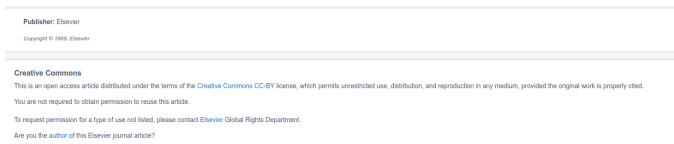
- **New Insights on the Characterization of the Ionic Liquid Crystal 1-Ethyl-3-Methylimidazolium Decylsulfate,** C. D. Rodríguez-Fernández, Y. Arosa, E. López Lago, J. Salgado, P. Verdía, E. Tojo, O. Cabeza, L. M. Varela and R. de la Fuente, *J. Phys. Chem. C,* **123**(51), 31196 – 31211 (2019).

  – **Journal information:** Impact factor: 4.189. Category: Materials Science, Multidisciplinary. Ranking inside Category: 90/314 (Q2)

  – **Author Contribution:** Conceptualization, Methodology, Software, Formal analysis, Validation, Investigation, Data

Curation, Writing - Original Draft, Writing - Review & Editing , Visualization.

- **Microstructure, dynamics and optical properties of metal-doped imidazolium-based ionic liquids,** C. D. Rodríguez-Fernández, H. Montes-Campos, E. López-Lago, R. de la Fuente and L. M. Varela, *J. Mol. Liq.,* **317**, 113866 − 113879 (2020).

  – **Journal information:** Impact factor: 6.165. Category: Physics, Atomic, Molecular & Chemical. Ranking inside Category: 4/37 (Q1).

  – **Author Contribution:** Conceptualization, Methodology, Software, Formal analysis, Validation, Investigation, Data Curation, Writing - Original Draft, Writing - Review & Editing , Visualization.

- **Accuracy of refractive index spectroscopy by broadband interferometry,** Y. Arosa, C. D. Rodríguez-Fernández, A. Doval, E. López Lago, R. de la Fuente, *Measurement,* **187**, 110225 (2022).

- **Journal information (2020):** Impact factor: 3.927. Category: Instruments & Instrumentation. Ranking inside Category: 12/64 (Q1).

- **Author Contribution:** Formal analysis, Validation, Writing – original draft, Writing – review & editing.

Accuracy of refractive index spectroscopy by broadband interferometry

Author: Yago Arosa,Carlos Damián Rodríguez-Fernández,Alejandro Doval,Elena López Lago,Raúl de la Fuente
Publication: Measurement
Publisher: Elsevier
Date: January 2022
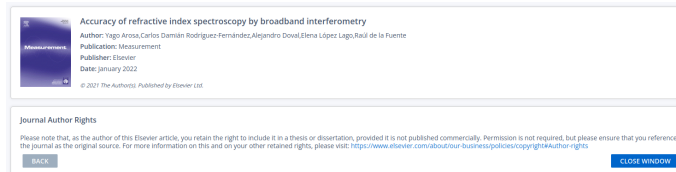
© 2021 The Author(s). Published by Elsevier Ltd.

Journal Author Rights

Please note that, as the author of this Elsevier article, you retain the right to include it in a thesis or dissertation, provided it is not published commercially. Permission is not required, but please ensure that you reference the journal as the original source. For more information on this and on your other retained rights, please visit: https://www.elsevier.com/about/our-business/policies/copyright#Author-rights

BACK

CLOSE WINDOW

List of publications related to this thesis

Journal Articles

- **Structural and physical properties of a new reversible and continuous thermochromic ionic liquid in a wide temperature interval:[BMIM]$_4$ [Ni(NCS)$_6$],** E. López Lago, J.A. Seijas, I. de Pedro, J. Rodríguez, M.Pilar Vázquez-Tato, J. A. González, E. Rilo, L. M. Segade, O. Cabeza, C. D. Rodríguez-Fenández, Y. Arosa, B. Algnamat, L. M. Varela, J. Troncoso and R. de la Fuente, *New J.Chem.,* **42**(19), 15561 − 15571 (2018).

Proceedings

- **White light spectral interferometer for measuring dispersion in the visible-near infrared**, Y. Arosa, C. D. Rodríguez-Fernández, B. S. Algnamat, E. López-Lago, and R. de la Fuente, in III International Conference on Applications in Optics and Photonics (AOP) 2017, Faro (Portugal). Proceeding in *Proceedings of Third International Conference on Applications of Optics and Photonics* **10453**, 104532R, 2017.

- **White light spectral interferometry for measuring dispersion of the thermo-optic coefficient of liquids**, C. D. Rodríguez-Fernández, Y. Arosa, B. S. Algnamat, E. López-Lago and R. de la Fuente, in XXXVI Reunión Bienal de la Real Sociedad Española de Física 2017, Santiago de Compostela (Spain). Proceeding in *Libro de Resúmenes de la XXXVI Reunión Bienal de la RSEF*, ISBN: 978-84-17219-78-9.

- **Estudio de la birrefringencia del cristal líquido iónico 1-etil-3-metilimidazolio decilsulfato**, C. D. Rodríguez-Fernández, Y.

Arosa, E. López-Lago, R. de la Fuente, P. Verdía and E. Tojo, in XII Reunión Nacional de Óptica (RNO) 2018, Castellón (Spain). Proceeding in *Libro de resúmenes XII Reunión Nacional de Óptica*, ISBN: 978-84-09-03559-5.

- **Interferometría de luz blanca resuelta espectralmente (ILBRE): una técnica para la obtención de la dispersión cromática en un amplio espectro**, Y. Arosa, C. D. Rodríguez-Fernández, E. López-Lago and R. de la Fuente, in XII Reunión Nacional de Óptica (RNO) 2018, Castellón (Spain). Proceeding in *Libro de resúmenes XII Reunión Nacional de Óptica*, ISBN: 978-84-09-03559-5.

- **Predicting refractive index dispersion of ionic liquids**, C. D. Rodríguez-Fernández, Y. Arosa, B. S. Algnamat, E. López-Lago, L. M. Varela, and R. de la Fuente, in Frontiers in Optics + Laser Science (FiO+LS) 2019, Washington D.C (USA). Proceeding in *Frontiers in Optics + Laser Science APS/DLS (OSA Technical Digest)*, **JTu4A.33**, (2019).

- **Outreaching in pandemic times: from schools to Social Networks**, C.D. Rodríguez-Fernández, B. Carnero, M. Canabal, D. Ínsua-Costa, A. Doval, A. Muñoz-Ramos, R. Sánchez-Cruz, R. Liñares, X. González-Iglesias, M.T. Flores-Arias, in XII Reunión Nacional de Optoelectrónica (OPTOEL) 2021, Online. Proceeding in *Libro de actas XII Reunión Española de Optoelectrónica*, ISBN: 978-84-18471-75-9.

- **Live Streaming Outreach: Twitch as an Alternative in Pandemic Times**, C.D. Rodríguez-Fernández, B. Carnero, M. Canabal, D. Ínsua-Costa, A. Doval, A. Muñoz-Ramos, R. Sánchez-Cruz, R. Liñares, X. González-Iglesias, M.T. Flores-Arias, in Hands-on Science (HSCI) 2021, Online. Proceeding in *Hands-on Science: Education Activities Challenges and Opportunities of Distant and Online Teaching and Learning*, ISBN: 978-84-8158-899-6.

324

- **Outreaching Optics During the COVID-19 Pandemic: From Face-to-Face to Social Networks**, C.D. Rodríguez-Fernández, B. Carnero, M. Canabal, D. Ínsua-Costa, A. Doval, A. Muñoz-Ramos, R. Sánchez-Cruz, R. Liñares, X. González-Iglesias, M.T. Flores-Arias, in Education and Training in Optics & Photonics Conference (ETOP) 2021, Online. Proceeding in *Education and Training in Optics & Photonics Conference 2021 (OSA Technical Digest)* **Th4A.3**, 2021.

- **A comprehensive transmedia activity to commemorate the International Day of Light 2021 on social networks**, C.D. Rodríguez-Fernández, B. Carnero, M. Canabal, D. Ínsua-Costa, A. Doval, A. Muñoz-Ramos, R. Sánchez-Cruz, R. Liñares, X. González-Iglesias, M.T. Flores-Arias, in European Optical Society Annual Meeting (EOSAM) 2021, Rome (Italy). Proceeding in *European Optical Society Annual Meeting, EPJ Web of Conferences* **255** (12003), 2021.

- **Ionic liquids as tunable refractive index fluids**, C. D. Rodríguez-Fernández, E. López Lago, C. Schröder and L. M. Varela, in European Optical Society Annual Meeting (EOSAM) 2021, Rome (Italy). Proceeding in *European Optical Society Annual Meeting, EPJ Web of Conferences* **255** (5002), 2021.

- **USC-OSA Student Chapter and USC-EPS Young Minds Section: our activities in 2020 and 2021**, C.D. Rodríguez-Fernández, B. Carnero, M. Canabal, D. Ínsua-Costa, A. Doval, A. Muñoz-Ramos, R. Sánchez-Cruz, R. Liñares, X. González-Iglesias, M.T. Flores-Arias, in XIII Reunión Nacional de Óptica 2021, Online. Proceeding in *Libro de Resúmenes de la XIII Reunión Nacional de Óptica*, ISBN: 978-84-09-37622-3.

This thesis is devoted to expand the current knowledge about the optical properties of ionic liquids, a family of tunable compounds which offers the unique opportunity to the field of photonics of designing materials with task-specific photonic responses. We aim to describe the key elements to tailor the optical response in ionic liquids, namely material dispersion, nonlinear optical response, absorption spectrum or liquid crystalline character, pointing out the clues which, in future, will facilitate their use as photonic materials. In order to accomplish this task, a hybrid experimental and computational methodology is employed, which allows us to understand the relation of the structure of ionic liquids at macroscopic, mesoscopic and microscopic scales with their optical response.